SANDIA REPORT

SAND2000-1559
Unlimited Release
Printed July 2000

Joining Si_3N_4 for Advanced Turbomachinery Applications

S. Jill Glass, Ronald E. Loehman, F. Michael Hosking, John J. Stephens, Paul T. Vianco, Mike K. Neilsen, Charles A. Walker, John P. Pollinger, F. Michael Mahoney, and Capt. Brian G. Quillen

Prepared by
Sandia National Laboratories
Albuquerque, New Mexico 87185 and Livermore, California 94550

Sandia is a multiprogram laboratory operated by Sandia Corporation, a Lockheed Martin Company, for the United States Department of Energy under Contract DE-AC04-94AL85000.

Sandia National Laboratories

Issued by Sandia National Laboratories, operated for the United States Department of Energy by Sandia Corporation.

Available to DOE and DOE contractors from
U.S. Department of Energy
Office of Scientific and Technical Information
P.O. Box 62
Oak Ridge, TN 37831

Telephone: (865)576-8401
Facsimile: (865)576-5728
E-Mail: reports@adonis.osti.gov
Online ordering: http://www.doe.gov/bridge

Available to the public from
U.S. Department of Commerce
National Technical Information Service
5285 Port Royal Rd
Springfield, VA 22161

Telephone: (800)553-6847
Facsimile: (703)605-6900
E-Mail: orders@ntis.fedworld.gov
Online order: http://www.ntis.gov/ordering.htm

DISCLAIMER

Portions of this document may be illegible in electronic image products. Images are produced from the best available original document.

SAND2000-1559
Unlimited Release
Printed July 2000

Joining Si_3N_4 for Advanced Turbomachinery Applications

S. Jill Glass* and Ronald E. Loehman
Ceramic Materials Department

F. Michael Hosking, John J. Stephens, and Paul T. Vianco
Joining, Coating, and Net Shaping Department

Mike K. Neilsen
Materials Mechanics Department

Charles A. Walker
Thin Film, Vacuum, and Packaging Department

Sandia National Laboratories
P. O. Box 5800
Albuquerque, NM 87185-0367

John P. Pollinger
Tetralux Engineering Services
334 Via Colusa
Redondo Beach, CA 90277

F. Michael Mahoney
Saint Gobain Abrasives
MS420-601
1 New Bond St.
Worcester, MA 01615-0008

Captain Brian G. Quillen
(formerly with Air Force Research Laboratory,
Kirtland Air Force Base, NM 87117)

Abstract follows.

* Primary author to contact for additional information.

Abstract

The main objective of this project was to develop reliable, low-cost techniques for joining silicon nitride (Si_3N_4) to itself and to metals. For Si_3N_4 to be widely used in advanced turbomachinery applications, joining techniques must be developed that are reliable, cost-effective, and manufacturable. This project addressed those needs by developing and testing two Si_3N_4 joining systems; oxynitride glass joining materials and high temperature braze alloys. Extensive measurements were also made of the mechanical properties and oxidation resistance of the braze materials. Finite element models were used to predict the magnitudes and positions of the stresses in the ceramic regions of ceramic-to-metal joints sleeve and butt joints, similar to the geometries used for stator assemblies.

Two silicon nitride materials (AlliedSignal's AS800 Si_3N_4 and Morgan Matroc's Si_3N_4) were successfully joined using compositions from the Y_2O_3-Al_2O_3-SiO_2 (YAS) and SiO_2-Al_2O_3-SrO (SAS) oxide glass systems. Both joining glass systems produced average room temperature four-point bend strengths in the 400 MPa range. The YAS glass composition also produced strong joints over an extended temperature range with strengths as high as 555 MPa at 1000°C. Oxynitride glass joining occurs by a mechanism of glass melting, substrate wetting by the molten glass, counter diffusion of elements from the glass into the substrate and from the substrate into the glass, and dissolution of silicon nitride into the glass, changing it from an oxide glass to an oxynitride glass. The change of joint composition that occurs with the YAS glass and the AS-800 silicon nitride appears to be very favorable with respect to the properties at elevated temperatures. Oxynitride glass joining compositions can be applied using dry powder, thermal spray, and a slurry coating techniques. Treatments to control joint thickness met with limited success due to the complex relationship between the glass viscosity, crystallization behavior, interactions with the fixturing, and sample alignment. Treatments to crystallize the joint require additional work to identify times and temperatures that produce phases that nucleate homogeneously and do not weaken the joint. Practical implementation of the oxynitride joining technology was demonstrated by joining combustor sections and cylindrical pieces.

The goal of the high temperature braze alloy part of the study was to identify a brazing process to attach a superalloy sleeve to a silicon nitride stud as part of the stator assembly of an advanced turboengine for operational temperatures of 926°C (1699°F) and moderate mechanical loads. Three braze alloys were investigated: 92Au-8Pd, 60Pd-40Ni, and 65Pd-35Co (wt.%). The evaluation metrics were wetting tests and room temperature and elevated four-point bend strength, and plug-in-ring shear strength tests. Two issues were identified as the primary "hurdles" to the realization of a suitable metal/ceramic joint. They were: (1) minimizing the interaction between Pd-containing brazes and the silicon nitride, and (2) the dissolution of the Ni-based and Fe-based metal alloys by the high temperature braze metal during joint fabrication. Interactions between the Pd-containing brazes and the ceramic were addressed by using: (1) braze alloys with

limited Pd content (92Au-8Pd), and (2) a 4.0 μm thick Ti layer sputtered on the silicon nitride that promoted wetting and spreading of the braze and had sufficient thickness to act as a barrier between the braze and the silicon nitride. Reducing the extent of base alloy dissolution was achieved by lowering the brazing temperature and minimizing the brazing time. Four-point bend tests were performed on AS-800/AS-800 joint specimens at room and elevated temperatures (200 to 950°C). The room temperature bend strength of AS-800/AS-800 specimens with 4.0 μm Ti and the Au-Pd braze was ~300 MPa; the failure path was in the joint. The same system had average strengths of ~200 MPa at 600°C, ~150 MPa at 800°C, just below 100 MPa at 900°C, and ~ 30 MPa at 950°C. A plug-in-ring (silicon nitride in Hastelloy-S) test configuration that resembles the stator assembly was assembled and shear tested. Joints made with Au-Pd+2V and Ti-coated silicon nitride and Au-Pd with a sputter deposited Ti coating and bare silicon nitride had shear strengths of 40-50 MPa. A study was performed that examined the response of joints to extended, high temperature exposure. Optical metallographic observations of the silicon nitride four-point bend bar after aging for 200 days at 950°C showed some migration of the interfacial Ti away from the silicon nitride. Nevertheless, no strength degradation was observed. Direct "active" metal brazing to AS800 was accomplished with an Au-Pd-V brazing alloy system. The VN reaction layer increased in thickness as the V concentration was increased from 2 to 4 wt.%. Excellent four-point flexure and plug-in-ring shear strengths, 520 MPa and 53 MPa, respectively, were obtained at room temperature with the Au-8Pd-V-brazed AS800 test specimens. High temperature aging, 950°C for 100 days, resulted in delamination at the VN reaction layer on an AS800 sample brazed with the Au-8Pd-3V alloy. Direct brazing of AS800 with a Ni-19Cr-10Si brazing alloy was also demonstrated.

Creep and tensile properties of the braze alloys (92Au-8Pd, 60Pd-40Ni, and 65Pd-35Co) were measured for use in Finite Element Analysis (FEA) stress predictions. Two creep regimes were observed for the Palni alloy (60Pd-40Ni); a low to intermediate temperature regime (~250-550°C) and a high temperature regime (~650-950°C). The data for this alloy fit a power law creep in both regimes. The stress exponents and the activation energies from a power law fit to the data in each regime suggest a transition from dislocation climb controlled creep at lower temperatures to solid solution strengthening controlled creep at higher temperatures. The Paloro alloy (92Au-8Pd) also exhibited two distinct creep regimes; the low temperature regime (250-550°C) data fit the Garofalo sinh equation and the high temperature regime (550-850°C) fit a power law equation. Oxidation behavior of the braze alloys and interlayer materials was measured to aid in the selection of the best materials for use in metal/ceramic brazing. Because of the superior oxidation resistance of the Paloro alloy and its promising creep resistance, its coefficient of thermal expansion and modulus measurements were also measured, along with those for Paloro ABA (active braze alloy). Weight losses measured for Paloro ABA during oxidation measurements and microstructural evaluations suggested that the vanadium in this braze alloy was reacting with oxygen to form volatile oxides. Oxidation tests on the two candidate interlayer materials, Kentanium Gr162B and a Kovar alloy showed that Kentanium has better oxidation resistance.

Two types of joints that are commonly used in the stator assemblies are butt joints in which the end of a metal rod is brazed to the end of a ceramic rod, and sleeve joints in which a ceramic rod is brazed to the inside of a metal sleeve. Axisymmetric finite element models of braze joints between silicon nitride and a variety of metals were developed to study both configurations. Results from the butt joint analyses indicated that the use of single interlayers could either increase or reduce the residual stress levels generated in the silicon nitride, depending on the interlayer thickness. The use of composite interlayers between the base metal and silicon nitride dramatically reduced the residual stress levels in the silicon nitride when certain layer thickness combinations were used. Results from the sleeve joint analyses indicated that modifications to the metal sleeve and silicon nitride post geometry could have a significant effect on the residual stress state generated during the brazing operation.

Table of Contents

Introduction

Chapter 1. Oxynitride Glass Joining

Chapter 2. Metal/Ceramic Brazing

Chapter 3. Braze and Interlayer Properties

Chapter 4. Finite Element Analysis of Metal-to-Ceramic Brazing

Introduction

The purpose of the three-year (Sept. 1993 to Nov. 1996) Cooperative Research and Development Agreement (CRADA) between AlliedSignal Inc. (Allied) and Sandia National Laboratories (Sandia) was to develop reliable, low-cost, commercially viable techniques for joining silicon nitride (Si_3N_4) to metals. These joining techniques will facilitate the use of advanced materials (Si_3N_4 ceramics) in turbomachinery applications. Background information, information about the benefits to both Allied and Sandia, and a summary of the technology that was developed are included below in copies of Appendix A from the Cooperative Research and Development Agreement No. SC93/01199 and the Project Accomplishments Summary (~Sept. 24, 1997). The body of the report is divided into the following four chapters:

- Ch. 1. Oxynitride Glass Joining
- Ch. 2. Metal/Ceramic Brazing
- Ch. 3. Braze and Interlayer Praperties
- Ch. 4. Finite Element Analysis of Metal-to-Ceramic Brazing.

Appendix A for CRADA No. SC93/01199 (June 22, 1993).

Joining Si_3N_4 for Advanced Turbomachinery Applications

The main objective of this project is to develop reliable, low-cost techniques for joining silicon nitride (Si_3N_4) to itself and to metals. Si_3N_4 is being promoted for use in advanced turbomachinery because of its superior oxidation resistance and mechanical properties at high temperatures compared to many metals. Si_3N_4 ceramics are proposed for use as stators, airfoils, rotors, and seal plates in advanced, fuel-efficient turbomachinery. They will also be useful as high-temperature erosion control valves for jet engines and as light-weight components in aerospace actuator mechanisms.

Most high-temperature structural applications using Si_3N_4 ceramics require that they be joined to metals at some point. Techniques for making joints with acceptable properties at an affordable cost are not generally available. For Si_3N_4 to be widely used, joining techniques must be developed that are reliable, cost-effective, and manufacturable. This project will address those needs by developing suitable Si_3N_4 joining methods.

AlliedSignal Inc. (Allied) is a major manufacturer of turbomachinery for use in aerospace, military, automotive and industrial applications. Allied's Garrett Auxiliary Power Division (now known as Ceramic Components Division) has immediate requirements for turbine engines with a higher thrust-to-weight ratio and high fuel efficiency. Internal corporate technology assessments, as well as those conducted as part of the Departments of Energy's Advanced Turbine Technology Applications Project (ATTAP), clearly indicate that Si_3N_4 ceramics offer the highest potential for meeting these advanced heat engine objectives. Recent tests have shown that the high-erosion resistance of Si_3N_4 turbine stators can significantly extend the life and reduce the maintenance costs of auxiliary power supplies used to provide aircraft with power while on the ground. This particular application offers an important opportunity for the near-term commercial deployment of advanced ceramics in turbine engines and for the collection of valuable engineering reliability data on the in-field performance of ceramics.

This collaboration combines Sandia's expertise in joining, high-temperature phase behavior, and finite element modeling with Allied's special capabilities in Si_3N_4 fabrication, materials processing, and scale-up and commercialization. The project is divided into two parts. Allied will take the lead in the development of reliable, manufacturable techniques for high strength joints for ceramic turbocharger wheel/shaft assemblies. The development of this joining technology will reach a decision point for commercialization at the end of the first year of the project. Sandia will concentrate its efforts on developing practical methods for making strong Si_3N_4-metal joints that survive much higher temperatures than those currently in use. The higher-temperature joint development is on a longer time line that that has decision points on scale-up and commercialization at the ends of the second and third years of the project.

Project Accomplishments Summary

Title: **Joining Si_3N_4 for Advanced Turbomachinery Applications**

Background

The US share of the world aircraft turbine market has dropped from 70 percent in 1970 to 50 percent today. The aircraft engine industry is extremely competitive internationally, and small improvements in quality and performance can result in an extremely rapid gain in market share. The development of advanced materials and process techniques to improve the performance of aircraft engines will allow US aircraft engine manufacturers to compete against heavily subsidized, foreign companies. One area where improvements can be made is in the development of joining technology in the aircraft engine manufacturing process.

Si_3N_4 is being promoted for use in advanced turbomachinery because of its superior oxidation resistance and mechanical properties at high temperatures compared to most metals. These qualities make Si_3N_4 ideal for use as stators, airfoils, rotors, and seal plates in advanced, fuel-efficient turbomachinery. Most high-temperature structural applications require Si_3N_4 to be joined to metals; however, techniques for making Si_3N_4-metal joints with acceptable properties at an affordable cost are not readily available. For Si_3N_4 to be widely used, joining techniques must be developed that are reliable, cost-effective, and manufacturable.

Prior to initiation of the project, the state-of-the-art for ceramic to metal joining was braze materials that were limited to operating temperatures below 400°C. Also, there were no suitable joining technologies for joining materials such as Si_3N_4 to itself to allow simple ceramic shapes to be bonded together to produce complex shapes such as combustors, stator vane rings, and fuel nozzle shrouds. The laboratory expertise(s) that Sandia provided to this program, complementing Allied Signal's capability to make and test high strength, high reliability Si_3N_4, included the following:

- braze preparation and processing,
- braze mechanical characterization,
- and the capability to perform finite element analyses of braze joint configurations for ceramic to metal joining.

Sandia's capabilities for designing, preparing and characterizing novel glass bonding materials, and applying these materials to real Si_3N_4 parts, using techniques such as thermal spraying, were essential for the ceramic to ceramic bonding part of the program.

By combining the ceramic joining expertise and experience of Sandia National Laboratories and Allied Signal, CRADA 1199 seeks to improve the competitiveness of the structural ceramics industry and to extend the range of applications which utilize structural ceramics, resulting in improved energy efficiency and reduced environmental impact.

Description:

The purpose of this collaboration was to develop reliable, low-cost, commercially viable techniques for joining silicon nitride (Si_3N_4) to metals and Si_3N_4 to itself. These joining techniques will facilitate the use of advanced materials (Si_3N_4 ceramics) in turbo machinery applications. Allied Signal's role was to develop brazes and processes that could be used to extend the low temperature range of joining technologies (cryogenic to 400°C). Sandia's role was to extend the high temperature range of joining capabilities (400°C to 1370°C). Sandia performed the low temperature testing, and Allied Signal provided the high-temperature mechanical testing.

This program has made significant contributions to advancing the knowledge and capabilities for processing and modeling ceramic-ceramic and ceramic-metal joints for a wide range of commercial applications. Our approach has been a multi-pronged effort to develop and evaluate high-temperature braze alloy joints, oxynitride glass joints, and ceramic joints from pre-ceramic polymers. We achieved success with each approach and focused our efforts on the first two. We have developed metal braze joints with 900°C strengths as high as 50% the room-temperature joint strength of 350 MPa - 370 MPa. For reference, the room temperature strength of the ceramic is between 550 MPa and 700 MPa. The impressive high-temperature strengths of the oxynitride joints are more than double any previously reported for this temperature. These joint materials also exhibit excellent creep-rupture properties at temperatures as high as 900°C. A spray-coating technique that will allow oxynitride joints to be produced between ceramic components with complex shapes that cannot be manufactured in one piece was developed. CRADA 1199 also developed the capability to model residual stresses in ceramic-metal braze joints with various geometries. The models account for the creep and plastic behavior of the brazes using a unified creep-plasticity model incorporating data obtained at Sandia. The braze property data required to accurately model residual stresses are generally not readily available. The finite element models have been very helpful for suggesting geometrical and materials modifications that reduce residual stresses.

The success and demonstrated performance of the developed high-temperature, ceramic-metal braze and ceramic-ceramic oxynitride glass joining techniques are allowing Allied Signal to begin planning evaluation for application of these technologies into a variety of current and future aerospace that will result in the incorporation and exploitation of advanced structural ceramics.

Benefits to the Department of Energy:

One of the major technologies proposed by DOE/DP laboratories is the incorporation of advanced materials into structural systems. Structural composites and bonded interfaces are present in all weapons systems. The joining technology developed in this project enhances the joining capabilities for existing combinations of materials used in various weapons components and systems. Additionally, the application of these design tools should lead to improved fabrication techniques and better reliability in future designs. The materials, process, and finite element models developed in this program enhance our abilities to design and characterize interfaces used in nuclear weapons systems. For example, the next generation neutron tube (MC4300) may utilize a braze alloy that is similar

in composition and contains the same active element that was developed in this program for Si_3N_4 joining. Utilizing glasses similar to the oxynitride glass developed in this program may also allow additional flexibility in the use of cermet-containing components, currently difficult to produce with complex geometries. A wide variety of experimental programs of interest to DOE/DP will also benefit from the bonding techniques and processes developed in this collaboration.

Economic Impact:

The braze and glass joining technologies developed by Sandia plan to be utilized by Allied Signal to protect and grow its US manufacturing operations for aerospace and potentially automotive turbo-machinery. Although it is impossible to estimate a quantitative economic impact, Allied Signal's current aerospace turbo-machinery business is approximately $2.5 billion per year. In addition, the performance of automotive hybrid vehicle turbo-generators can be driven towards the desired performance and manufacturing cost goals by utilizing structural ceramics in the turbine hot sections. Again, this was enabled by the advanced joining technologies, opening up a potentially huge market for Allied Signal and the US car manufacturers. Further elaboration is as follows:

- A number of current aerospace applications at Allied Signal are being evaluated for implementation of silicon nitride components where the Sandia-developed joining technologies are now a potential enabler for the silicon nitride material substitution. Ceramic-metal seals have been demonstrated to result in order of magnitude improvement in seal performance on rotating turbo-machinery such as jet turbofan engines, aircraft auxiliary power turbines, and industrial power generation turbines. Poor seal performance in turbo-machinery such as jet engines is one of the major repair and warranty costs for these engines. A significant limiter and cost driver for implementing the ceramic-metal seal technology is the lack of low-cost and rigorous attachment techniques.

- Allied Signal is the world's largest manufacturer of aircraft auxiliary power turbine units, APUs, with 75% of the market. They are at the forefront in developing and implementing structural ceramics in gas turbines to raise operating temperatures (resulting in significant improvements in fuel economy, output power, and reduction in unit size) and improve hot-section, component durability compared to current superalloy metal components such as blades, nozzles, and turbine wheels. Allied Signal is currently demonstrating significant durability and performance improvements by inserting silicon nitride nozzles in commercial passenger aircraft APUs such as Alaska Airlines Douglas MD-80s. The silicon nitride components are being held back from commercialization because twenty-three individual nozzles are required for each APU and the resulting combined cost of the nozzles and required supporting metallic mechanical glass technologies now allow them to consider fabricating one piece rings of twenty-three brazed or glass bonded nozzles, or sub-elements, which will allow significant reductions in supporting metal attachment structure costs and help move towards low enough costs to achieve commercialization.

- Allied Signal Ceramic Components is also supporting potential efforts in liquid fueled rocked engine applications where silicon nitride components are being proposed for the combustion section structures. These are complex and large structures and will require multiple high temperature attachments between ceramic components and between ceramic and metal components. The availability of these new braze and oxynitride glass bonding technologies are

now allowing these component applications to be proposed and development/evaluation pursued in conjunction with US rocket engine manufacturers.

- Finally the US big three automotive manufactures and the US government are pursuing advanced hybrid electric automotive vehicles. One potential hybrid propulsion power system being developed is the turbo-generator. Allied Signal is involved in many aspects in developing automotive turbo-generators, from developing and supplying structural ceramic components to turbo-generator developers Allison Engine Co. and Teledyne, to also developing and demonstrating complete turbo-generators for Ford. The silicon nitride ceramic components for these turbo-generators require low cost and rigorous ceramic-ceramic and ceramic-metal attachments as the turbo-generators' cost must be very low to achieve automotive commercialization (costs at least 10X less than aerospace costs). The Sandia technologies again have become enablers for consideration to allow low-cost attachments for silicon nitride turbine wheels to metal shafts and to allow simplified fabrication of complex thin-wall shaped silicon nitride components such as combustors and turbine scrolls. The silicon oxynitride glass bonding technology is being evaluated as an effective technique to join simple shaped partial sections of combustors or scrolls into the very complex final turbo-generator final components.

Project Status:

The project is complete. CRADA 1199 started September 1993, and completed November 1996.

ADDITIONAL INFORMATION

Sandia National Laboratories/Department of Energy Facility Point of Contact for Information on Project

S. Jill Glass
Sandia National Laboratories
P.O. Box 5800 MS 0367
Albuquerque, NM 87184-0367
Tel: (505)845-8050
Fax: (505)844-4816
sjglass@sandia.gov

Company Size and Points of Contact

Allied Signal, Inc.
Annual Sales: (1996) $15 billion
Number of Employees: 85,000
Point of Contact: Dr. John Pollinger
Ceramic Components
2525 W. 190th St.
P.O. Box 2960
Torrance, CA 90509-2960
Tel: (310)512-5654
Fax: (310)512-5901

Project examples

Photos of silicon nitride turbo-generator combustors, the APU ceramic nozzles and their performance benefits, a corresponding picture of a one-piece metal nozzle ring, turbine engine starter wheels with the braze shaft attachment, and a turbine engine thermocouple sheath requiring a high temperature braze attachment to Kovar metal are available from AlliedSignal.

Technology Commercialization

The first step to commercializing the two joining technologies, which is to demonstrate effective technology transfer from Sandia to Allied Signal, was completed at the end of the first quarter of 1997.

The second step is to disseminate the capability of the two joining technologies to the various end-use applications and materials engineers (in process during 1996). In addition there are plans to perform more extensive applications and test cell evaluations of the joint technologies for applications including turbine combustor and scroll joining for automotive turbo-generators. APU design engineers are currently examining modified APU nozzle and nozzle attachment designs that would potentially take advantage of the braze and oxynitride glass joining technologies to achieve lower costs and better performance. A number of other Allied Signal proprietary turbo-machinery applications that can benefit from structural ceramics implementation are currently being investigated. This investigation will require joining technologies.

Metal-to-ceramic brazing is being investigated for a variety of defense, automotive, and aircraft applications. Two common types of joints are butt joints in which the end of a metal rod is brazed to the end of a ceramic rod, and sleeve joints in which a ceramic rod is brazed to the inside of a metal sleeve. Axisymmetric finite element models of braze joints between silicon nitride and a variety of metals were developed to study both butt joints and sleeve joints. Results from the butt joint analyses indicated that the use of single interlayers could either increase or reduce the residual stress levels generated in the silicon nitride depending on the thickness of the interlayer. The use of composite interlayers between the base metal and silicon nitride dramatically reduced the residual stress levels in the silicon nitride when certain layer thickness combinations were used. Results from the sleeve joint analyses indicated that modifications to the metal sleeve and silicon nitride post geometry could have a significant effect on the residual stress state generated during the brazing operation.

Chapter 1. Oxynitride Glass Joining

I. Objectives

A. Applications

Applications for ceramic-ceramic joining using oxide and oxynitride glasses include those where simple shape pieces of ceramic are bonded together to allow the fabrication of complex shapes that cannot be manufactured as one piece. This joining capability will help overcome the need for the expensive, low-yield forming processes used to produce complex shapes. Specific applications of Si_3N_4-Si_3N_4 joining technology of interest to our industrial partner include automotive turbogenerator combustors and turbine blade doublets for the Harrier Jet Engine (Fig. 1). Our objectives in this part of the CRADA study were to produce joints with high strength over a wide range of temperatures using an oxide glass that is transformed into an oxynitride glass during the joining process and to identify processing strategies to improve its thermal stability.

B. Joining and Performance Requirements

The primary processing requirement for joining is that the joining glass melts and bonds at temperatures below that at which Si_3N_4 degradation begins (~1800°C). The glass must not degrade the properties of the Si_3N_4. To facilitate the use of the glass in a manufacturing environment the joining process must not require significant applied pressures or hot-isostatic pressing. The joining glass must also be applicable to complex shapes in a reproducible manner.

The primary performance requirements are that the joining glass produces bonds that exhibit good strength relative to the base Si_3N_4 at both low temperature and elevated temperatures. As a reference point the room temperature four-point bend strength of AlliedSignal AS-800 Si_3N_4 is 872 MPa and the 1400°C four-point bend strength is 621 MPa. For sustained use the glass must exhibit good thermal stability and retain its strength after exposure to high temperatures and thermal cycling.

C. Materials

Two Si_3N_4 materials were the primary focus of this study. The first was Allied Signal's AS-800 Si_3N_4 joined with compositions in two glass systems (Sections III.A) and the second was Morgan Matroc's Si_3N_4 joined with two Sr-Celsian based glasses (Section III.B). A limited number of joining experiments was also conducted with Allied Signal's GS-44 Si_3N_4 (Section III.A) and the SiAlON-based glass composition (YAS-2) selected for optimization with AS-800 Si_3N_4 (Section VIII.A.7).

II. Background

There are four general classes of techniques for joining ceramics to metals or ceramics to ceramics. These include mechanical attachments such as press-fits, braze filler metals, oxide and oxynitride glass compositions, and diffusion bonding A general review of ceramic joining can be found in Ref. 1. Specifics for Si_3N_4 joining techniques can be found in Ref. 2. Information on oxide and oxynitride joining technique can be found in Ref. 3-7. General information on the processing and properties of oxynitride glasses can be found in Ref. 8-10. Room temperature and high temperature strength results for various silicon nitride joining methods are described below and shown in Fig. 2.

Early studies of oxynitride glass joining Si_3N_4 by Johnson and Rowcliffe showed maximum room temperature strengths of ~460 MPa.[11] Johnson and Blum joined Si_3N_4 using preceramic polymers.[12] The maximum strength at room temperature was 240 MPa, and the average strength at 1000°C for the best joining conditions (joining temperature = 1750°C) was 146 MPa. Ceccone et al. used the partial transient liquid phase bonding method for producing joints.[13] The average and maximum room temperature strengths were 566 and 698 MPa (97% of the Si_3N_4

strength), respectively. An average strength of 128 MPa, representing 18% of the Si_3N_4 strength, was retained up to 800°C in air. In work by Peteves and Suganuma,[14] solid state bonding of Si_3N_4 ceramics was achieved using Fe-Cr Alloy interlayers. The average strength at room temperature was 770 MPa and at 900°C it was 200 MPa. Hadian and Drew brazed Si_3N_4 with Ni-Cr-Si alloys.[15] The best average room temperature strength was 118 MPa and the average strength at 900°C was 220 MPa. The increased strength at the higher temperature was attributed to the reduction in the mismatch strain. Suganuma showed the bend strength of a Mo joint between two pieces of Si_3N_4 was ~360 MPa at room temperature and 200 MPa at 1000°C.[16] In the oxynitride approach used by Takeuchi et al.,[17] Y_2O_3-Al_2O_3-SiO_2 (YAS) joints produced without a hot isostatic pressing (HIP) treatment gave room temperature and 1200°C temperatures of 250 and 160 MPa respectively. Following a HIP treatment, the room temperature and 1200°C strengths were improved to 620 and 370 MPa, respectively. Further optimization of the oxynitride joining process using a composition assumed identical to the Si_3N_4 grain boundary gave a maximum strength at 1250°C of 640 MPa after a HIP treatment at 1800°C. This strength corresponds to 82% of the Si_3N_4 strength.

The joint thickness and crystallinity may be important for optimizing the strength and thermal stability. Johnson's and Rowcliffe's study indicated that joint strength was optimized at a joint thickness of 20-25 μm.[18] Joints less than ~25 μm allowed oxynitride crystals to grow across the joint improving the strength relative to thicker joints. Lower strengths measured for thinner joints were attributed to incomplete glass coverage.

Walls and Ueki used an adhesive with a β-SiAlON:glass ratio of 60:40 and showed that by controlling the joining pressure to a pressure above ~2 MPa, the room temperature strength could be optimized at 650 MPa.[19] The applied pressure was believed to be necessary to ensure homogeneous spreading of the β-SiAlON glass adhesive and to reduce the likelihood of pore formation during densification of the adhesive layer. Both Walls' and Takeuchi's studies indicated that a post-HIPing procedure produced strength improvements relative to the pressureless joining procedure. Walls found a strength of ~975 MPa after HIPing.

III. Si_3N_4 Materials and their Respective Joining Glass Systems

A. AlliedSignal's AS-800 and GS-44 Si_3N_4 (Compositions and Properties)

Allied Signal's AS-800 and GS-44 grades of Si_3N_4 were used in this study. Most of the work focused on joining the AS-800 Si_3N_4. The compositions of the two materials are shown in Table 1 and their properties are shown in Table 2. Representative microstructures of these and similar materials can be found in Ref. 20 and 21.

Table 1. Compositions of AlliedSignal[i] GS-44 and AS-800 Si_3N_4.

Material	Composition (wt%'s)
GS-44 Si_3N_4	8% Total (Y + M + A)
AS-800 Si_3N_4	5.1 AO, 1.7 Y_2O_3, 1.2 BO, 3.42 SiO_2

AO and BO are proprietary sintering aids.

[i] AlliedSignal Inc., Ceramic Components, Torrance, CA.

Table 2. Properties of Allied Signal's AS-800 and GS-44 Si_3N_4.

Property	Sintered AS-800 Si_3N_4	Sintered GS-44 Si_3N_4
Flexural strength (4-pt bend) (MPa)		
Room Temp	872	1028
900°C		697
1040°C		621
1100°C		437
1200°C	687	
1300°C	646	
1400°C	621	
Weibull modulus (room temp.)	>20	31.4
Fracture toughness @ 20°C (MPa√m)	9.0	8.1
Thermal conductivity (W/mK)		
20°C	80	35
1400°C	25	
Density (g/cm^3)	3.3	3.2
Elastic modulus (GPa)	310	310
Vickers Hardness @ 10 kg load (kg/mm^2)	1650	1460
Thermal expansion coeff., 50-1000°C ($x10^{-6}$/°C)	3.6	3.4
Slow crack growth threshold (% fast fracture)		
900°C		>60%
1040°C		>60%
1100°C		>50%
1204°C	>90%	
1371°C	>83%	
Tensile creep life (max stress for >1000 hr life) (MPa)		
1250°C	212	
1300°C	140	
1370°C	90	

A.1 Oxide and Oxynitride Glass Joint Compositions Based on the AS-800 Additives

Two series of oxide joining compositions based on the sintering additives in AS-800 were chosen to study the formation of amorphous or crystalline phases during joint processing. Each series contains 20-100 vol% of the additive components, which were present at a constant vol% ratio relative to each other, plus Si_3N_4. The two series of compositions are designated LY (Table 3) and LYSS (Table 4). The LY series contained the three major additives in the AS-800 Si_3N_4 (AO, Y_2O_3, SiO_2)[ii] and the LYSS series contained all five additive components (AO, Y_2O_3, SiO_2, BO). The Si_3N_4 was Ube E10 Si_3N_4 powder containing 1.22 wt% oxygen.

[ii] Although no separate SiO_2 is added to the glass powder, SiO_2 appears as an additive because it is present in the Si_3N_4 powder. AO and BO are proprietary sintering oxides.

Table 3. LY series of glass compositions.

Comp. Designation.		Si_3N_4	SiO_2	AO	Y_2O_3	Totals
LY-20	v/o compounds	80	7.5	8.7	3.8	100
(20 vol%	wt. powders	261.2	10.6	56.6	18.8	347.2
additives)	wt% powders	75.2	3.1	16.3	5.4	100
LY-40	v/o comps.	60	15.1	17.4	7.5	100
(40 vol%	wt. pwdrs.	195.9	28.7	113.2	37.6	375.5
additives)	wt% pwdrs.	52.2	7.7	30.2	10.0	100
LY-60	v/o comps.	40	22.6	26.1	11.3	100
(60 vol%	wt. pwdrs.	130.6	46.8	169.8	56.5	403.7
additives)	wt% pwdrs.	32.348	11.599	42.069	13.984	100
LY-80	v/o comps.	20	30.2	34.8	15.0	100
(80 vol%	wt. pwdrs.	65.3	64.9	226.4	75.3	431.9
additives)	wt% pwdrs.	15.2	15.0	52.4	17.4	100
LY-100	v/o comps.	0	37.7	43.5	18.8	100
(100 vol%	wt. pwdrs.	0	83.0	283.1	94.1	460.2
additives)	wt% pwdrs.	0	18.0	61.5	20.4	100

Table 4. LYSS series of glass compositions.

Comp. Designation		Si_3N_4	SiO_2	AO	Y_2O_3	BO	SiC	Totals
LYSS-20	v/o comps.	80	7.5	6.2	2.7	2.0	1.5	
(20 vol%	wt. pwdrs.	261.2	10.6	40.6	13.5	9.6	4.8	340.3
additives)	wt% pwdrs.	76.8	3.1	11.9	4.0	2.8	1.4	
LYSS-40	v/o comps.	60	15.1	12.5	5.4	4.1	3.0	
(40 vol%	wt. pwdrs.	195.9	28.7	81.2	27.0	19.2	9.5	361.5
additives)	wt% pwdrs.	54.2	7.9	22.5	7.5	5.3	2.6	
LYSS-60	v/o comps.	40	22.6	18.7	8.1	6.1	4.4	
(60 vol%	wt. pwdrs.	130.6	46.8	121.8	40.5	28.7	14.3	382.8
additives)	wt% pwdrs.	34.1	12.2	31.8	10.6	7.5	3.7	
LYSS-80	v/o comps.	20	30.2	25.0	10.8	8.2	5.9	
(80 vol%	wt. pwdrs.	65.3	64.9	162.4	54.0	38.3	19.1	404.0
additives)	wt% pwdrs.	16.2	16.1	40.2	13.4	9.5	4.7	
LYSS-100	v/o comps.	0	37.7	31.2	13.5	10.2	7.4	
(100 vol%	wt. pwdrs.	0	83.0	203.0	67.5	47.9	23.8	425.3
additives)	wt% pwdrs.	0	19.5	47.7	15.9	11.3	5.6	

A.2 Oxide Glass Joint Compositions in the SiAlON System

SiAlON[iii] based compositions were also chosen because they form larger volumes of liquid phase at lower temperatures than the compositions in A.1. The solution of Al and O into the Si_3N_4 substrate is expected to decrease the volume of amorphous phase in the joint after bonding. Y_2O_3, which is one of the sintering additives in AS-800, can, in the presence of Al and O, form a solid solution with Si_3N_4 (Y-SiAlON). Three series of compositions from the Si_3N_4-SiO_2-Al_2O_3-AlN phase diagram in Fig. 3 were selected.

(A) Oxide-based
Composition located on the SiO_2-Al_2O_3 tie-line in Fig. 3.(B) Si_3N_4-based
Based on the composition located on the tie-line between the Si_3N_4, which contains about 5 mol% SiO_2, and Al_2O_3.
(C) β-SiAlON-based
Compositions in the β'-SiAlON solubility region shown in Fig. 3.

Each series of compositions contained three different levels of Y_2O_3 (0, 10, and 30 wt%) as shown in Table 5. The A-2 and A-3 glasses were also called YAS-1 and YAS-2 respectively. A composition called YAS-3 with less SiO_2 than A-3 was later added based on the assumption that it would produce a less viscous glass (less SiO_2).

Table 5. Glass powder compositions in wt%.

Designation	Composition (wt%)				
	Y_2O_3	Al_2O_3	SiO_2	AlN	Si_3N_4[iv]
A-1	0	30	70	-	-
A-2 (YAS-1)	10	27	63	-	-
A-3 (YAS-2)	30	21	49	-	-
YAS-3	40	30	30		
B-1	0	42.8	-	-	57.2
B-2	10	38.5	-	-	51.5
B-3	30	30.0	-	-	40.0
C-1	0	47.84	-	19.23	32.93
C-2	10	43.06	-	17.3	29.64
C-3	30	33.49	-	13.46	23.05

B. Morgan Matroc's[v] Si_3N_4

Morgan Matroc's commercial, hot-pressed Si_3N_4 containing Y_2O_3 and Al_2O_3 as densification aides was used. Property data provided by the manufacturer are shown in Table 6. Electron microprobe analysis of the Si_3N_4 grain boundary composition revealed an average composition of approximately 5 wt% Al_2O_3. Analysis of the Y_2O_3 content was less conclusive, but it can reasonably be estimated at 10 wt%. This gives an overall grain boundary composition of 5 wt% Al_2O_3, 10 wt% Y_2O_3, and 85 wt% Si_3N_4.

[iii] SiAlONs are solid solutions of Al and O in Si_3N_4 of the formula $Si_{6-z}Al_zON_{8-z}$ (up to z values of 4.2).
[iv] Contains ~3.43 wt% SiO_2.
[v] Morgan Matroc Ltd., Bewdley Road Stourport-on-Severn, Worcestershire DY13 8QR England

Table 6. Morgan Matroc Si_3N_4 properties.

Property	Value
Density	3.3 g/cm^3
Open Porosity	0 %
Flexural Strength @ 20°C	850 MPa
Thermal Conductivity @ 20°C	18 W/m K
Thermal Expansion Coefficient 20-1000°C	3.3 x10^{-6}/°C
Thermal Shock Resistance	>600 ΔT (°C)
Specific Heat	800 J/kg K
Maximum Use Temperature	1100°C

** Provided by manufacturer

B.1 Sr-Celsian Based Glasses

Two compositions were chosen in this glass system because of their potential for crystallizing into monoclinic celsian (with the stoichiometric composition $SrO\text{-}Al_2O_3\text{-}2SiO_2$) at temperatures above 1000°C. Figure 4 shows the phase diagram for the SrO, SiO_2, Al_2O_3 ternary, along with the positions of the SAS-5 and SAS-10 glasses.[22] The other advantages of the celsian phase as a joining material include thermal stability, high melting point (1710°C)[23], and a low coefficient of thermal expansion (CTE) of 2.29x10^{-6}/°C. SiO_2, SrO, and Al_2O_3 powders were used to make the glass compositions. Compositional data and thermal expansion coefficients measured for these glass samples are shown in Table 7.

Table 7. Oxide glass compositions for joining Morgan Matroc Si_3N_4.

Sample	SiO_2:SrO:Al_2O_3 (wt%)	SiO_2:SrO:Al_2O_3 (mol%)	CTE (x10^{-6}/°C)
SAS-5	51:44:5	64:32:4	8.54
SAS-10	49:41:10	62:31:7	8.46

IV. Preliminary Evaluation of Joining Glass Compositions

A. AS-800 Si_3N_4 Joining Systems

A.1 Oxide and Oxynitride Glass Joint Compositions Based on the AS-800 Additives

Preliminary experiments were run at 1600 and 1700°C with four compositions *similar* to those described in Section III.A.1 to investigate the effect of different components on the formation of amorphous or crystalline phases during processing.
(1) AO, Y_2O_3, SiO_2 (main oxide additive components of AS-800 Si_3N_4)
(2) AO, Y_2O_3, SiO_2, BO (main AS-800 additive components + BO)
(3) AO, Y_2O_3, SiO_2, and Si_3N_4 (main AS-800 additive components + Si_3N_4)
(4) AO, Y_2O_3, SiO_2, BO, and Si_3N_4 (main AS-800 additive components + BO + Si_3N_4)

Only the compositions from (4) formed a significant amount of amorphous phase. The crystalline phases detected at both temperatures were $M_{10}(SiO_4)_6O_2$, which is a disilicate phase, and $M_{10}(SiO_4)_6O_2$, which is an apatite phase (M is a generic metallic element). The other samples showed only the disilicate phase at both temperatures, except for compositions from (3), which contained both at 1700°C.

Further evaluations of glasses in this system using the LY and LYSS series of compositions in Tables 3 and 4 showed that although the LYSS compositions adhered to the Si_3N_4 above 1500°C, there was significant decomposition after holding at 1500-1650°C for 30 min in atmospheric nitrogen. This was attributed to furnace leaks. The apatite phase (identified as the H-phase), which is also found in the AS-800 material, was identified in these glasses. Because insufficient glass was found for the above compositions, the SiO_2 content was lowered. Even at 1600°C, SiO_2 remains relatively viscous and prevents the formation of a glassy liquid that can be quenched to form a bulk glass. Because of the success with the YAS SiAlON glass compositions (Section IV.A.2), no further research was conducted on the LY and LYSS compositions.

A.2 Oxide Glass Joint Compositions in the SiAlON System

Glasses were prepared by mixing the appropriate weight percents of the oxide constituents shown in Table 5. The glass material was formed by melting 300 g of oxide powder in a platinum crucible at 1600°C for four hr and fritting into water. The glass frit was subsequently annealed at 920°C for three hr. The annealed glass frit was then milled by a motorized mortar and pestle and air-classified to a particle size range of 10-45 μm. Experiments were conducted by heating at 30°C/min to temperatures between 1300 and 1700°C in static N_2. A summary of the results for experiments with these nine compositions is shown in Table 8.

Table 8. Results summary for the nine glass compositions shown in Table 5.

	Starting Composition		Sintered Composition		Bonded Compositions		Joined Compositions		
	Starting powders (wt.%)	Chemical Composition (XRD)	Processing Parameters	Chemical Composition (XRD)	Processing Parameters	Chemical Composition (XRD)	Processing Parameters	Description of Joint Region (SEM)	Chemical Composition (EDS) Al/Si/Y/La
A-1	30 Al_2O_3 70 SiO_2	Al_2O_3 SiO_2	---	---	---	---	---	---	---
A-2	27 Al_2O_3 63 SiO_2 10 Y_2O_3	Y_2O_3 Al_2O_3	1550°C 30 m N_2	SiO_2 $Al_6Si_2O_{13}$ (glass)	1550°C 30 m N_2	SiO_2 $Al_6Si_2O_{13}$ (glass)	1550°C 30 m N_2	glass isolated mullite grains (isolated silica grains)	26/64/10/yes 79/20/ 1 /no
A-3	21 Al_2O_3 49 SiO_2 30 Y_2O_3	Y_2O_3 Al_2O_3	1400°C 30 m N_2	SiO_2 (glass) $(Al_6Si_2O_{13})$ $(Y_3Al_5O_{12})$ Y-Si-O	1400°C 30 m N_2	SiO_2 (glass) $(Al_6Si_2O_{13})$	1400°C 30 m N_2	glass isolated SiO_2(-Al, Y) grains isolated Y-Si-O crystals	30/50/20/yes 3/95/ 2 /no 0/47/53/no
B-1	42.8 Al_2O_3 57.2 "SN"	α-Si_3N_4 Al_2O_3	1600°C 30 m N_2	β'-SiAlON α-Si_3N_4 Al_2O_3	1700°C 30 m N_2	β'-SiAlON β-Si_3N_4 (w)	---	No bonding, no joining insufficient L phase; note incomplete Rx after sinter	---
B-2	38.5 Al_2O_3 10 Y_2O_3 51.5 "SN"	α-Si_3N_4 Al_2O_3 Y_2O_3	1600°C 30 m N_2	β'-SiAlON (glass)	1700°C 30 m N_2	β'-SiAlON (glass)	1700°C 30 m N_2	glass small grains (SiAlON)	similar to A-2
B-3	30 Al_2O_3 30 Y_2O_3 40 "SN"	α-Si_3N_4 Al_2O_3 Y_2O_3	1600°C 30 m N_2	β'-SiAlON $Y_3Al_5O_{12}$ α-Si_3N_4 (w) Y-Si-O(-N)?	1700°C 30 m N_2	β'-SiAlON $Y_3Al_5O_{12}$ $Al_6Si_2O_{13}$	1700°C 30 m N_2	glass small grains (SiAlON) needles ($Al_6Si_2O_{13}$+N?) SiAlON grains at interface	36/33/31/yes 74/24/ 2 /no /no
C-1	47.84 Al_2O_3 32.93 "SN" 19.23 AlN	α-Si_3N_4 Al_2O_3 AlN (w)	no sinter step	---	1700°C 30 m N_2	β'-SiAlON Al_2O_3 α-Si_3N_4?	---	No bonding, no joining insufficient L phase; note incomplete Rx after sinter	---
C-2	43.06 Al_2O_3 10 Y_2O_3 29.64 "SN" 17.30 AlN	α-Si_3N_4 Al_2O_3 Y_2O_3 AlN (w)	no sinter step	---	1700°C 30 m N_2	β'-SiAlON Al_2O_3 AlN	1700°C 30 m N_2	glass pockets glass at interface needle grains ($Al_6Si_2O_{13}$) isolated SiO_2 grains	47/26/27/yes less Y,Si/yes+ /no
C-3	33.49 Al_2O_3 30 Y_2O_3 23.05 "SN" 13.46 AlN	α-Si_3N_4 Al_2O_3 Y_2O_3 AlN (w)	no sinter step	---	1700°C 30 m N_2	β'-SiAlON $Y_3Al_5O_{12}$ $Al_6Si_2O_{13}$	1700°C 30 m N_2	glass pockets glass interface needle grains ($Al_6Si_2O_{13}$) SiAlON grains at interface	53/26/21/yes 33/33/33/yes+ 82/14/ 4/weak

Wetting angle measurements conducted with the YAS-3 glass on AS-800 Si_3N_4 from 1100 to 1500°C in atmospheric nitrogen heated at 20°C/min are shown in Fig. 5. The best results were obtained with composition YAS-2 (also known as A-3), which is the eutectic composition in the Y_2O_3- Al_2O_3-SiO_2 ternary system (30 wt% Y_2O_3-21 wt% Al_2O_3-49 wt% SiO_2). The eutectic temperature is 1387°C. A joint formed with this composition at a temperature of 1500°C is shown in Fig. 6.

B. Morgan Matroc Si_3N_4 System

B.1 Sr-Celsian Based Glasses

Preliminary evaluations of the two compositions from the SiO_2-SrO-Al_2O_3 (SAS) glass system were conducted by measuring the coefficient of thermal expansion, conducting glass crystallization experiments, measuring contact angles, and observing melting and decomposition of the glass compositions on Morgan Matroc Si_3N_4. The parameters measured during these experiments, which were used in choosing the joining temperature range, are shown in Table 9.

Table 9. Evaluations of the Morgan Matroc oxide joining glasses.

Property	SAS-5 Glass	SAS-10 Glass
T_g (glass transition temperature from DTA results)	745°C	770°C
T_g (glass transition temperature from dilatometer results)	740°C	774.8°C
T_c (onset of crystallization)	1120°C	1100°C
CTE ($x10^{-6}$/°C)	8.54	8.46
Crystallized Phases		
@1000°C for 30 min	amorphous	
@1000°C for 60 min		amorphous
@1000°C for 300 min	$SrAl_2Si_2O_8$, PDF#38-1454	amorphous
@1150°C for 60 min		amorphous
@1200°C for 30 min	$SrSiO_2$, PDF#34-0099	
@1300°C for 60 min		amorphous
@1500°C for 60 min		amorphous
@1550°C for 60 min		amorphous
Temperature regime for wetting	1300°C	1325°C
Decomposition temperature	1480°C	1510°C
Contact angle at 1325°C		
@ 1 min	80	42
@ 9 min	35	29
@ 19 min	21	18
@ 29 min	10	17
@ 39 min	6	12

V. Optimization and Mechanisms of Joining

A. AS-800 Si_3N_4 Joining with YAS-2 SiAlON Glass

A.1 Glass Preparation and Joint Fabrication Procedures

The YAS-2 joining glass composition, which is the ternary eutectic in the Y_2O_3- Al_2O_3-SiO_2 system (composition: 30 wt% Y_2O_3:21 wt% Al_2O_3:49 wt% SiO_2, eutectic temperature = 1387°C), was selected for optimization. A glass transition temperature of 875°C was measured by differential thermal analysis.

Test specimens for joining were made by stamping a thin layer (≈500 μm) of the glass powder onto a Si_3N_4 substrate with a second Si_3N_4 substrate placed on top of the glass powder layer. The joining "sandwich" specimen was then placed inside a BN crucibleand covered with a BN lid. In addition to the joining specimens, small pressed pellets (5 mm diameter x 5 mm height) consisting only of the joining glass powder were placed in a separate BN crucible and heat-treated along with the joining specimen.

Joining experiments were conducted in an Astro furnace.[vi] The furnace chamber was evacuated and heated to 600°C under vacuum. At 600°C, subatmospheric N_2 was introduced such that 1 atm N_2 was achieved at 1000°C during heating. The furnace was then heated at 30°C/min to the specified joining temperature. Separate joining tests were conducted in 50°C intervals from 1100-1700°C in 1 atmosphere static N_2 pressure. After a hold time of 30 min at the joining temperature, samples were furnace-cooled to room temperature.

A.2 Joint Evaluations

Joined samples were machined in half perpendicular to the joint and observed in an optical microscope for a qualitative examination of bonding. Samples that exhibited adequate bonding under an optical microscope were mounted in epoxy, polished and carbon-coated for scanning electron and electron microprobe analyses.

SEM micrographs were taken of the joint region and electron microprobe analysis was conducted as follows: a 100 μm wide line-beam raster scan was stepped in 2 μm increments over a distance of 400 μm across the Si_3N_4 substrate and joint region, perpendicular to the joint. The 100 μm wide line-beam was used to average detection limits at equal distances from the joint interface. Thus, a 100 μm x 400 μm area was analyzed on each sample that included a significant area of the Si_3N_4 substrate unaffected by the joining process to establish changes in composition relative to the parent substrate material. The electron microprobe was used to detect weight fractions of cations which were subsequently converted into their oxide equivalents; reliable detection of oxygen and nitrogen was not considered possible with this equipment. EDS analyses of the joining glass pellets heat-treated under the same conditions as the joining specimens were also conducted.

A.3 Microstructural Results

Optical microscopy of the joining sandwich specimens after heat-treatment revealed that Si_3N_4 substrates were successfully bonded at temperatures as low as 1300°C. Coherent bonding along the Si_3N_4 substrate/glass joint interface was observed in specimens heat-treated between 1350-1600°C, whereas specimens heat-treated at 1300°C exhibited regions of bonding separated by unbonded areas. At temperatures greater than 1600°C, significant joint decomposition was observed.

Figure 7 shows back-scattered electron micrographs of Si_3N_4 substrates joined at 1300, 1350 and 1400°C. The micrograph of the specimen heat-treated at 1300°C shows one of the

[vi] Thermal Technology, Inc., Astro Div., Santa Rosa, CA.

bonded regions along the substrate/joint interface. The joint is composed of a thin (~10 μm) amorphous layer at the substrate/joint interface and a thicker (~40 μm) crystalline central region. At 1350°C, the amorphous layer increases in thickness to (~15-20 μm) as the crystallized region becomes thinner. At 1400°C, the joint region has become completely amorphous. All specimens heat-treated at 1400°C or higher formed only amorphous joints.

Compositions of joints formed between 1300-1600°C were obtained using electron microprobe analysis. The concentrations of Y_2O_3, Al_2O_3, AO, and BO measured at the center of the joint are shown as a function of temperature in Fig. 8. The bars shown on the Y axis denote the initial concentrations of Y_2O_3 and Al_2O_3 in the joining glass. The SiO_2 contents of the joints are not shown.

The electron microprobe data reveal significant diffusion between the glass joint and the Si_3N_4 substrate. With increasing temperature starting at 1300°C, increasing amounts of AO and BO, with concurrent decreasing amounts of Al_2O_3, were detected in the joint region. Because the only source of AO and BO in this system is the Si_3N_4 substrate, which contains no Al_2O_3, it is evident that the diffusion is driven by an ion exchange process between the amorphous joint and the amorphous grain boundary phase in the Si_3N_4. The presence of Y_2O_3 in the starting joint composition as well as the grain boundary phase results in a small Y concentration gradient between the two amorphous phases, resulting in a fairly constant Y_2O_3 content in the joint for all temperatures.

Evidence of counter-diffusion was also observed outside of the joint region. Fig. 9 shows a joining specimen heat-treated at 1500°C; the presence of Al is shown as bright spots in the micrograph. The specimen consists of a 25 μm-wide joint region between two Si_3N_4 substrates. Diffusion of Al into the substrate is clearly evident. After 30 min at 1500°C, the diffusion zone is approximately 90 μm wide. Electron microprobe data obtained from all specimens heat-treated between 1300-1600°C showed that the distance of Al diffusion into the Si_3N_4 substrates corresponded to the distance at which depletion of A and B could be detected. Figure 10 shows the concentration of Al_2O_3 in the Si_3N_4 substrate as a function of distance from the substrate/joint interface for different joining temperatures. It is interesting to note that after 30 min at 1600°C, a 200 μm diffusion zone (approximately 8 times the width of the joint) had formed in the Si_3N_4 substrate.

In addition to the counter-diffusion of cations between the joint and substrate, it was anticipated that the nitrogen solubility potential of an oxide joint composition would result in dissolution of Si_3N_4 grains at the interface. Because the Si_3N_4 grains would dissolve as Si and N ions, the amount of Si_3N_4 dissolved in the joint could be determined from the ratio of mass absorption coefficients of SiO_2 and Si_3N_4 and microprobe measurements of Si levels in the joint. The results from specimens heat-treated between 1300-1600°C are shown in Fig. 11 as the wt.% Si_3N_4 dissolved as a function of temperature. No Si_3N_4 was detected in the joint at temperatures up to 1450°C; however, significant amounts were detected at 1500 and 1600°C.

A.4 Joining Mechanism Discussion

Results from joining experiments between 1100-1700°C have shown that coherent chemical bonds can be formed along a Si_3N_4/oxide glass interface. Electron microprobe analysis has revealed that chemical reactions at different joining temperatures can greatly influence the composition of the joint region. For manufacturing processes, it is desirable to form a strong chemical bond at the lowest possible temperature. As the joining temperature increases, the susceptibility of the joining material to volatilization becomes a critical issue. Joining must be conducted in a nitrogen or inert atmosphere to protect the Si_3N_4 substrate and in such atmospheres at elevated temperatures, SiO_2 becomes the most unstable component. Volatilization of SiO gas leads to the formation of bubbles in the joint that can produce debonding along the interface.

Obviously, the hold time at the joining temperature will also affect the formation of the chemical bond, although the effect of time would not be as strong as the effect of temperature. In the discussion below, the joining time for all results is constant at 30 min.

In the temperature range 1100-1200°C, negligible bonding occurred. The joining glass is apparently too viscous to flow well in this temperature range and only weak bonds with little interfacial coverage between the substrates were observed. At 1300°C, stronger bonds formed although a coherent interface was still not observed; the joint region was composed mainly of bridged areas between the substrates.

It was anticipated that 1300°C would be high enough in temperature for the joining glass to flow well and completely bond the substrates. Many sealing glasses form bonds at 100-300°C above their T_g; the T_g of the joining glass in this study was measured at 875°C. SEM observation of the joining specimen heat-treated at 1300°C, however, revealed another reason why a complete bond did not form. Figure 12 shows a higher magnification micrograph of the joint region formed at 1300°C (cf. Fig. 7a), along with a micrograph of the joining glass pellet fired along with the joining specimen. The joint is composed of a thin amorphous layer at the Si_3N_4 interface and a thicker crystallized region in the center. The glass pellet fired at 1300°C exhibits the same type of crystallization that occurred in the central region of the joint.

EDS analysis of the glass sample identified the bright phase as $Y_2Si_2O_7$ and the darker phase as mullite corresponding to the phases expected from the ternary phase diagram at 1300°C. Thus, the central region of the joint crystallized in a manner expected of its composition, decreasing the amount of glass available to flow between the substrates to form a coherent chemical bond. On the other hand, a thin layer of the joint next to the Si_3N_4 substrate remained amorphous. This behavior can be explained by the electron microprobe measurements made across the joint/substrate region shown in Fig. 13. In the middle of the joint, Y_2O_3 and Al_2O_3 were detected in proportion to the original joining glass composition; in the Si_3N_4 substrate, Y_2O_3, AO and BO were detected in proportion to the composition of the grain boundary phase. The thin amorphous layer in the joint corresponds to an area where A and B have diffused from the grain boundary phase into the joint, stabilizing the glass structure. At higher temperatures, diffusion from the grain boundary phase would be expected to increase and stabilize more of the glass structure and this is observed at 1350°C in which a smaller region of the joint crystallized (see Fig. 7b).

Between 1400-1600°C, coherent, amorphous joints were formed (Fig. 7c). There are two reasons for this behavior. Electron microprobe data showed that at 1400°C, A and B have diffused throughout the joint, stabilizing the glass structure. In addition, the joining temperature has surpassed the eutectic temperature of the glass composition (1387°C). Thus, even in the absence of A and B diffusion from the grain boundary phase, crystallization of the joint would not be expected at this temperature. Joining glass pellets fired at 1400-1600°C were amorphous.

At temperatures above 1387°C, no crystallization would be expected to occur and changes in the composition of the chemical bond are driven by an ion exchange process. Large chemical potential gradients lead to counter-diffusion of Al, La, and Sr cations between the glass joint and the amorphous grain boundary phase. In addition to changing the composition of the joint, the ion exchange process produces a diffusion zone of varying Al_2O_3, AO and BO content in the Si_3N_4 substrate. The presence of Y in both the joining composition and the Si_3N_4 substrate provides little driving force for Y diffusion.

In addition to cationic diffusion, the dissolution of Si_3N_4 grains at the substrate interface changes the composition of the joint from an oxide to an oxynitride glass. The incorporation of N is well-known to strengthen the silicate glass structure;[24] however, the dissolution of Si_3N_4 grains does not become significant until 1500°C. At temperatures greater than 1600°C, volatilization of

SiO led to the formation of bubbles within the joint and debonding along the substrate/joint interface.

The effective temperatures of the mechanisms described above can be used to define a temperature range for successful joining of Si_3N_4 substrates. This is summarized in Fig. 14 for the system used in this study, showing a useful temperature range for joining between 1387-1600°C. The results of this series of experiments showed that 1400°C for 30 min in N_2 appeared to produce the best joints. These process parameters were used as the starting point for plate joining experiments for the bend strength measurements in Section VIII.A.

B. Morgan Matroc Si_3N_4 Joining with Sr-Celsian Based Glasses

B.1 Glass Preparation and Joint Fabrication Procedures

Details of the preparation of the SAS-5 and SAS-10 glass compositions can be found in Ref. 25.

B.2 Joint Evaluations

Samples were potted in epoxy resin and sectioned perpendicular to the interface using a low-speed diamond saw. The samples were then ground, polished and coated with approximately 200 Å of carbon to make the sample electrically conductive to prevent charging of the sample. Electron microprobe scans were used to analyze the interdiffusion of the glass and the Si_3N_4 grain boundary constituents. Quantitative analysis of the composition of the wetted region was measured using a JEOL scanning electron microprobe. Twenty μm long line scans with a 1 μm beam were oriented parallel to the interface and were stepped from the substrate into the melted glass in 2 μm steps. The line scans started outside the diffusion zone in the Si_3N_4 and went into the glass as far as possible (until encountering a crack in the glass). Analytical raw data were automatically corrected for instrumental effects. Matrix effects were handled by the Bence-Albee oxide analysis routine correction procedure.[26] This routine ignored nitrogen and assumed oxygen to be present in the usual stoichiometric ratios. The reason for using this routine is that nitrogen X-rays are preferentially absorbed by carbon in the chamber. Carbon is used to coat the sample; carbon is part of the atmosphere inside the probe (because of the hydrocarbons from the oils used in both the diffusion and roughing pumping systems); and carbon is the major element in the windows of the X-ray detectors. Use of this procedure presents problems with calculating the concentrations of Si, because all Si is taken to be present in the form of SiO, instead of Si_3N_4. This problem is of only minor importance because the focus of the diffusion analysis is on the other oxides in the glass and the elements in the Si_3N_4 grain boundary.

B.3 Microstructural Results

Secondary electron micrographs and back-scattered electron (BSE) images were used to obtain qualitative documentation of the diffusion zones in the melted glass/substrate samples. Elemental distribution photomicrographs were used to obtain semi-quantitative diffusion analysis for the Y, Al, Si, and Sr concentrations across the interface. BSE images reveal distinct zones. Additionally, elemental distribution photomicrographs tracing Y, Al, and Sr distributions across the interface reveal the movement of ions between the glass and the Si_3N_4. Representative BSE images for SAS-5 and SAS-10 samples are presented in Figures 15 a and b, respectively. These figures reveal dissolution of Si_3N_4 grains at the interface.

B.4 Joining Mechanisms

The primary bonding mechanism involved in SiO_2-Al_2O_3-SrO system is the interdiffusion of cations. Electron microprobe analysis of wetted Si_3N_4 substrates revealed significant diffusion of components between the glass and the substrate. Diffusion of Sr^{2+} from the glass into the substrate was significant and the penetration varied with joining temperature and time as shown in Fig. 16 for SAS-5 and in Fig. 17 for SAS-10.

The diffusion of Sr ions into the Si_3N_4 is accompanied by a diffusion of Y ions from the Si_3N_4 grain boundary into the molten glass. This diffusion is characterized by a depletion zone at the glass/Si_3N_4 interface, which, in some cases, drops the Y_2O_3 concentration close to 0 wt%. The width of this depletion zone, defined as the distance from the initial drop in concentration on the Si_3N_4 side to the subsequent rise in concentration on the glass side of the interface, is also dependent on wetting temperature, as shown in Figures 18 and 19. The initial glass compositions contained no Y_2O_3. Electron microprobe results reveal Y diffusion throughout the glass region, tapering off to concentrations of less than 2 wt% at the outer limit of the glass. This yields maximum penetration depths for Y diffusion of greater than 250 μm (as in Fig. 20). This diffusion pattern is also evident in Y elemental diffusion maps (as in Fig. 21).

This counter-diffusion of Sr^{2+} and Y^{3+} ions is controlled by conservation of charge in the diffusion zone. This can be seen in a magnification of the microprobe scans across the interface (Fig. 22). In this microprobe analysis of SAS-5 wetting Si_3N_4 at 1400°C for 15 min, the concentration of Y^{3+} ions drops from 3.2 to 1.6 wt% across the 75 to 85 μm range. The Sr^{2+} ion concentration across this range increases from 4 to 6.4 wt%; Al^{3+} concentration remains constant. This correlates to a decrease in Y^{3+} content of 0.018 moles and an increase in Sr^{2+} content of 0.027 moles. These changes are consistent with a diffusion of 2 Y^{+3} for every 3 Sr^{+2} ions to maintain ionic neutrality in the region.

Because Al_2O_3 is present in both the glass and grain boundary phase, the driving force for its diffusion is relatively low. The absence of Al_2O_3 diffusion in SAS-5 can possibly be attributed to a saturated Si_3N_4 grain boundary phase. The strong diffusion patterns of Sr^{2+} and Y^{3+} ions, however, driven by concentration gradients and controlled by the conservation of ionic charge, serve as one of the two bonding mechanisms.

Mecartney, Sinclair and Loehman reported dissolution of Si_3N_4 at the interface with a molten MgO-Al_2O_3-SiO_2 glass and subsequent penetration of glass into the Si_3N_4.[27] This was then followed by crystallization of Si_2N_2O via:

$$SiO_2(l) + Si_3N_4 \rightarrow 2Si_2N_2O$$

This mechanism resulted in a joint characterized by amorphous and interlocking Si_2N_2O crystalline regions. Although XRD analysis of the 50 μm reaction layer after wetting of the Si_3N_4 by SAS-5 and SAS-10 glasses showed no evidence of Si_2N_2O crystals, it did reveal an amorphous region together with β-Si_3N_4. Furthermore, a BSE image of SAS-10 wetting at 1500°C (Fig. 23 compared to a BSE image of SAS-5 at only 1350°C (Fig. 24) clearly show signs of Si_3N_4 surface penetration by the glass and possibly some dissociation of the Si_3N_4. Black particles in the SAS-10 glass are either precipitated crystals (possibly Si_2N_2O) or partially dissolved Si_3N_4 grains.

VI. Glass Powder Preparation for Substrate Coating

A. YAS-2 Glass

The appropriate wt%'s of yttria, silica, and alumina powders were mixed together and pre-melted to produce the eutectic composition. The glass was melted in a Ta-coated graphite crucible. The glass was ground manually in a mortar and pestle and then separated into three different particle size distributions using an air classifier.[vii] The particle size distributions are shown in Table 10.[viii] The fine particle size cut was used for joining experiments in which glass powder was

[vii] Acucut Model 812.

[viii] Measured using a Coulter[R] LS Particle Size Analyzer.

pressed onto the Si_3N_4 substrate (Sec. VII.A) and for the slurry coating of the substrate (VII.B). The superfine powder was used for the thermal spray coating procedure (Sec. VII.C.).

Table 10. Particle size distributions for air-classified YAS-2 glass powder.

Label	Mean	Std. Dev.	95% CI
Super Fine	15.24 μm	10.5 μm	0-35.8 μm
Fine	37.7	19.1	0.353-75.1
Coarse	73.48	21.8	30.8-116

B. SAS-5 and SAS-10 Glasses

The SAS glasses were made by dry mixing the oxide powder constituents in a ball mill for one hr using Lucite mixing balls. After mixing, samples were pressed under an applied load of one metric ton using a hydraulic press. The pressed powders were furnace heated to 1600°C in air in a Pt crucible and quenched in room temperature water. After removal from the crucible glass batches were manually ground to a 75 μm particle size.

VII. Substrate Coating Processes for Bend Bar Specimens

Initial experiments used the glass powder process (Section A) to coat the AS-800 Si_3N_4 with joining glass. Later joining experiments used the thermal spraying (Section B) and the slurry coating process (Section C). All three processes produced AS-800 joints with similar strengths but the thermal spray and slurry coating processes were less messy, allowed easier fixturing, and could be used on curved surfaces. The glass powder technique was used for the Morgan Matroc Si_3N_4 samples.

A. Glass Powder

Glass powder from the fine particle size distribution was poured onto and then gently pressed on top of the bottom block of Si_3N_4 after it was inserted into the joining fixture. The mass of powder was ~0.2 g. Alumina paper[ix] was used between the joining fixture and the Si_3N_4 blocks to reduce the tolerance and to prevent the glass powder from reacting with the fixture. This procedure produced joints with average room temperature strengths of approximately 380 MPa and as high as 474 MPa, and 1000°C strengths of 555 MPa.

B. Thermal Spraying

All Si_3N_4 parts were sprayed with glass powder using the Alamo PG- 550 flame spray system.[x] Initial attempts at thermal spraying with glass powder (approximately 10-45 μm size cut) onto the Si_3N_4 substrate produced glass coatings with minimal adherence. The substrate surface was grit blasted with alumina powder and improved adherence was achieved. An optical micrograph of one of these specimens is shown in Fig. 25. The glass coating is quite thick and there are uncoated regions that probably occurred because the coating was fragile and broke off near the edges. Specimens were bonded together at 1500°C for 30 min and produced strong room temperature joints(Average= 294±97 MPa, Maximum=395 MPa) and an average 1000°C strength of 475±40 MPa. Despite the excellent strengths, further evaluation of a procedure for producing joints with thinner coatings with improved adherence was conducted. Blocks of Si_3N_4 were

[ix] Alumina Paper, Type APA-3, Zircar Products, Inc., 110 N. Main St., Florida, NY 10921.

[x] Alamo Supply Co., 1331 Upland Dr., Houston, TX 77043.

mechanically abraded with SiC grinding paper to improve the adherence of the glass powder. Although this procedure produced joints with an average room temperature strength of 422±47 MPa, it was not a reproducible procedure and we were concerned that it could degrade the strength of the Si_3N_4.

Grit blasting was also used to improve glass adherence to the Si_3N_4. Si_3N_4 blocks were grit blasted (20-50 psi) with alumina powder to increase the surface roughness. Because the Si_3N_4 surfaces appeared chipped after grit blasting, strength measurements were made on bend bars grit blasted under the same conditions. Four bend bars were tested for each condition. Figure 26 shows an SEM micrograph of the surface of one of the grit-blasted surfaces and the adjacent as-machined surface for comparison. Grit blasting produced a substantial decrease in the average strength of the Si_3N_4 as shown in Table 11 and hence this procedure for improving coating adherence was abandoned.

Table 11. Effect of grit blasting on the strength of AS-800 Si_3N_4.

Grit Blast Pressure (psi)	Strength (MPa)
As-machined	733±81
20	329±33
35	238±37
50	251±52

Further experiments focused on an optimization of thermal spraying parameters to produce adherent coatings on as-machined surfaces. The results of these tests showed that the following process parameters and procedures produced good coatings that were ~ 0.5-1 mil thick (12-25 μm) with the super fine powder size.

The procedure for thermally spraying the Si_3N_4 blocks included the following steps. The parts were loaded on a fixture that was then mounted in the thermal spray hood. The thermal spray gun, which had a glass nozzle, was aligned on the center line of the parts to be sprayed. The gun was set to a standoff distance of 4 in and was set to start and stop approximately 3 in from the end of the fixture. The gun was operated in the X stroke mode only with a stroke length of 16 in. The gases were turned on and set to the conditions shown in Table 12. The dust collector was turned on and the torch was lit. The torch was allowed to stabilize and flow and pressure settings were checked. The parts were then preheated by moving the torch across parts at a rate of 9 in/s. The manipulator counter was set for sixty-six passes (one pass is once across the substrate) and put into the automatic mode. After sixty preheat passes the powder was turned on and sprayed onto the parts for the six remaining counts. The gun was then shut down and the parts were allowed to cool to room temperature before removing them from the fixture.

Table 12. Gas pressures and flow rates used for thermal spraying.

Component	Pressure (psi)	Flow Rate (std. cubic cm/min)
Acetylene fuel	15	12.33
Oxygen	60	21.33
Air	57	
Gun air pressure	8	
Powder air pressure	13	

SEM micrographs of a good coating produced using this procedure are shown in Fig. 27. If the Si_3N_4 substrate became too hot, which occurred at lower traverse speeds, the glass blobs became flatter and had a tendency to spall off during cooling. Joints were produced with average room temperature strengths of 360±86 MPa and as high as 453 MPa. The average strength at 1000°C was 467±39 MPa.

C. Slurry Coating

During the thermal spray parameter optimization study an alternate procedure for coating the Si_3N_4 substrates was identified. A slurry of the YAS-2 glass powder was prepared by mixing the glass powder with isopropyl alcohol in a small vial. The vial was then shaken or stirred. The slurry was applied to the Si_3N_4 by dipping the wooden end of a cotton swab in the slurry and applying drops of the slurry to the Si_3N_4 surface. As much slurry as the meniscus would allow was applied to the surface and then allowed to dry. If the slurry coating seemed thin in any region, additional drops were applied until the coating had a uniform appearance. Approximately 0.006 g of glass powder was left on the joining face of the block (30 mm x 4.4 mm) after the isopropyl alcohol had evaporated.

Figure 28 shows an SEM micrograph of a slurry coating. The coverage of the surface by the glass is generally good and the coating thickness appears to be roughly 30-40 μm thick. Although these coatings are fragile, they adhere to the substrates well enough to allow casual handling of the substrates as they are inserted in the fixture. The slurry procedure produces joints with room temperature bend strengths in the same range as those obtained for thermal sprayed samples joined under the same conditions (323±31 MPa). Several samples were tested at 1000°C. They had an average strength of 270±98 MPa and a strength range between 134 and 363 MPa. Thus it appears that strengths comparable to the thermal spray process strengths can be achieved by the slurry coating process, but there may be problems with uneven surface coverage based on the variability in the strength data.

VIII. Joint Properties

A. AS-800 Si_3N_4 Joined Using YAS-2 SiAlON Glass

A.1 Joint Preparation and Strength Testing Procedures

Joint specimens were prepared from two 22.0 mm x 4.4 mm x 30.0 mm blocks of Si_3N_4 mounted one on top of the other along the 4.4 mm x 30.0 mm face. Unless otherwise noted, the glass coating was applied using the powder procedure described in Section VII.A. The blocks were inserted in the alumina/Mo fixture shown in Fig. 29 and a small load was applied using a Mo block with a mass of 138 g. This mass corresponds to a load of 0.010 MPa. Alumina paper was used to reduce the tolerance between the fixture and the blocks, and to hold the loose glass powder in place. The blocks and fixture were heated in flowing nitrogen at 30°C/min to 1500°C, held for 30 min, and then cooled at 100°C/min to room temperature. The joined blocks were then machined into ASTM C1211-92 size B bend bars.[28] Approximately eight bend bars were cut from each pair of joined blocks. The edges of the bend bars were chamfered.

Preliminary experiments with blocks of Si_3N_4 indicated that 1500°C produced higher strength joints than the 1400°C identified in Section V.A.4 as the optimum joining temperature. This higher temperature may be related to the larger size of the Si_3N_4 blocks and the thermal mass of the fixtures, and the slower heating of the Si_3N_4 that this produced. The limited dissolution of N

in the joint at temperatures of 1400°C may also have played a role in the lower strengths observed for this temperature. Strength specimens prepared at 1400°C were unbonded or had average strengths <160 MPa.

Figure 30 shows (a) optical and (b) SEM pictures of one of the joints produced at 1500°C with a hold of 30 min. The joint thickness generally varies between 10-20 μm and appears to be uniform within a given bend bar. The glass in the joint appears amorphous as was observed in Section V.A.4. The Si_3N_4 adjacent to the joint has a different appearance than the bulk Si_3N_4 as shown in Fig. 31. It is this region in which diffusion of elements of the YAS glass has occurred. This region is generally 50-70 μm thick for blocks joined at 1500°C for 30 min.

Samples were broken in four-point loading at room temperature according to the ASTM C1161-90 procedure. High temperature four-point bend tests were conducted in air at temperatures between 600 and 1000°C air according to the ASTM C1211-92 procedure.[29] Samples were heated at ~30°C/min and then held under a preload of 17 MPa (2.5 ksi) at temperature for 15 min prior to breaking. Samples were loaded at a rate of ~ 4 MPa/sec, which corresponds to a crosshead speed of ~0.5 mm/min (0.02 in/min).

A.2 AS-800 Si_3N_4 Four-Point Bend Strength

The room temperature four-point bend strengths of as-received AS-800 Si_3N_4 and AS-800 Si_3N_4 after exposure to heat treatments at 1000°C and 1500°C are shown in Table 13. Specimens were heated to 1000°C to simulate the conditions of the high temperature bend test and to 1500°C to simulate the joining conditions. The results show this did not have a significant effect on the Si_3N_4 strength.

Table 13. Four-point bend strengths of AS-800 Si_3N_4.

Conditions	Strength (MPa)	No. of samples
As-received tested at room temperature	733±81	15
Room temperature strength after exposure to 1000°C high temperature test conditions	832±70	5
Room temperature strength after exposure to 1500°C joining conditions	699±36	10
As-received tested at 1000°C	607±30	Unknown

A.3 Room Temperature YAS-2 Glass Joint Strength

The average room temperature joint strength for eleven bars fabricated in three separate joining runs at 1500°C for 30 min was 371±54 MPa. The strengths ranged from 277-435 MPa. The fracture surface of one specimen is shown in Fig. 32. The crack appears to have propagated primarily in the glass joint (notably at the failure origin), but also in the Si_3N_4. Cracks are apparent in the glass joining phase perpendicular to the original interface in some joints. XRD measurements of the fracture surface of one of these specimens showed only Si_3N_4 and an amorphous peak.

Tests were also conducted on joint bend specimens on which glass coatings had been thermally sprayed after grit blasting and after mechanically abrading the surface. The average room temperature strength of eight specimens coated after grit blasting was 294±97 MPa. The average room temperature joint strength of eight specimens coated after mechanically abrading was 422±47 MPa.

A.4 Room Temperature YAS-2 Glass Joint Strength after High Temperature (1000°C) Exposure

Joint strength specimens were heat treated at 1000°C to simulate the conditions of the high temperature bend test and tested at room temperature. This was to check whether the heating during the ramp to 1000°C may have promoted crystallization or other changes in the joint material that improved or degraded its strength. The average strength of YAS-2 oxynitride joints after heating to 1000°C was 206±62 MPa (3 samples), which represents a significant strength degradation from the strengths measured in VIII.A.3 (371±54 MPa). Figures 33a and b show low and high magnification SEM micrographs of a joint after the 1000°C heat treatment. Joint material has been partially extruded and the joint phase appears to have crystallized. XRD measurements of the fracture surfaces of samples treated or tested at 1000°C indicated the presence of trace amounts of yttrium silicate ($Y_5(SiO_4)_3O$)[xi] and Y_2O_3. The silicate may also have been strontium yttrium lanthanum oxide silicate, which is isostructural with barium yttrium lanthanum oxide silicate.[xii] The presence of these phases confirms that crystallization has occurred in the joint.

A.5 YAS-2 Glass Joint Strength at Elevated Temperatures

Strength tests were conducted over the temperature range from 600 to 1100°C. The joint specimens used in these tests were prepared using all three of the substrate coating procedures. At this point in the study the thermal spray procedure had been optimized such that good coatings could be produced on as-machined Si_3N_4 surfaces. Joined blocks for which room temperature strengths > 300 MPa were obtained, were used for high temperature testing. Three or more specimens were tested at each temperature. Specimens tested at temperatures greater than 1000°C generally failed at temperatures of ~ 1050°C under the 17 MPa preload. The average strength as a function of temperature is shown in Fig. 34 along with the bend strength of AS-800 Si_3N_4.

A.6 YAS-2 Glass Joint Stress-Rupture Tests

Stress rupture tests were conducted on size B bend bars in the 4-pt loading configuration. The data are shown in Table 14 and plotted in Fig. 35 as the applied stress vs. lifetime.

A.7 Discussion of YAS-2 Glass Joint Strengths

The room temperature strengths of the YAS-2 joints are modest and represent approximately 60% of the room temperature strength of the base AS-800 Si_3N_4. The samples on which the glass had been applied by thermal spraying after grit blasting the surfaces, exhibited lower strengths, apparently due to damage in the Si_3N_4 introduced by the grit blasting procedure (See Fig. 26). As described in Section VII.B, the strength of grit blasted Si_3N_4 was approximately half the original value, even for the lowest grit blasting pressure (20 psi). Although the grit blasting process improves the adhesion of the thermal spray coating, the strength degradation indicated that further work was needed to optimize the adherence of thermally sprayed coatings using the thermal spray process parameters themselves.

[xi] Powder Diffraction File #31-336.

[xii] Powder Diffraction File # 27-43.

Table 14. Stress rupture data for YAS-2 glass joints.

Test Temperature (°C)	Applied Stress (MPa)	Lifetime (hr)	Residual Strength (MPa) (if survived >100 hr)
1000	50	0.24	
1000	150	0.01	
1000	250	0.01	
975	100	0.18	
975	150	0.08	
975	250	0.02	
950	150	0.91	
950	250	0.18	
950	350	0.04	
900	250	100+	301
900	325	4.94	
900	350	8.02	
900	400	0.01	
800	350	100+	621
800	400	0.01	
800	450	0.01	

Fracture of the joined specimens appears to originate in the joint and subsequent crack propagation occurs both in the joint and in the base Si_3N_4. The cracks in the oxynitride glass joining phase, which are perpendicular to the joint, are consistent with the combination of the higher thermal expansion oxynitride joint phase and the lower thermal expansion of the base Si_3N_4. As the sample is cooled from the processing temperature the joint phase contracts more than the Si_3N_4 producing tensile stresses in the joints that leads to cracking perpendicular to the interface. The cracks do not appear to degrade the joint strength and may even provide some relief of the thermal mismatch stresses.

The average strengths at 1000°C are approximately 80% of the base Si_3N_4 strength and are higher than the average room temperature strength. The increased strength at high temperature may be due to either crystallization of the grain boundary phase or due to the decreased thermal expansion mismatch strain between the joint phase and the base Si_3N_4 relative to the mismatch at room temperature. The fracture surfaces of the joints tested at high temperature also reveal thermal expansion mismatch cracks perpendicular to the original interface; however, they only cover approximately two thirds of the fracture surface. In the region where crack propagation began, and extending approximately one third of the way across the fracture surface, the surface is glassy in appearance and does not exhibit any cracks.

The high temperature strengths obtained in this study are approximately twice as high as strengths commonly reported for similar oxynitride joints. Although Takeuchi et al.[30] reported

similar average joint strengths at 1250°C and one strength as high as 640 MPa, their process used a high pressure nitrogen HIPing step. No details were provided regarding the HIPing so it is not known whether glass encapsulation or glass phase HIPing were used and no details were provided regarding the Si_3N_4 composition except that it had a yttria-alumina-silica grain boundary.

The explanation for the excellent high temperature strength of these YAS joints relative to other oxynitride joints has not been identified. Stability of the oxynitride joints at high temperature appears to have been a problem with other oxynitride systems except Takeuchi's. One possible reason is that producing a joint with a different composition than that of the grain boundary of the silicon nitride promotes diffusional transport between the joint and the base material. The composition of the oxynitride glass joint after joining has better strength, a higher melting point, and better thermal stability than the starting YAS composition. Supporting evidence for this hypothesis are the strength results obtained for the same glass joining composition and GS-44 Si_3N_4. Although the joint strength for this system were in the same range at room temperature (303±113 MPa) as measured to AS-800 Si_3N_4, the GS-44 joints did not survive the pre-load at 1000°C. Another explanation for the low strengths obtained in previous studies may have been the presence of organics in the starting materials and deleterious reactions between the fixtures and the joining atmospheres with the glass joining material. Poor strengths may also have been due to incomplete joint coverage due to too low a temperature during joining or decomposition reactions due to excessive temperatures.

The lower room temperature joint strengths following heat treatment at 1000°C appear to be due to the decomposition or crystallization of the joint.

A.8 YAS-2 Glass Joint Hardness

Vickers hardness measurements were made in the glass joint and the AS-800 Si_3N_4 substrate as a function of joining temperature and joining time at temperature. Measurements were made with a Vickers diamond indenter at a load of 1.96 N. The indentations were made approximately 10-15 μm apart in the joint. Figure 36 a shows how the hardness varies across a YAS-2 joint and into the substrate for a joining temperature of 1400°C and a joining time of 15 min. Figure 38b shows how the hardness of the joint has increased for 1500°C for 30 min.

The results for hardness vs. temperature (time=30 min) and hardness vs. time (temperature=1400°C) are presented in Tables 15 and 16 and shown in Figures 37 and 38. Despite the variability in the data the hardness of the joint itself generally increases with joining temperature as the concentration and diffusion distance of the grain boundary elements from the Si_3N_4 increase. At temperatures greater than or equal to 1500°C the concentration of dissolved N also increases significantly. The joint hardness does not change with joining time for a joining temperature of 1400°C. This provides evidence that the dissolution of Si_3N_4 into the glass at higher temperatures, and conversion to an oxynitride glass occurs, is primarily responsible for the change in the glass. The incorporation of nitrogen into a silicate glass network has been shown to increase the hardness and fracture toughness of glasses as well as lower its coefficient of thermal expansion. All three of these trends are considered advantageous for higher strength joints.

Table 15. YAS-2 glass joint hardness vs. temperature (time=30 min).

Temperature Time	1300°C 30 min	1350°C 30 min	1400°C 30 min	1450°C 30 min	1500°C 30 min	1600°C 30 min
Joint						
Hardness	8.3	7.0	8.2	7.6	8.9	11.1
Std. Dev.		0.9	0.5	0.9		0.8
# indents	1	5	4	3	1	2
Matrix						
Hardness	17.0	15.4	17.3	14.0	14.6	14.4
Std. Dev.	1.1	0.7	1.2	0.8	0.9	1.1

Table 16. YAS-2 glass joint hardness vs. time (temperature=1400°C).

Temperature Time	1400°C 7.5 min	1400°C 15 min	1400°C 30 min	1400°C 60 min	1400°C 120 min
Joint					
Hardness	7.3	6.8	8.2	7.2	7.9
Std. Dev.	0.7	0.1	0.5	0.4	0.4
# indents	4	4	4	6	17
Matrix					
Hardness	15.5	15.0	17.3	15.2	14.8
Std. Dev.	1.0	1.4	1.2	1.0	0.6

B. Morgan Matroc Si_3N_4 Joined with SAS-5 and SAS-10 Celsian-Based Glasses

B.1 Joint Preparation and Strength Testing Procedures

The preparation and strength testing procedures were similar to those for AS-800 Si_3N_4. Approximately 0.2 g of loose glass powder was applied to the long side of the block. Joining was conducted in a flowing N_2 atmosphere at 1450°C for 30 min using a heating rate of 30°C/min and a cooling rate of ~ 100°C/min. Nine bars of each glass joining material (SAS-5 and SAS-10) were prepared. Five to six of each were used for room temperature strengths and two of each were used for testing at elevated temperatures (900 and 1000°C). One of each composition was archived.

B.2 Morgan Matroc Si_3N_4 Four-Point Bend Strength

According to the manufacturer's data in Table 6 the flexural strength of this material at 20°C is 850 MPa.

B.3 Room Temperature Joint Strength

The average and maximum strengths of the SAS-5 joints were 178±182 MPa and 470 MPa, respectively. The average and maximum strengths of the SAS-10 joints were 225±91 MPa and 376 MPa, respectively. The maximum strengths are shown in Fig. 34 for comparison with the AS-800 results.

B.4 Joint Strength at Elevated Temperature

Both of the SAS-5 specimens failed under the preload of 17 MPa approximately 15 min into the 20 min hold at 1000°C prior to testing. As a result we decided to test the SAS-10 specimens at 900°C. The strengths of the two SAS-10 specimens at 900°C were 370 and 45 MPa.

B.5 Discussion of Strength Results

Room temperature joint strengths achieved using SAS-10 and SAS-5 glass interlayers are encouraging. The maximum room temperature strength of 470 MPa, attained using SAS-5 glass, is approximately 55% of the room temperature flexure strength of the base Si_3N_4. Observation of the fractured test bars indicates that incomplete coverage of the Si_3N_4 by the glass was a major factor in the strength variability, especially for the low strengths. The joining was carried out in the middle of the optimum joining temperature spectrum for the SAS-10 glass (1300-1550°); use of a higher joining temperature will likely provide for more fluidity in the glass and better substrate coverage. Joining was carried out at the upper end of the optimum joining temperature spectrum (1200-1450°C for the SAS-5 joining. Although coverage appeared to be better, it was inconsistent along the length of the joint. More controlled application of the glass powder prior to joining should produce better coverage. The fact that the maximum strength was achieved at the end of the joined plates (for SAS-10 joining) and in the middle of the joined plates (for SAS-5 joining) is indicative of poor coverage. The high strengths of the SAS-10 at 900°C may be related to the crystallization of celsian for this composition. These results provide a promising starting point for future optimization in this system.

IX. Joining Process Parameter Optimization Using 4-Pt. Bend Strength Measurements

A. Introduction

Although this study demonstrates that oxynitride glass joints produced without a post-HIPing procedure exhibit very good strengths over a wide temperature range, a completely amorphous joint is not expected to be able to provide thermal stability and sustained strength at temperatures greater than 1000°C. Process optimization was studied to determine whether improved thermal stability and higher temperature capabilities could be achieved by controlling the joint thickness or by joint crystallization. Previous studies have shown that joint strength can be optimized by decreasing the joint thickness to a limiting value.[31] Bend strength of the joint was used to quantify whether a given process produced an improvement in the joint. The optimization study focused on controlling joint thickness using the initial joint thickness and the time at the joining temperature. Joint crystallization was studied as a function of Si_3N_4 and AlN additions to the glass and as a function of heat treatments at temperatures below the joining temperature. Because of the possible importance of fixturing and the local atmosphere created by the fixturing in the vicinity of the joint, different fixturing arrangements were also evaluated (Section D).

B. Joint Thickness Experiments

Process parameters that were expected to affect joint thickness for a given initial thickness (controlled by the amount of glass powder or thermal spray coating thickness) were the joining temperature (T), time (t), and applied pressure (P). The joining time and temperature were expected to affect the thickness either because of the tendency of the glass to flow out of the joint and wet the adjoining faces of the silicon nitride blocks or because it penetrated into the adjoining substrate. Time could be controlled by either controlling the time at the joining temperature or by controlling the cooling rate. Note that the typical joint thickness for a blocks processed under standard conditions (heating rate=30°C/min, hold at 1500°C for 30 min, cooling rate = 100°C/min) produced joints whose thickness varied between 15-20 μm. Typical strengths for these joints were 371±54 MPa at room temperature and 502±52 MPa at 1000°C.

Unfortunately there were a number of complications that made it impossible to evaluate the effect of joint thickness on strength. The first was that the same amount of starting glass powder often produced joints with different thicknesses. There was variability from one set of blocks to the next and even within a given set of blocks and within a given bend bar (one of 7-8 machined from the parent blocks). For example in one set of blocks used to make bend bars the joint thickness varied from ~2 μm at the center of the block to ~ 11 μm at the edge. Within a given bend bar that had been produced from thermally sprayed blocks the thickness varied from ~4-14 μm. In another bend bar that was made with standard conditions (1500°C for 30 min, cooled at 100°C/min) and slurry-coated the joint thickness varied from 7-13 μm. This may have been due to differences in fixturing from run to run, such as the initial position of the silicon nitride blocks in the fixture, variability in the coating technique, and variations in the amount of powder placed between the blocks even when it was nominally the same.

Another complicating factor was that it was not possible to look at the effect of joining time and temperature alone on the joint thickness and strength because the longer times at temperature or slower cooling rates sometimes produced crystallization within the joint, which itself is expected to have a strong effect on the strength (see Section C.2). Also, the slower cooling rate did not always produce a thinner joint as expected based on the glass flowing out of the joint over time. This may have been due to an increase in the glass viscosity as the composition changed with time.

In one set of experiments two sets of blocks, for which it appeared that we had equivalent starting thicknesses, were held for 150 min at a temperature of 1500°C (everything else was the same as the standard process parameters). We were able to produce joints that were thinner than the standard joint thickness. Representative thicknesses for joints in the two sets of blocks were ~5-8 μm and 3-4 μm. The average strengths at room temperature and 1000°C for the thicker sample were 317±109 MPa and 308±118 MPa, respectively. The average strengths at room temperature and 1000°C for the thinner joints were 270±78 and 306±38 MPa, respectively. Therefore the strengths were not higher for the thinner joints and not higher than the 15-20 μm joints produced under standard conditions at room temperature.

C. Crystallization Experiments

Two general crystallization approaches were used to try to improve the high temperature properties of the YAS joints. One was to add Si_3N_4 or AlN to promote the crystallization of phases such as β–SiAlON (C.1). The other was to heat treat at temperatures below the joining temperature to induce crystallization of the glass joint (C.2).

C.1 Doping the Joining Glass with Si_3N_4 or AlN

Preliminary experiments to improve the joint properties at high temperature used large additions of Si_3N_4 or AlN to the glass phase. The idea behind adding the Si_3N_4 to the glass was that β–SiAlON grains would be produced in the joint, increasing its strength. Preliminary experiments using Si_3N_4 additions indicated that needle-like grains formed in the joint region as shown in Fig. 39. Their composition is $Al_6Si_2O_{13}$. The YAS-2 and YAS-3 glass compositions were doped with 50 wt% Si_3N_4 or 50 wt% AlN. These joining experiments were run at 1500 or 1600°C for 30 min. At 1500°C there were large areas of non-bonding in the AlN and Si_3N_4 doped joints. The dopant materials did not appear to react and melt sufficiently during joining to form enough liquid phase. At 1600°C, the Si_3N_4-doped glass exhibited significant shrinkage and produced a poor joint. The AlN doped glass appeared to bond; the interface was filled with materials; however, the conclusion was that with 50 wt% dopant, there was not enough coverage due to lack of liquid formation.

The next set of experiments used YAS-2 and YAS-3 glasses doped with 10 wt% Si_3N_4 or AlN at 1500°C for 30 min. Three of the four samples had minimal bonding. The YAS-2 glass sample doped with 10 wt% Si_3N_4 was "bonded well" but there were bubbles in the joint. This may have been due to the increased concentration of Si in the joint, hence increasing the likelihood of SiO volatilization. To avoid volatilization the joining temperature or the SiO_2 content of the glass would need to be lowered.

The next set of experiments used 2 and 5 wt% additions of either Si_3N_4 or AlN. Joints with 2 and 5 wt% AlN powder also produced poor glass coverage and bonding. Both dopant additions produced joints that exhibited more cracking than undoped glass. AlN-doped glass joints in this experiment were also almost twice as thick (2 and 5% both ~50 μm) as Si_3N_4-doped glass joints (7.5 μm for 2% vs. 25 μm for 5%). When either 2 or 5 wt% of Si_3N_4 was added to the joint there was some evidence of crystallization.

To promote greater crystallization, the cooling rate was reduced to 10°C/min and 1°C/min from the normal rate of 100°C/min. Curiously the joints were thicker (~50 μm), the glass was more extensively cracked than glass cooled at the faster rate, and no further crystallization was observed. The joints may be thicker because the composition of the glass changes more during slow cooling producing a more viscous glass that does not flow out of the joint as well.

The results of this series of tests suggest that doping with AlN or Si_3N_4 has a limited effect on the crystallization and produces poorer glass coverage and bonding.

C.2 Heat Treatments of the Joint

C.2.1 Longer Holds at the Joining Temperature

Joints were held at 1500°C for 60, 150 min and 180 min compared to the standard hold of 30 min. Extensive crystallization was observed for the sample held at 1300°C for 180 min. Thermal spray coated strength samples treated in this manner exhibited an average room temperature strength of 304±145 for 60 min and 294±91 MPa for 150 min. This is somewhat lower than the strength values obtained for the standard 30 min hold time of 371±54 MPa; however, because it is well within the standard deviation, it is not possible to say that the longer temperature has degraded the strength. A set of slurry-coated bend specimens was also held for 150 min. The average room temperature strength was only 202±44.

Joint strengths were also measured at 1000°C. Thermal spray coated samples held for 60 min exhibited an average strength of 374±70 MPa, whereas samples held for 150 min exhibited an average strength of 307±79 MPa. These strengths are lower than the 502±52 MPa strength measured at 1000°C for samples held for 30 min at 1500°C. Thus there is no conclusive evidence that longer holds at the joining temperature that promote crystallization are better for the joint strength (although the hardness results might indicate that they should be better), and based on the high temperature strengths they may be worse.

C.2.2 Slow Cooling from the Joining Temperature

Experiments were conducted in which the cooling rate for the undoped YAS-2 glass joints was reduced to 1°C/min from the standard 100°C/min. This reduction in cooling rate produced a joint that is 6-7 μm thick vs. the 15-20 μm joint that is normally observed. This may be due to the fact that with slower cooling rates the glass is at a high temperature for longer time and may be flowing out of the joint, or that more of it is dissolving in the adjacent Si_3N_4 as shown in Fig. 40. There is no evidence of crystallization in the joint but some Si_3N_4 grains may have become detached from the substrate material. Strength samples cooled at 1°C/min from the joining temperature to a temperature of 900°C, instead of at the standard cooling rate of 100°C/min, exhibited an average room temperature strength of 374±36 MPa. Two samples that had been slow

cooled at 1°C/min were tested at 1000°C; however, they failed at ~ 28 MPa during the heatup to 1000°C and thus appear to have been significantly weakened. Based on limited results, slow cooling does not appear to have a detrimental effect on the room temperature strength, but it degrades the high temperature strength.

C.2.3 Holding at Temperatures Below the Joining Temperature

Initial evidence that holds at temperatures below the joining temperature might degrade the strength are the results of the experiments in which bend bars were heat-treated at 1000°C to simulate the conditions of the high temperature bend test. As shown previously in Fig. 33, this treatment produces crystallization of the joint and degrades strength to a value of 206±62 MPa. XRD measurements on the fracture surfaces of joints tested at 1000°C or heat-treated at 1000°C and then broken at room temperature showed $Y_5(SiO_4)_3O$ and trace Y_2O_3, whereas as-joined samples (1500°C for 30 min) were amorphous.

Experiments were conducted in which a two hr hold at 1300°C was added during slow cooling at 1°C/min from the joining temperature. This temperature was chosen based on Differential Thermal Analysis (DTA) results for YAS-2 glass and YAS-2 glass that had been reacted with AS-800 Si_3N_4 prior to the DTA analysis. The DTA showed that some kind of reaction was occurring in the temperature range from 1300-1200°C. Thus this temperature was an educated guess at a temperature that would promote crystallization.

Sectioned samples showed that there was a considerable amount of crystallization in the joint region after holding at 1300°C as shown in Fig. 41. The large crystals observed in the joint were not identified, but based on X-ray diffraction analyses of the samples treated at 1000°C and the back-scattered electron image they may be a yttria disilicate phase.

Strength samples held at 1300°C for 120 min and slow cooled at 1°C/min between 1500 and 900°Cexhibited an average strength of 173±71 MPa. This low strength may have been due to the crystallization; however, the use of a different fixture (see Section 9.4 for discussion of fixtures) and poor machining of these samples may have contributed to the formation of a poor bond.

Experiments were also conducted in which a hold at 1400°C for 24 hr was used for samples that had been joined at 1500°C for 30 min. Crystallization of Si_3N_4 grains within the amorphous joint occurred as shown in Fig. 42a; however, the 1400°C heat-treatment also produced volatilization of material from the joint as shown in Fig. 42b and a change in joint composition as shown in the electron microprobe traces in Fig. 43a & b. There has been more interdiffusion of the original constituents of the joint into the adjoining silicon nitride and vice versa. In particular, the concentration of AO in the joint has more than doubled. This may also reflect the loss of SiO due to volatilization, leaving a composition that has relatively more of the other elements.

The results of these tests indicate that crystallization treatments that involve holding at temperatures below the joining temperature are not beneficial; however, further studies are recommended because of the limited strength data and because there may be a hold temperature and time that produce small crystals in the joint that improve its strength. In addition no high temperature tests have been conducted on samples held at temperatures from 1200-1300°C. Although the strengths for room temperature strengths were lower the strengths at higher temperatures may be better.

D. Fixturing and Atmosphere Effects

Although the evaluation of different fixturing configurations was not a formal part of the study, different fixtures were employed when we attempted to make join several sets of blocks in

the same furnace run. Two new fixture designs were used (Fig. 44a and b). The major difference between the fixture shown in Fig. 44a and the standard fixture (Fig. 31) is that the silicon nitride blocks are directly exposed to Mo and no alumina paper is used. The major difference between the fixture shown in Fig. 44b and the conventional fixture is that a large part of the surface is exposed and no alumina paper is used. Although we have not identified why, these fixturing configurations produced blocks that either were significantly weaker than those produced in the standard fixture, were not joined, broke easily after removal from the fixture, or were discolored and appeared to be poorly bonded. Possible explanations include poor alignment, different local atmosphere, interactions with the Mo in the fixtures, and the absence of the alumina paper.

Argon was used as the furnace atmosphere for several runs instead of nitrogenIt also appeared to have a detrimental effect on the joint appearance and strength. For one run in argon, blocks that were joined in the standard fixture had an average room temperature strength of 214±21 MPa.

X. Practical Implementation of Oxide Joining Technology

AlliedSignal Ceramic Components provided a set of AS800 Si_3N_4 rings cut from approximately cylindrical combustors with a 44 mm outer diameter and a 3.65 mm wall thickness to rejoin to demonstrate that the oxynitride glass joining technology could be used to join large, complex shape parts. The rings were cut from the cylinder at a slight angle and then ground so that the faces were parallel. The finish on the faces to be joined appears similar to that used for the AS-800 coupons (ASTM C 1161-90 finish). Alignment marks were penciled on the outside of the rings indicating the best match for the joint surfaces.

Fixturing for the rings was complicated by the angle at which the rings were cut from the cylinder. It required a very specific alignment for the rings, and because we wanted to limit the exposure to the furnace atmosphere, a very specific alignment for the jig. The jig was fabricated from an alumina furnace tube with an inner diameter slightly larger than the outer diameter of the rings. The tube was first cut at an angle similar to that of the ring walls, then split to form two clamshell sections as shown in Fig. 45. The alumina sections were then held in place by molybdenum blocks like bookends. A 304 g molybdenum block was used as a top weight, which produced an applied load similar to that used for the rectangular blocks.

The rings were slurry-coated with YAS-2f glass in isopropyl alcohol. The coatings were allowed to dry and then stacked on a sheet of alumina paper in the furnace. The two halves of the jig were placed snugly against the stacked rings. Thin strips of alumina paper were used between the jig and the rings to ensure close contact. It proved more difficult than anticipated to achieve proper alignment; the slurry coating was fragile and precluded any rotation or shifting to facilitate better alignment.

The rings appeared to bond very well. Some mottled white features were observed on the surface. The rings were misaligned in the jig leaving a 1 mm offset on part of the circumference. Some bubble formation occurred at these sites. No gaps were observed, the glass joint appears uniform and thin as shown in Fig. 46.

Cylinders of GS44 Si_3N_4 were also joined as a demonstration that the oxynitride glass joining technique could be applied to complex shapes. Two half inch diameter cylinders were slurry-coated. Fig. 47 shows a good joint although fixturing proved again to be a challenge and there is slight misalignment of the cylinders.

XI. Summary

Two commercial sources of silicon nitride have been successfully joined using optimized compositions from the Y_2O_3-Al_2O_3-SiO_2 (YAS) and SiO_2-Al_2O_3-SrO (SAS) oxide glass systems. Both joining glass systems produced average room temperature four-point bend strengths in the 400 MPa range. The YAS-2 glass composition also produced strong joints over an extended temperature range. At 1000°C joint strengths as high as 555 MPa were obtained. This is twice as high as what has been obtained previously at this temperature for joints that were not given a HIPing treatment after joining.

Temperatures of ~1500°C for times of ~30 min in a nitrogen atmosphere produced the best joints in the YAS system. In the SAS system a joining temperature of ~1450°C for 30 min produced good joints. Joining occurs by a mechanism of glass melting, substrate wetting by the molten glass, counter diffusion of elements from the glass into the substrate and from the substrate into the glass, and dissolution of silicon nitride into the glass changing it from an oxide glass to an oxynitride glass. The change of joint composition that occurs with the YAS glass and the AS-800 silicon nitride appears to be very favorable with respect to the properties at elevated temperatures. This may be the difference between the YAS joints in this study and those in previous studies.

Joining compositions can be applied using a dry powder technique, a thermal spray technique, and by a slurry coating technique. Although the initial amount of glass can be controlled with each of these techniques, the thermal spray technique is the best in terms of coating thickness uniformity, the strength of the coating prior to the joining treatment, and as a technique for use on complex shapes. In addition to the glass coating thickness prior to joining, factors that control the joint thickness include the time at temperature, cooling rate, fixturing, and the occurrence of crystallization.

Treatments to control joint thickness met with limited success due to the complex relationship between the glass viscosity, crystallization behavior, interactions with the fixturing, and the alignment of the samples. Treatments to crystallize the joint require additional work to identify times and temperatures that produce phases that nucleate homogeneously and do not weaken the joint.

Practical implementation of this technology was demonstrated by joining sections of a combustor and cylindrical pieces.

XII. Recommendations for Future Work

A. AS-800 Si_3N_4 Joining with YAS-2 Oxynitride Glass

- Measure room and high temperature joint strength after high temperature exposure at additional temperatures (limited 1000°C tests were done). Examine cross sections and fracture surfaces of heat-treated joints to determine the extent of crystallization.

- Evaluate how BO and AO additions to YAS-2 glass affect the CTE and crystallization behavior.

- Fabricate additional GS-44 Si_3N_4 samples to test over a broader temperature range to determine whether the good high temperature strength of YAS joints with AS-800 is due to the improvement in the high temperature capability of the glass due to the incorporation of the sintering aids that are specific to AS-800 silicon nitride.

- Conduct additional work on the effect of joint thickness on joint composition and properties. In principal a joint that is very thin and has the same composition as the silicon nitride should have a strength and thermal stability that is similar to the silicon nitride.

B. Morgan Matroc Si_3N_4 Joining with SAS-5 and SAS-10 Celsian-Based Glasses

- Two joining profiles were completed. Morgan Matroc Si_3N_4 blocks were joined with SAS-5 and SAS-10 (Section VIII.B.1) glass at 1450°C for 30 min. For future joining experiments, the following heat/time profiles are recommended based on the wetting characteristics for the glass compositions:

SAS-5:	1400°C for 30 min
	1500°C for 30 min
	(other times at the temperatures of 1400-1500°C may also be beneficial)
SAS-10:	1500°C for 30 min
	1550°C for 30 min
	(other times for these temperatures)

- Crystallization of celsian has been partially successful in SAS-5 bulk glass samples heated to 1000°C for 5 hr, but this appears to be a sluggish crystallization. Nucleating agents are recommended for celsian crystallization treatments following joining.

XIII. REFERENCES

1. Joining of Ceramics, Edited by M. G. Nichols, Chapman and Hall, New York, 1990.
2. K. Suganuma, "Joining Non-Oxide Ceramics," pp. 523-531 in Engineered Materials Handbook, Vol. 4, Ceramics and Glasses, ASM International, 1991.
3. P. A. Walls and M. Ueki, "Mechanical properties of β-SiAlON Ceramics Joined Using Composite β-SiAlON-Glass Adhesives," J. Am. Ceram. Soc., 78 [4] 999-1005 (1995).
4. P. A. Walls and M. Ueki, "Joining SiAlON Ceramics Using Composite β-SiAlON-Glass Adhesives," J. Am. Ceram. Soc., 75 [9] 2491-97 (1992).
5. H. Takeuchi, Y. Takano, A. Yamakawa, and M. Miyake, "Joining of Silicon Nitride Ceramics," pp. 147-161 in Tokyo Fine Ceramics, Mar. 1993.(In JPRS-JST-94-009, 5 May 1994)
6. S. M. Johnson and D. J. Rowcliffe, "Mechanical Properties of Joined Silicon Nitride," J. Am. Ceram. Soc., 68 [9] 468-72 (1985).
7. M. L. Mecartney and R. Sinclair, "Silicon Nitride Joining," J. Am. Ceram. Soc., 68 [9] pp. 472-478 (1985).
8. R. E. Loehman, "Oxynitride Glasses and Silicon Nitride Processing," Ceramic Proc., Jan-Feb. 1982, pp. 35-49.
9. R. E. Loehman, "Preparation and Properties of Oxynitride Glasses," J. Non-Crystal. Solids, 56, pp. 123-134 (1983).
10. T. Rouxel, M. Huger, and J. L. Besson, "Rheological Properties of Y-Si-Al-O-N Glasses-Elastic Moduli, Viscosity and Creep," J. Mater. Sci., 27, pp. 279-284 (1992).
11. S. M. Johnson and D. J. Rowcliffe, "Mechanical Properties of Joined Silicon Nitride," J. Am. Ceram. Soc., 68 [9] 468-72 (1985).
12. S. M. Johnson and Y. D. Blum, "Joining of Silicon Nitride with Preceramic Polymers," Phase I Report for SRI Project No. PYD-5759, March 1995.
13. Ceccone et al., "Application of the Partial Transient Liquid Phase Bonding Method for Joining Silicon Nitride Ceramics," presented at ECER'S 95, Oct. 2-76, 1995 in Riccione, Italy.
14. S. D. Peteves and K. Suganuma, "Solid State Bonding of Si_3N_4 Ceramics with Fe-Cr Alloy Interlayers," Ceram. Trans., Vol. 35, pp. 229-238, (1993).
15. A. Hadian and R. A. L. Drew "Strength and Microstructure of Brazed Silicon Nitride Ceramics with Ni-Cr-Si Alloys," J. Am. Ceram. Soc., 79 [3] 659-65 (1996).
16. K. Suganuma, "Joining Non-Oxide Ceramics," pp. 523-531 in Ceramics and Glasses, Vol. 4, Engineered Materials Handbook, ASM International, (1991).
17. H. Takeuchi, Y. Takano, A. Yamakawa, and M. Miyake, "Joining of Silicon Nitride Ceramics," pp. 147-161 in Tokyo Fine Ceramics, Mar. 1993.(In JPRS-JST-94-009, 5 May 1994)
18. S. M. Johnson, D. J. Rowcliffe, "Mechanical Properties of Joined Silicon Nitride", J. Amer. Ceram. Soc., 68, [9] 468-472 (1985).
19. P. A. Walls and M. Ueki, "Mechanical properties of β-SiAlON Ceramics Joined Using Composite β-SiAlON-Glass Adhesives," J. Am. Ceram. Soc., 78 [4] 999-1005 (1995).
20. J. P. Pollinger, "Improved Silicon Nitride Materials and Component Fabrication Processes for Aerospace and Industrial Gas Turbine Applications," Proceedings of the International Gas Turbine and Aeroengine Congress and Exposition, Houston, TX, June 5-8, 1995.
21. C-W. Li, S-Ch. Lui, and J. Goldacker, "Relation between Strength, Microstructure, and Grain-Bridging Characteristics in *In Situ* Reinforced Silicon Nitride," J. Am. Ceram. Soc., 78 [2] 449-59 (1995).
22. Fig. 755, pg. 257 of Phase Diagrams for Ceramists, The American Ceramic Society, 1964.
23. Fig. 5462, pg. 244, Vol. 4, Phase Diagrams for Ceramists, The American Ceramic Society, 1981.

24. R. E. Loehman, J. Non-Cryst. Solids, 56, pp. 123-134 (1983).
25. B. G. Quillen, MS Thesis, "Silicon Nitride Joining Using a Sr-Celsian-Based Glass Interlayer," U. of New Mexico, July 1996.
26. W. F Chambers, "BA85: A Bence-Albee Oxide Analysis Routine with Mineral Code Capabilities," SAND90-1702, Sandia National Labs, Jan. 1991.
27. M. L. Mecartney, R. Sinclair, R. E. Loehman, "Silicon Nitride Joining", J. Amer. Ceram. Soc., 68, [9] 472-478 (1985).
28. C1161-90. Standard Test Method for Flexural Strength of Advance Ceramics at Ambient Temperature.
29. C1211-92. Standard Test Method for Flexural Strengths of Advanced Ceramics at Elevated Temperatures.
30. H. Takeuchi, Y. Takano, A. Yamakawa, and M. Miyake, "Joining of Silicon Nitride Ceramics," pp. 147-161 in Tokyo Fine Ceramics, Mar. 1993.
31. S. M. Johnson and D. J. Rowcliffe, "Mechanical Properties of Joined Silicon Nitride," J. Am. Ceram. Soc. 68 [9] 468-72 (1985).

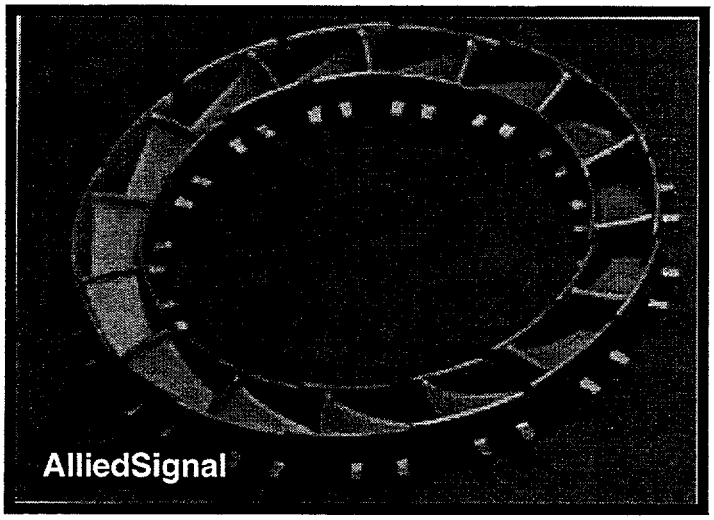

(a)

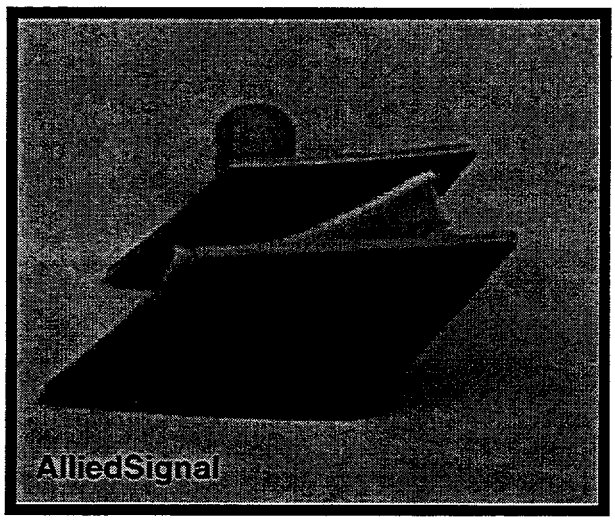

(b)

Fig. 1. (a) Si_3N_4 automotive turbogenerator combustors and (b) Harrier jet engine turbine blade doublets.

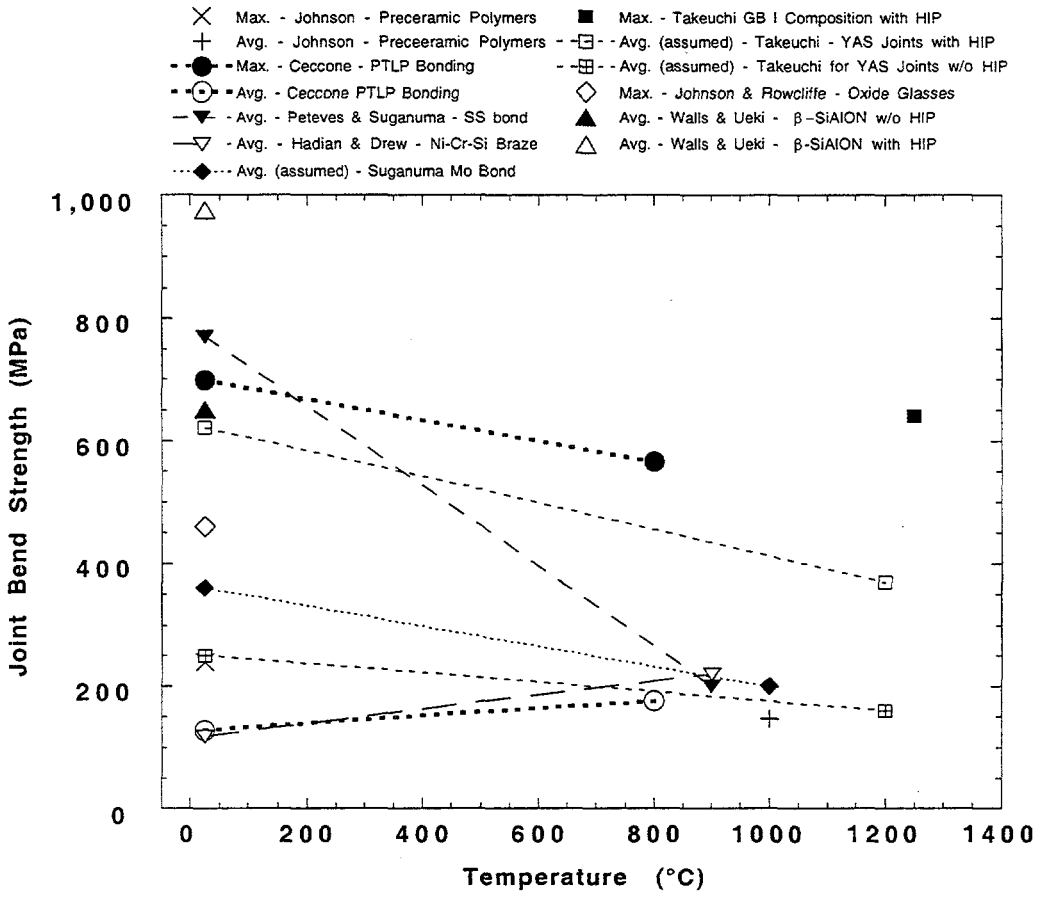

Fig. 2. Room temperature and high temperature joint strength results for various silicon nitride joining methods. Lines are shown to guide the eye and do not necessarily reflect actual trends. The average strength was assumed in cases where it was not specified in the original reference.

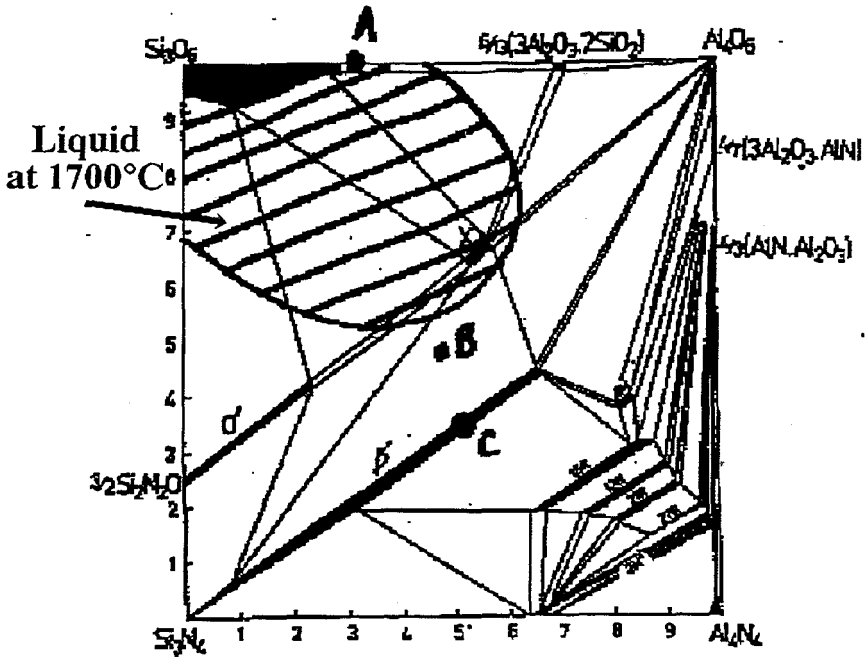

Fig. 3. Three sets of compositions from the Si_3N_4- SiO_2-Al_2O_3-AlN phase diagram.

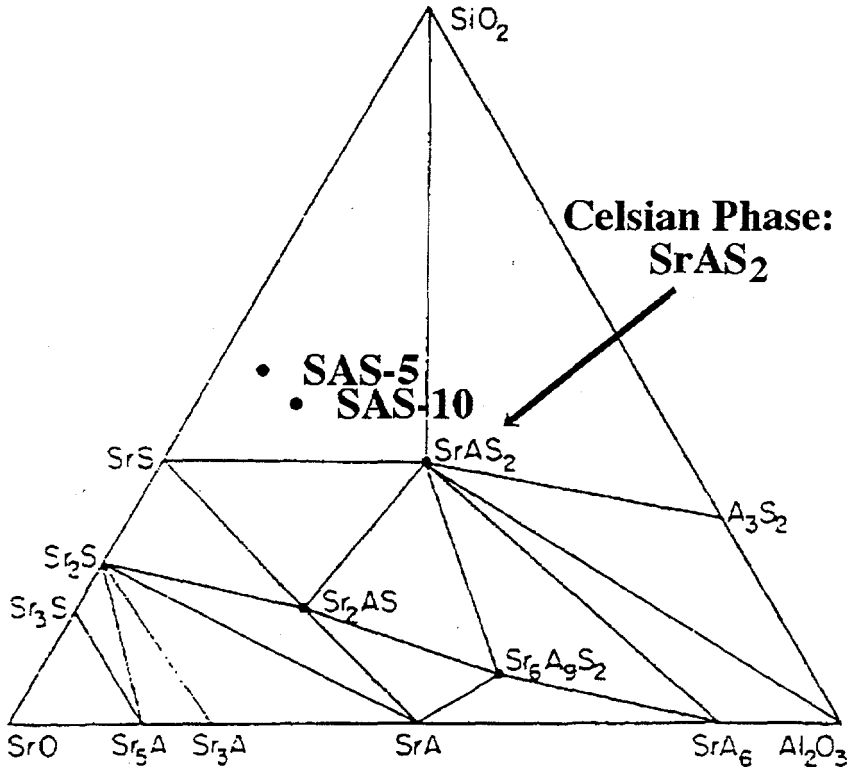

Fig. 4. The SrO, SiO_2, Al_2O_3 ternary phase diagram along with the positions of the SAS-5 and SAS-10 glasses.

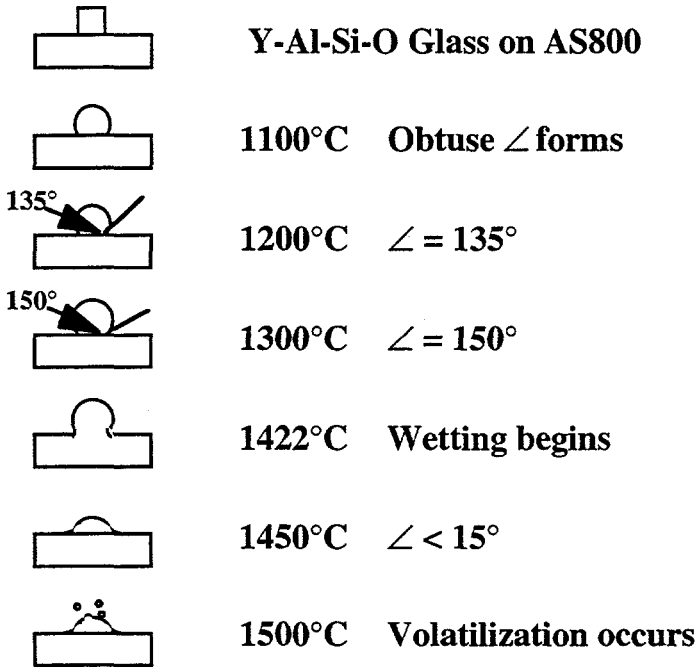

Fig. 5. Wetting angle as a function of temperature for YAS-3 glass on AS-800 Si_3N_4 substrate.

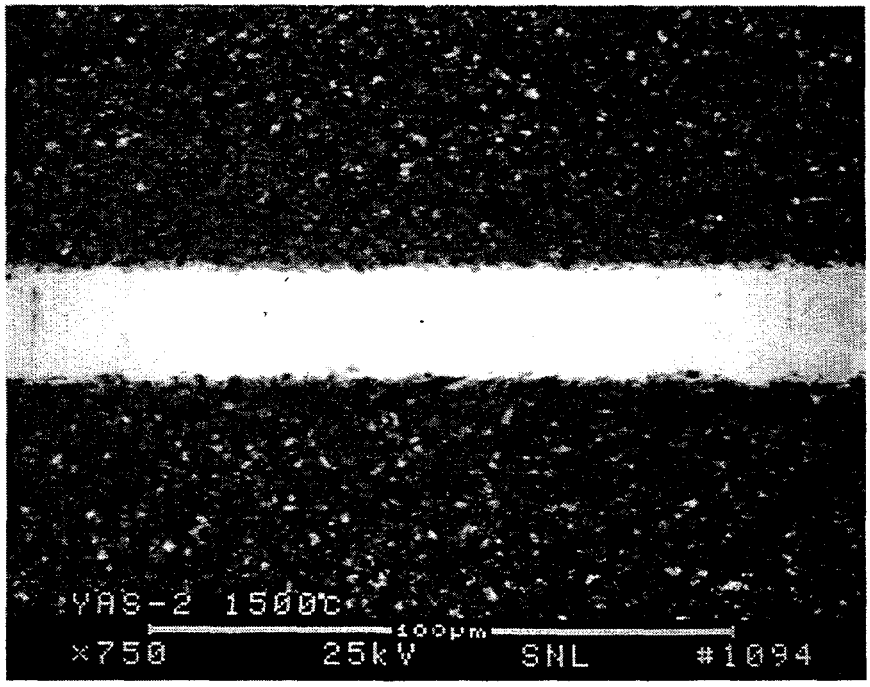

Fig. 6. Backscattered electron micrograph of a Si_3N_4/YAS-2 joint formed at 1500°C.

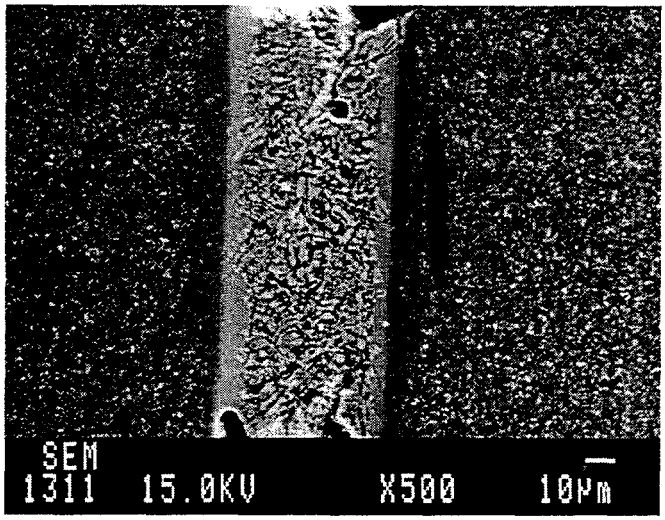

(a)

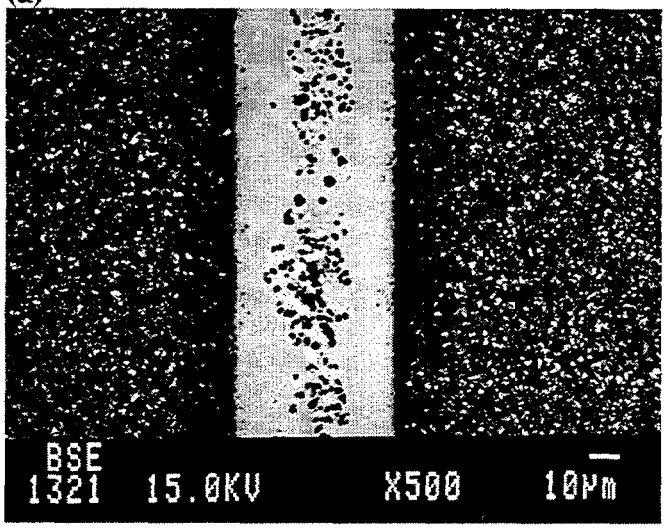

(b)

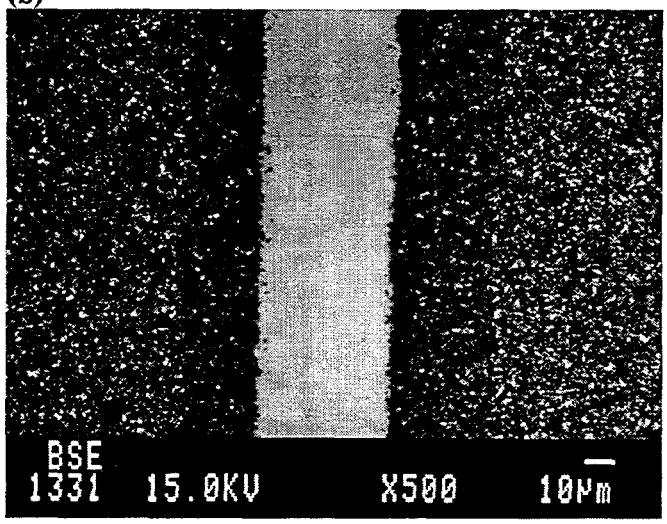

(c)

Fig. 7. Back-scattered electron micrographs of Si_3N_4 substrates joined with YAS-2 glass at (a) 1300, (b) 1350, and (c) 1400°C.

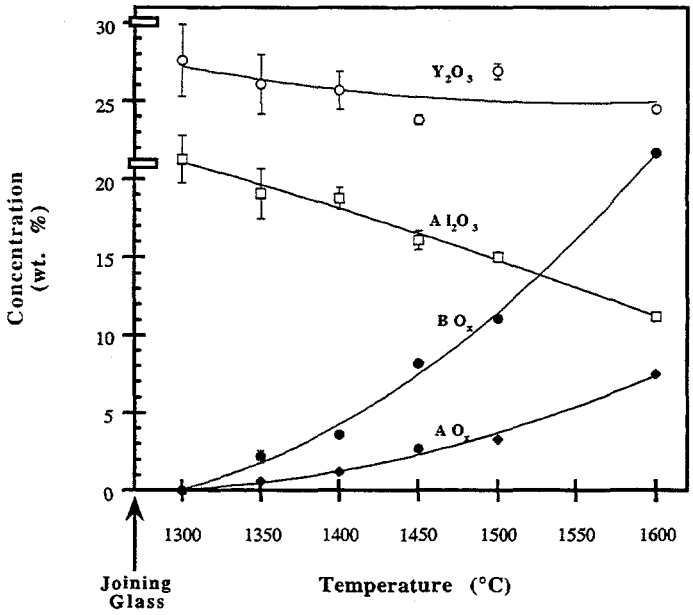

Fig. 8. Average oxide content measured at the center of the joint as a function of temperature. The starting composition is shown on the left axis.

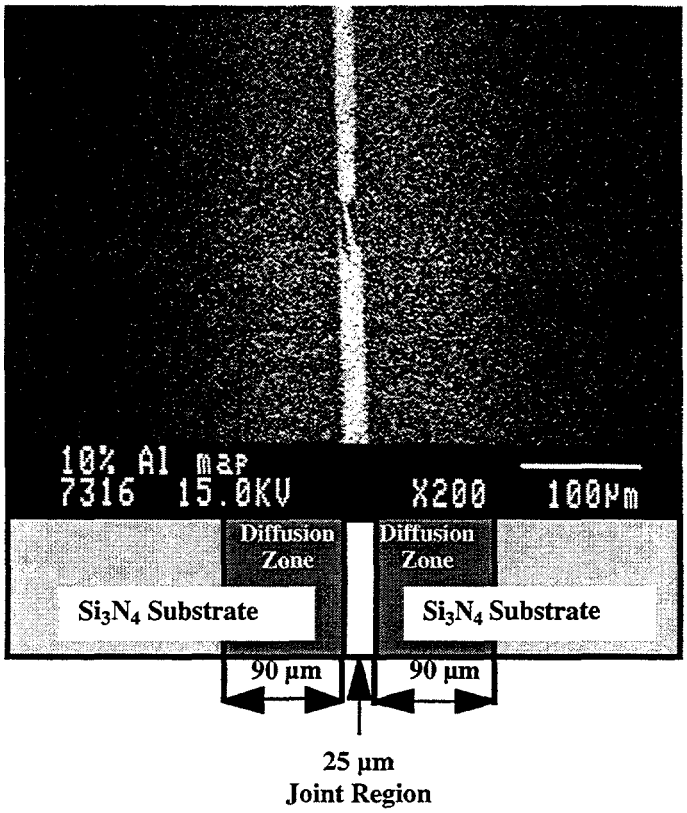

Fig. 9. Al diffusion zone in Si_3N_4 substrate after heat-treatment at 1500°C. The presence of Al is shown as bright spots in the micrograph.

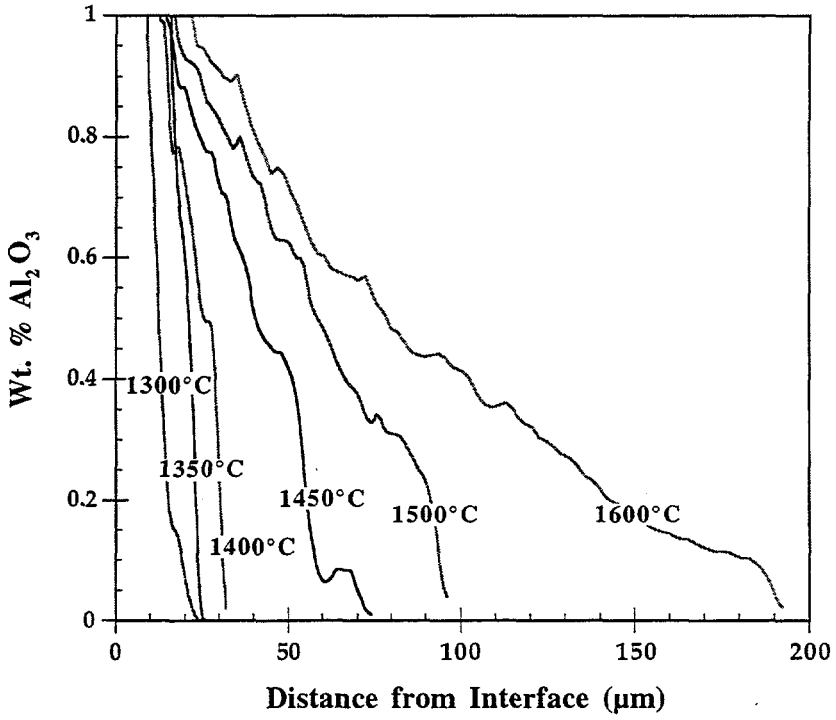

Fig. 10. Al_2O_3 content as a function of distance from the joint/substrate interface.

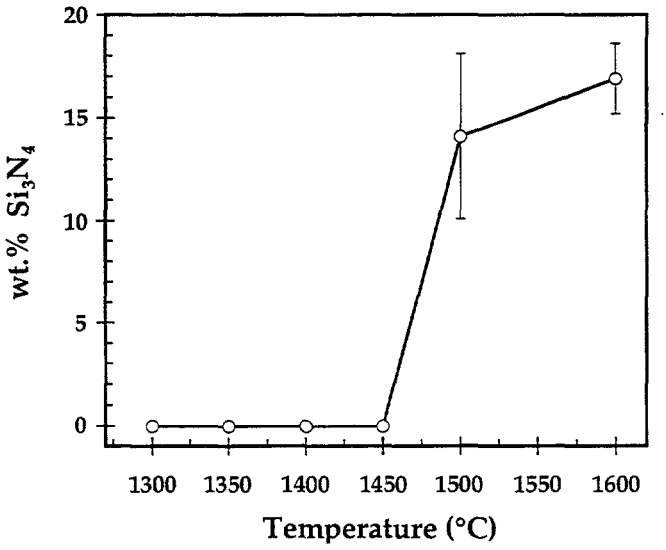

Fig. 11. Average Si_3N_4 content in the joint region as a function of temperature.

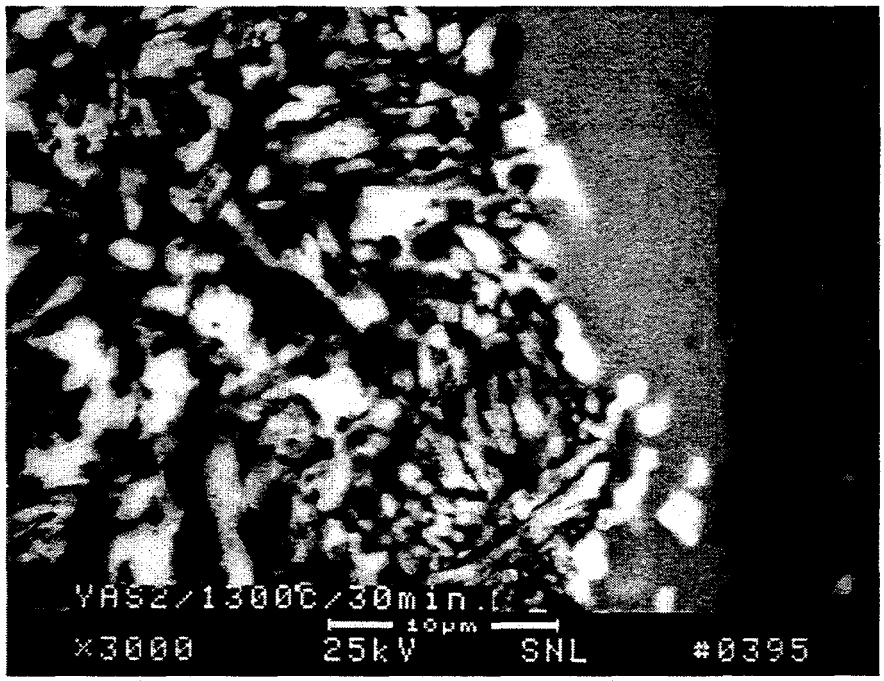

(a)

(b)

Fig. 12. (a) A higher magnification micrograph of the joint region formed at 1300°C (cf. Fig. 7a), along with (b) a micrograph of the joining glass pellet fired along with the joining specimen. The joint is composed of a thin amorphous layer at the Si_3N_4 interface and a thicker crystallized region in the center.

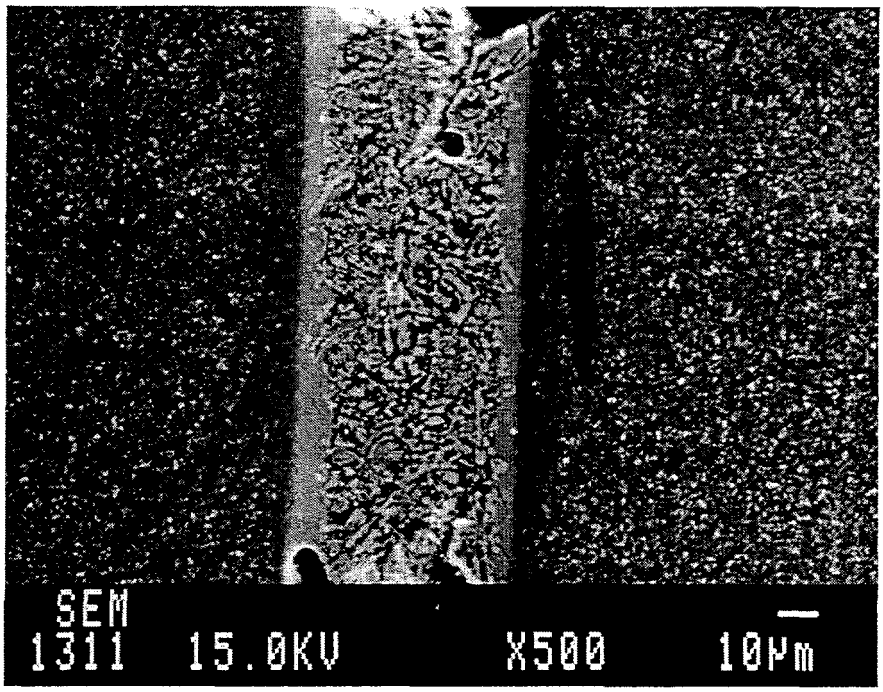

(a)

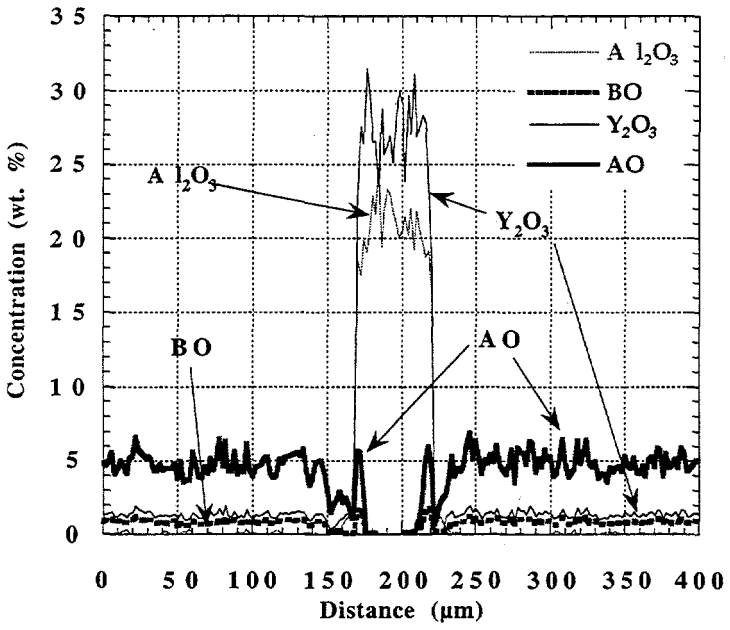

(b)

Fig. 13. (a) Back-scattered electron micrograph of Si_3N_4 joined with YAS-2 glass at 1300°C for 30 min. (b) Electron microprobe measurements made of the oxide constituents across the joint/substrate region shown in (a).

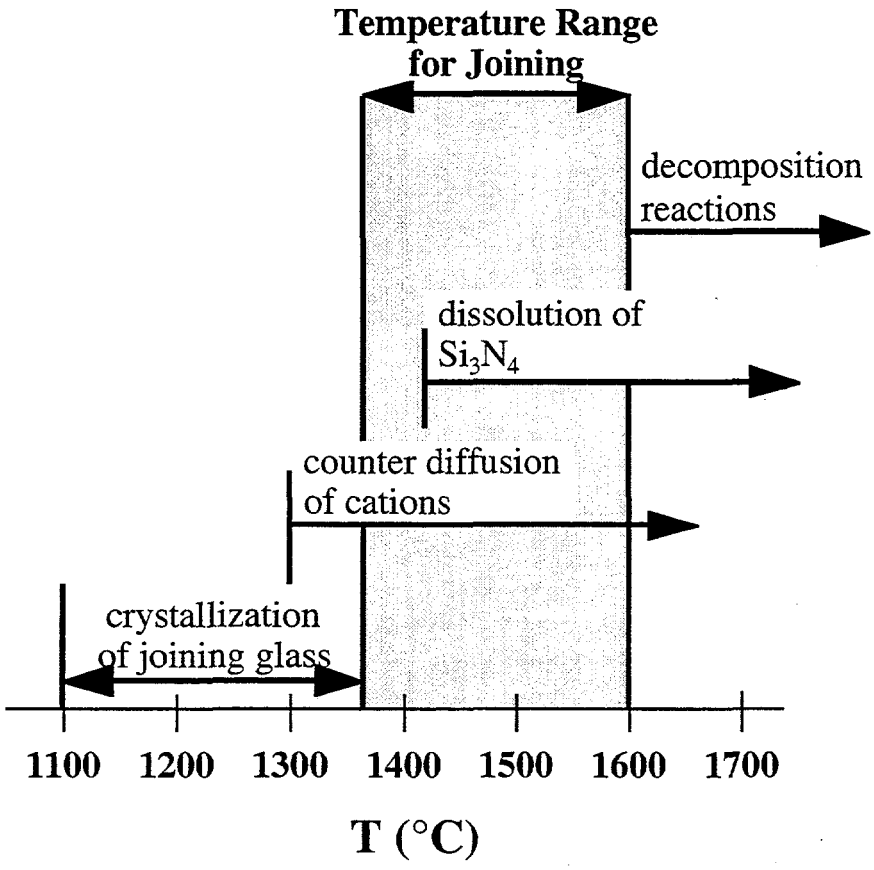

Fig. 14. Mechanisms of joining as a function of temperature.

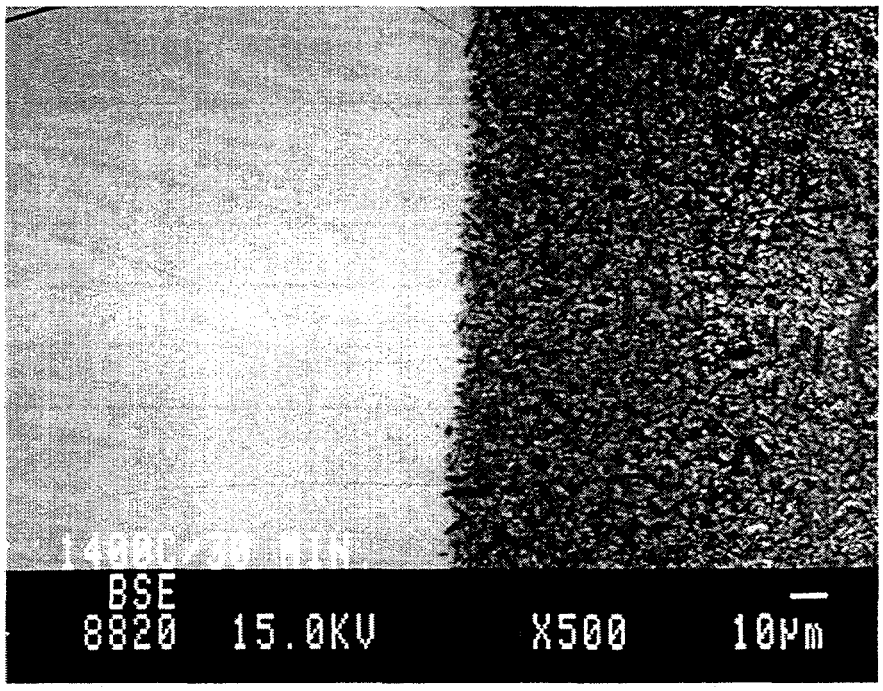

(a)

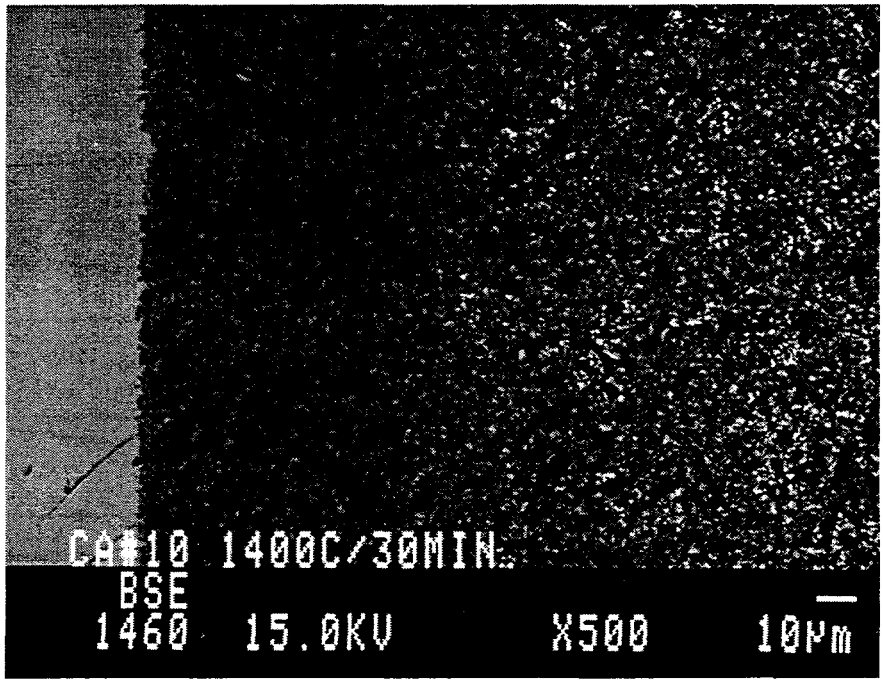

(b)

Fig. 15. Representative BSE images of (a) SAS-5 and (b) SAS-10 glass joints. These figures reveal dissolution of Si_3N_4 grains at the interface.

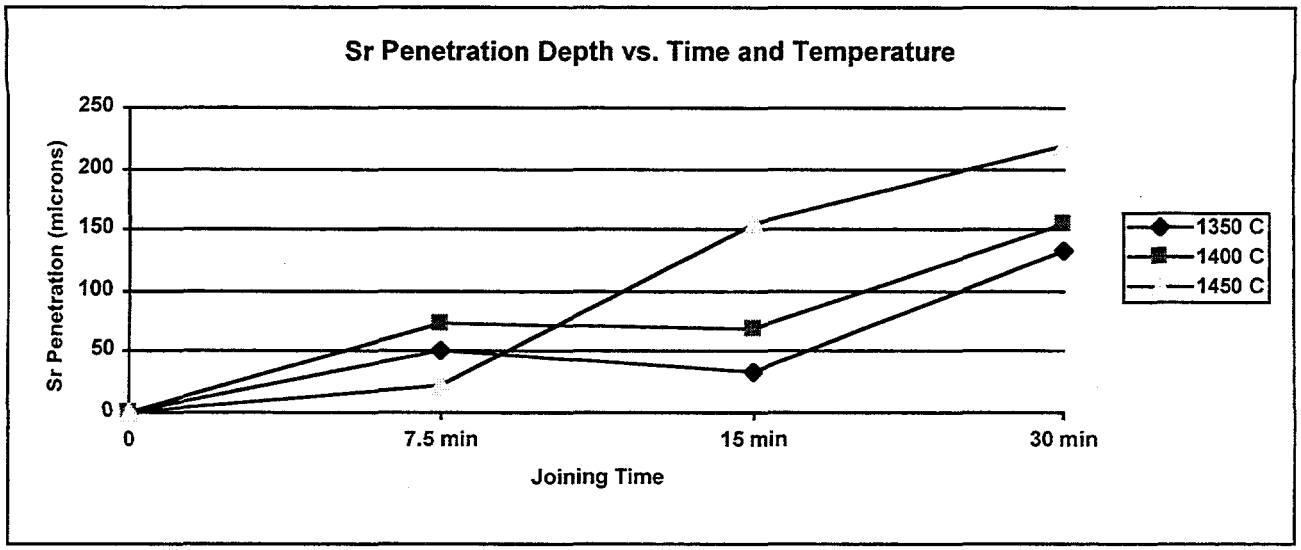

Fig. 16. Maximum Sr penetration depth vs. joining temperature and time for SAS-5 wetted Si_3N_4. Data presented at 0 min are inferred and do not reflect actual measurements.

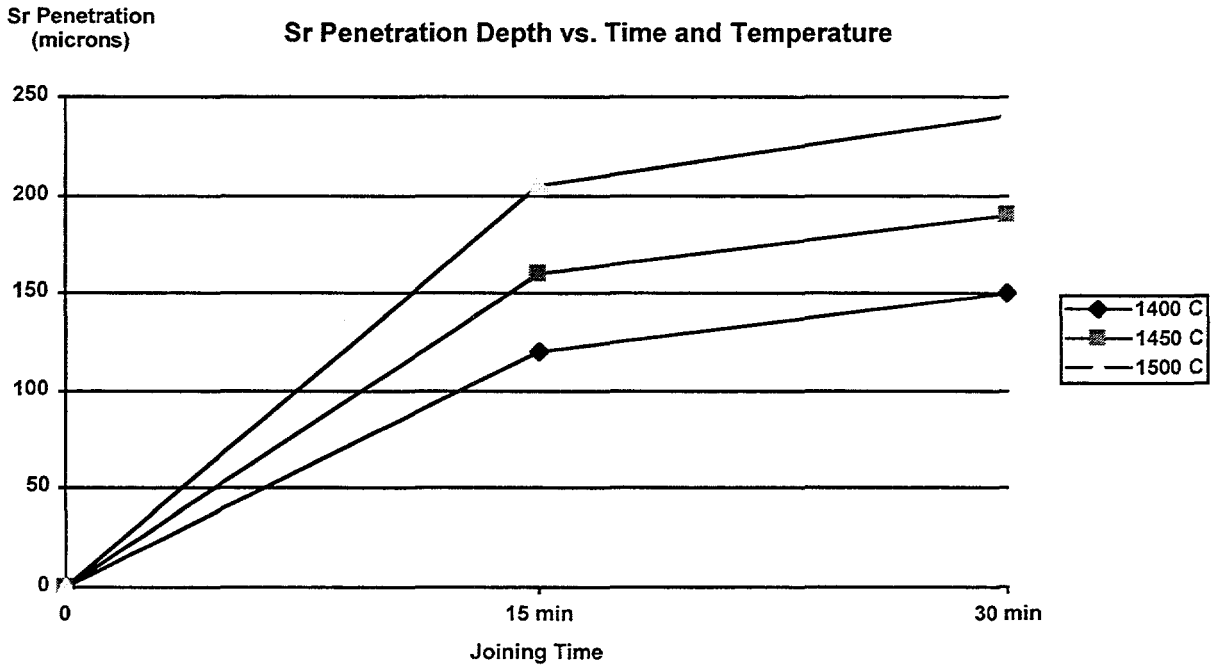

Fig. 17. Maximum Sr penetration depth vs. joining temperature and time for SAS-10 wetted Si_3N_4. Data presented at 0 min are inferred and do not reflect actual measurements.

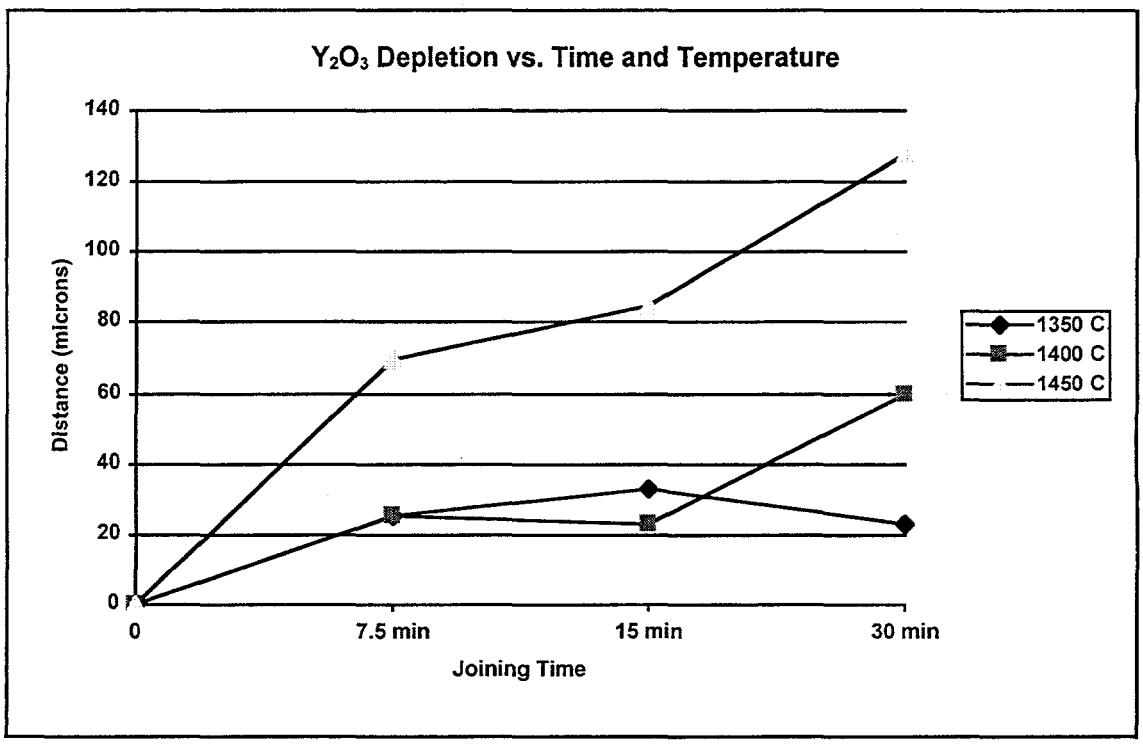

Fig. 18. Y_2O_3 Depletion in SAS-5 wetting of Si_3N_4 vs. time and temperature. Data presented at 0 min are inferred and do not reflect actual measurements.

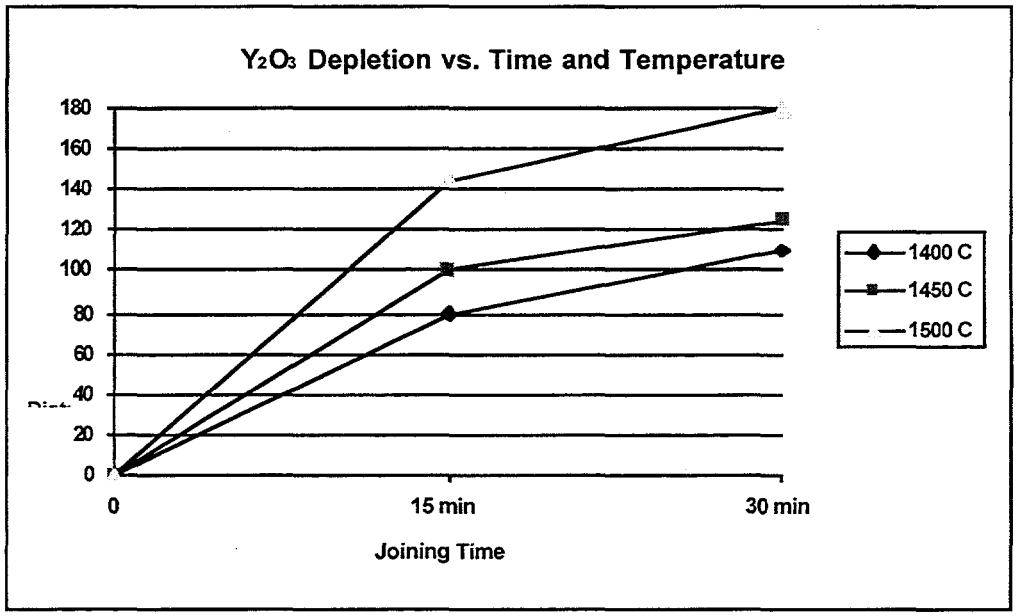

Fig. 19. Y_2O_3 Depletion in SAS-10 wetting of Si_3N_4 vs. time and temperature. Data presented at 0 min are inferred and do not reflect actual measurements.

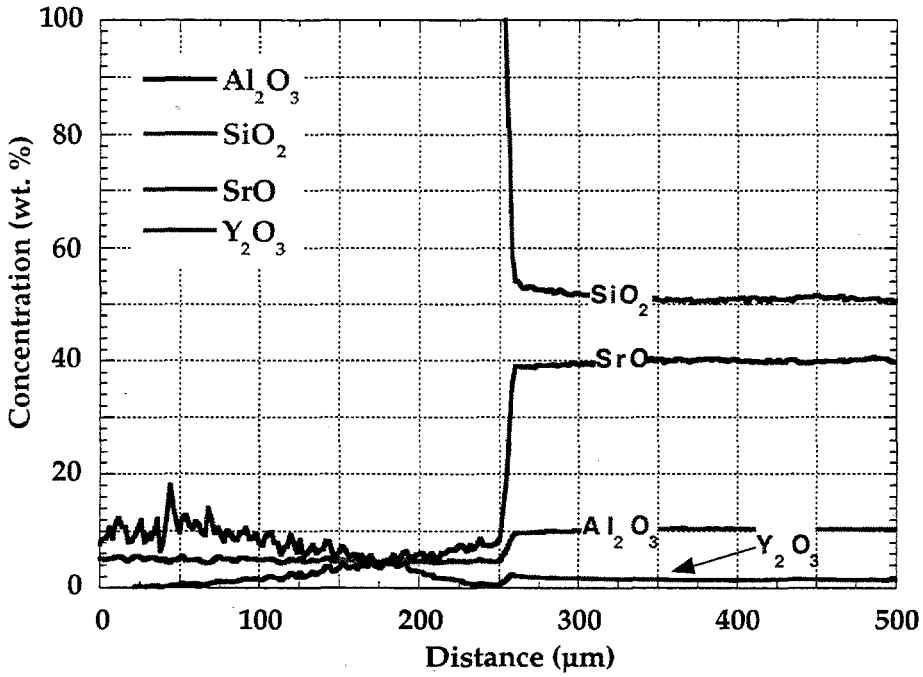

Fig. 20. Electron microprobe results for SAS-10 wetting Si_3N_4 at 1500°C for 30 min show a maximum diffusion depth for Y of greater than 250 μm. The glass is on the right of the 250 μm position and the Si_3N_4 is on the left.

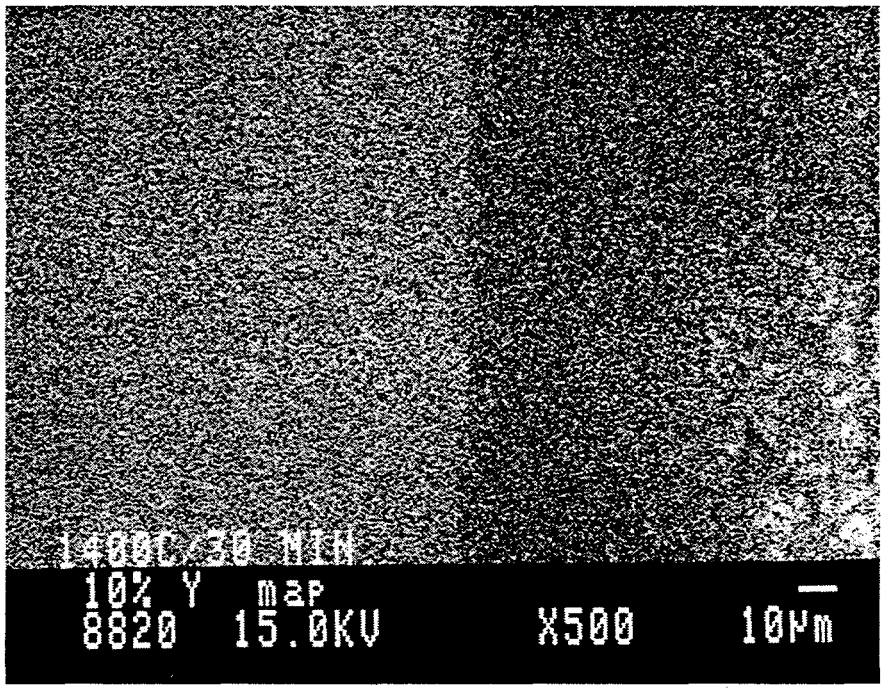

Fig. 21. 10% Y distribution map for SAS-5 glass (left side) wetting Si_3N_4 (right side) at 1400°C for 30 min.

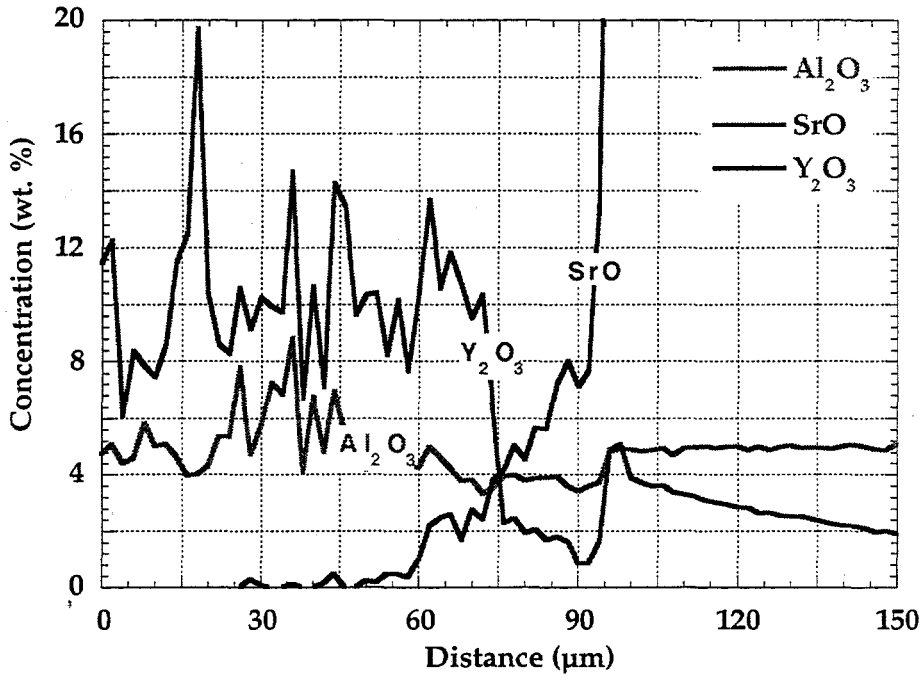

Fig. 22. Magnified electron microprobe analysis of the diffusion zone in SAS-5 wetted Si_3N_4 at 1400°C for 15 min, showing counter-ion diffusion. This counter-diffusion of Sr^{2+} and Y^{3+} ions is controlled by conservation of charge in the diffusion zone. This can be seen in magnification of microprobe scans across the interface. The glass is to the right of the 75 μm position.

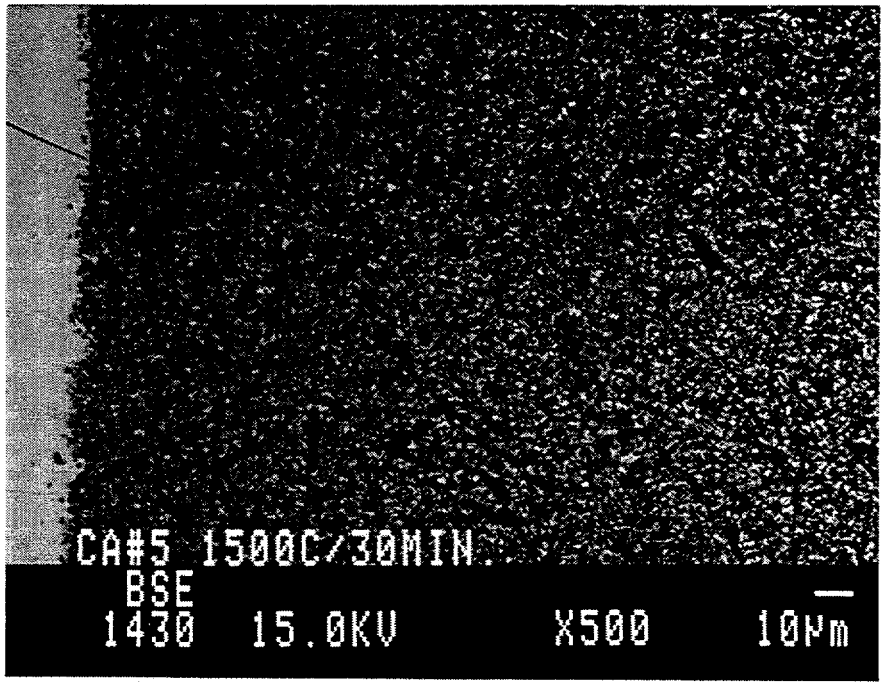

Fig. 23. BSE image of SAS-10 glass (left side) wetting Si_3N_4 (right side) at 1500°C for 30 min. Note the black Si_3N_4 particles that have broken off into the glass region.

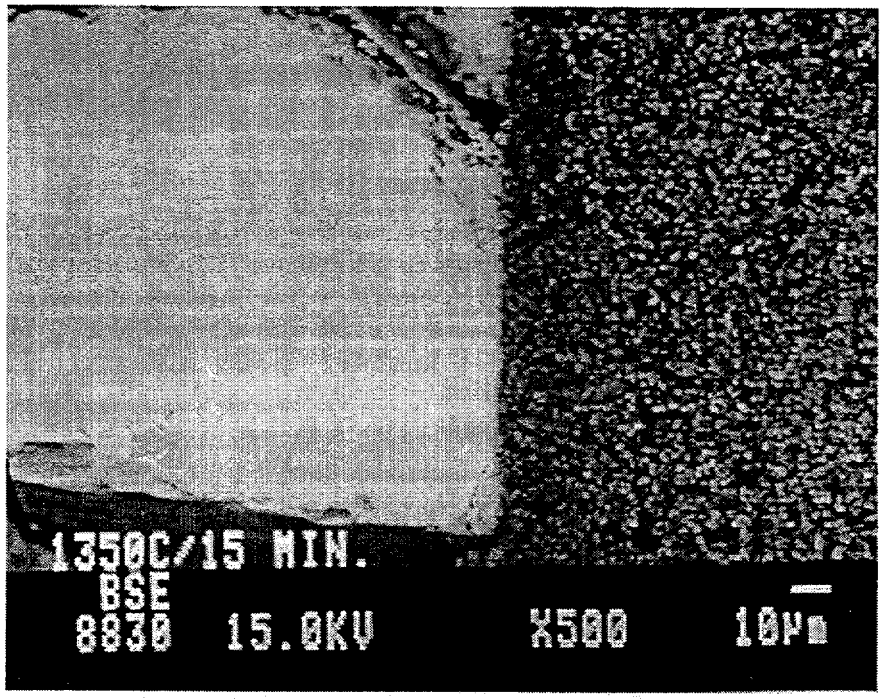

Fig. 24. BSE image of SAS-5 glass (left side) wetting Si_3N_4 (right side) at 1350°C for 15 min. Note the relative uniformity of the Si_3N_4 glass interface.

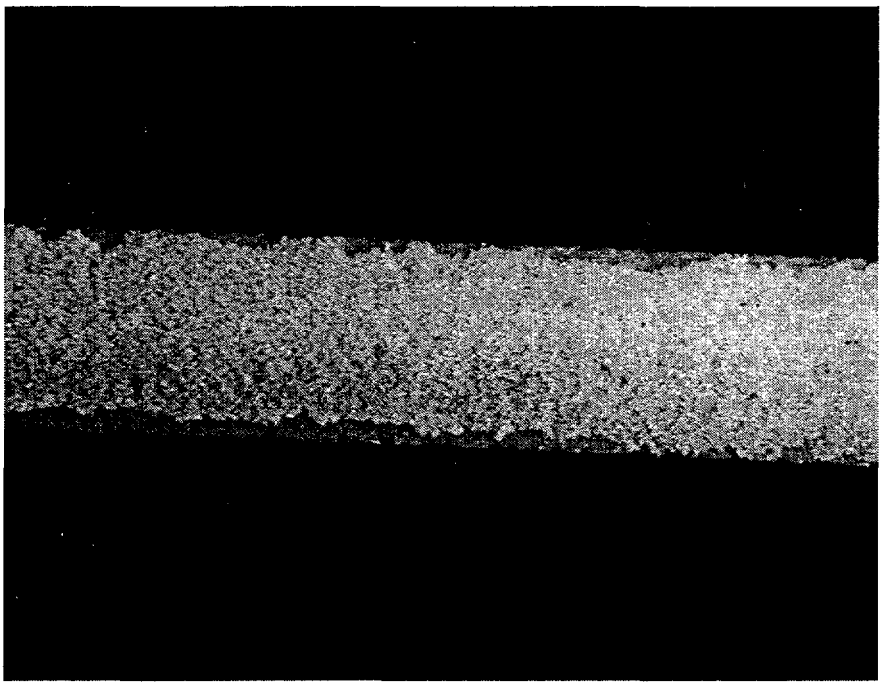

Fig. 25. An optical micrograph of a grit blasted and thermal spray coated AS-800 Si_3N_4 specimen is shown.

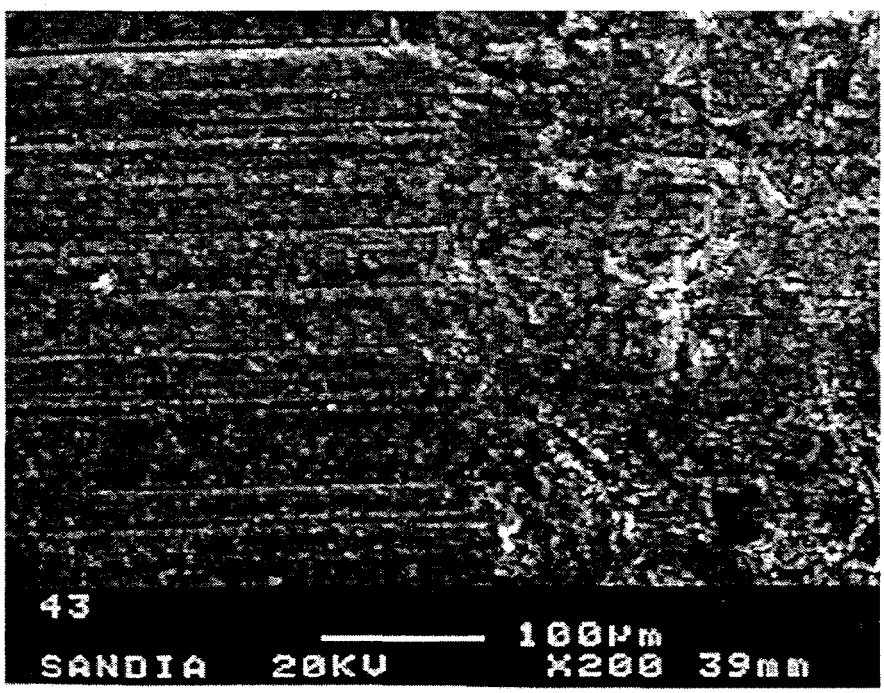

Fig. 26. SEM micrograph of grit-blasted surface (right) and the adjacent as-machined surface (left) of AS800 Si_3N_4 .

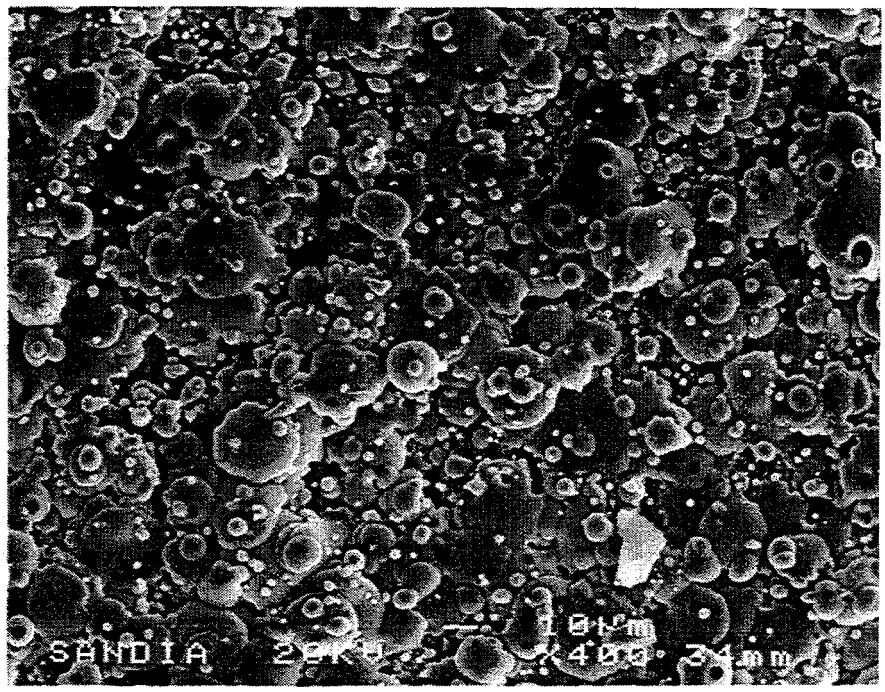

(a)

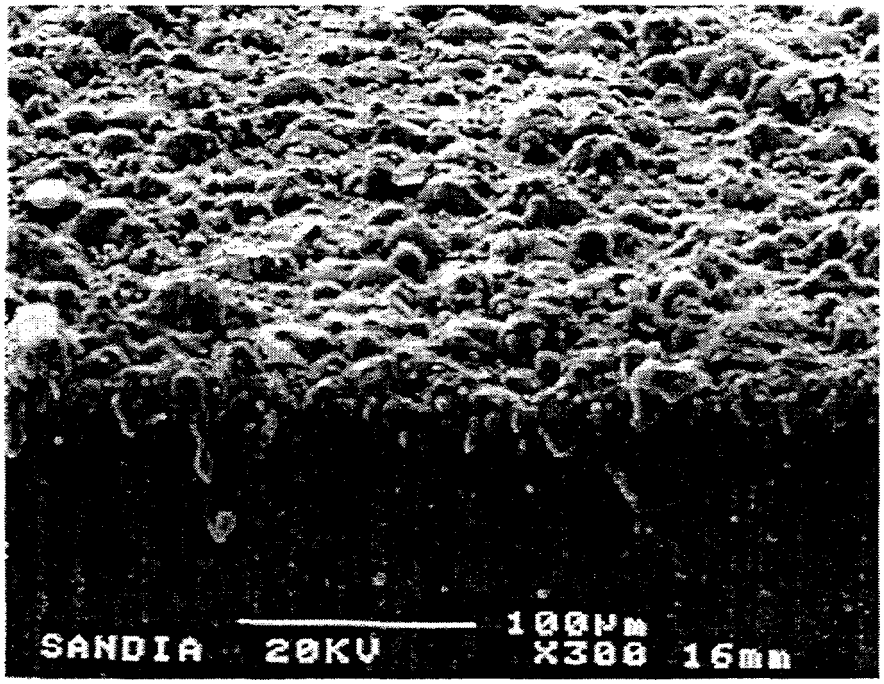

(b)

Fig. 27. SEM micrographs showing (a) top and (b) oblique views of a good thermally sprayed coating on AS-800 Si_3N_4.

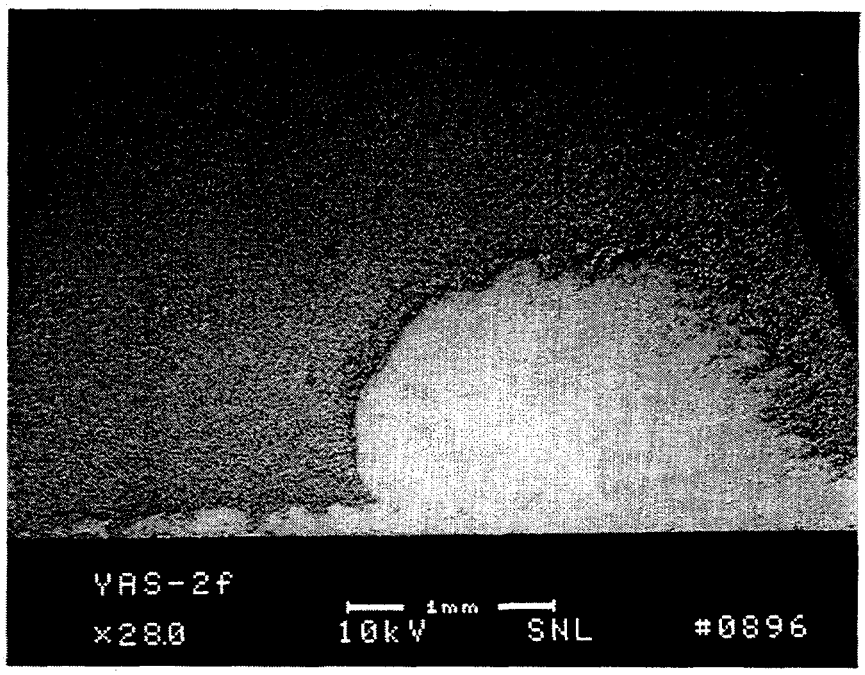

(a)

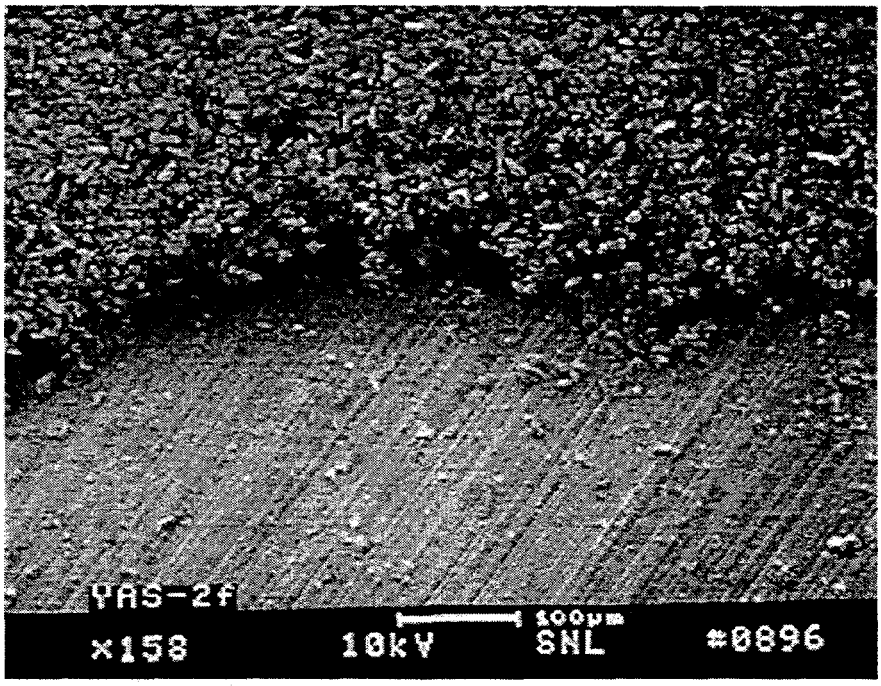

(b)

Fig. 28. SEM micrographs of a slurry-coated AS-800 Si_3N_4 sample. (a) low magnification (b) higher magnification

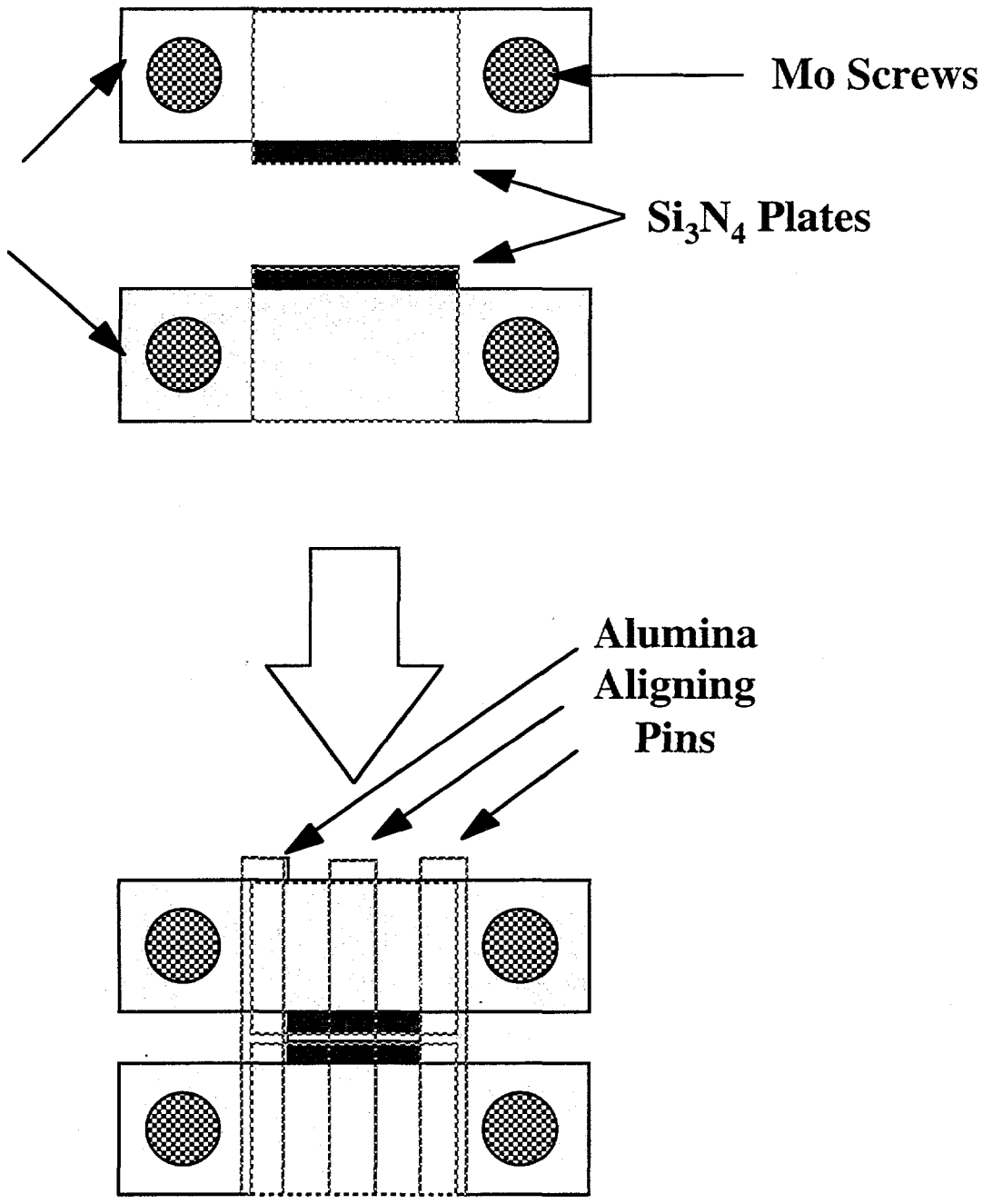

(b)

Fig. 29. The alumina/Mo fixture used for joining two 22.0 mm x 4.4 mm x 30.0 mm blocks of Si_3N_4. (a) Top view (b) Side view.

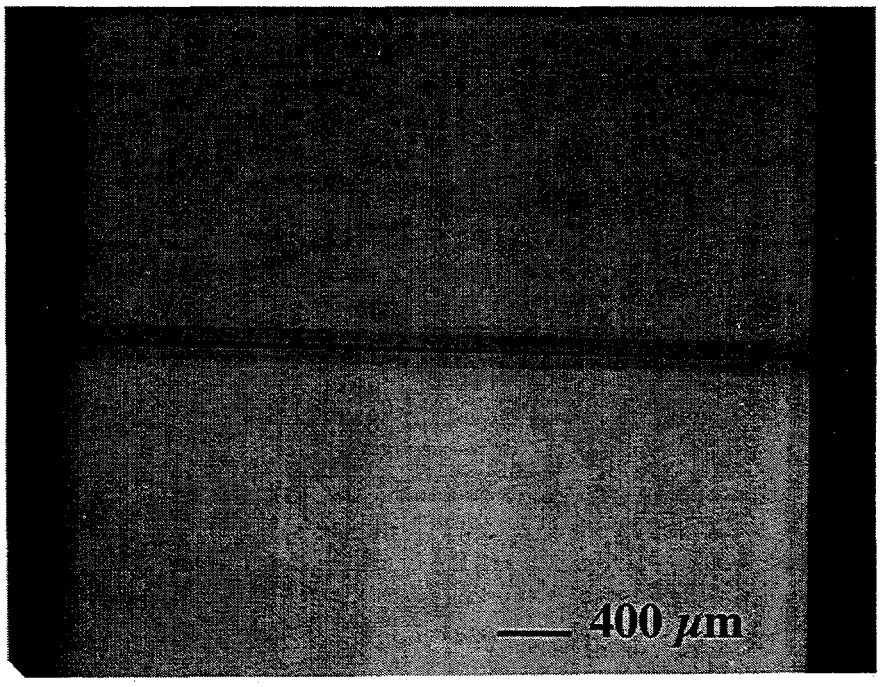

(a)

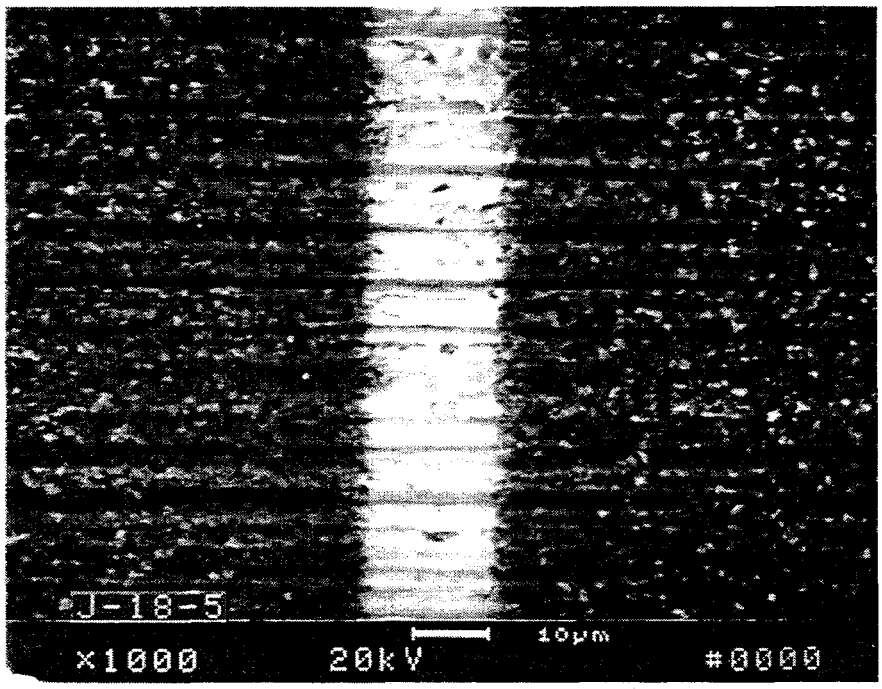

(b)

Fig. 30. (a) Optical and (b) SEM micrographs of a YAS-2 glass joint produced at 1500°C.

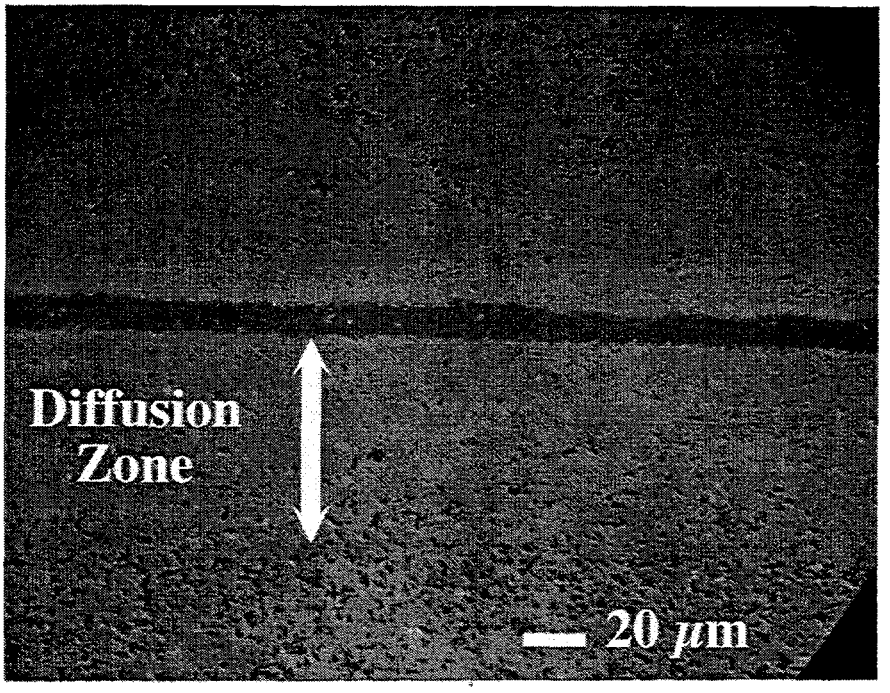

Fig. 31. The appearance of the diffusion zone in the Si_3N_4 adjacent to the joint. This region is generally 50-70 μm thick for blocks joined at 1500°C for 30 min.

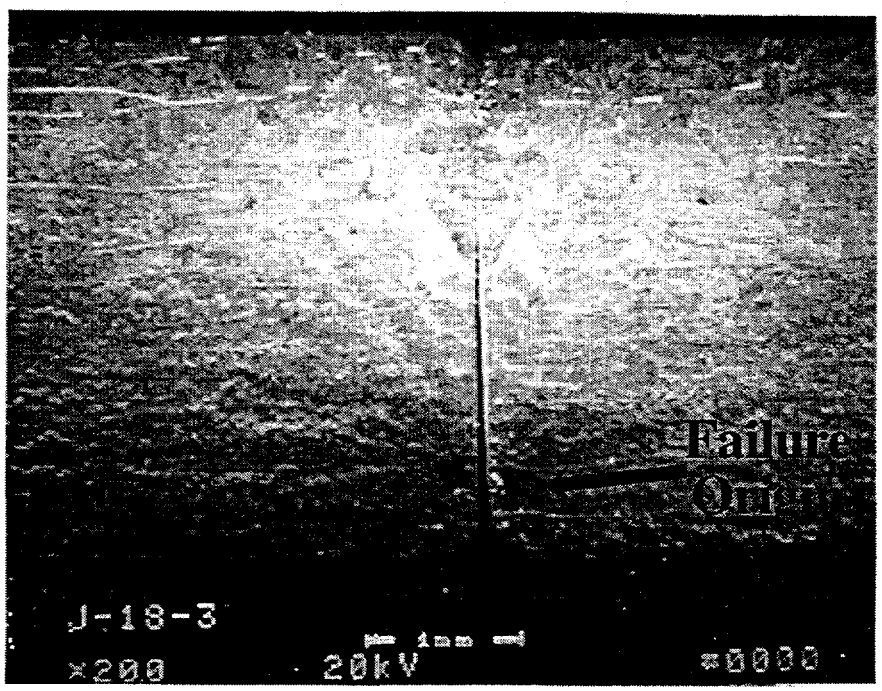

(a)

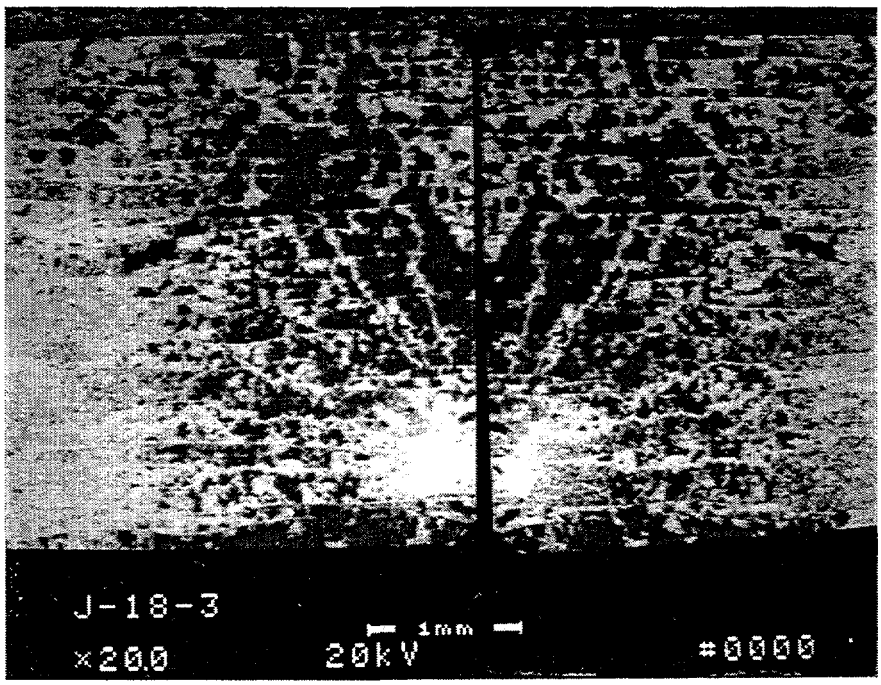

(b)

Fig. 32. (a) SEM and (b) BSE micrographs of the fracture surface of a room temperature strength specimen. The fracture has propagated primarily in the glass joint (notably at the failure origin), but also in the Si_3N_4. There are cracks in the joining phase perpendicular to the original interface.

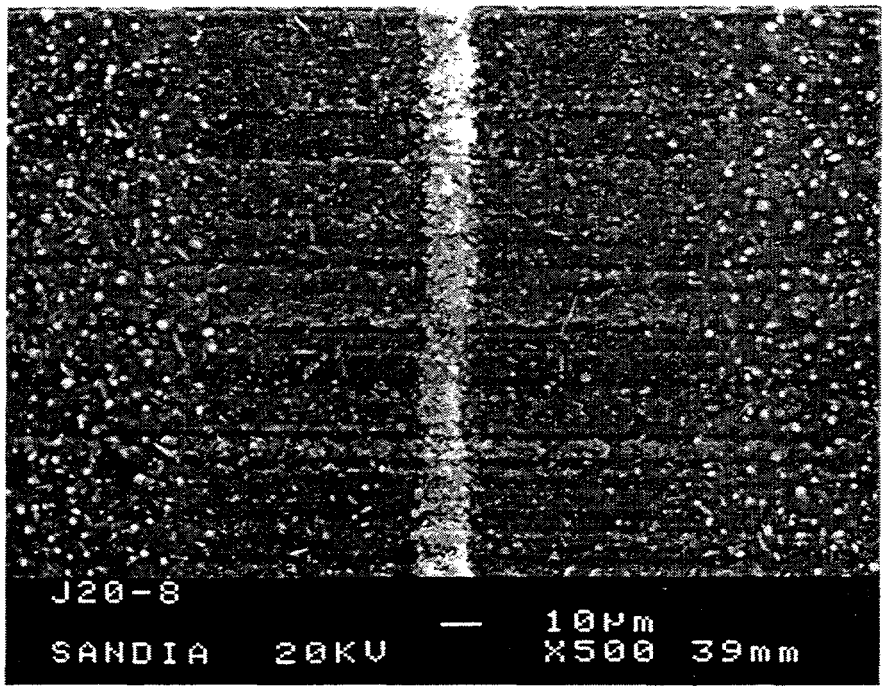

(a)

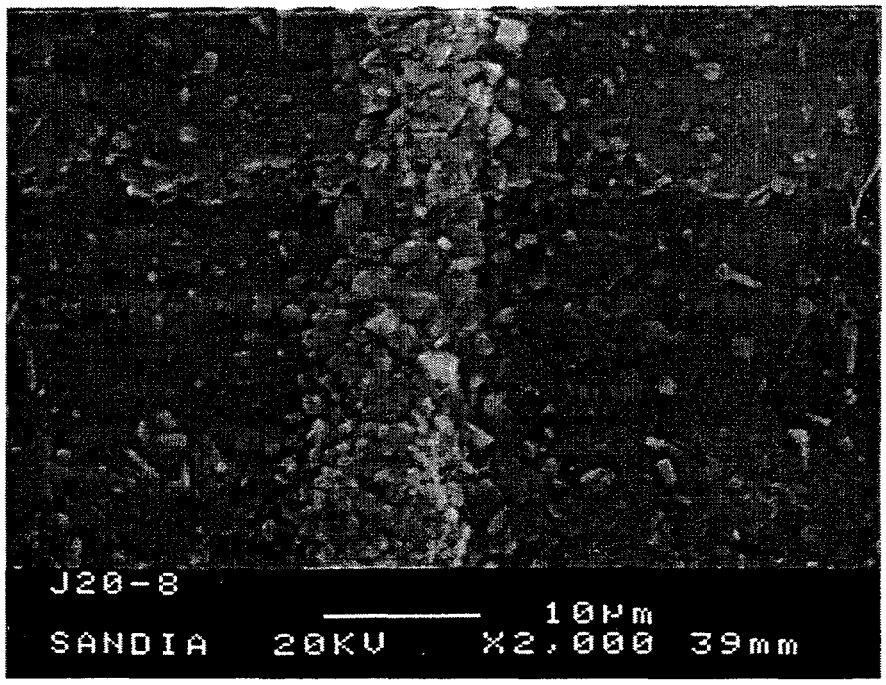

(b)

Fig. 33. (a) Low and (b) high magnification SEM micrographs of a YAS-2 glass joint after the 1000°C heat treatment. The joint phase appears to have crystallized and partially extruded from the joint.

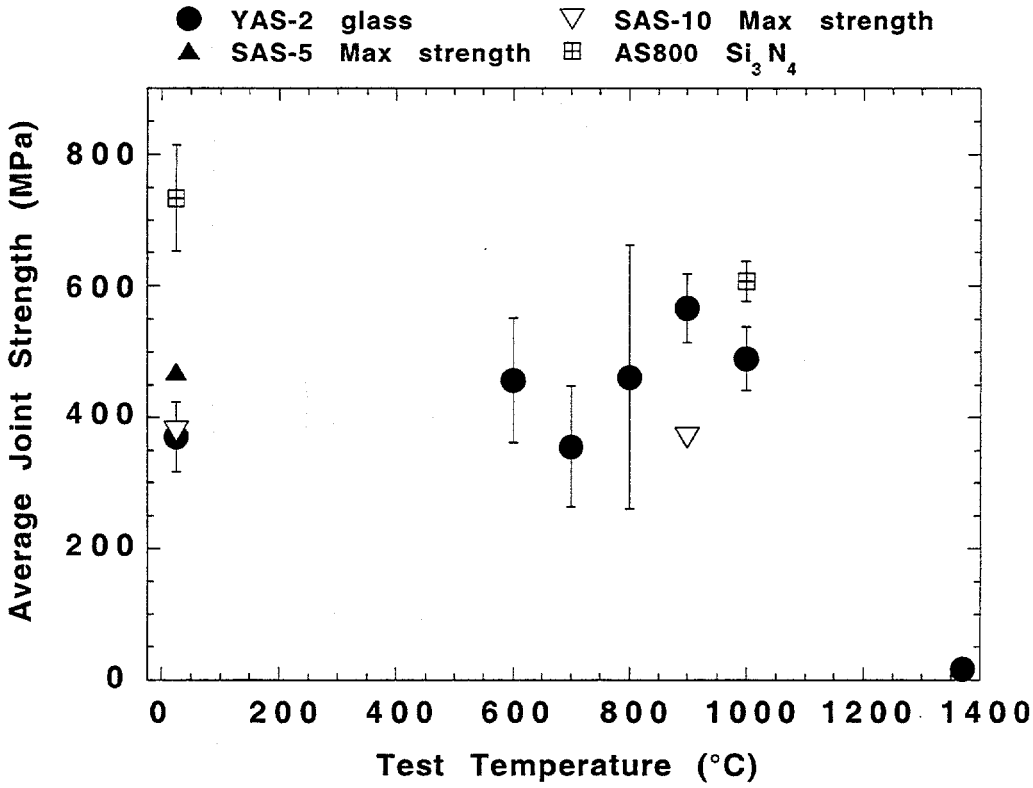

Fig. 34. The average four-point bend strength as a function of temperature for AS800 Si_3N_4 and oxynitride glass joints.

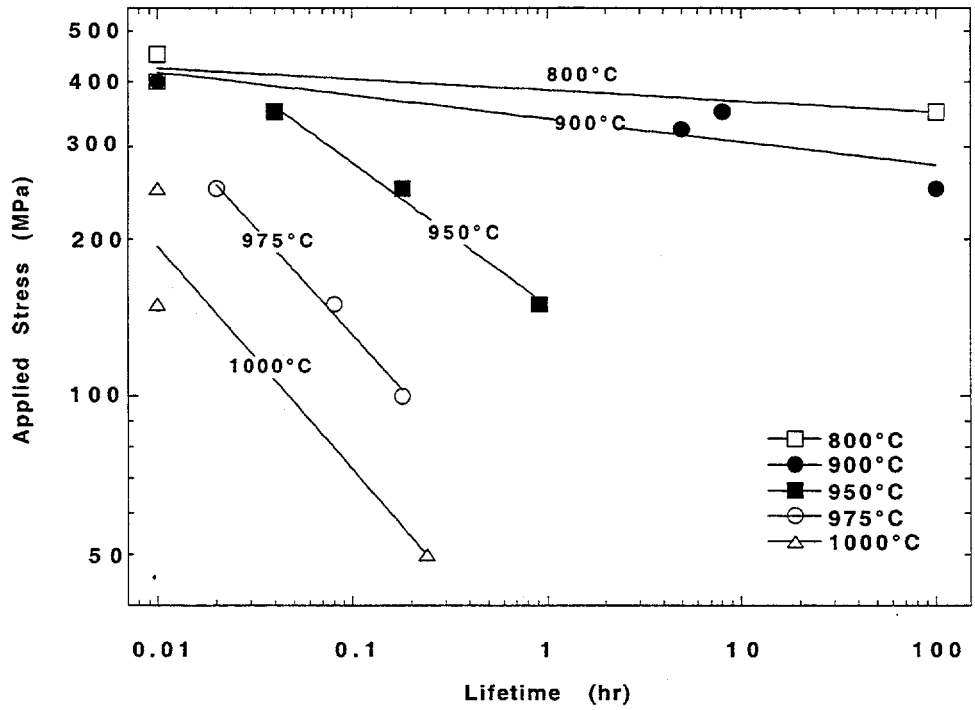

Fig. 35. The flexural stress-rupture results for YAS-2 glass joints.

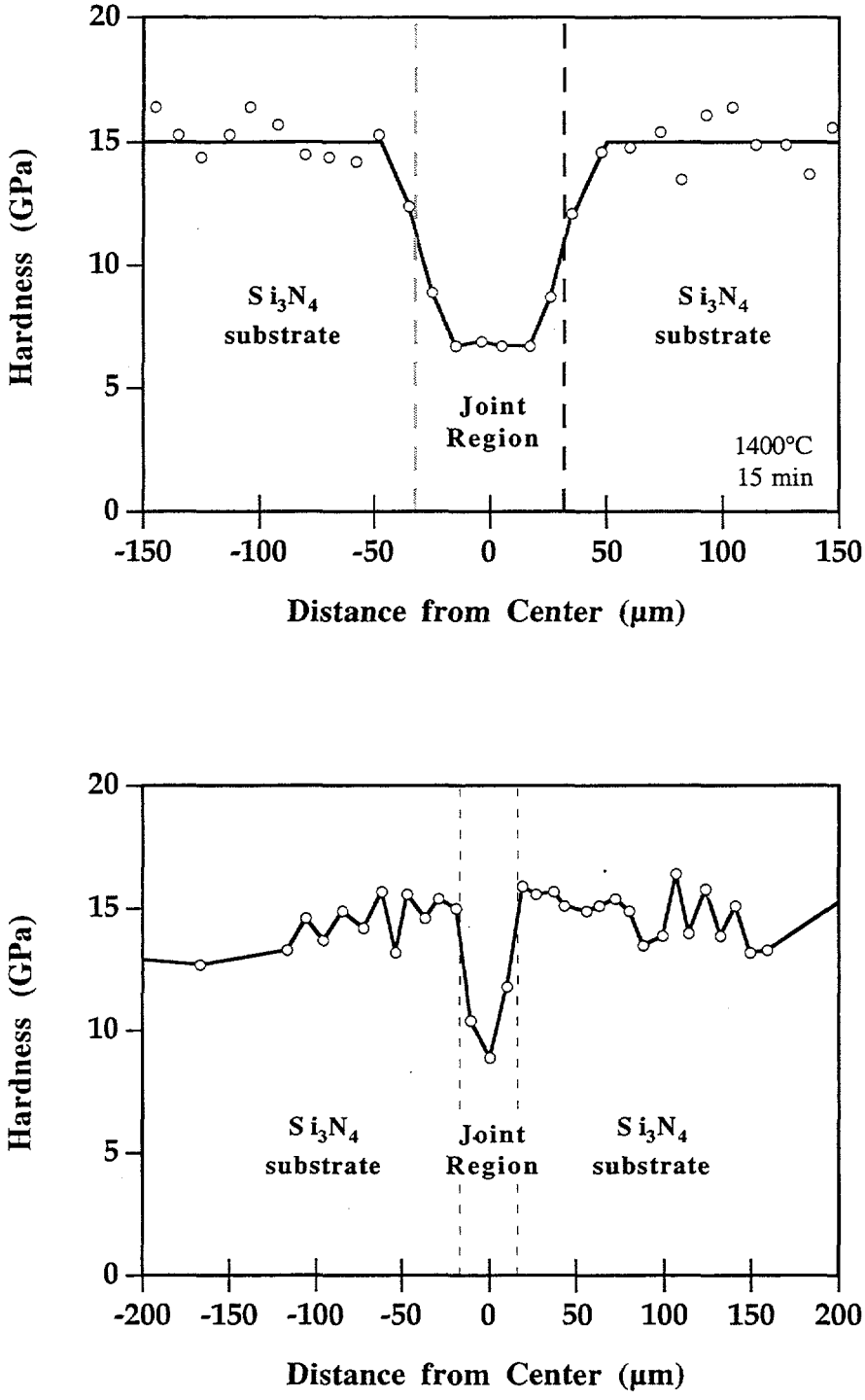

Fig. 36. (a) Vickers hardness as a function of distance from the joint center for 1400°C and 15 min (YAS-2 glass). (b) Vickers hardness as a function of distance from the joint center for 1500°C and 30 min (YAS-2 glass).

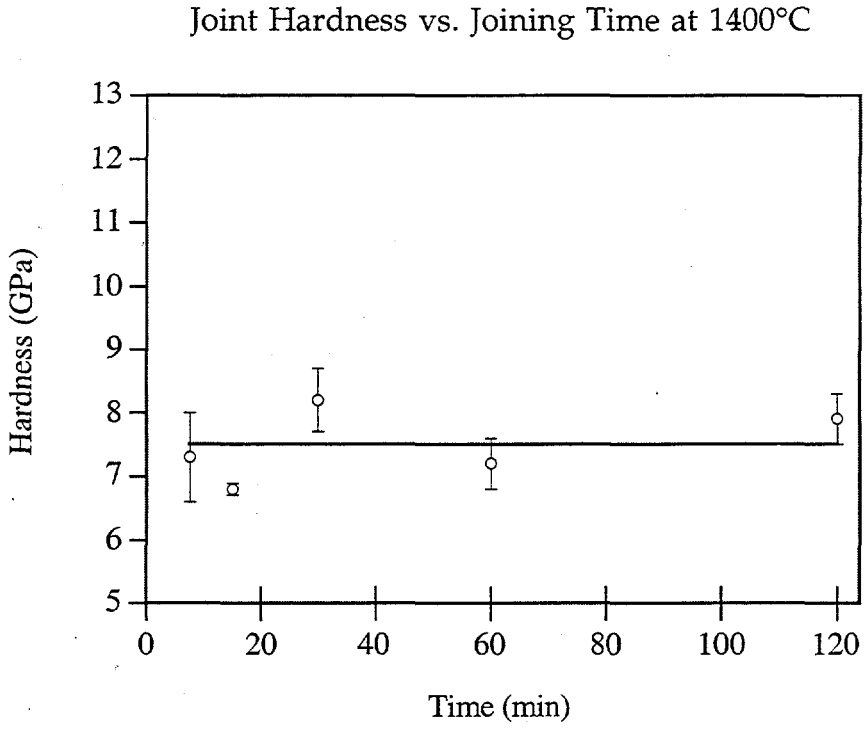

Fig. 37. Vickers hardness of a YAS-2 glass joint vs. time at 1400°C.

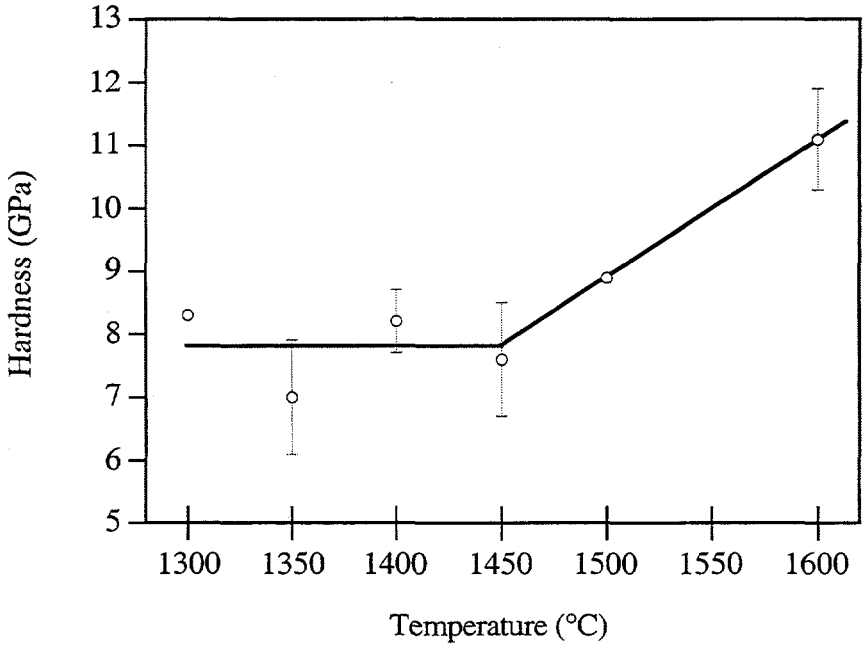

Fig. 38. Vickers hardness of a YAS-2 glass joint vs. temperature for a time of 30 min.

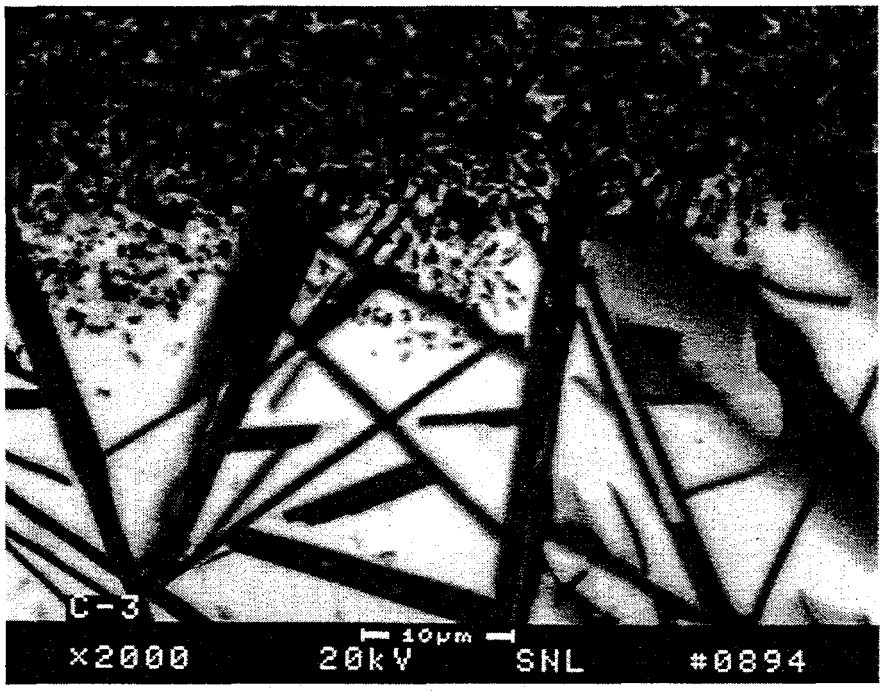

Fig. 39. BSE micrograph of a YAS/ Si_3N_4 interface after Si_3N_4 additions to the glass. The needle-like grains have a composition of $Al_6Si_2O_{13}$.

(a)

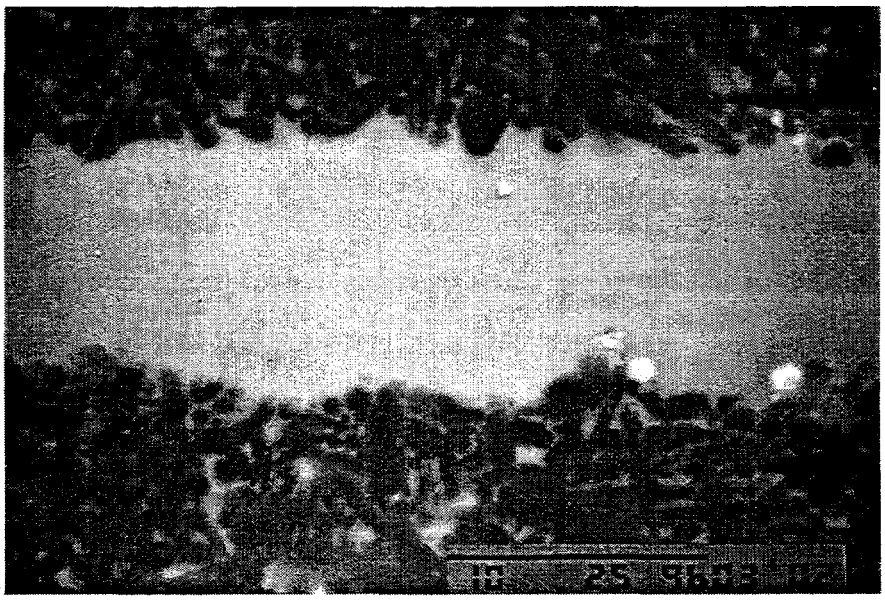

(b)

Fig. 40. Comparison of a) bulk Si_3N_4 and b) Si_3N_4 adjacent to the YAS-2 glass joint. Some of the joint glass appears to be present in the Si_3N_4 and the grains are more rounded than in the bulk.

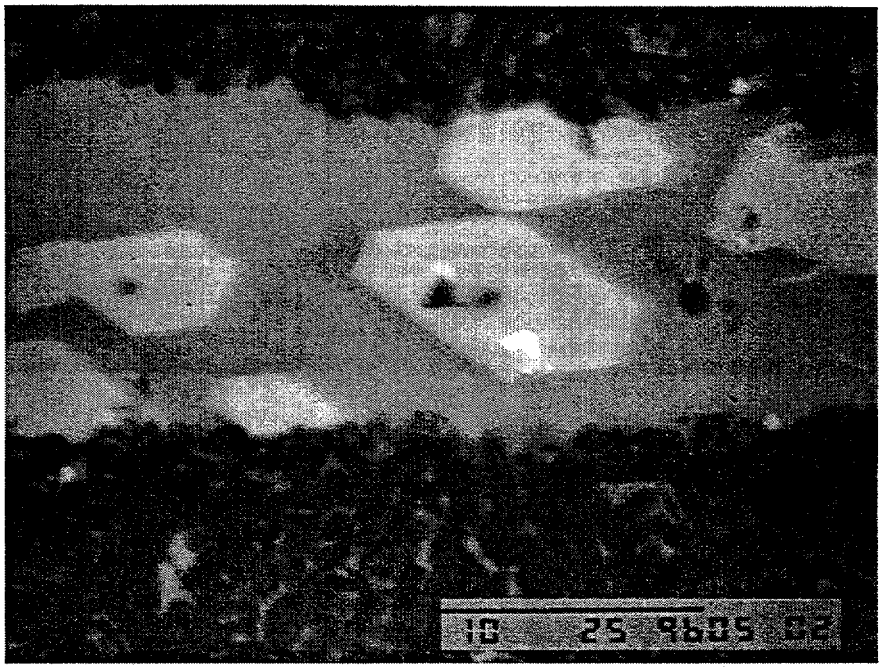

Fig. 41. A sample held at 1300°C for 2 hr exhibits a considerable amount of crystallization in the joint region.

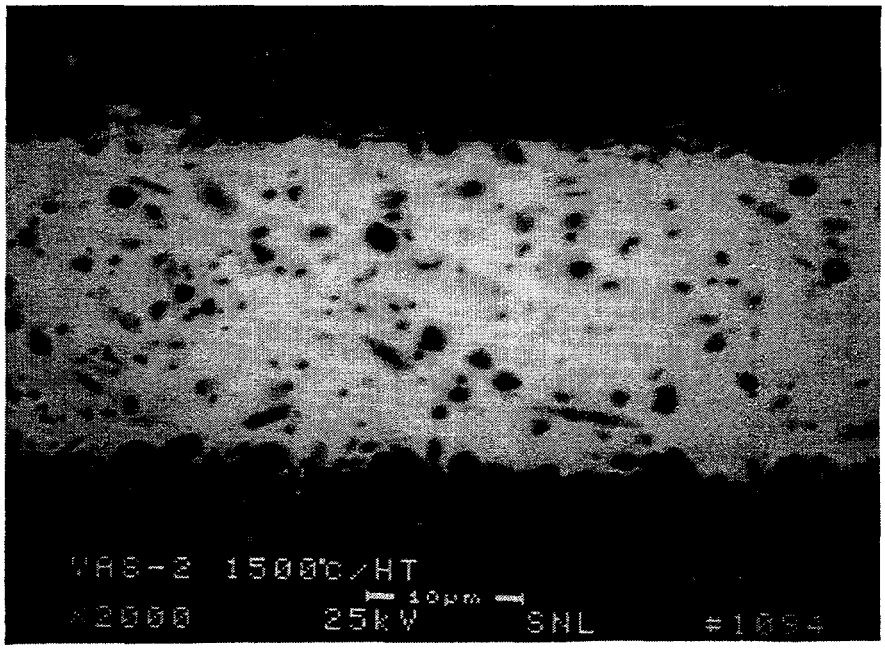

(a)

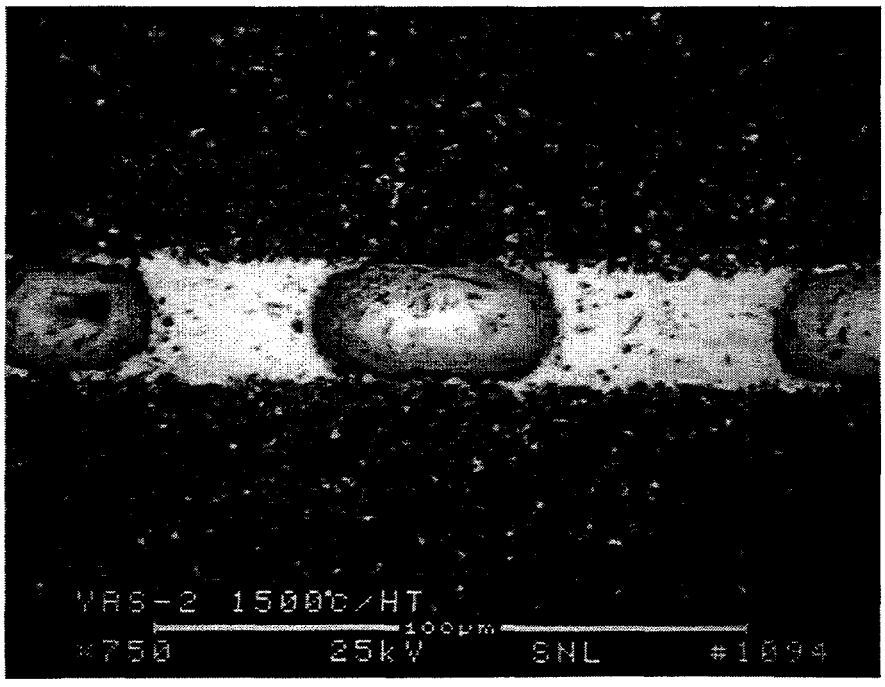

(b)

Fig. 42. (a) Crystallization within a YAS-2 joint that was heat treated at 1400°C for 180 min. (b) Low magnification micrograph of bubbles that indicate volatilization has occurred.

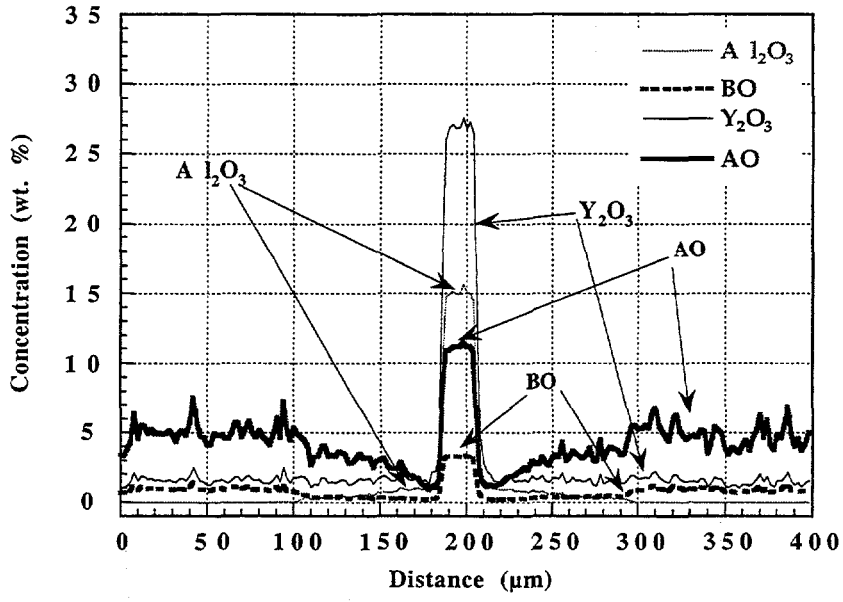

(a)

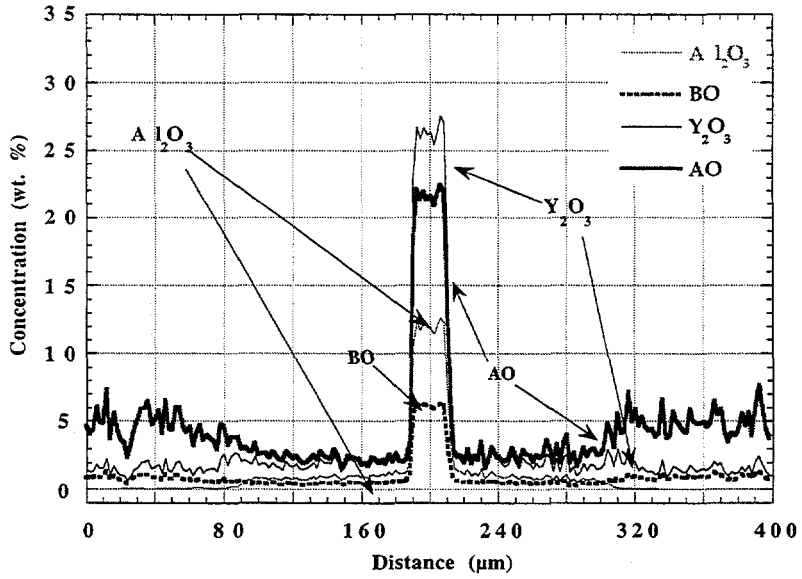

(b)

Fig. 43. (a) Electron microprobe compositional profile of a YAS-2 glass joint processed at 1500°C for 30 min. (b) The joint in (a) after heat treatment at 1400°C for 24 hr. (AO and BO are proprietary sintering aids)

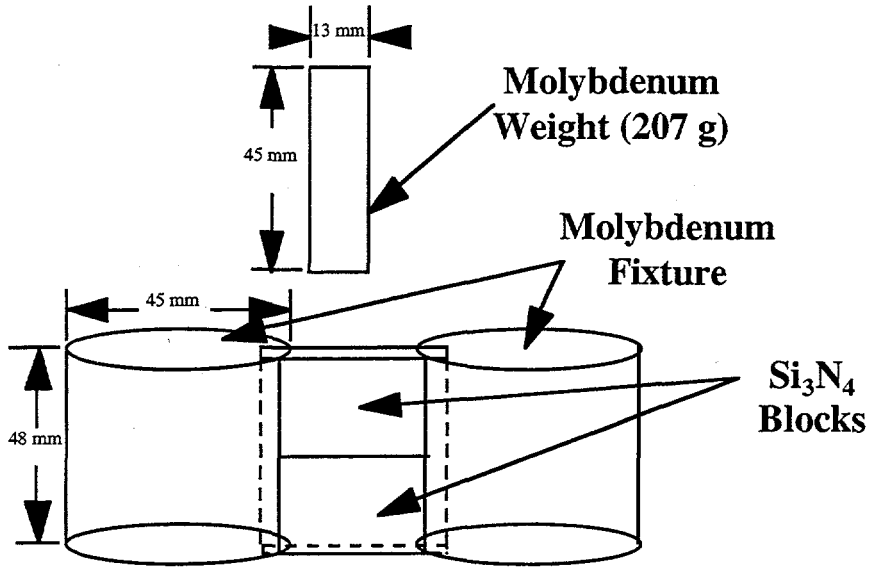

(a)

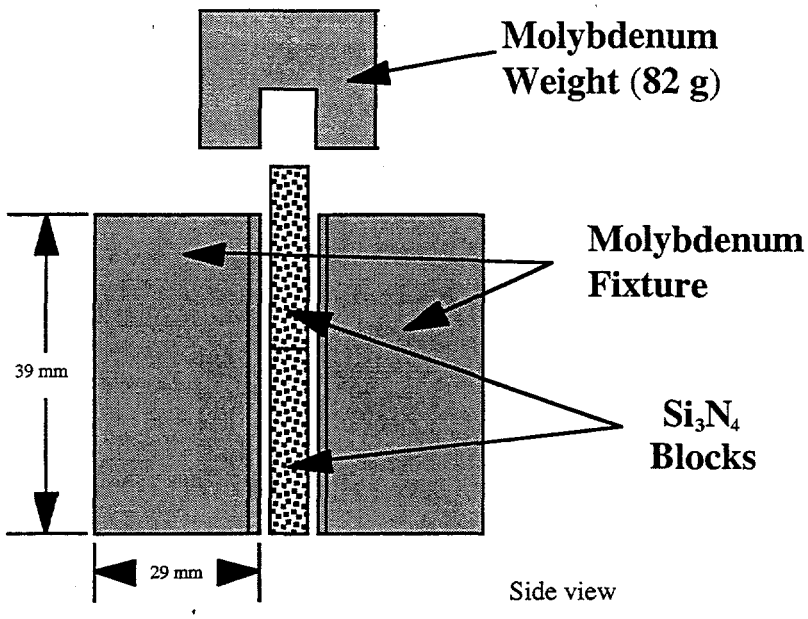

(b)

Fig. 44. (a) Schematic of the Mo heavy-weight fixture (b) Schematic of the Mo light-weight fixture.

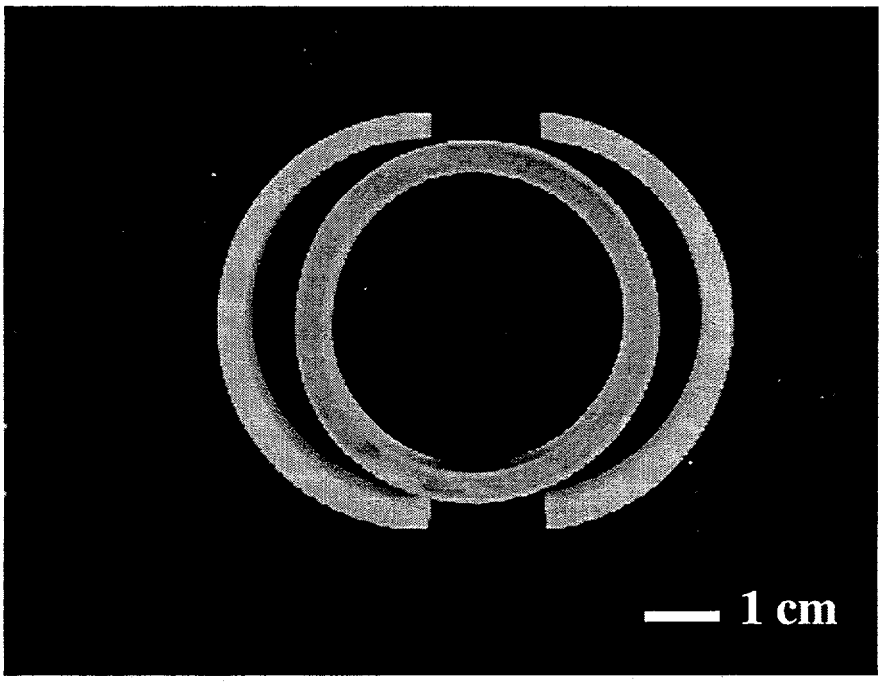

Fig. 45. The fixturing arrangement for two slices of a combustor ring. The alumina tube was cut at an angle similar to that of the ring walls, then split to form two clamshell sections that were held in place against the ring sections.

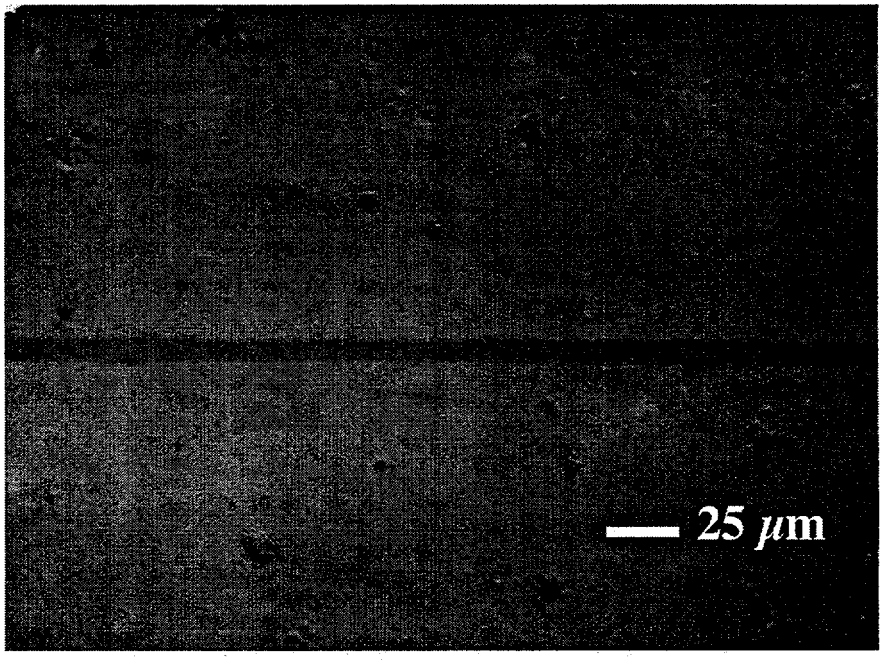

Fig. 46. The YAS-2 glass joint between two slices of an AS-800 Si_3N_4 combustor ring.

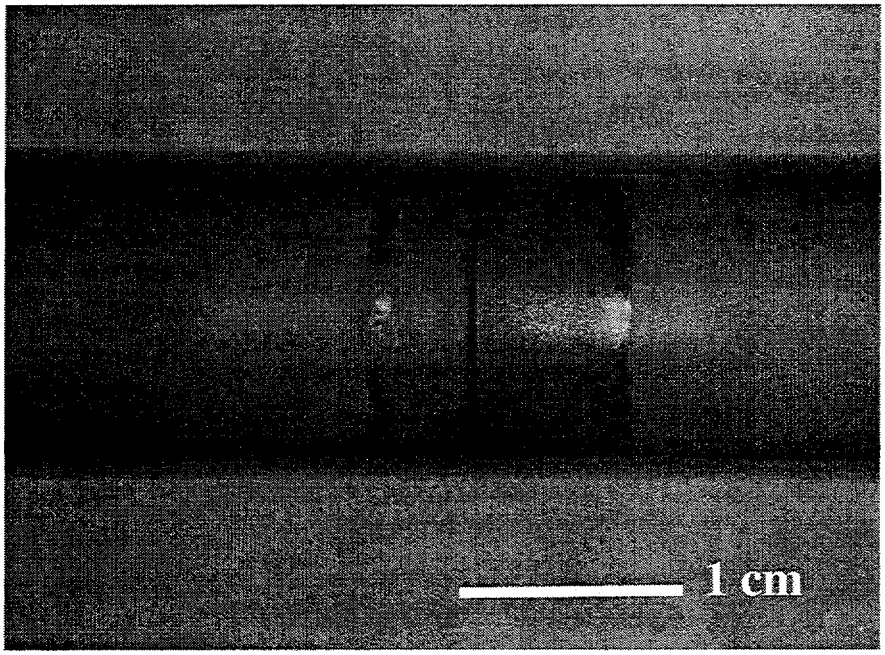

Fig. 47. A joint between two GS-44 silicon nitride cylinders slurry-coated with YAS-2 glass.

Chapter 2. Metal/Ceramic Brazing

I. Objectives

A. Applications

The introduction of ceramic components into the hot section of advanced turbomachinery requires that joining processes be developed for the assembly of the metal and ceramic components. Early approaches used mechanical fastening techniques to secure the ceramic to the metal. In the absence of an integrated interface, thermal expansion mismatch stresses can be relieved by the different materials simply sliding past one another. However, the mechanical fastening technique was also accompanied by higher machining costs needed to form the ceramic (and metallic parts), the added weight of fastener assemblies, and the concern for fasteners "coming loose", resulting in mechanical failure of the assembly.

An alternative approach to mechanical fastening techniques is filler metal joining, that is, *brazing*. Realization of a suitable braze joint has two requirements: (1) that the molten braze alloy wet the faying surfaces of the parts that are to be joined together and (2) that the joint maintain suitable mechanical properties (strength, creep resistance, etc.) and physical properties (corrosion resistance, oxidation resistance, etc.) while the product is in service.

The objective of the present study was the development of a braze joint to attach silicon nitride stator vanes to a low expansion, Ni-based, super alloy mounting ring. This assembly is targeted for a portion of the compressor section of an advanced gas turbine engine. The product designations that were targeted for this application included the F22, 131 and 331 small auxiliary power unit (APU) engines and the -500 APU for larger aircraft systems. The operating environments characteristic of APU applications, and the stator-ring braze joint area in particular are generally low load regimes (torque, axial and bending) with respect to the yield strength of the metal ring. Mechanical and thermal fatigue are severe (albeit, the loads are nominal) owing to the elevated operating temperatures of the joint. The operating temperatures of the stator/ring assembly are high due to its proximity to the combustion ("hot") section of the engine and compressive heating of the air flow; those temperatures are in the range of 900-1000°C (1652°F - 1832°F), which clearly exceed the upper limits of traditional brazing technology.

B. Technology Background

The objective of this study was the development of a "high temperature" braze joint between a metal and silicon nitride. The term, "high temperature," is used to describe the service temperature regime of 926°C (1699°F) that was anticipated for this brazement. In order to accommodate this service temperature, the solidus and liquidus temperatures of the filler metal must be similarly high, allowing for a temperature margin between the maximum operating temperature and the nominal solidus temperature of the braze alloy. Moreover, the process temperatures should exceed the liquidus temperature of the filler metal by 20-40°C (36 - 72°F) to assure complete melting of the braze alloy with sufficient fluidity to fill gaps and holes.

Process temperatures in the range of 1200 to 1300°C (2192 to 2372°F) pose a number of *materials compatibility* issues in metal/silicon nitride joints (aside from the traditional residual stress concerns that encompass metal/ceramic joining). Those issues include (1) molten braze alloy/base metal interactions, (2) molten braze alloy/silicon nitride interactions, and (3) interactions between the braze joint materials and the atmosphere.

Interaction between the molten braze alloy and the base metal include dissolution or erosion of the base metal by the molten braze alloy and the diffusion of filler metal constituents into the base metal.[1] The extent of erosion is a function of the compositions of the base metal and braze alloy, as well as a function of the process temperature and the time-of-contact between

the molten filler metal and the base metal. The higher the working temperature and/or the longer the duration of contact between the molten braze alloy and the base metal, the greater will be the extent of erosion. Erosion, as well as the diffusion of filler metal into the base metal, impact the joint integrity, not only by chemistry changes to the braze alloy and the base metal, but also by widening the joint gap. Insufficient braze alloy to compensate for the additional space results in void formation.

Although regarded as extremely stable to adverse environments (corrosives, elevated temperatures, etc.), ceramics can also be degraded. Reactions between the silicon nitride and molten braze alloys have been observed. Santella noted significant joint cracking when brazing silicon nitride with Au-Pd and Au-Ni-Pd filler metals with Pd contents in excess of 25 wt.%.[2] The cracking was caused by the formation of silicides such as Pd_2Si as the filler metal reacted with the silicon nitride, causing the latter to dissociate into Si(s) and N_2(g). Joint strength was further degraded by the presence of excessive voiding caused by the release of N_2 gas in the dissociation reaction.[3]

Lastly, interactions between the braze alloy or base materials and the atmosphere at elevated temperatures can degrade the ceramic and metal components. Silicon nitride will dissociate in low partial pressure N_2 environments (e.g., vacuum) at temperatures in excess of 1000°C.[4] The dissociation products include the formation of elemental Si and the evolution of N_2 gas. The gas release can produce voids within the joints.

C. Design Constraints

The design constraints for the 331-200 nozzle attachment and support system braze joint were determined from the product specifications are listed in Table 1. In all cases, the maximum values of the design criteria were targets for the present work. *The primary guideline that was used to begin a screening process for metal section and brazing filler metal, was an operating temperature of 926°C (1699°F).*

Table 1. Design constraints of metal/ceramic braze joints.

Operating Temperatures:.....		704°C (1299°F) min, **926°C (1699°F)** max.
•Load Capabilities:	Torque:	0.14 kg-m (12 lb-in) min., 4.03 kg-m (350 lb-in) max. (1 cm (0.4 in) moment arm)
	Bending:	222 N (50 lb_f) min., 2726 N (614 lb_f) max.
	Axial:	222 N (50 lb_f) min., 444 N (100 lb_f) max.
•Fatigue Life:		20,000 cycles (R=0) combined loads
•Creep Rupture:		20,000 hours (load unknown)

The joint geometry is shown schematically in Fig. 1. The joint was a cylindrical sleeve with a silicon nitride stator post. Several geometries were identified for this joint, depending

upon the engine size that was targeted. In the present evaluation, the post had a nominal diameter of 0.76 cm (0.300 in) and the metal sleeve had an outer diameter of 1.03 cm (0.406 in). The sleeve height was 1.27 cm (0.500 in) and extended above a 0.508 cm (0.200 in) high base. The overlap within the sleeve was not designated explicitly, although best practices typically call out an overlap of at least three diameters. The preferred gap for a braze joint of this application was established as nominally 0.508 cm (0.200 in) In the event that an interlayer were required, the inner diameter of the metal sleeve would be reduced until reaching a safe design value; then, the outer diameter would be increased to maintain a similar wall thickness. These dimensions present an approximate notion as to the size of the metal/ceramic braze joint.

The sleeve joint configuration described above was assessed with respect to the anticipated dimensional changes arising from thermal expansion mismatch between the silicon nitride post and the metal sleeve. Upon heating the greater thermal expansion coefficient of the metal sleeve would cause it to expand to a greater degree than the silicon nitride post producing a situation in which there be insufficient braze alloy present in the joint to fill it during the cycle peak. During cooling after the brazing temperature/time sequence had been completed, the filler metal would solidify at its solidus state. This temperature would constitute the zero stress state. Further temperature decreases to room temperature would cause the build-up of residual stresses arising from the thermal expansion mismatch between the silicon nitride and the metal sleeve. Having the lower thermal expansion coefficient and being the confined (inner) member, the silicon nitride would be put into compression during the cooling cycle. The metal sleeve, as the outer member and having the larger thermal expansion coefficient, would be placed under a tensile residual stress. It is preferred that the ceramic be under a state of compression because of its tendency to fail catastrophically under tensile stresses.

II. Materials Selection

A. Base Metal

At the inception of this project, AlliedSignal had targeted Inconel™ 4005-3,[i] an experimental, low expansion alloy made by Inco Alloys, International, to be the stator ring material. This material has suitable oxidation resistance, high temperature strength and microstructural stability as well as density, and thermal expansion coefficient properties that were better than those of the traditional high temperature, low thermal expansion coefficient alloys such as Inconel™ 903, 907, 909, and 718.

Further evaluation of the 4005-3 alloy raised some concerns as to its applicability for the proposed service conditions. First of all, there was a concern that the Cr levels, and to a lesser extent, the Al levels (3.0 and 5.4 wt.%, respectively) in 4005-3 were insufficient to support the dynamic oxidation resistance required for the proposed operating temperatures. Secondly, the 4005-3 alloy is a *precipitation hardened alloy*; that is, it derives its strength from the morphology of precipitates that result from a precisely controlled thermal treatment. Inadequate thermal treatment or excessive thermal exposure ("overaging") will degrade the mechanical properties of the alloy. Overaging is the primary concern for the use of 4005-3 at operating temperatures of 900-950°C (1652 - 1742°F) that were targeted for this application.

Therefore a survey was conducted to identify commercially available, low thermal expansion, high service temperature alloys that would have better oxidation properties, good high temperature microstructural stability, retained strength and corrosion properties

[i] Nominal wt.% composition, 33Ni-31Co-27Fe-5.3Al-3Nb-0.5Ti + minor additions.

commensurate with the proposed service applications. Hastelloy™-S (trademark of INCO Alloys, International) was selected. The nominal composition of the Ni-based Hastelloy™-S alloy was: 61Ni-16Cr-15Mo-3Fe-2Co-1W-0.5Si-0.3Mn-0.3Al, plus trace elements. As a solution-annealed alloy, optimum mechanical properties are retained in high temperature service (thermal stability); dimensional stability is also realized because precipitation reactions will not take place. The alloy also offered low coefficient of thermal expansion (mean CTE, 20-1063°C, 16.0 ppm/°K) and excellent oxidation resistance up to 1093°C (1999°F), due to the Al and high Cr contents.[5] A drawback of the Hastelloy™-S alloy is that it has a density of 8.75 g/cc (0.32 lb/cu. in.) whereas the 4005-3 alloy has a density of 7.79 g/cc (0.28 lb/cu.in.), producing a weight penalty in rotating applications.

Stock Hastelloy™-S is provided in the solution treated condition. Fig. 2 is a differential interference contrast, optical micrograph of the as-received microstructure from bar stock. An ASTM grain size (ASTM E112) of 5-6 was measured. The microstructure is characterized by string inclusions that delineate the forming direction of the bar stock. The hardness of the alloy on the HRB scale (100 g, 1/16 in. ball, 5 readings) was 90.6±0.3. On the Vickers scale, 300 g load, 15 s dwell time, and five measurements, the hardness was 645.2±5.8 kg/mm^2.

B. Silicon Nitride

The silicon nitride used in this project was AlliedSignal's AS-800. This ceramic has a maximum working temperature of 1400°C. Flexure strengths at room temperature and at 1093°C were 717 MPa (104 ksi) and 607 MPa (88 ksi), respectively. The mean coefficient of thermal expansion between 20 and 1000°C (68-1832°F) is 3.9 ppm/°C (2.2 ppm/°F). This value is to be compared with that of the Hastelloy™-S with a mean value of 16.0 ppm/°C (8.9 ppm/°F) illustrating the thermal expansion mismatch between the two.

As silicon nitride is not generally wet by molten (non-activated) braze alloys, it was necessary to promote wetting. One such approach was the deposition of a wettable metallic film on the surface of the silicon nitride. Titanium (Ti) has been shown to have excellent adhesion to silicon nitride as well as providing a wettable surface for braze alloys. Ti is stable at the anticipated high process temperatures (1100-1300°C).

Two coating techniques were examined: (1) sputter deposition at 260°C (403°F) and (2) electron beam evaporation (vacuum) without direct substrate heating. Evaporation techniques have been preferred by other investigators because sputtering tends to entrap carrier gas (typically Ar) in the layer.[6] Sputter depositions were performed on as-ground or polished silicon nitride surfaces. The evaporation technique was also used on both as-ground and polished surface finishes. Polishing was performed with 3 μm diamond paste. The polished and as-ground samples were scrubbed with detergent, rinsed in acetone, rinsed in alcohol, and then dried prior to introduction into the equipment. A 2.0 μm (79 μin) thick Ti film was deposited in all cases.

The Sebastian™ pull test was performed on films deposited under one of the three deposition/surface finish variations (i.e., sputter/polished, evaporated/polished, and evaporated/ground); a total of three (3) tests were performed per deposition/surface category. The adhesion strengths are presented in Table 2. The film deposited by sputtering on the polished surface had adhesion strengths that reached the maximum testable by the Sebastion™ system. All failures took place in the epoxy that bonded the test stub to the film. In the case of an evaporated film on the polished surface, one test stub fell off; a second test showed a relatively low strength of 19.8 MPa (2880 psi), with failure at the Ti film/silicon nitride interface. A third test reached a high pull strength of 75.1 MPa (10,900 psi); however, the failure was at the Ti film/silicon nitride interface. It was clear that adhesion was weaker for the evaporated film on

the polished surface, as the failure mode was consistently at the Ti coating/silicon nitride interface. Because good adhesion was demonstrated between the *sputtered*, 2.0 μm thick Ti film and the AS-800 silicon nitride surface the sputtering technique was selected for Ti film depositions for the remainder of this project.

Table 2. Sebastian™ pull test data for 2.0 μm thick Ti film on AS-800 test blocks.

Surface Condition	Depos. Process	Sebastian Pull Test (MPa) Test #1	Test #2	Test #3
Polished	Sputtered	76.5 (FF)*	75.1 (EF)	92.3 (EF)
Polished	Evaporated	FDC**	20.0 (FF)	75.1 (FF)
Ground (as-rec.)	Evaporated	82.0 (EF)	82.7 (EF)	92.3 (EF)

* "FF," Film Failure for separation of the film from the substrate; "EF," Epoxy Failure for separation of the pin from the film; the film remained intact on the substrate.
** "FDC," Failed During Clamping is a film failure while setting up the test (very weak joint).

Finally, the Sebastion™ pull tests that were performed on the ground surface (tested with the evaporated film), exhibited strengths that exceeded those achievable by the apparatus. In all cases, the failure took place within the epoxy. Recall that the test data of evaporated films on the polished surface showed poor adhesion, with failures at the film/silicon nitride interface. The high strengths and epoxy failure of the test series on as-ground specimens illustrated a mechanical locking of the epoxy deposited into the rough, as-ground silicon nitride surface. This interlocking mechanism could potentially occur with the braze alloys, thereby providing an additional bonding mechanism for the braze joint, along with the intrinsic adhesion of the sputtered Ti film on the silicon nitride. Thus brazing was performed on as-ground surfaces.

C. Interlayer Materials

The thermal expansion mismatch between the Hastelloy™-S (16.0 ppm/°C at 20-1063°C) and the AS-800 silicon nitride (3.9 ppm/°C at 20-1000°C) warranted an investigation into potential joint interlayers. The use of an interlayer material is based upon one of two principles. The first is to employ a material with a thermal expansion coefficient value between those of the metal and ceramic. When placed in the braze joint, the interlayer reduces the residual stress gradient at each interface by having a thermal expansion coefficient intermediate to those of the base materials. The second approach is to use a compliant material (low modulus and/or low yield strength) that will deform under the residual stress field, thus accommodating the residual stress in the joint. The interlayer material must also survive the high temperature and operating environment.

Two materials appeared to be promising interlayer materials. The first material was the low thermal expansion, commercial alloy, Kovar™.[i] The nominal composition of Kovar™ is 28.96Ni-17.37Co-0.24Mn-0.11Si-0.014C-0.002Al-0.07Cu-0.08Cr-bal.Fe (wt.%).[7] The modified variation designated F1466 (ASTM Vol. 10.04) with lower Si and Cr contents was used. The lower Si and Cr additions assist braze alloy wetting, yet still provide adequate oxidation protection. The alloy melting temperature is 1450°C (2642°F).

[i] Trademark of Carpenter Technologies.

The thermal expansion coefficient, yield strength, tensile strength, elongation, and elastic modulus data are provided in Table 3. The yield strength and ductility of Kovar™ are comparable to those for the Hastelloy™-S base metal; however, the tensile strength and elastic modulus of Kovar™ are considerably lower. Therefore, residual stress relief will be provided by both the intermediate thermal expansion coefficient of Kovar™, as well as by recoverable and non-recoverable deformation resulting from the lower elastic modulus and reduced yield strength, respectively.

Table 3. Literature data of thermal expansion and mechanical properties of Hastelloy™-S, Kovar™, AS-800 silicon nitride, and Kentanium™ K162B materials.

Material	Melting Temp. (°C)	TCE* (ppm/°C)	YS** (MPa)	UTS*** (MPa)	Elong. (%)	Elastic Modulus (GPa)
Hastelloy™-S	1335-1380	16.0 (20-1093°C)	383	849	55	212
AS-800		3.9 (20-1000°C)		601 (at 20°C)		310
Kovar™	1450	13.1 (20-1100°C)	345	517	30	138
Kentanium™		8.3 (20-648°C)		772	21	406

*TCE=thermal coefficient of expansion, **YS=yield strength, ***UTS=ultimate tensile strength

The second interlayer material was a cemented composite with the trade name Kentanium™ Grade K162B.[ii] An optical micrograph of the material is shown in Fig. 3. This material is comprised of titanium carbide (TiC) particles in a matrix phase of a Ni-Mo alloy. The particles have a central core (black) and an outer shell (dark gray). Energy dispersive x-ray analysis determined the central core to be TiC and the outer shell to be the result of an alloying reaction between the TiC particle and the Ni in the matrix phase, forming a Ti-Ni-C composition. The available mechanical properties of the K162B are listed in Table 3. A comparison of the K162B properties and those of the Hastelloy™-S and AS-800 silicon nitride show that the K162B has greater stiffness than either of the base materials and limited ductility. Therefore, its benefit in reducing residual stresses is *not* provided by deformation. Its benefit as an interlayer material is based on having a thermal coefficient of expansion that is intermediate between that of the metal and silicon nitride materials.

In order for the K162B to be considered for this application, it required suitable oxidation resistance. In the absence of literature data, its oxidation resistance was inferred by examining the oxidation resistance of monolithic TiC and that of a similar TiC composite (TN-20) that is sintered with a Ni-Mo material.[8,9] Fig. 4 is a plot of the parabolic oxidation rate constant, k^2, as a function of the reciprocal temperature (°K) for the monolithic TiC and the TN-20 composite. The two materials have similar oxidation rates. As a further illustration, the oxidation rate of monolithic TiC is plotted against that of Kovar™ in Fig. 5.[10] It is evident that the oxidation of TiC is comparable to that of the Kovar™ alloy. Therefore, it was concluded that the K162B

[ii] Kennemetal, Inc.

composite had acceptable oxidation properties, as well as suitable mechanical properties, to be a candidate interlayer material for this application.

In summary, the materials, Kovar™ F1466 and Kentanium™ K162B were selected as interlayer materials for the high temperature braze joints between Hastelloy™-S and AS-800 silicon nitride. The mechanism for relieving the residual stress build-up caused by the thermal expansion mismatch was based upon deformation in the case of Kovar™ and an intermediate thermal coefficient of expansion in the case of the K162B.

D. Filler Metals

Candidate filler metals were identified initially based on the operating temperature criterion of 926°C (1699°F). A minimum temperature cushion of 50 to 75°C (122 to 167°F) between the solidus temperature and the 926°C (1699°F) value was considered adequate under the anticipated loading conditions. A subsequent criterion was that the brazing alloy have excellent oxidation resistance. Three commercial alloys were identified: 92Au-8Pd ("Paloro"), 65Pd-35Co ("Palco"), and 60Pd-40Ni ("Palni").[iv] Compositions, including tramp elements, were certified by factory documentation. The nominal melting temperature ranges are listed in Table 4. The high precious metal contents (Au and Pd) and to a lesser extent, the Ni and Co contents, provided adequate oxidation resistance at elevated temperatures. The oxidation resistance of the filler metals was confirmed by weight gain measurements; the results of those tests are presented in the following section (*Materials Properties*). In terms of cost, the Palni and Palco alloys were favored as lower cost alternatives to the Au-based Paloro filler metal.

Table 4. Brazing filler metal compositions, melting temperature ranges, and specified designations.

Alloy (wt.%)	Melting Temperature (°C)	Designation
92Au-8Pd	1200 - 1240	Au-Pd or "Paloro"
65Pd-35Co	1230 - 1235	Pd-Co or "Palco"
60Pd-40Ni	1238	Pd-Ni or "Palni"

The braze alloys were used in foil form of nominal stock thickness of 0.003 in (0.051 mm). The proper shapes were simply cut from the foil.

Very good wetting properties were anticipated for these alloys on the Hastelloy™-S and Kovar™ interlayer materials. The primary constituents of the braze alloys, Au and Pd, form solid solutions with the Ni and Fe that are main constituents of the substrate and interlayer materials, respectively. Therefore, significant reaction between the filler metals and the metal members (Hastelloy™-S and Kovar™) was expected as the basis for the wetting process. The formation of brittle intermetallic particles as part of the interface reaction was not expected. A similar assessment was made of the interaction between each of the three filler metals and the

[iv] WESGO, Belmont, CA.

Kentanium™ composite interlayer material (largely through interactions with the matrix Ni-Mo material).

The metals comprising the braze alloys were not conducive to wetting of the silicon nitride because they are not "active" elements. Therefore, a Ti metal coating was used on the silicon nitride to promote wetting by the molten filler metals. Dissolution of Ti into the molten braze alloy did not degrade the properties of the braze alloys.

An attempt was made to make the filler metals active by the direct addition of Ti to them. Because the melting/casting facilities were not available with which to fabricate the binary alloys plus Ti, the Ti was added by sputtering a Ti coating onto the surfaces of the braze alloy sheet stock. The thicknesses of the sputtered Ti coatings were determined so that the filler metals had nominal Ti "additions" of 2 wt.%. Two procedures were used: In the first approach, the Ti was deposited on a single side of the foil strip. Then, two sheets were added to the joint with the Ti layers sandwiched together so that the Ti reacted with the silicon nitride only after the braze alloy had melted. Segregation of the Ti towards the silicon nitride interface would duplicate the mechanism of braze alloy wetting observed for lower melting temperature active filler metals. The Ti coating thicknesses for the Palni were 3.55 μm (140 μin), for the Palco 3.74 μm (147 μin), and for the Paloro alloys were 6.0 μm (236 μin).

The second approach was to coat both foil surfaces with Ti, each surface receiving one-half of the nominal thicknesses listed above. This technique was used initially with only the Palni and Palco alloys. The Ti layers were covered with a 1.0 μm layer of Pd to prevent the Ti coating from prematurely reacting with the silicon nitride prior to melting of the braze alloy. For both approaches, the Ti layers exhibited excellent adhesion to the braze foils.

III. Braze Joint - Assembly Processes

A. Process Parameters

The initial task in the development of a brazing process was to confirm the melting temperatures of the braze alloys. The melting temperature ranges for the three candidate braze alloys were:

92Au-8Pd	1200 - 1240°C (2192 - 2264°F)
65Pd-35Co	1230 - 1245°C (2246 - 2273°F)
60Pd-40Ni	1238°C (2260°F)

as per the nominal manufacturers data sheets. The studies began with the metal substrates, Hastelloy™-S and Kovar™ due to early availability. The work was then extended to the Kentanium™ interlayer material and the AS-800 silicon nitride.

Initial wetting experiments were performed on Kovar™ and Hastelloy™-S metal alloy blanks measuring 2.54 x 2.54 x 0.476 cm (1.0 x 1.0 x 0.1875 in), the broad surfaces of which had been polished to √32 finishes. Each of the braze alloys was available as 0.076 mm (0.003 in) thick foil. In order to better evaluate the wetting process, the foils of braze alloy were converted into braze "balls" by melting foil segments on an alumina substrate. Because the braze alloys were non-active, they did not wet the alumina surface. Foils segments measuring 0.74 x 0.74 x 0.0076 cm (0.29 x 0.29 x 0.003 in) were cut from the stock material. This size specimen was calculated to produce a ball with a diameter of 0.2 cm (0.079 in). The braze alloy foils were melted under the following furnace cycle (750 mtorr Ar):

(1) 25°C - 1270°C, 10°C/min (77°F - 2318°F, 18°F/min)
(2) 1270°C (2318°F), 10 min
(3) 1270 - 25°C, <10°C/min (2318 - 77°F, <18°F/min)

The 92Au-8Pd and 60Pd-40Ni readily formed the ball geometry; the 65Pd-35Co samples would not. The latter alloy spread slightly but not retract upon itself. None of the three alloys adhered to the alumina substrate. All wetting experiments were performed with the braze alloys in the ball form (or approximately so for the Pd-Co alloy).

The initial wetting experiments used the same furnace profile for all three alloys (Phase 1 profile):

(1) 25 - 1100°C, 10°C/min (77°F-2012°F, 18°F/min)
(2) 1100°C (2012°F), 5 min
(3) 1100 - 1280°C, 5°C/min (2012 - 2336°F, 9°F/min)
(4) **1280°C (2336°F), 7 min**
(5) 1280 - 1100°C, 5°C/min (2336-2012°F, 9°F/min)
(6) 1100 - 25°C, furnace cool (2012 -77°F)

Four braze balls were wetted on each of one Kovar™ and one Hastelloy™-S substrates.

Visual observations made of the samples are summarized in Table 5. Both the 60Pd-40Ni and 65Pd-35Co alloys exhibited spreading on the Hastelloy™-S base metal, but were accompanied by moderate erosion of the surface. The 92Au-8Pd also wet the Hastelloy™-S surface, but with considerably more erosion than was noted with the Pd-based alloys. Likewise, the Au-Pd alloy caused significant erosion of the Kovar™ substrate. The Pd-Ni and Pd-Co alloys caused limited erosion of the Kovar™ surface, forming the traditional sessile drops or "hemispherical caps." The wetted areas were cross sectioned and examined by optical microscopy. The severity of the surface erosion was clearly demonstrated by these analyses. Fig. 6 is a cross sectional view of the sessile drop region of the 92Au-8Pd alloy on Kovar™. The thinning of the sample in Fig. 6 is illustrative of the extent of erosion by the Au-Pd alloy on Hastelloy™-S. The more limited erosion by the 60Pd-40Ni and 65Pd-35Co alloys on Kovar™ is represented by that of the Pd-Ni alloy in Fig. 7. There is a very small amount of base metal erosion underneath the hemispherical cap of braze.

Table 5. Visual observations of Phase I wetting experiments.

Braze Alloy	Hastelloy™-S	Kovar™
60Pd-40Ni	complete spreading, moderate erosion ("divot")	spreading into hemispherical caps
92Au-8Pd	complete spreading, severe erosion	complete spreading, severe erosion.
65Pd-35Co	complete spreading, moderate erosion ("divot")	spreading into hemispherical caps

The initial wetting experiments indicated that a furnace cycle modification was necessary to limit the extent of base metal erosion. Distinct furnace schedules were developed for each of

the alloys; this difference was the maximum temperature used to melt the respective braze alloys. The furnace cycle (750 mtorr Ar) is summarized in a consolidated form below:

(1) 25°C - 1100°C, 10°C/min (77 - 2012°F, 18°F/min)
(2) 1100°C (2012°F), 5 min
(3) 1100°C - **T°C**, 5°C/min (2012-**T°F**, 9°F/min)
(4) **T°C (T°F), t min**
(5) **T°C** - 1100°C, 5°C/min (**T** - 2012°F, 9°F/min)
(6) 1100°C - 25°C (2012 - 77°F), furnace cool

where the (temperature, time), or **(T°C, t min)** combinations were:

60Pd-40Ni	1260°C (2300°F), 7 min
65Pd-35Co	1260°C (2300°F), 7 min
92Au-8Pd	1280°C (2336°F), 4 min

The same wetting experiment was repeated with these cycles and designated as Phase II. Observations of the specimens are provided in Table 6. There was a slight improvement towards minimizing the extent of erosion of the base metals by the filler metals; however, the magnitude of erosion was still excessive. In the case of the 65Pd-35Co alloy, the peak temperature was too low to allow wetting of the substrates, although the filler metal did appear to have melted.

Table 6. Visual observations of Phase II wetting experiments.

Braze Alloy	Hastelloy™-S	Kovar™
60Pd-40Ni	complete spreading, minor erosion	spreading into hemispherical caps
92Au-8Pd	complete spreading, moderate to severe erosion	complete spreading, minor erosion.
65Pd-35Co	some brazing, no wetting	some brazing, no wetting

Another change was made to the furnace schedules to reduce the erosion of the base metals. The schedule revision was referred to as Phase III:

(1) 25 - 1100°C, 10°C/min (77°F-2012°F, 18°F/min)
(2) 1100°C (2012°F), 5 min
(3) 1100 - **T°C**, 5°C/min (2012 - **T°F**, 9°F/min)
(4) **T°C (T°F), t min**
(5) **T** - 1100°C, 5°C/min (**T°F**-2012°F, 9°F/min)
(6) 1100 - 25°C (2012 - 77°F), furnace cool

where the (temperature, time), or **(T°C, t min)** combinations were:

60Pd-40Ni	1260°C (2300°F), 4 min
65Pd-35Co	1270°C (2318°F), 7 min
92Au-8Pd	1260°C (2300°F), 7 min

The peak temperature of the 65Pd-35Co alloy was raised from 1260°C (2300°F) to 1270°C (2318°F) to increase wetting. Visually, the use of the Phase III conditions appeared to reduce the extent of erosion; however, when metallographic cross sections were performed, the extent of erosion had only slightly diminished.

Because the peak temperatures were nearing the minimum margin above the alloys' liquidus temperature, any further lowering of the peak temperature would likely prevent melting and spreading of the braze alloys. The time periods were not altered because they were considered to be a "fine tuning" to the process for potential geometries. Therefore, the above furnace schedules were used for subsequent evaluations, bearing in mind that further changes might be warranted for specific part geometries.

A second approach towards limiting the dissolution of the Hastelloy™-S alloy was by the braze alloys was examined. An electroplated Ni layer of nominal thickness of 5.5 μm (220 μin.) was deposited on the Hastelloy™-S surface as a reaction barrier. Although the Phase III peak process time and temperature were also used here, the test sequence was given a new designation as Phase IV.

Wetting tests indicated that the Ni had diffused into the substrate material. The Ni diffusion zone was delineated by a much smaller grain size compared with the remainder of the substrate. The optical micrograph in Fig. 8 is of the sample that was exposed to the 65Pd-35Co thermal cycle (1270°C, 7 min, 750 mtorr Ar) and was located far from the braze alloy sessile drop. The Ni layer did not appear to significantly limit the extent of base metal dissolution by the molten braze alloy. Therefore, the use of a Ni barrier layer was not a viable option towards reducing base metal erosion. Adjusting the processing parameters appeared to be the only viable recourse.

As the silicon nitride is not wet by the metallic filler metals, a 2.0 μm (79 μin) Ti metal coating was sputtered onto it. Initial wetting experiments were performed with the Phase III brazing conditions. The wetting was quite poor with the braze alloy in many cases having formed a ball. Fig. 9 is an optical micrograph of the cross section of the sessile drop of the 60Pd-40Ni alloy on the AS-800 silicon nitride. Aside from there being no noticeable Ti layer remaining on the silicon nitride surface, it appears that the braze alloy had dissolved a portion of the silicon nitride (much like the filler metals eroded the substrate metals). A higher magnification of the interface is shown in Fig. 9(b). Obvious in the higher magnification photograph are two features: (1) the formation of voids at the braze alloy/silicon nitride interface and (2) cracks in the braze alloy. Silicon nitride erosion, voids, and cracks in the filler metal were also observed with use of the 65Pd-35Co alloy.

At first, it was believed that the furnace atmosphere (750 mtorr Ar) may have been contaminated, thereby contaminating the specimen surfaces. The furnace system was checked for leaks or backwash from the pumping systems using residual gas analysis (RGA). At cold (25°C) and hot (1290°C) conditions; the impurity levels were:

H_2:	3.8×10^{-8} atm	
He:	0 atm	
C	3.3×10^{-9}	
H_2O:	2.3×10^{-8}	
N_2:	1.7×10^{-7}	
O_2:	0	
Ar:	4.0×10^{-10}	
H.C.	1.1×10^{-8}	(hydrocarbons)

These conditions are "clean" by both industrial as well as research-and-development standards. Therefore furnace contamination was ruled out.

A review of the literature for brazing processes using similar filler metals at these temperatures revealed the potential for decomposition of the silicon nitride by contact with metallic elements.[11-13] At elevated temperatures and small partial pressures of N_2, the silicon nitride decomposes in the presence of a metal (particularly Ti and Pd) to form brittle Ti-silicides and Pd-silicides, along with the evolution of N_2 gas. Therefore, silicon nitride decomposition appeared to be the source of the braze joint morphology observed in Fig. 9.

Further observations of cross sections of the wetting samples of the 60Pd-40Ni and 65Pd-35Co on the Ti (2.0 μm) coated AS-800 indicated that the loss of the Ti layer was responsible for the overall poor wettability of those braze alloys. It was hypothesized that the Ti layer was dissolved by the molten braze alloy, thus allowing the latter to contact the underlying silicon nitride. The loss of Ti through sublimation of the film under the processing temperatures was discounted due to the presence of the 750 mtorr Ar atmosphere. At 1250°C (2282°F), the vapor pressure of Ti is approximately 10^{-6} atm.

To produce a ceramic/ceramic joint, the following problems needed to be addressed:

- Maintain a sufficiently thick Ti layer to which the braze alloy could wet.
- Limit the reaction between the braze alloys and silicon nitride by :
  - (a) changing the brazing process
  - (b) reduce the amount of Pd in the braze alloy
  - (c) increase the amount of Ti at the interface.

The process parameters were changed to reduce the time spent by the molten braze alloy at peak temperatures. Therefore, *the Phase V* process parameters were developed with the same peak temperatures and hold times as were developed in the Phase III (and IV) cycle. Faster ramp rates were used as described below:

(1) 25 - 1200°C, 25°C/min (77 - 2192°F, 45°F/min)
(2) 1200°C (2192°F), 4 min
(3) 1200 - **T°C**, 10°C/min (2192°F - **T°F**, 18°F/min)
(4) **T°C (T°F), t min**
(5) **T** - 925°C, 25°C/min (**T°F**-1697°F, 45°F/min)
(6) 925 - 500°C, 10°C/min (1697 - 932°F, 18°F/min)
(7) 500 - 25°C (932-77°F), Furnace cool

where the (temperature, time), or **(T°C, t min)** combinations were:

60Pd-40Ni	1260°C (2300°F), 4 min
65Pd-35Co	1270°C (2318°F), 7 min
92Au-8Pd	1260°C (2300°F), 7 min

Initial tests were performed with the 750 mtorr Ar atmosphere. However, in the course of trying to identify the source of the poor wettability of the Ti-coated silicon nitride, it was decided to proceed with experiments conducted in vacuum (nominal 10^{-5} to 10^{-6} atm).

First, it was necessary to determine the impact of the revised furnace cycle on the wetting of the Hastelloy™-S metal substrate. Shown in Fig. 10 are SEM (SE) micrographs of the braze joints showing the braze alloy/Hastelloy™-S base metal interfaces for each of (a) 65Pd-35Co, low magnification; (b) 65Pd-35Co, high magnification, (c) 92Au-8Pd, low magnification; (d)

92Au-8Pd, high magnification; and (e) 60Pd-40Ni filler metal at low magnification, only. The interface between the 65Pd-35Co alloy and the Hastelloy™-S material shows a structurally distinct zone 7-10 μm (276-394 μin) thick at the interface proper; however, Energy Dispersive X-ray Analysis (EDXA) did not reveal a compositional difference from that of the bulk Hastelloy™-S alloy. EDXA spectra were also taken at a distance of 25 μm from the interface and at a second point in the center of the joint. Moving from the interface towards the center of the joint showed a decreasing concentration of Ni and Cr that had apparently been dissolved from the base metal and an increase in Co and Pd. The boundary between the 92Au-8Pd braze alloy and the Hastelloy™-S alloy was distinct, but showed not distinguishable features, even at the higher magnification. EDXA were not taken of these specific samples; however, later work would reveal considerable Au diffusion into the Hastelloy™-S material. Gold (Au) was observed to have infiltrated the base metal along the grain boundaries as well as by means of intragranular, volume diffusion. Lastly, in the case of the 60Pd-40Ni alloy, there was no distinguishable boundary between the braze alloy and the substrate members. These evaluations determined that the braze alloys exhibited adequate wettability of the Hastelloy™-S material under the potential furnace schedule.

Adequate wetting of the Kovar™ substrates using the Phase V cycle was also demonstrated; an in-depth analysis of the interface regions of these couples was deferred.

Returning to consideration of the wetting of silicon nitride substrate, a second processing change that was made was to alter the amount of Pd in the braze alloy. Therefore, studies were concentrated on the 92Au-8Pd braze alloy, despite a cost disadvantage in commercialization of this material. Nevertheless, work continued to a limited extent with the 60Pd-40Ni alloy as a lower cost alternative to the precious metal based alloy.

To test each of these modifications, a piece of Ti sheet was placed next to the specimen(s). The Ti monitor was checked for discoloration and ductility after the furnace run, as an indicator of the condition of the furnace atmosphere. The following observation was made: The Ti monitors became severely embrittled when exposed to the Phase III cycle under 750 mtorr Ar. Clearly, a source of contamination was present. The embrittlement was less severe when the Ti monitors were exposed to the Phase V cycle and the Ti monitors exhibited no embrittlement when processed in vacuum conditions. *Conclusion: The faster cycle (Phase V) provided an additional advantage to the brazing process* . These results also showed that *the inert atmosphere could potentially degrade substrate wettability.*

An increase in the amount of Ti deposited on the silicon nitride surface was examined as a means of improving wettability. The previously used 2.0 μm (79 μin) was increased to 4.0 μm (157 μin) and 6.0 μm (236 μin). Examination of the films after sputter deposition indicated adequate adhesion of them on the silicon nitride substrate (as-ground condition). Because the thicker films would also serve as a *barrier layer* between the molten braze alloy and the silicon nitride, the films had to remain in place throughout the brazing process. In the absence of a braze alloy/silicon nitride reaction, adhesion of the Ti layer need only be adequate to retain the coating in place until melting had occurred. Dissolution of the broken-apart film would result in the Ti returning to the interface, much as was the case with Ti-activated brazing filler metals, and redepositing there to serve as the adhesion layer. (In fact, the suitability of this latter concept was tested; the results are presented later). Silicon nitride samples deposited with 2.0, 4.0, and 6.0 μm of Ti exhibited wetting by all three filler metals when processed by Phase III or Phase V cycles *under vacuum conditions.* Wetting improved in the order of increasing Ti layer thickness, and was slightly better with the Phase V cycle as opposed to the Phase III cycle. Wettability, in general, and its improvement with Ti thickness, were most dramatic with the 92Au-8Pd alloy as compared to the two Pd-based alloys. The 60Pd-40Ni alloy was better than the 65Pd-35Co, likely a result of the lower process peak temperature of the former material. The fact that the braze alloys wet the silicon nitride surface with 2.0 μm of Ti, a condition that did not wet in the

past under 750 mtorr Ar conditions, accentuated the detrimental effects of the inert atmosphere. *Using the lower Pd-containing 92Au-8Pd alloy and thicker Ti layers* indicated the potential for a successful, high temperature brazing process with the AS-800 silicon nitride.

An evaluation of the need for the Ti layer to remain adherent to the silicon nitride to serve as a barrier layer was exemplified in the following experiments. The filler metals were modified into "active braze alloys" by the introduction of Ti directly onto the braze alloys. Because melting facilities for small lots of brazing alloys with Ti additions were not readily available, the Ti was added by sputter depositing Ti coatings directly on the braze alloy foil (pseudo-cladding arrangement, details are found in section II.D). The Ti coating thickness provided a nominal Ti concentration of 2 wt.%. Upon melting of the filler metals, the Ti would dissolve into braze alloy and then precipitate on the silicon nitride as part of the brazing process to serve as the adhesion layer between the filler metal and the silicon nitride. Adding Ti directly to the brazing filler metals met with only limited success (Phase III, Ar atmosphere). The samples showed improved wetting; however, voids at the braze alloy/silicon nitride interface and familiar cracks in the braze alloy (perpendicular to the thickness vector) confirmed that the braze alloy had reacted with the ceramic. Although these experiments discounted the "novel" approach towards making Ti-activated braze alloys for this application, it did point out the need for the Ti layer to be deposited *on the silicon nitride* in order to fulfill its second function as a barrier layer between the braze alloy and the ceramic. *Therefore, Ti must be deposited on the silicon nitride (not merely be present in the braze joint) so as to serve as a barrier between the molten braze alloy and the ceramic.* The aforementioned success of the thicker Ti layer, the lower Pd Au-Pd alloy, and vacuum conditions preempted any further work on this approach of "active" braze alloys.

To this point, brazing process development was guided primarily by the wetting of the brazing alloys on the Hastelloy™-S, Kovar™, and AS-800 silicon nitride. The second interlayer material that was selected for this study was the cemented composite, Kentanium™ Grade K162B, comprised of TiC particles in a matrix of Ni-Mo alloy. At the point at which the study of Kentanium™ was begun, the decision had been made to target the 92Au-8Pd alloy as the preferred braze alloy from the performance aspects. Some ancillary wetting tests were performed with the Pd-Ni and Pd-Co filler metals; the results were quite similar to those documented for the Au-Pd braze alloy.

The ceramic content of the Kentanium suggested the need for a Ti layer to promote wetting of the braze alloys. In initial trials, a 2.0 μm Ti layer was deposited on the wetting samples; the specimens were processed according to the Phase III furnace cycle, using a 750 mtorr Ar atmosphere, using the Au-Pd braze alloy. Fig. 11 shows SEM micrographs of a cross section of the wetting sample at the braze/Kentanium™ interface. The lower magnification view in Fig. 11(a) shows an apparent diffusion zone from the surface. Fig. 11(b) shows no appreciable thickness of braze alloy, suggesting that the filler metal had diffused into the substrate structure, through the Ni-Mo matrix phase. This trend was confirmed by EDXA, which showed the interparticle matrix within the diffusion zone contained Au, Ni, Pd, and Ti; the Au and Pd signals were absent in the bulk Kentanium™.

Energy dispersive x-ray analyses (EDXA) determined the diffusion depths of the braze alloys for the respective Phase V cycles:

(1) 60Pd-40Ni,	< 3.2 mm (0.125 in);
(2) 65Pd-35Co,	0.84 mm (0.033 in); and
(3) 92Au-8Pd,	1.93 mm (0.076 in)

This behavior of the braze alloys on the composite material caused two concerns. The first addresses unpredictable mechanical properties of the interlayer materials due to the change

in composition. SEM and EDXA studies performed on Kentanium™ samples for all three braze alloys showed no discontinuities (cracks, voids, etc.) in the material that had braze alloy interdiffused into it. The second issue is the removal of braze alloy from the joint area as it infiltrates the interlayer. The physical loss of material raises the potential problem of insufficient braze alloy in the gap to effect a fully integral joint.

In summary, the development of a high-temperature brazing process for Hastelloy™-S and AS-800 silicon nitride (and taking account of the Kovar™ and Kentanium™ interlayer materials) began with the wettability study of the various substrate materials. The results of those tests indicate that use of the 92Au-8Pd filler metal and Phase V (vacuum, nominal 1260°C, 7 min) furnace cycle offered the most promising approach. Potential concerns about base metal dissolution and penetration of the composite interlayer would need to be more fully addressed during processing of actual joints.

B. Electron Microprobe Analyses (EMPA)

Electron microprobe analyses (EMPA) were performed at the braze alloy/substrate interface and near-interface regions to understand the physical metallurgy of the joint. Wetting samples of 92Au-8Pd on each of Hastelloy™-S and Kovar™ samples were evaluated; the analysis of the silicon nitride interface was performed on one side of a four-point bend bar joint. The Hastelloy™-S/Au-Pd and Kovar™/Au-Pd couples were fabricated by the Phase V process as it is written above; the silicon nitride sample (with 4.0 μm Ti) was processed under a modified Phase V process that was different from the nominal schedule only by reducing the peak temperature hold time from 7 min to *4 min.*

Shown in Fig. 12a is an SEM micrograph of the near-surface region of a Hastelloy™-S specimen, the surface of which had been wetted by the 92Au-8Pd braze alloy. Accompanying the SEM micrograph is an EMPA trace (b) that is representative of ten such traces made across the same region as depicted in (a). The grain boundaries have been infiltrated by the braze alloy as shown by the image contrast in (a) and confirmed by the EMPA trace in (b). The grain boundaries were enriched with Au and Pd derived from the braze alloy, and depleted in Ni, Mo, and Fe that were constituents of the Hastelloy™-S material. Interestingly enough, the Cr content of the base metal was not significantly altered at the impacted grain boundary areas. The dissolution of Ni into the Au-Pd braze alloy as it infiltrated the grain boundaries suggests the possible formation of a lower melting temperature phase based upon the Au-Ni binary phase diagram.

Compositional variations extended beyond the immediate infiltration region of the grain boundaries to the grain interiors. In the grain interiors that neighbored the infiltrated grain boundary, an enrichment of Ni and depletion of Mo was observed near that boundary. In addition bulk diffusion of Au had taken place in the intragrain volume. The increased Au content in the grain interior by 4-5 at.% was accompanied by an *increase* in the Mo concentration (2-3 at.%) and a decrease in the Ni and Cr contents of approximately equal amounts of 3-4 at.%. The entire reaction zone extended some 200 μm (0.008 in.) into the Hastelloy™-S material from the surface.

The SEM and representative EMPA trace (one of ten such traces) from the as-fabricated sample of 92Au-8Pd on Kovar™ are shown in Fig. 13(a) and Fig. 13(b), respectively. It is apparent from both the SEM micrograph and EMPA trace that the extent of diffusion by the braze alloy elements into the Kovar™ base metal was considerably reduced (approximately 80 μm, or 0.003 in) compared to the case of the Hastelloy™-S. Grain boundary infiltration by the Au-Pd filler metal was much less prevalent in the Kovar™ specimen; rather, bulk diffusion appeared to dominate the braze alloy migration. The Au and Pd elements exhibited a gradual

decrease in concentration from the specimen surface, into the bulk material. Complementing the decrease in Au and Pd contents was an increase in Fe, Co, and Ni to the nominal Kovar™ alloy composition values. Gold (Au) and Pd migration into the Kovar™ alloy appeared to have occurred to the same extent as evidenced by the composition of the braze alloy at the surface. The braze alloy that remained at the surface also contained a significant amount of Fe (approximately 7 at.%) caused by some dissolution of the base metal. Too little braze alloy was available on the Hastelloy™-S surface with which to make a similar analysis.

The same SEM/EMPA analysis was performed on the AS-800 silicon nitride bend barr specimen that had been coated with 4.0 μm of Ti. The processing condition for this particular sample was 1260°C and a reduced period of 4 min. An SEM micrograph of the analyzed region and representative EMPA trace are shown in Fig. 14 (a,b). The EMPA trace shows considerable overlap of the individual, elemental traces. While some of this overlap can be traced to the finite material volumes from which the x-ray signals emanated, a fraction of the overlap also represents explicit reactions between the various constituent elements. From a processing point-of-view, it is apparent that, to a large extent, a majority of the Ti layer remained at the silicon nitride surface and was not dissolved by the molten braze alloy.

A Ti-Pd-Si-(Au) composition was observed between the Ti layer and the bulk braze alloy. This interface structure appears to confirm previous studies and analyses of Ti-activated braze alloys that were wetted to silicon nitride.[14-16] A reaction takes place between Ti and the silicon nitride to form Ti_xN_y (x=y=1) and Si. N_2 gas escapes or forms TiN. The free Si reacts with the remaining Ti to form one or several titanium silicides ($TiSi_2$ or Ti_5Si_3). From the results shown in Fig. 14(b), the presence of free Pd from the braze alloy competes with Ti to form silicides, as well, probably, Pd_3Si.[17] The Si-containing layer may be a mixture of separate silicides (plus Au) or a single compound. Fig. 14(b) shows that Pd-Si compounds were also observed in the bulk braze alloy.

In an ancillary experiment, the process conditions were modified from those of Phase V by lowering the brazing temperature, yet maintaining the brazing time at 4 min. Fig. 15a and b are the SEM micrograph and representative EMPA trace for the silicon nitride wetting sample that was processed at 1235°C for 4 min. The principle observation to note was that the formation of Ti-silicide at the interface between the silicon nitride (Ti) and the braze alloy was not generally accompanied by the presence of Pd there. Rather, Pd formed Pd-silicides at a distance away from the immediate interface region, in the bulk braze alloy. An Au "barrier" was present at the interface. The stoichiometry derived from the elemental traces indicates that the Pd_2Si intermetallic is the predominant composition of those silicide particles.

Silicon nitride/Au-Pd wetting samples that were processed at 1215°C for 4 min were analyzed . The braze alloy melted fully and filled the joint gap. The full thickness of the Ti layer was retained. The Pd-Si compounds were less frequently observed in either the bulk braze alloy or at the silicon nitride/braze alloy interface reaction region. In those locations where they were observed, the Pd_2Si stoichiometry was measured. A second observation pertaining to the interface reaction layer was an absence of Ti-Si compound formation there (Fig. 16). The Si signal quickly diminished without a "shelf" as the analysis region moved away from the bulk silicon nitride, into the interface reaction zone. This is contrary to the Si signal observed in Fig. 14(b). These results are encouraging as they suggest that brazing parameter adjustments offer an additional processing window with which to minimize detrimental interfacial reactions between the filler metal and the silicon nitride.

IV. Braze Joint - Testing (As-Fabricated)

A. Four-Point Bend Test Evaluation

Wetting tests showed that the 92Au-8Pd alloy was the most promising braze alloy with respect to melting temperature, material interaction with the silicon nitride, and oxidation resistance. It was also determined that a minimum Ti coating thickness of 4.0 μm would be required on the silicon nitride to promote wetting and to serve as a barrier layer to prevent interaction between the silicon nitride and the Pd in the braze alloy. The nominal process parameters for the 92Au-8Pd alloy were those utilizing the Phase V profile with peak brazing conditions of *1260°C, 7 min.* and performed in vacuum conditions.

In the following section mechanical test protocols, data, and results are presented. Although the bulk of the analysis was performed on the preferred Au-Pd system, data pertinent to the Pd-Ni and Pd-Co braze alloys that was obtained early in the program are also included.

The load bearing capacity of the braze joint was determined by tensile strength measurements, using the four-point bend technique. The four-point bend specimen geometry follows ASTM C1161-90, specimen configuration B (Fig. 17). The process used to fabricate the test bars is shown in Fig. 18. Fabrication of the samples began by using material measuring 25.4 x 25.4 x 6.45 mm (1.000 x 1.000 x 0.252 in); these samples were referred to as the "parent block". The 25.4 x 6.45 mm edge-surface was used for the faying surface to which the joint was made. The metal surfaces were ground to √32 finish. The silicon nitride specimens were similarly constructed with all surfaces appropriately ground. The Kovar™ and Kentanium™ interlayer materials flats were ground to dimensions that matched the faying surfaces to be joined between the two parent blocks (i.e., 25.4 x 6.45 mm). The thicknesses of the interlayer materials that were evaluated in this study were 1.59 and 3.18 mm (0.0625 and 0.125 in).

The gap thickness of the braze joints between two substrate materials was controlled to a nominal value of 51 μm (0.002 in) by the placement of 51 μm diameter W wires within the gap along with the braze alloy foils. A slight pressure was applied to the substrates during the melting process, forcing them together to the prescribed separation distance. The 76 μm (0.003 in.) braze thickness provided a slight excess of material for the nominal gap thickness to assure that the joint would be completely filled with braze alloy.

The brazing joint assembly was fabricated from the substrate parent blocks, braze alloys, etc. in the following manner. The components were stacked vertically so that gravity, along with a supplemental mass of approximately 454-908 g (1-2 lb) forced them together. The stack was secured in a graphite fixture. Stop-off™ was added to prevent bonding between the specimen and the fixture surface. The fixture was designed to provide sufficient space between it and the sample to accommodate the thermal expansion mismatch between the two materials. The supplemental mass was then placed on top of the stack. The specimen-plus-fixture was placed into the vacuum furnace and subjected to the brazing schedule.

After brazing the specimens were removed from the fixture. The broad faces of the sample were ground to the 4.0 mm (0.157 in.) dimension shown in Fig. 17. Then, the sample was cut up into individual test bars. Seven were obtained per parent block assembly: five interior bars and two bars from the edge. Each bar was ground to the final dimension 3.0 mm (0.118 in.). Although recommended in ASTM Specification C1161-90, chamfers were not added to these test specimens.

Room temperature four-point bend strength testing was conducted in the fixture in Fig. 19. The load was applied at a constant displacement rate of 0.50 mm/min (0.02 in/min). The maximum load was used to calculate the tensile failure stress, S:

$$S = (3PL) / (4bd^2) \qquad (1)$$

where P is the maximum load; L is the outer support span (40 mm); b is the specimen width (4.0 mm); and d is the specimen thickness (3.0 mm).

The four-point bend test was also used to evaluate similar base material joints at elevated temperatures. These tests were performed by AlliedSignal Ceramic Components. The test temperatures were 600, 800, 900, and 950°C (1112, 1472, 1652, and 1742°F). The specimen was pre-loaded to a nominal stress of approximately 17 MPa (2.5 ksi); this load was termed the "alignment load." The temperature was increased to the test value and held for 20 min to assure temperature stabilization, after which, the sample was loaded to failure. The fracture surfaces of room temperature and elevated temperature specimens were examined to determine the failure mode.

Fig. 20 shows the mean (and ± one standard deviation) four-point bend strengths (room temperature) of the Hastelloy™-S / Hastelloy™-S couples in (a) and the Kovar™ / Kovar™ metal/metal joints in (b). The joints were fabricated with the 60Pd-40Ni, 65Pd-35Co, and 92Au-8Pd braze alloys under the respective Phase V conditions, in vacuum. The number in parentheses is the number of test bars evaluated. In all but two cases of the Kovar™ joints with the Pd-Ni alloy and one case of Hastelloy™-S with the Pd-Ni braze, the samples did not fracture but simply bent up to the maximum load. In those cited exceptions, failure occurred in the joints, and revealed an extensive degree of void formation. These results suggest that wetting by the Pd-Ni braze alloy was somewhat more limited than was the case with the other filler metals. The strengths of the Au-Pd joints were comparable to those of the Pd-Ni and Pd-Co joints in the case of the Kovar™ substrate material. However, the strengths of Au-Pd joints made to the Hastelloy™-S base metal were significantly lower than the Pd-based braze alloys. Because failure did not take place at the joints the lower strength was attributed to a lower strength in the Hastelloy™-S base metal.

For both the Kovar™ and Hastelloy™-S filler metals joints, the strength variability, as illustrated by the standard deviation, was clearly greater for the Au-based braze alloy than the Pd-Ni and Pd-Co alloys.

In addition to observations made of the fracture surfaces from the limited number of samples failed in the braze joint, metallographic cross sections were made of four-point bend bars that were assumed to represent the particular test series. The cross sections of the Kovar™ and Hastelloy™-S samples assembled with the Pd-Ni and Pd-Co braze alloys appeared similar to those of the wetting (sessile drop) samples. The filler metal and base metal sections of the joints were crack free. The four-point bend braze joints between the Au-Pd alloy and Kovar™ and the Au-Pd alloy and Hastelloy™-S showed the interdiffusion of Au (and Pd) into the base metals via grain boundaries as well as by bulk diffusion as was observed with the wetting specimens. Shown in Fig. 21 is a SEM micrograph of the cross section of an untested, four-pint bend sample. There is a large unfilled area in the joint. Similar voids were observed intermittently through the joint and clearly indicated an absence of braze alloy. X-ray dot maps of the specimen showed that the braze alloy elements had diffused along the Hastelloy™-S grain boundaries as well as into the bulk material, just as was illustrated by the SEM images and EMPA analysis of the wetting sample (Fig. 12). The morphology of the unfilled regions viewed from the fracture surface of a specimen that had separated in the joint is shown in Fig. 22 and exemplifies features that are consistent with base metal dissolution. The fracture mode analysis suggested that joint integrity could be jeopardized by the braze alloy dissolution/infiltration of

the Hastelloy™-S base metal. The physical loss of the braze alloy, resulting in the creation of unfilled regions, would clearly reduce the load supporting footprint of the braze joint. Adjustment of the brazing process parameters (time and temperature) offer the only alternative means of alleviating this phenomenon.

Four-point bend strength tests were conducted at elevated temperatures. Tests on Hastelloy™-S/Hastelloy™-S and Kovar™/Kovar™ couples brazed with the 92Au-8Pd alloy (Phase V, vacuum) were performed at 200, 400, 600, 800°C, 900°C, and 950°C (392, 752, 1112, 1472, 1652, and 1742°F). The 200, 400, 600, and 800°C test samples of the Hastelloy™S /Hastelloy™-S couples exhibited anomolously low strengths; observations indicated that poor joint formation had taken place during fabrication. These data were discarded. Fig. 23 is a graph of the joint strengths as a function of temperature. In both material categories, the joint strength dropped with increasing temperature. The Hastelloy™S/Hastelloy™-S joints failed within the braze joint proper for all but one test sample at 800°C; however, the strength of this particular test was not recorded by the operator. On the other hand, only two (2) samples of the Kovar™/Kovar™ couples exhibited joint failures, one at 900°C and the other at 950°C. Otherwise, the samples simply deformed under the load and the data in Fig. 23 represented the maximum load. The test strengths at 200 and 400°C were not reported by the operator because the joints did not fracture; the bars deformed under the applied load.

Shown in Fig. 24 are SEM micrographs of the fracture surface of the Hastelloy™-S/Hastelloy™-S sample tested at 950°C. The low magnification view in Fig. 24(a) illustrates the fracture surface morphology of the entire failure surface. Two distinct morphological features were observed; these are shown in Figs. 24(b) and 24(c). The surface features in Fig. 24(b) indicated dissolution of the base metal by the braze alloy during joint formation. Because of the possible formation of low melting temperature phases on the Hastelloy™-S grain boundaries, in-situ melting of that material cannot be ruled out. Fig. 24(c) is the surface morphology that is representative of the traditional ductile failure mode of the material. The presence of even small areas of this failure morphology in regions with an overall morphology like that in (b) confirmed that a mechanical bond was present (albeit, to a limited extent). Similar fracture surface morphologies were observed for the 900°C and 800°C specimens. The fracture surfaces of the Kovar™ samples that failed within the joint had a morphology similar to that of Fig. 24(c).

Room temperature, four-point bend tests were also performed on Kentanium™/Kentanium™ braze joints that were fabricated with the 92Au-8Pd alloy, Phase V furnace cycle, and the vacuum environment. Seven test samples were evaluated. A metallographic cross section was performed of one of the un-tested four-point bend sample. Low and high magnification SEM micrographs of the joint region shown in Fig. 25(a) and Fig. 25(b), respectively clearly demonstrate the infiltration of the braze alloy into the matrix of the composite material, the same as was observed on the earlier wetting study. The original gap of 51 μm (0.002 in) was reduced to less than 1 μm (4×10^{-5} in). Diffusion of the braze alloy extended approximately 1000 μm (0.040 in) from the initial gap interface position, on both sides of the gap. Irrespective of the extensive diffusion of the braze alloy into the composite material, there were no indications of voids or cracking that would suggest a limited strength to the joint or modified composite material.

The Kentanium™/Kentanium™ joint strengths were 650±200 MPa (94±29 ksi). While the braze joint showed very good strength, there was considerable scatter as the strength values ranged from a minimum value 406 MPa (59 ksi), which was quite acceptable, to a maximum of 944 MPa (137 ksi). A detailed SEM/EDAX analysis of the fracture surfaces of braze joints made with the Au-Pd alloy was not performed. Low magnification visual assessments indicated that failure proceeded through the sample along the braze joint.

Four-point bend tests were also performed on silicon nitride/silicon nitride braze joints. Tests were used to optimize the Ti coating as well as for the selection of a suitable braze alloy from amongst the three choices. Tests of AS-800/AS-800 braze joints began with the use of the Pd-Ni, Pd-Co, and Au-Pd alloys and a 2.0 μm (79 μin) thick Ti coating applied to the AS-800 surface. The Pd-Ni and Pd-Co joints were fabricated under Phase III, 750 mtorr Ar conditions. The Au-Pd joints were processed under Phase V, vacuum conditions. The silicon nitride failed to remain joined after fabrication with the Pd-Ni and Pd-Co filler metals. The cross sections of these joints fabricated clearly revealed consumption of the Ti layer accompanied by attack of the silicon nitride. Interface void formation (N_2 gas evolution) and embrittled filler metal (silicide formation) were noted.

Results were somewhat more encouraging with the Au-Pd alloy; two test series were performed with this braze alloy (A and B). The strength values were (A) 96±48 MPa (14±7 ksi) and (B) 137±41 MPa (20±6 ksi). These results are shown in Fig. 26. As previously noted, the next step was the introduction of the Ti layers onto the braze alloy foils in order to simulate the latter as "active" braze alloys (with equivalent 2 wt.% Ti contents). All of those tests were performed under the Phase III furnace schedule, using a 750 mtorr Ar partial pressure atmosphere. Two tests series were performed with the Au-Pd and Pd-Ni alloys; a single test series was conducted with the Pd-Co alloy. The results from all of the tests are also shown in Fig. 26. This modification of the filler metal content improved the strength; however, the mean strength values for the Pd-Ni and Pd-Co alloys remained very low.

The joint strength improvement associated with changing from a 2.0 μm (79 μin) thick Ti layer to the 4.0 μm (157 μin) thick layer is demonstrated by the four-point bend strength data shown in Fig. 27 for the Au-Pd braze alloy on the AS-800 silicon nitride (Phase V, vacuum for all conditions). The strengths more than doubled from ~ 100 MPa to over 300 MPa. Also included in Fig. 27 is the performance of the Pd-Ni alloy with 4.0 μm Ti (Phase V, vacuum). The presence of even the modest strength of the Pd-Ni alloy attests to the benefits of the thicker Ti layer as a barrier to filler metal interaction with the silicon nitride. The improved joint quality of AS-800/Au-Pd/AS-800 joints is observed in a comparison of cross sectional views by optical micrographs in Fig. 28. Voids indicative of poor wetting and joint filling of the 2.0 μm Ti joints were absent from joints formed with the 4.0 μm Ti layer.

The AS-800 (4.0 μm Ti) /AS-800 (4.0 μm Ti) joints fabricated with the Au-Pd braze alloy were also tested at elevated temperatures. The test data are shown in Fig. 29. Two minima in the strength data were observed. One minima was observed at a test temperature of approximately 200°C and a second at the maximum test temperature of 950°C. The fracture surfaces were not examined in detail to confirm adequate joint fabrication prior to testing. Should such an analysis provide no evidence of faulty sample fabrication, then the tests should be repeated because the trend of the data at 200 and 400°C was not entirely expected.

The fracture surface morphologies of samples that were tested at 600 - 950°C were thoroughly examined. Shown in Fig. 30 are low and high magnification SEM micrographs of a sample tested at 600°C. The surface morphology was comprised largely of microvoid coalescence and plastic deformation of the braze alloy. X-ray dot maps of the surfaces confirmed that the fracture path was in the braze alloy. As the test temperature increased an increasing amount of the fracture path occurred at the interface region in the vicinity of the Ti layer. The fracture morphology resulting from 950°C test exemplifies this pattern, and is shown in Fig. 31. The fracture path exhibited no preference for either side of the gap, jumping between the two sides, resulting in the macroscopic features of the surface. As with the sample tested at 600°C, the 950°C test specimen surface was examined by X-ray dot maps and clearly showed the Ti signal. This indicated the fracture path was near the interface regions. This trend in the

temperature dependence of the fracture morphology suggests that with increasing test temperature, the interface region became weaker.

Lastly, once the metal/metal, Kentanium™/Kentanium™, and silicon nitride/silicon nitride tests confirmed that an acceptable braze joint was feasible between the like materials using the Au-Pd filler metal (4.0 μm Ti) on the AS-800 (Phase V furnace cycle, 1260°C, 7 min; and vacuum environment), the next step was to fabricate metal/ceramic braze joints between the Hastelloy™-S alloy and AS-800 silicon nitride. The four-point bend strength sample configuration was also used. The joint gaps between the Hastelloy™-S and the interlayer, as well as that between the interlayer and the AS-800 silicon nitride, were maintained at 50.8 μm (0.002 in.) by the placement of W wires with the braze alloy.

Two changes were made to the Phase V furnace cycle for the metal/ceramic joining efforts but the process was still identified as the "Phase V" process. Those changes were: (1) The brazing time was decreased from 7 min to *4 min* to lessen the extent of base metal dissolution. (2) The cooling cycle was altered to allow a slower temperature ramp through the solidification step, from 10°C/min to 5°C/min (18 to 9°F/min. In addition, the cooling step from 1100°C (2012°F) to 25°C (77°F) was allowed to proceed as a furnace cool, which was significantly slower than the forced cooling at a rate of 10°C/min used in the like-material joints. The furnace cycle (in vacuum) is shown below:

(1) 25 - 1200°C, 25°C/min (77 - 2192°F)
(2) 1200°C (2192°F), 4 min
(3) 1200 - **1260°C**, 10°C/min (2192 - **2300°F**, 18°F/min)
(4) **1260°C (2300°F), 4 min.**
(5) **1260** -1100°C, 5°C/min (**2300** - 2012°F, 9°F/min)
(6) 1100 - 25°C (2012 - 77°F), Furnace cool.

The first specimen was assembled with the 1.59 mm (0.0625 in) thick Kovar™ interlayer. The sample was intact after removal from the furnace, but failed during grinding to fabricate the four-point bend bars. The failure path was at the interface between the braze alloy and the AS-800 silicon nitride. Two specimens were assembled with a 3.18 mm (0.125 in) Kovar™ interlayer. Although such an interlayer thickness is clearly impractical, the failure of it to produce a sound joint in this experiment would clearly indicate that a suitable joint in this configuration was probably unachievable. The first sample assembled with 3.18 mm (0.125 in) thick Kovar™ interlayer had the same failure mode as with the 1.59 mm (0.0625 in) thick interlayer. The second specimen failed via a crack through the silicon nitride; the joint remained intact. This latter observation was confirmed when the braze joint was cross sectioned. Shown in Fig. 32 are optical micrographs of cross sections of the Hastelloy™-S/Kovar™ joint (Figs. 32(a) and 32(b)) and Kovar™/AS-800 silicon nitride joint (Figs. 32(c) and 32(d)). The sections were etched to reveal the braze alloy microstructure. The two joints showed excellent integrity with no indication of deformation or crack formation in the braze alloy nor in the near-interface region of the substrate materials. Nevertheless, the failure of the silicon nitride clearly indicates excessive thermal expansion mismatch stresses.

The above tests were repeated with the 1.59 mm (0.0625 in.) and 3.18 mm (0.125 in.) thick Kentanium™ interlayers substituted for the Kovar™ interlayer material. The same modified Phase V furnace cycle was used. Both specimens failed during the final grinding steps to make the four-point bend bars; the failure path was at the braze alloy/AS-800 interface.

A modification of the cooling cycle to allow for the reduction in the level of residual stresses was evaluated. Three holding steps were introduced into the cooling cycle; each step was designed to allow one of three microstructural processes to take place so as to reduce the

residual stresses. The first hold was at 925°C (1697°F) for 60 min to allow creep deformation processes to occur in the Au-Pd braze alloy. The second hold was at 625°C (1157°F) for 120 min to allow recrystallization processes in the braze alloy that were expected to further reduce the residual stress levels. Finally, the third hold at 200°C (392°F) for 120 min supported recovery processes. The revised furnace schedule was designated "Phase VI."

The first sample assembled with the Phase VI schedule used a 3.19 mm (0.125 i.) thick Kovar™ interlayer. The sample fractured during the grinding process. The failed specimen showed fracture through the silicon nitride as well as at the braze alloy/AS-800 interface with the latter predominating. Even the use of a combined 1.58 mm (0.0625 in) thick Kovar™ and Kentanium™ interlayers (joined by the Au-Pd braze alloy) produced premature failure of the specimen.

The results using the Kovar™ and Kentanium™ interlayer materials, Phase V (modified) and Phase VI cycles indicated that the residual stresses caused failure primarily at the braze joint interface with the AS-800 silicon nitride. Because adequate strength of that interface was demonstrated by the AS-800/AS-800 braze joints, it became apparent that, owing to the elevated temperature strength of the AS-800 silicon nitride (where such thermal expansion mismatch failures were rare), the failure path had changed from the bulk silicon nitride to the interface region.

It also became apparent that the "parent block" sample configuration used to make the four-point bend bars was prone to excessive residual stresses. Moreover, the sample geometry (and hence residual stress levels) did not represent the actual application design of the braze joint, it was concluded that to "fairly" evaluate the braze joint system, it was necessary to assess it in a geometry more representative of the application.

B. Plug-in-Ring Sleeve Joints

The design of the plug-in-ring sleeve joint (Fig. 33) was based on the dimensions of the sleeve joint to be used in the actual applications. The extent of the study was limited to an evaluation of the room temperature performance of the joints. Because of the difference in thermal expansion coefficients between the silicon nitride and the Hastelloy™-S materials, cooling from the brazing temperature would place both the silicon nitride and the braze joint into residual compression (hoop and radial components). This is the optimal condition for the both structures. Simple elastic stress analysis indicates that as the service temperature increases, the magnitude of the compressive stresses would decrease until they reach zero at the braze alloy melting temperature. However, permanent deformation to the braze alloy (or Hastelloy™-S) during the cooling phase may cause the residual stresses to become *tensile* prior to the assembly reaching the melting temperature of the braze alloy. Therefore future work should be directed to evaluating joint strength at the 950°C (1742°F) level.

The plug-in-ring sample configuration also allows evaluation of the joint shear strength. By applying a load to the plug in a test frame, the plug is pushed through the sleeve, causing the joint to fail in a shear mode. The test configuration selected for these samples resembled that of the anticipated application. A standardize plug-in-ring test is available (ASTM F 1044-87).

Two configurations were developed (Fig. 33), one without an interlayer and the other with an interlayer sleeve of nominal 0.51 mm (0.020 in) wall thickness. The dimensions of the two versions of the Hastelloy™-S sleeve, the Kovar™ interlayer (Kentanium™ was not used in this study), and the AS-800 silicon nitride plug are shown in the figure. The dimensions of the parts were developed so that a braze joint at room temperature would have a nominal thickness

of 51 μm as recommended for Au-based alloys.[18] However, it was necessary to determine the joint size at the melting temperature of the braze alloy to ascertain that sufficient capillary flow could take place at the time of brazing. It was computed that the 51 μm (0.002 in) gap would expand to 94 μm (0.0037 in) at the brazing temperature (1260°C, 2300°F), a value that was deemed adequate to allow capillary flow by the braze alloy.

The silicon nitride (solid) cylindrical plugs required a Ti coating to promote wetting by the braze alloy. A coating thickness of 4.0 μm (157 μin) Ti was applied over approximately 9.5 - 10 mm (0.38 - 0.40 in.) of the cylinder outer surface, beginning from one end of the cylinder. The part was continuously rotated in the sputtering chamber during deposition. High temperature tape was used to mask the area on which the Ti coating was not desired. The coating process took approximately one hour per sample.

The assembly of the parts to form a joint is shown in Fig. 34. The silicon nitride cylinder was supported by an alumina pedestal so that the bond area defined by the extent of the Ti-coated cylinder that overlapped the Hastelloy™-S sleeve was 7.6 mm (0.300 in.) This left approximately 2.5 mm (0.100 in.) exposed on top with which to form a fillet. The amount of braze alloy was computed from the expected gap at the time of melting of the Au-Pd filler metal. The Au-Pd filler metal was used in wire form. Because the gap was not sufficiently big to allow the foil to be pre-placed directly into the joint the wire was wrapped about the top of the joint. Capillary action was expected to carry the molten braze alloy through the gap. The same configuration was used whether or not the interlayer system was targeted.

Initially, two assemblies were built, one with the Kovar™ interlayer and the other without it. In both cases, the original Phase V (i.e., 1260°C, 7 min), vacuum process was used; the longer time period was maintained to ensure that flow would take place in the joint. The specimens exhibited a significant displacement of the silicon nitride cylinder off-center, indicating its movement during the process. It became obvious that the gaps had widened to the extent that the braze alloy did not fill the entire volume, although wetting of the metal and silicon nitride surfaces appeared to be more than adequate. Further observation indicated that considerable dissolution of the Hastelloy™-S and Kovar™ had occurred. The entire Kovar™ interlayer had been dissolved and approximately one-half of the Hastelloy™-S cross section had been lost.

These first results clearly indicated that *base metal dissolution* was the primary issue to be addressed. The approach was to reduce the process temperature and/or process time. The conditions that were to be evaluated included:

1260°C (2300°F)	4 min
1245°C (2373°F)	7 min
1245°C (2373°F)	4 min
1235°C (2255°F)	4 min
1225°C (2237°F)	4 min
1215°C (2219°F)	4 min*
1200°C (2192°F)	4 min*
1175°C (2147°F)	4 min*

All of the conditions were initially assessed for Au-Pd alloy wettability using the wetting sample plates of Hastelloy™-S, Kovar™, and 4.0 μm Ti coated silicon nitride blocks. The condition followed by the (*) indicated that actual plug-in-ring samples were constructed under those parameters. All other parameters of the Phase V schedule remained the same. It should be recalled that the 92Au-8Pd alloy has a solidus temperature of 1200°C and liquidus temperature of 1240°C.

SEM micrographs of the cross sections of the three wetting sample substrate types fabricated at 1200°C for 4 min are shown in Fig. 35. The wetting samples of Hastelloy™-S and Kovar™ (Figs. 35(a) and 35(b)) exhibited excellent spreading of the Au-Pd alloy at all temperatures. There was a decrease in the extent of erosion of the base metals; however, it was not completely eliminated. The microstructural morphology was largely unchanged with the exception of extent, as compared with samples fabricated at the higher brazing temperatures. The AS-800 silicon nitride wetting sample showed excellent wetting by the braze alloy; however, the extent of spreading was noticeably diminished at 1200°C and 1175°C; this point is illustrated in Fig. 35(c). The micrographs in Figs. 35(a) and 35(b) suggest that, given the solidus and liquidus temperatures of the Au-Pd alloy, melting point depression due to base metal dissolution had occurred in the joints. For the AS-800 silicon nitride specimen for which there was no dissolution, a decrease in the spreadability of the alloy was observed.

Two plug-in-ring cylinder samples were fabricated with the 1215°C, 4 min brazing process conditions; one specimen was made with the Kovar™ interlayer while the other was made without it. Metal erosion was still present, but to a lesser degree than was observed with the 1260°C, 7 min condition. Displacement of the AS-800 plug precluded any mechanical testing. In the next trial, the brazing temperature was dropped to 1175°C; the time remained at 4 min. The Kovar™ interlayer was included in this sample. Although flow of the braze alloy appeared to be somewhat sluggish compared to earlier tests, it showed excellent wetting on all of the surfaces. A second sample, in this case, without the interlayer, was fabricated under the same conditions. Each of the samples fabricated without the interlayer at the two peak temperatures was mechanically tested. In addition, a specimen (no interlayer) was fabricated at the 1200°C, 4 min processing condition. An excellent joint was obtained.

It was apparent from visual observations that the best results of the plug-in-ring test samples were obtained at 1175°C and 1200°C, and for a 4 min time period. An example of an assembled test specimen, along with the set up configurations with and without an interlayer are shown in Fig. 36. Substrate monitors of the wetting performance of the Au-Pd on each material confirmed excellent wetting for each of the specimens. Shown in Fig. 37 are optical micrographs of the cross section of a plug-in-ring specimen (having the Kovar™ interlayer) that was processed at 1175°C for 4 min. The view in Fig. 37(a) is that of a Hastelloy™-S sleeve and the silicon nitride; the start of the Kovar™ interlayer is just out-of-view. The silicon nitride incurred no cracking along its bond length or outside the joint in the fillet area. This picture also illustrates the extent of erosion to the Hastelloy™-S by the Au-Pd filler metal. A comparison of the wall thicknesses both inside and outside of the joints indicates an erosion of 43 μm (0.0017 in). This level of erosion can be considered as acceptable, particularly for the relatively thick walls of the Hastelloy™-S sleeve, and because the capillary fill did not appear (nor was likely) to be affected. Also, the supply of braze alloy to fill the joint should be able to accommodate the extra volume created by the enlarged gap.

Erosion of the Kovar™ interlayer was slightly more extensive (Fig. 37(b)). The nominal thickness of the as-fabricated, interlayer sleeve wall was 0.51 mm. A survey of the entire joint revealed that the interlayer wall thickness had been reduced to approximately 0.33 mm (0.013 in.). The extent of erosion had clearly decreased compared to that observed with the 1260°C (2300°C) process temperature in which the interlayer had been completely dissolved into the braze alloy.

At 1175°C and 4 min process conditions, wetting of the silicon nitride was excellent (Fig. 37(c)). The Ti was retained at the interface as is evident in the micrograph. Observations of the sputtered Ti film where it had *not* been wetted by the braze alloy, indicated that the Ti film had spalled from the surface of the silicon nitride.

Lastly, two samples were fabricated (one with the interlayer, one without the interlayer) using a brazing condition of 1175°C and 2 min. Both samples showed excellent wetting.

As a final exploratory effort, test specimens were constructed in which the Au-Pd brazing alloy was activated by metal additions. Two techniques were used. A special batch of Au-Pd-2 wt% V was fabricated. In the second approach, the braze alloy was modified by the previously discussed technique of sputtering the active element onto the surface of the foil so that upon melting, the active ingredient would mix with the braze alloy and then segregate at the ceramic/braze alloy interface to effect the necessary adhesion. The Ti was sputtered to a thickness of 3 μm (118 μin) on both sides of the foil as a nominal 2 wt.% addition. Therefore, both of the modified alloys would not require the Ti layer to be deposited on the silicon nitride surfaces.

Prior to the fabrication of the plug-in-ring samples using either V or Ti additions, modifications were made to the test sample geometry because of concern about whether the processing temperatures would allow adequate wetting of the braze alloy through the gap. Therefore, a modification was made to the Hastelloy™-S sleeve that would widen the gap. This modification was made only to the Hastelloy™-S sleeve design that did *not* use the Kovar™ interlayer. The inner diameter was increased from a nominal value of 7.76 mm (0.3057 in) to 7.82 mm (0.3077 in); this increase of the inner diameter meant that the gap at room temperature was increased from a nominal 51 μm (0.002 in) to 76 μm (0.003 in). In order to maintain the wall thickness, the outer diameter was increased from 10.31 mm (0.406 in) to 10.36 mm (0.408 in). The increase in the gap would allow the preplacement of the braze alloy preform directly in the braze joint. It was anticipated that the presence of braze foil in the joint would facilitate the movement of the molten alloy into the gap region from the top of the joint.

Three samples were produced with the Au-Pd+2V alloy and two specimens were assembled with the Ti-coated silicon nitride. The furnace process was modified to be 1225°C (2237°F), 1 min for two of the three tests with the Au-Pd+2V samples and both of the Ti-coated Au-Pd specimens. The third Au-Pd+2V samples was built to the 1215°C (2219°F), 4 min process schedule. All of these samples were targeted for mechanical testing.

Visual observations were made of the samples assembled with the Au-Pd-2V braze alloy and Ti-coated Au-Pd alloy (1225°C, 1 min, vacuum). Both of the samples made with the Ti-modified braze alloy exhibited excellent wetting. In the case of the Au-Pd-2V alloy, wetting was poor on one of the specimens (1225°C, 1 min) and good-to-excellent on the other two samples.

The mechanical tests were performed on a limited number of the plug-in-ring specimens. The strengths are represented as shear stresses (load divided by the load bearing area). The specimens with 4.0 μm Ti on the AS-800 cylinder and processed for 4 min at 1175°C and 1215°C had maximum shear stresses of 41 MPa (6.0 ksi) and 42 MPa (6.1 ksi). These stress correspond to applied loads of approximately 8 kN (1800 lb) in both cases. A similarly fabricated sample that was processed under 1175°C for a reduced time of 2 min exhibited a shear stress of 40 MPa (5.8 ksi). The initial Hastelloy™-S sleeve geometry was used in these specimens; no interlayer was present.

The sample that was processed at 1175°C for 4 min was cross sectioned after testing to determine the failure mode. A view is shown in Fig. 38. These samples were made with the revised Hastelloy™-S sleeve geometry that allowed pre-placement of braze alloy in the joint. The joint showed excellent wetting of all surfaces. Cracks were not observed in the silicon nitride. The fracture path was entirely at the braze alloy/silicon nitride interface. An attempt to perform the same analysis on the specimen that was processed at 1215°C failed when the silicon nitride plug fell from the sleeve.

Two plug-in-ring samples were fabricated with bare silicon nitride and with the Au-Pd alloy that was "activated" by sputter depositing Ti on it to an equivalent weight percent of 2%. The brazing process conditions were 1225°C for 1 min. The shear strength values for the two samples were 45 MPa (6.5 ksi) and 51 MPa (7.4 ksi).

The plug-in-ring sleeve joint configuration provided a suitable representation of the actual service application on which this work was based. More importantly, the residual stress state was more consistent with that of the application. The samples were used to define the processing parameters. The samples exhibited excellent strength levels. Moreover, cracking was not observed in the silicon nitride slugs. As noted earlier, high temperature testing would provide valuable data as to the applicability of this joint for the specified service conditions.

V. Aging Study

Long-term, high temperature service for a braze joint raises the likelihood that solid state diffusion processes may take place in the braze alloy, at the braze alloy/substrate interface, and in the substrate material. Any subsequent change to the physical metallurgy of the braze joint may alter the physical and mechanical properties of the product. Should those property variations prove to be detrimental to the performance of the braze joint, then they must be fully characterized, and the microstructural mechanisms identified to limit their impact on the product reliability.

Aging samples were created for both microstructural analysis as well as to assess the impact of solid state aging on the four-point bend strength of the braze joints. The microstructural samples were sessile drop specimens of Au-Pd braze alloy/substrate couples, the substrates being Hastelloy™-S, Kovar™, and AS-800 (4.0 μm Ti). The Kentanium™ interlayer material was not evaluated. In the case of the four-point bend strength tests, "similar" material joints (i.e., Hastelloy™-S/Hastelloy™-S, Kovar™/Kovar™, and AS-800/AS-800) were used in the study.

The aging matrix was as follows:

Microstructural analysis (sessile drop samples):
Temp.: 575°C (1067°F), 950°C (1742°F)
Time: 100, 200, 300 days

Mechanical strength (four-point bend tests):
Temp.: 575°C (1067°F), 950°C (1742°F)
Time: 100, 200 days

Microstructural studies were performed through metallographic cross sections. A single sample was aged per condition. On selected samples of the Hastelloy™-S base metal, an electron microprobe analysis (EMPA) was performed to identify the chemistry of specific features observed in the samples. The cross sectional samples with Kovar™ and AS-800 were visually assessed for changes, including the presence of cracks in the microstructure; no such damage was observed. The samples were subsequently archived.

The four-point bend tests were performed on a minimum of three samples; typically four samples were evaluated. The bend bars were aged after having been sectioned from the parent block specimen and ground to dimension. An extra sample was aged to confirm the aged microstructure that was observed in the corresponding sessile drop specimens. All other test protocols were the same as those described earlier.

A. Microstructural Analyses

The microstructural analysis of the Hastelloy™-S specimens indicated that Au diffusion, both in the bulk as well as along the grain boundaries occurred. Shown in Fig. 39 are SEM micrographs of the near-surface region of the specimen in (a) the as-fabricated condition, (b) 575°C (1067°F), 300 days, and (c) 950°C (1742°F), 300 days. Aging at 575°C caused a slight increase in the width of the (Au) infiltrated, grain boundary phase development. The only change in the composition of the grain boundary phase was a 1-2 at.% decrease in the Ni content (between the as-fabricated sample and that exposed to the 575°C, 300 days aging condition). Concurrent with that decrease in Ni was an increase in the Au content of similar magnitude; the other elemental concentrations did not change significantly. These trends are illustrated in Fig. 40, which shows a representative EMPA trace through the overall reaction zone of the Hastelloy™-S/Au-Pd sample that was aged at 575°C for 300 days. The EMPA trace in Fig. 40 can be compared against that of the as-fabricated EMPA trace in Fig. 12(b). The distance of bulk (intragranular) Au diffusion was approximately 0.20 mm (0.008 in) into the substrate, from the surface, for the as-fabricated condition. A similar extent of Au diffusion was observed after aging at 575°C for 300 days.

The concentration of Au in the grain interior was similar to that observed in the as-fabricated samples (4-5 at.%). Also, the Mo content was higher by a similar amount, and the Ni and Cr contents lower to compensate for the Au and Mo trends as was observed in the as-fabricated condition. These trends can also be seen in Fig. 40.

Additional grain boundary infiltration was observed when the aging temperature was increased to 950°C (Fig. 39(c)). The spatial dimensions of the "web" of that phase became smaller after aging, allowing for a distinction to be made between the distance of diffusion in the as-fabricated condition and that realized after aging. The grain boundary phase has exhibited only very small changes in composition with respect to the as-fabricated condition. Those changes were the same trends as noted between the 575°C, 300 day specimens: i.e., a small increase (1-2 at.%) in the Au content accompanied by a similar decline in the Ni content. All other elemental concentrations did not show any apparent changes with respect to the as-fabricated state. The extent of bulk Au diffusion in the grain interiors had increased with the 950°C, 300 day heat treatment, from approximately 0.20 mm (0.008 in.) in the as-fabricated and 575°C aged specimens, to 0.66 mm (0.026 in.). The composition of the grain interiors, including the Au content, was largely unchanged with the exception of the Mo concentration. The higher Mo contents that were observed in the as-fabricated and 575°C aged samples, had returned to levels that were representative of the bulk alloy. Small changes in the other elemental concentrations in the grain interiors, together compensated for the decreased Mo content.

An artifact that was observed with the Hastelloy™-S samples after aging at 950°C for 300 days, that was not observed in the as-fabricated or 575°C, 300 days aged samples, was the formation of a particulate phase on the grain boundaries of the bulk Hastelloy™-S material, away from the infiltrated grain boundary regions. This phenomenon is shown in Fig. 41(a). The EMPA technique was used in the bulk Hastelloy™-S material just outside of the Au bulk diffusion zone and infiltrated grain boundaries to determine the composition of those particles; a representative trace is shown in Fig. 41(b). The particles appeared to be comprised of Ni, Mo, and Cr; the exact compositions could not be specified because the particle size was of the same order as the x-ray sampling volume of the electron beam (2-3 μm). As a result, the material beyond the individual particles contributed to the signal, thereby giving a false compositional measurement.

Examination of the AS-800/AS-800 samples aged at 950°C for 200 days revealed no gross degradation to the joint region or interfaces. An optical micrograph is shown in Fig. 42 of

the four-point bend bar specimen subjected to the aging treatment. Diffusion of the Ti away from the interface is revealed by the widening of the region containing the darker phase.

B. Four-Point Bend Tests

Four-point bend strengths were measured for specimens aged for 100 and 200 days at 950°C. The results appear in Fig. 43. A nominal strength increase was observed after aging the Hastelloy™-S/Hastelloy™-S samples for 100 days. However, that strength increase was lost upon extending the aging time to 200 days. Joints aged for 100 days did not fail catastrophically; the maximum strength was a result of bending deformation of the specimen. The same failure was observed in the as-fabricated samples. Aging for 200 days caused the strength to decrease to levels commensurate with the as-fabricated condition. In this case, two of the three samples failed in the braze joint. The third showed only general deformation of the bend bar. This failure mode suggests the following scenario: The strength of the joint increased after 100 days as a result of the thermal treatment of the bulk Hastelloy™-S material. The source of the strength increase in the Hastelloy™-S appears to be an age strengthening of the substrate. Product literature shows the potential for some age strengthening of the alloy under heat treatment conditions represented by the aging parameters. Apparently, the present experiments confirmed that the strengthening property had been engaged, and was responsible for the observed test behavior. Clearly, the joint strength surpassed that of the bulk alloy in that case. The strength decrease after 200 days appeared to reflect a decrease in the strength of the braze joint below that of the yield strength of the base metal. Examination of the four-point bend sample that was not tested suggested that diffusion of braze alloy into the bulk alloy may have jeopardized the integrity of the original joint gap.

The Kovar™/Kovar™ samples exhibited lower strength after the solid state aging treatment. Only one sample of the 200 day aging treatment failed in the joint. The maximum strength was the result of general deformation of the bend bar, the reduced strength was caused by a loss of strength in the Kovar™ material. The strength loss was a result of general microstructural recrystallization and recovery processes. As an interlayer material, this trend is actually beneficial to the joint performance. As a softer material, the Kovar™ is more capable of accommodating the thermal expansion mismatch stresses between the Hastelloy™-S and silicon nitride.

Lastly, the AS-800/AS-800 joints also exhibited a nominal decrease in strength from the as-fabricated value after the 100 day aging. The mean bend bar strength increased slightly after 200 days aging, being not significantly different for the previous two data sets . Failure took place within the joint. Therefore, in overall trend, the AS-800/AS-800 joints appeared to show the least sensitivity to the aging treatment. In the expected absence of any solid state interactions between the braze alloy constituents and the silicon nitride, these test results suggest that the metallurgy of braze alloy probably does not change dramatically during this aging period. Examination of the joint microstructure suggested some transport of the Ti compound particles away from the interface, into the bulk braze alloy by Ti diffusion.

VI. Alternative Filler Metals

A. Vanadium Activated Au-Pd Filler Metal Alloys

A.1 Materials Selection

As an alternative to metallizing silicon nitride and then brazing it with conventional filler metals, a new class of brazing alloys has been developed that permit direct wetting of non-coated

surfaces. Most commercial alloys are based on Ag and Au systems. These alloys have relatively low brazing temperatures, in the range of 800 to 1050°C, compared to the high service temperature requirements of the project's application. As described in previous sections, extended joint exposures to temperatures of 900 to 950°C will require filler metals with a high melting temperature, typically above 1200°C, and exceptional thermomechanical properties. The 60Pd-40Ni, 65Pd-35Co, and 92Au-8Pd (wt.%) alloys were specifically selected to meet these service temperature boundary conditions. Unfortunately, none of the alloys forms a direct metallurgical bond with silicon nitride. One approach to overcome this problem is to apply a metallic coating to the Si_3N_4 surface. This overcoat chemically reacts with both the nitride and brazing alloy to form the final metallurgical bond. A variety of metal coatings can be utilized, with Ti being the most popular candidate. Depending on the interfacial reactions, other metals can be substituted to enhance wetting. Another approach is to incorporate the active element in the composition of the brazing alloy. This class of filler metals is commonly referred to as active brazing alloys (ABA's). Recent activity in this area has included using V as the active elemental constituent. The interest in V is due to its ability to be furnace brazed in dry hydrogen, something not possible with Ti because of its propensity to hydride.

To complement the non-activated brazing component of this project, a series of "active" brazing alloys was chosen that could be processed in inert and reducing (i.e., hydrogen) atmospheres. The compositions were based on the Au-Pd-V system. The starting point of each composition was the commercial alloy 92Au-8Pd.[v] Three Au-Pd-V compositions were investigated. Wetting experiments were conducted with alloys having either 2, 3, or 4 wt. % V. Solid state aging tests were performed on 3V-sectioned wetting samples. The aging conditions were 950°C and 100 days. Four-point bend testing was done with specimens brazed with the 3V-containing alloy. Because each alloy had a developmental composition and the amount of material was limited, only selected tests were conducted. Additional plug-in-ring shear test samples were fabricated with only the 2V-composition. The shear samples consisted of a Hastelloy-S outer ring, an AS-800 silicon nitride plug, and a braze foil preform (see "Braze Joint - Testing" section for more detailed specimen and test procedure information).

A.2 Braze Joint - Assembly Processes

Wetting, aging, and mechanical test specimens were brazed in either a dry hydrogen atmosphere or vacuum (approx. 7 mPa). Similar substrates were used for the wettability and aging tests (square pieces with a punched-out braze preform). The samples were initially processed at a peak temperature of 1270°C in hydrogen. The nominal hydrogen furnace profile consisted of a 25°C/min ramp-up from furnace ambient to 1200°C, a hold at this temperature for four min, continued heating to 1270°C at 10°C/min, a four min hold at the peak temperature, a ramp-down to 925°C at 25°C/min, and a final furnace cool. Plug-in-ring shear test specimens were processed in vacuum at a lower peak temperature of 1215°C to minimize the dissolution reaction between the liquid braze and the metal Hastelloy-S outer ring. The 1215°C brazing profile was the same as the 1270°C profile, except for its peak temperature.

A.3 Wettability and Aging Tests

The wetting and aging samples were visually inspected and cross-sectioned to characterize the interfacial reactions and braze microstructures. Metallography, scanning electron microscopy, and electron microprobe analyses were conducted in support of the investigation. The as-brazed four-point bend and ring-in-plug test samples were not thermally aged and were mechanically tested at room temperature.

---

[v] American Welding Society (AWS) Brazing Alloy Classification BVAu-8; WESGO, Inc.'s "Paloro" Alloy.

Wettability was assessed by measuring the contact angle formed between the braze and silicon nitride or metal substrates. The typical measure of good brazeability is a contact angle of 30-45° or less. Wetting is clearly poor as the angle increases and exceeds 60°. For this investigation, excellent wetting was observed on silicon nitride for both the 3 and 4V-containing alloys, with contact angles of 5-10°. The 2V composition gave slightly higher contact angles of 30-35° in dry hydrogen, although the results were still very acceptable. Comparable wettability was also obtained with the 2V alloy when processed in vacuum.

Microstructural analyses revealed a relatively balanced reaction between the constituents of the Au-Pd-V alloys and the AS-800 silicon nitride substrates. Representative scanning electron microscopy (SEM) images are shown in Figures 44 and 45. The primary reaction occurs between V and silicon nitride. A reaction layer of VN forms at the interface and thickens with increasing V concentration. The resulting free Si reacts with the Pd in the braze alloy to form Pd_2Si throughout the joint. One possible reaction is as follows:

$$6Pd + 4V + Si_3N_4 \rightarrow 4VN + 3Pd_2Si$$

The results of the V-N and Pd-Si reactions are illustrated in the elemental maps of Fig. 46. Electron microprobe elemental traces across the braze interface are also presented in Fig. 47. These compositional analyses clearly show the segregation of V to the braze interface and the formation of palladium silicides in the braze, primarily along grain boundaries and near the nitride reaction layer. This balanced, dual reaction between the V and silicon nitride at the interface and the evolving N_2 and Pd in the braze limits unwanted porosity that could be generated by excess N_2 in the joint.

Although excellent wetting was observed with these alloys, a potential high temperature service problem was revealed after aging Au-8Pd-3V/ AS-800 silicon nitride samples for 100 days at 950°C. The braze separated from the silicon nitride substrate sometime during the 100 day exposure. Preliminary post-failure analysis suggested that the failure occurred at the VN layer, although the exact path of failure could not be resolved. It was not clear whether delamination occurred on the braze or silicon nitride side of the nitride layer. Regardless of its location, this particular system could yield premature failures when exposed to extended high temperature (> 0.8 homologous temperature) service conditions.

A.4 Room Temperature Four-Point Bend and Plug-in-Plug Mechanical Tests

Four-point bend tests were conducted with Au-8Pd-3V-brazed AS-800 silicon nitride specimens, conforming to ASTM Specification C1161-90, Sample Configuration "B". Base samples were brazed together at 1270°C in dry hydrogen for four minutes with 30 x 22 x 4 mm AS-800 silicon nitride blocks along their 30 mm sides. The brazed samples were ground, cut into rough blanks with a diamond saw, and then ground again to the final test dimensions of 45 x 3x 4 mm. All samples were tested at room temperature at a speed of 0.5 mm/min.

The average failure stress of the AS-800 silicon nitride/Au-8Pd-3V samples was 520 MPa ± 114, with failures occurring primarily in the AS-800 silicon nitride. Stresses ranged from 400 to 716 MPa. These values compared very well to the baseline strengths of the Au-8Pd vacuum brazed, Ti-coated AS-800 silicon nitride test pieces, which ranged from 107 to 453 MPa, with an average four-point bend maximum stress of 302 MPa ± 88 (Paul's Fig. 27). A single filler metal preform, 0.003" (0.076 mm) thick, was used to fabricate the baseline samples, with 4 μm of sputtered Ti on the AS-800 pieces.

Plug-in-ring shear tests were performed with samples brazed with the Au-8Pd-2V active filler metal. The AS-800 silicon nitride plugs were not metallized. Hastelloy-S was the outer ring material. No interlayer was used between the AS-800 and Hastelloy-S pieces. The test specimens were processed in vacuum at 1215°C for 4 min to minimize dissolution of the Hastelloy-S piece. The tests were conducted at a nominal crosshead speed of 0.076 mm/min, with an engagement length of 7.6 mm. The tested samples generally failed at the silicon nitride and braze interface, with occasional traces of braze left on the silicon nitride piece. The maximum shear stress was 41 MPa. Subsequent tests examined the effects of a higher brazing temperature and shorter brazing time on shear strength. The second set of samples was processed at 1225°C for 1 minute, once again in vacuum. The set's average maximum shear strength was 53 MPa ± 13, a small improvement in strength over the 1215°C, 4 min processed sample. As a baseline comparison, similar samples were fabricated, using 4 μm of sputtered Ti on AS-800, Au-8Pd preforms, and Hastelloy-S. These baseline samples, brazed at 1215°C for four min, yielded a maximum shear stress of 42 MPa.

B. Ni-Cr-Si Filler Metal Alloys

B.1 Materials Selection

Recent work by Hadian and Drew,[19] suggests that Ni-based brazing alloys, having the same at. % ratio as AWS Brazing Alloy Classification BNi-5 (Ni-19Cr-10Si, wt.%), but with varying Si contents, can be used to directly wet silicon nitride. The reaction product at the braze interface is CrN. The authors found that the joint strength and microstructures were greatly affected by the alloy composition and brazing time. Brazing was conducted at 1220°C under a partial pressure of nitrogen, with time at peak temperature ranging from 5 to 15 minutes. The resulting free silicon from the Cr and silicon nitride reaction increases the Si content in the filler metal and produces a higher silicide-loaded microstructure, particularly with brazing alloys already high in Si. The result is a very brittle structure that is prone to cracking. Hadian and Drew concluded that a composition of Ni-19.6Cr-5.2Si should yield silicon nitride braze joints with room temperature four-point bend strengths of 115 MPa.

An investigation was conducted to determine the feasibility of using these Ni-Cr-Si alloys to braze AS-800 silicon nitride. To facilitate the investigation, two commercially-available compositions were selected for the study. The alloys were based on the AWS BNi-5 classification. The first alloy met the BNi-5 composition specification and has a melting range of 1078-1135°C. The material came in powder form on a transfer tape. The second alloy was an amorphous foil, 40 μm (0.0015 in) thick, with a modified BNi-5 composition of Ni-19Cr-7.3Si-1.5B and a melt range of 1052-1144°C. Additional Si, 300 μin. thick, was sputter-deposited on the AS-800 silicon nitride test pieces, when brazing with the latter alloy, to roughly maintain the conventional BNi-5 Ni-Cr-Si compositional ratio (at.%), as defined in Hadian's and Drew's work. The actual deposition, however, was generally thicker than required, although the net wt.% Si after brazing did not exceed 12.5 %.

B.2 Braze Joint - Assembly Processes

Wetting experiments were conducted using similar materials and processing conditions as described in the Au-Pd+V section. The tests were performed in vacuum with peak brazing temperatures of 1150°C for the BNi-5 alloy and 1160°C for the modified BNi-5 alloy. The brazing profile involved ramping at a rate of 25°C/min. to 1030°C, holding at temperature for four min, continuing the ramp at 10°C/min to the specified peak temperature, holding at peak temperature for four min, cooling to 975°C at 5°C/min, and finally furnace cooling.

B.3 Wettability Tests

Visual inspection of the wetting samples initially suggested good braze wettability. The solidified braze droplets had relatively low contact angles, typically 10-20° or less. The only potential problem was the observation of what appeared to be fine cracks or a "haze" on the braze surface. This observation was made on both the Ni-19Cr-10Si and Ni-19Cr-7.3Si-1.5B wetting samples. Samples were then cross-sectioned to further investigate whether the cracks extended into the braze. A Ni-19Cr-10Si on AS-800 silicon nitride sample is shown in Fig. 48.

The cracks clearly extended into the bulk braze and near the braze interface. Preliminary analysis suggests the formation of brittle silicides in the joint, resulting from the release of excess Si by the silicon nitride and Cr reaction, which subsequently caused the cracks. Even though the cracks are unacceptable, the wetting results demonstrate the feasibility of using Cr as an "active" element to directly braze AS-800 silicon nitride. As suggested by Hadian and Drew, a Ni-Cr-Si alloy, containing a lower Si concentration, should yield fewer silicides in the joint and consequently reduce joint brittleness and cracking. Because extensive Ni-Cr-Si alloy development was not planned for in the original CRADA scope of work, this investigation was terminated. Even with the potential for improved four point bend strength using a lower Si content (e.g., Hadian's and Drew's Ni-19.6Cr-5.2Si alloy), the improvement probably could not match the strength of a Au-8Pd+3V brazed AS-800 specimen.

VII. Summary

1. The goal of this study was to identify a suitable brazing process to attach a super alloy sleeve to a silicon nitride stud as part of the stator assembly of an advanced turboengine for aviation applications. The operational temperature of the joint would be 926°C (1699°F) under moderate mechanical loads.

2. The Superalloy selected for this joint was Hastelloy™-S, a nickel-based material produced by INCO Alloys, International. Interlayer materials chosen to alleviate thermal expansion mismatch residual stresses, were Kovar™ and a composite material, Kentanium™ Grade K162B. Three braze alloys were investigated: 92Au-8Pd, 60Pd-40Ni and 65Pd-35Co (wt.%). The evaluation metrics were wetting tests and room temperature and elevated four-point bend strength, and plug-in-ring shear strength tests. Microstructural and four-point bend strength tests were also conducted on specimens subjected to long-term, high temperature (solid state) aging treatments.

Prototype metal/ceramic braze joints were fabricated with the plug-in-ring test specimen, the dimensions of which were selected to represent the actual stud/sleeve application.

3. Two materials-related, manufacturing issues were identified as the primary "hurdles" to the realization of a suitable metal/ceramic joint. They were: (1) minimizing the interaction between Pd-containing brazes and the silicon nitride that produced interfacial voiding and brittle silicide phase formation in the braze alloy, and (2) the dissolution of the Ni-based and Fe-based metal alloys by the high temperature braze metal during joint fabrication.

4. Poor silicon nitride joint quality resulting from the interaction between the molten Pd-containing brazes and the ceramic was addressed using two approaches. (1) Braze alloys with limited Pd content were used. The 92Au-8Pd braze alloy was chosen from the three candidate materials, based upon this criterion. (2) A 4.0 μm thick Ti layer sputtered on the faying surface of the silicon nitride provided the surface necessary to promote wetting and spreading of the

braze alloy on the silicon nitride. It also had sufficient thickness to act as a barrier between the braze alloy and the silicon nitride.

Reducing the extent of base alloy dissolution (Hastelloy™-S and Kovar™) was achieved by lowering the brazing temperature and minimizing the brazing time.

5. Four-point bend tests were performed on Hastelloy™-S/Hastelloy™-S, Kovar™/Kovar™, and AS-800/AS-800 joint specimens at room temperature and elevated temperatures (200 to 950°C). Room temperature tests of the Hastelloy™-S/Hastelloy™-S, Kovar™/Kovar™ systems with Au-Pd alloy showed average strengths from just over 400 MPa to almost 500 MPa. Failure was primarily by deformation of the bars; the joints themselves remained intact. The room temperature, four-point bend strength of the AS-800/AS-800 specimens with 4.0 μm Ti on the AS-800 and Au-Pd braze was ~300 MPa; the failure path was in the joint. The room temperature bend strength of AS-800/AS-800 specimens brazed with Paloro ABA (3% V) was significantly higher at 520 MPa, and failure occurred primarily in the AS-800.

Although there is a significant strength decrease with temperature for Kovar/Kovar and Hastelloy-S/Hastelloy-S joints brazed with Paloro, the strengths between 600 and 950°C are higher than 100 MPa. AS-800(4 μm of Ti)/AS-800(4 μm of Ti) joints brazed with Au-Pd braze have average strengths of ~200 MPa at 600°C, ~150 MPa at 800°C, just below 100 MPa at 900°C, and ~ 30 MPa at 950°C. Failure within the braze joints proper took place with the Hastelloy™-S/Hastelloy™-S and AS-800/AS-800 specimens. The strength decrease of the Kovar™/Kovar™ braze joints was caused by a strength loss in the Kovar™ base metal; in nearly all these cases, the joints did not fail.

The plug-in-ring (silicon nitride in Hastelloy-S) test configuration that resembles the 331-200 nozzle attachment and support system was assembled and shear tested. Joints made with Au-Pd+2V and Ti-coated silicon nitride and Au-Pd with a sputter deposited Ti coating and bare silicon nitride had shear strengths of 40-50 MPa.

6. A study was performed that examined the response of the bi-material joints to extended, high temperature exposure. An in-depth microstructural analysis of the aged joints was limited to that of the Hastelloy™-S/Hastelloy™-S couples. Aging in the solid state condition resulted in the increased formation of grain boundary phase further into the specimen at 950°C (1742°F). Bulk diffusion of Au also increased at that temperature; these effects were insignificant after similar aging treatments at 575°C (392°F). Optical metallographic observations of the silicon nitride four-point bend bar after aging for 200 days at 950°C showed some migration of the interfacial Ti away from the silicon nitride. Nevertheless, no strength degradation was observed.

7. Direct "active" metal brazing to AS800 silicon nitride was accomplished with a Au-Pd-V brazing alloy system. The VN reaction layer increased in thickness as the V concentration was increased from 2 to 4 wt.%. Brazing temperatures and times were lowered to minimize base material dissolution and brittle silicide formation. Excellent four-point flexure and plug-in-ring shear strengths, 520 MPa and 53 MPa, respectively, were obtained at room temperature with the Au-8Pd-V-brazed AS800 test specimens. High temperature aging, 950°C for 100 days, resulted in delamination at the VN reaction layer on an AS800 sample brazed with the Au-8Pd-3V alloy.

8. Direct brazing of AS800 with a Ni-19Cr-10Si brazing alloy was demonstrated. The "active" reaction was CrN and free Si. The resulting Si content in the joint, however, was increased by this interfacial reaction and produced an extensive network of brittle silicides that cracked on cooling. The cracking problem can be reduced by lowering the initial Si content of the filler metal.

VIII. Appendix

A. Monel K500 Assemblies

The 92Au-8Pd brazing alloy and process were applied to the rotating axle assembly shown in Fig. 49. In the figure is the stack-up of individual segments as well as one of the finished components. The diameter of the primary part of the assembly was 2.03 cm (0.800 in.). The thicknesses and compositions (where appropriate) of the joint segments were:

• Monel™ K500	1.27 cm (0.500 in)	66Ni-29.5Cu-2.7Al-0.6Ti + trace elements
• Nickel,	0.76 mm (0.030 in)	
• Kullite 1700 composite	3.18 mm (0.125 in)	90W-6Ni-2Fe-2Cu (W particles in 60Ni-20Fe-20Cu binder)
• Nickel	0.76 mm (0.030 in)	
• AS-800 silicon nitride	2.54 cm (1.0 in)	
• Nickel	0.76 mm (0.030 in)	
• Kullite 1700	3.18 mm (0.125 in)	
• Nickel	0.76 mm (0.030 in)	
• Monel™ K500	1.27 cm (0.500 in)	

The assemblies were made by stacking the parts vertically. The applied force on the joints was the weight of the parts themselves. Tungsten wires 51 μm (0.002 in.) in diameter were placed into each of the joints to control the gap thicknesses to that dimension. The faces of the AS-800 silicon nitride cylinder were coated with 4.0 μm Ti.

The assemblies were fabricated using a modified Phase V program in vacuum. The brazing conditions for the first and second assembled units were 1215°C (2219°F), 4 min and 1200°C (2192°F), 4 min. Visual inspection of the joints showed excellent wetting by the 92Au-8Pd braze alloy. These two units were shipped to AlliedSignal for torque testing. The torque test on the unit processed at 1200°C showed nearly zero load bearing capacity; the failure path was at the braze joint /AS-800 interface. The other unit failed at a relatively small load due to crack propagation in the AS-800 silicon nitride. Both results, when examined in light of the data from the aforementioned experiments, suggested that excessive residual stresses had developed in the joints, forcing failure at the AS-800 interface or within the material, itself. The use of 1.52 mm (0.060 in) thick Ni layers or replacing the Ni layers with 0.76 mm (0.030 in) Mo interlayers were identified as possible approaches towards reducing the residual stresses.

A second issue arose in the fabrication of this joint, that was also encountered in the main body of the experimental program, was the brazing of a composite material. In the present case, the composite material was the Kullite 1700 (90W-6Ni-2Fe-2Cu) comprised of W particles in a 60Ni-20Fe-20Cu binder phase. In this case, the impact of the reaction was more complex than was the braze alloy infiltration of the Kentanium™ composite material.

A low magnification SEM micrograph of the joint region between the K500 and the AS-800, which included the two Ni layers and the Kullite 1700, is shown in Fig. 50 (a). The joint had been processed at 1200°C for 4 min. The Ni layers to either side of Kullite material were 50% dissolved, but only on side adjacent to the Kullite alloy. Dissolution of Ni was negligible from the side of either the K500 or the AS-800 materials. A higher magnification view of the Ni/Kullite interface is shown in Fig. 50 (b). These micrographs, along with compositional X-ray dot maps, were used to develop the following scenario. The Au-Pd braze alloy caused dissolution of the Fe-Ni-Cu matrix phase of the Kullite 1700. The liquid comprised of Au, Ni, Fe, and Cu then readily attacked the Ni layer, dissolving into it by a distance of approximately one-half its thickness.

An examination was made of the K500/Ni and AS-800/Ni interfaces. Dissolution of the braze alloy into the K500 first interface left a small gap; in some locations, braze alloy was present (Fig. 51(a) while in other regions, voids were present due to the loss of filler metal (Fig. 51(b)). The AS-800/Ni interface is shown in Fig. 52. In this case, a small braze filler metal gap was discernible by the presence of the Ti particles there. However, the limited gap appeared to meld into the Ni layer as the Au-Pd braze alloy diffused into the latter. The absence of the Au-Pd braze alloy in the gap region may have left behind a weakened joint structure that could not accommodate the residual stresses formed upon cooling. This scenario was confirmed by SEM/EDXA of the fracture surface of the assembly that was torque tested at AlliedSignal. There were only small, scattered traces of the Au-Pd braze alloy on the fracture surfaces. The AS-800 side showed primarily the ceramic and Ti; analysis of the Ni side revealed largely Ni.

These analyses showed clearly that material interactions between the braze alloy and the components of the joints needed to be minimized. A fourth assembly was fabricated in which the W wires were removed so that a filled gap could be realized, despite the diffusion of Au and Pd into the base metals. The brazing process time was reduced from 4 min to *1 min* to decrease the impact of molten metal contact on the dissolution of base materials. The results of this test confirmed the impact of thermal expansion mismatch between the silicon nitride and the K500 as a large dome crack formed in the silicon nitride in the unit that was cross sectioned. This approach proved to be successful perhaps in strengthening the interface, but was unsuccessful overall because it simply moved the failure from the joint proper into the silicon nitride. The results indicate that a more extensive effort, including additional process parameter adjustments as well as the consideration of barrier layers to limit the base metal/braze alloy interaction, will be required overcome this problem.

IX. REFERENCES

1. *Brazing Handbook*, p. 5, AWS, Miami, FL (1991).
2. M. Santella, "Joining of Ceramics for Heat Engine Applications", *Cer. Tech. Proj., Semiann. Rep..*, ORNL/TM-11984, March 1992, ORNL, Oak Ridge, TN.
3. M. Santella and L. Manley, "Strength and Microstructure of Titanium-Vapor-Coated Silicon Nitride Braze Joints," *Bull. Amer. Cer. Soc..*, pp. 513-527 (1988).
4. S. Peteves, "Nitride Ceramic Joining", 8th CIMTEC, World Ceramics Congress, Florence, Italy, June 28-July 4, 1994.
5. *Technical Information: Hastelloy™ Alloy S*, Haynes Inter., H-3003A, 1988.
6. Private conversation between F. Hosking and M. Santella, Oak Ridge National Laboratory, March 24, 1994.
7. L. Harner, "The Use of Fe-29Ni-17Co Alloy", pp.3-16 in *Low Thermal Expansion Alloys and Composites*, ed. by J. Stephens and D. Frear. TMS, Warrendale, PA (1994).
8. E. Nikolaiski, "On the Oxidation of Titanium Carbide," *Zeit. fur Phys. Chem. Neue Folge*, 24, p. 405, (1960).
9. G. Dzodziev, et al., "Oxidizability of Materials Based on TiC and TiN at Elevated Temperatures," *Sov. Powder Metall. and Metal Cer.*, 27, p. 323 (1988).
10. J. J. Stephens, F. Greulich and L. Beavis, "High Temperature Grain Growth and Oxidation of Fe-29Ni-17Co Alloy Leads," *Low Thermal Expansion Alloys, and Composites*, TMS, Warrendale, PA (1994).
11. S. Peteves, "Nitride Ceramic Joining", 8th CIMTEC, World Ceramics Congress, Florence, Italy (June 28-July 4, 1994).
12. G. Ceccone, S. Peteves, and M. Nicholas, "The Ceramic Connection", *The Materials Challenge*, (August 1994).
13. M. Santella, "Joining of Ceramics for Heat Engine Applications", *ORNL/TM-11984*, Mar. 1992, p. 193].
14. M. Naka, "Controlling of Ceramic-Metal Interfacial Structure Using Molten Metals", *Trans. JWRI*, 21, p. 1 (1992).
15. S. Peteves and M. Nicholas, "Evaluation of Brazed Silicon Nitride Joints: Microstructure and Mechanical Properties", *J. Amer. Cer. Soc.*, 79, p. 1553 (1996).
16. S. Kang, E. Dunn, J. Selverian, and H. Kim, "Issues in Ceramic-to-Metal Joining: An Investigation of Brazing a Silicon Nitrided-Based Ceramic to a Low-Expansion Superalloy", *Ceramic Bull.*, 68, p. 1608 (1989).
17. D. Johnson, "Ceramic Technology Progress Report", *ORNL/tm-12428*, Sept. 1993, Oak Ridge National Lab. pp. 167-179.
18. *Brazing Manual,* AWS, Miami, OH, p. 13 (1991).
19. A. M. Hadian and R. A. L. Drew, "Strength and Microstructure of Silicon Nitride Ceramics Brazed with Nickel-Chromium-Silicon Alloys," *J. Am. Ceram. Soc.*, Vol. 79, No. 3, pp. 659-665, (1996).

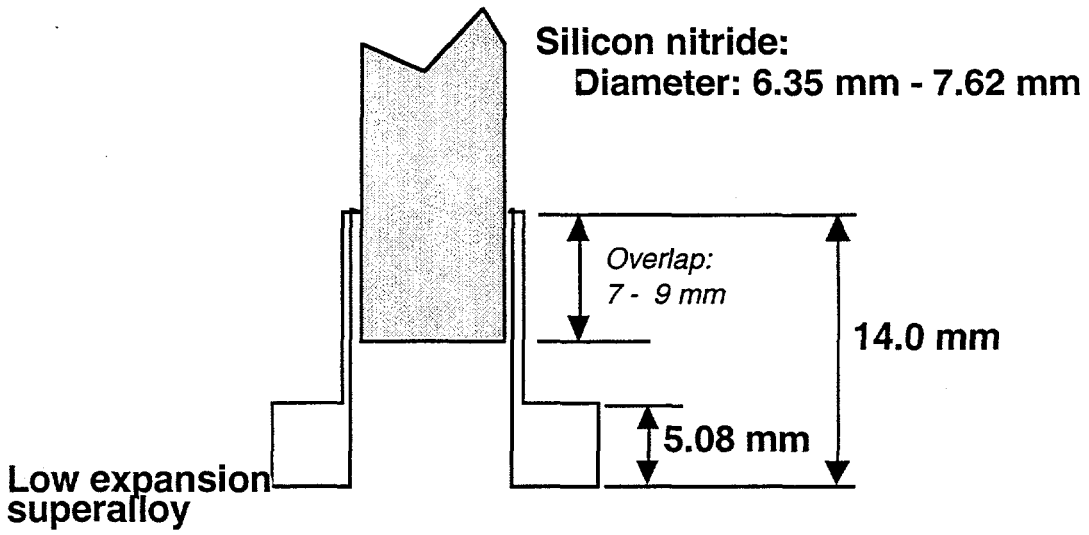

Fig. 1. Overlapping sleeve joint configuration for the stator mount for the AlliedSignal 331-200 nozzle attachment and support system.

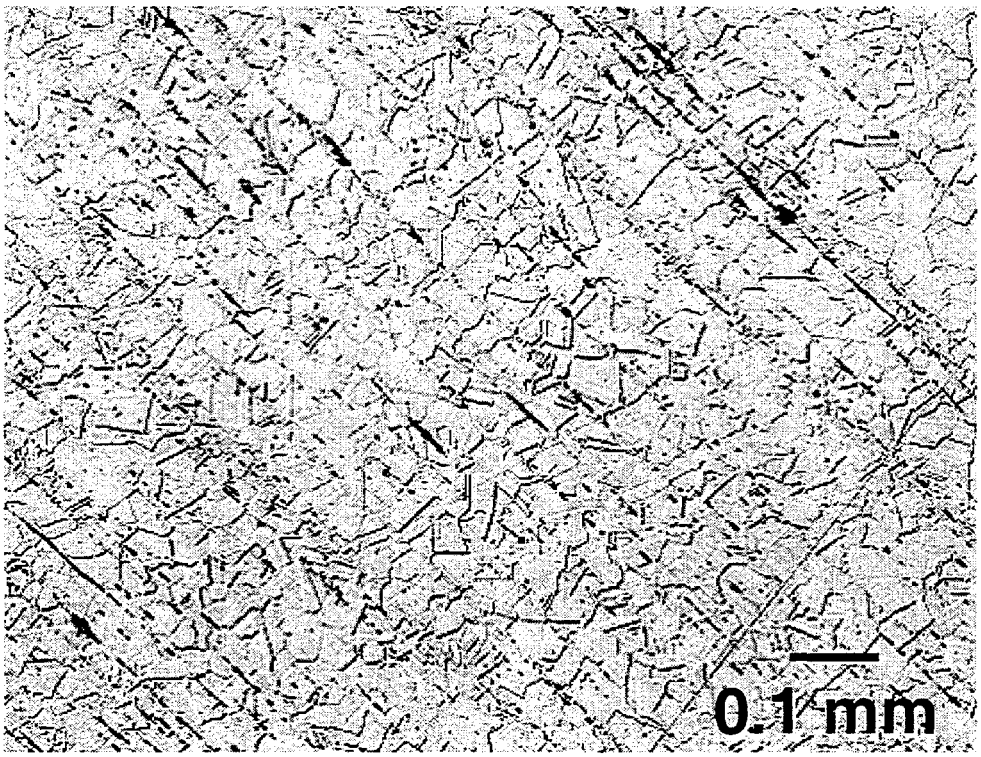

Fig. 2. Optical micrograph of the as-received Hastelloy™-S alloy.

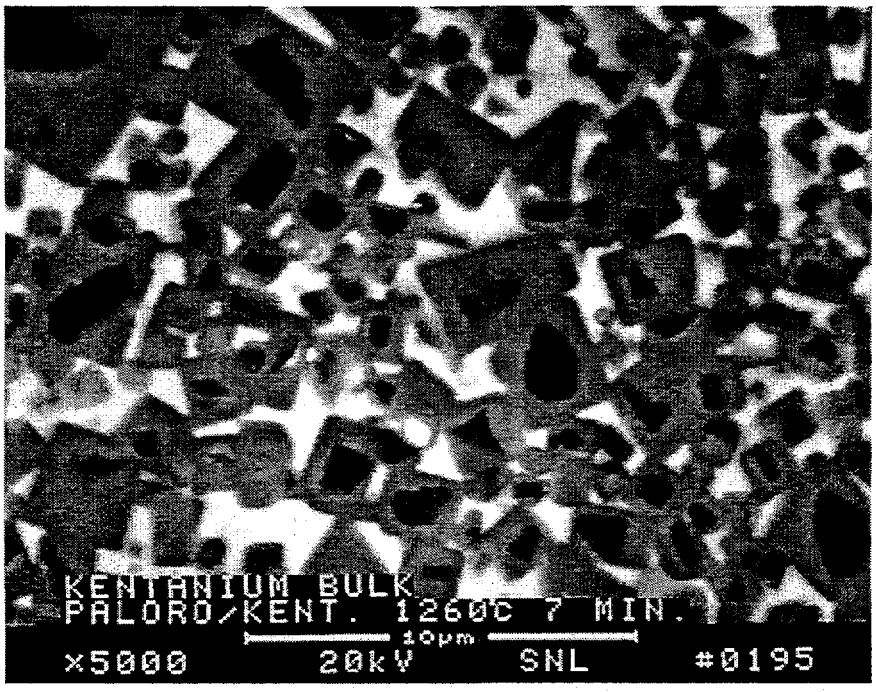

Fig. 3. Optical micrograph of the microstructure of the Kentanium™ cemented titanium carbide interlayer material. The black and gray particulates are the TiC phase; the light matrix is a Ni-Mo alloy.

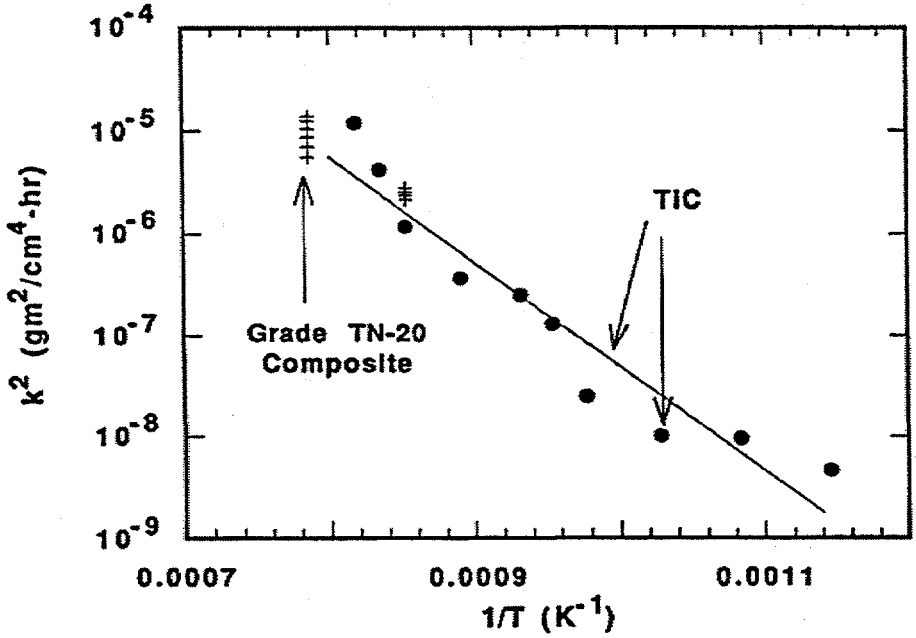

Fig. 4. The parabolic oxidation rate constant, k^2 (gm^2/cm^4-hr) as a function of the reciprocal temperature (°K) for monolithic TiC and a TiC/Ni-Mo composite similar to the K162B.

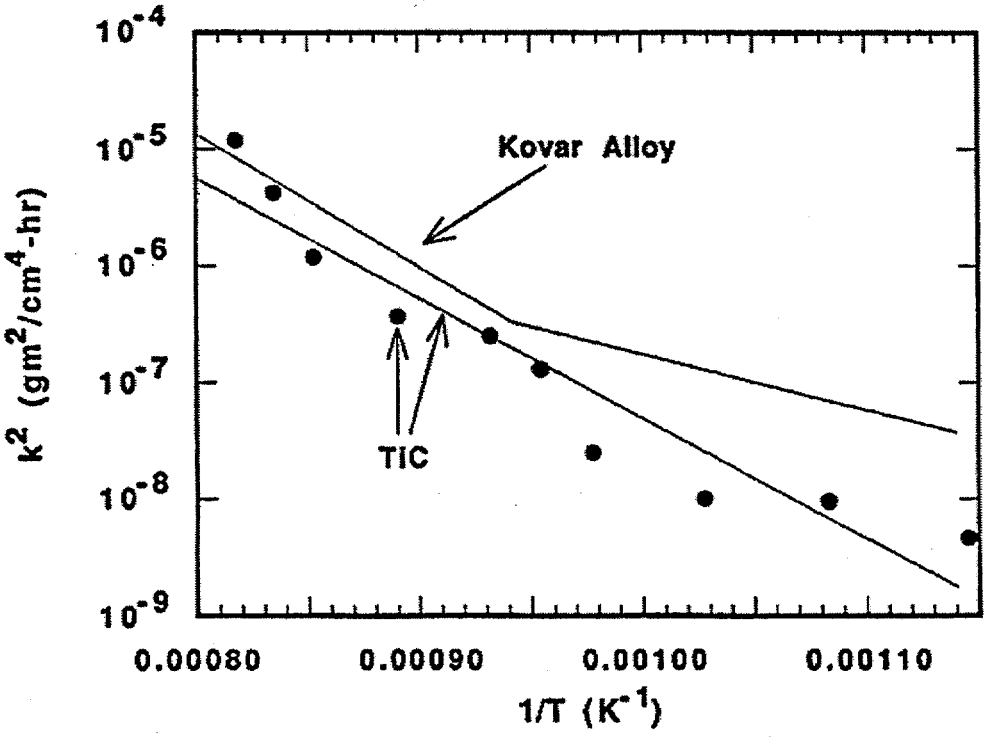

Fig. 5. The parabolic oxidation rate constant, k^2 (gm^2/cm^4-hr) as a function of the reciprocal temperature (°K) for monolithic TiC and Kovar™.

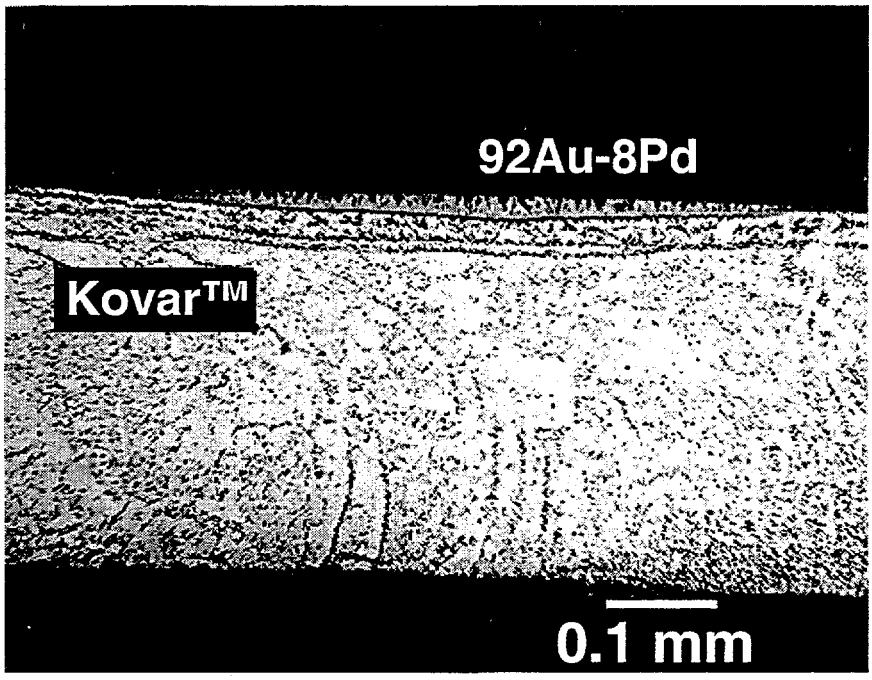

Fig. 6. Optical micrograph of the cross section of the Kovar™ sample after wetting by the 92Au-8Pd alloy under the Phase I furnace schedule (750 mtorr Ar).

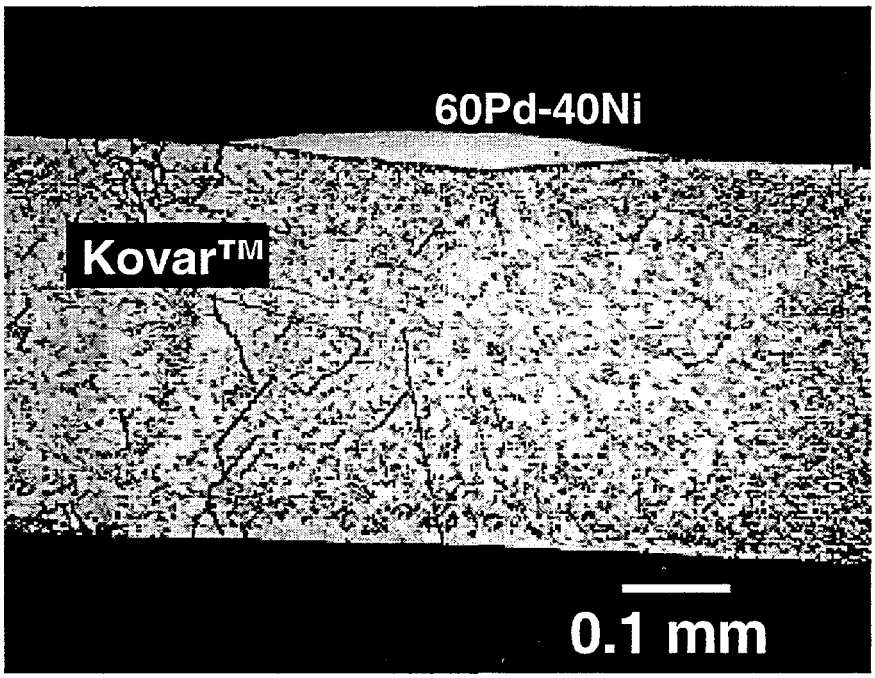

Fig. 7. Optical micrograph of the cross section of the Kovar™ sample after wetting by the 60Pd-40Ni alloy under the Phase I furnace schedule (750 mtorr Ar).

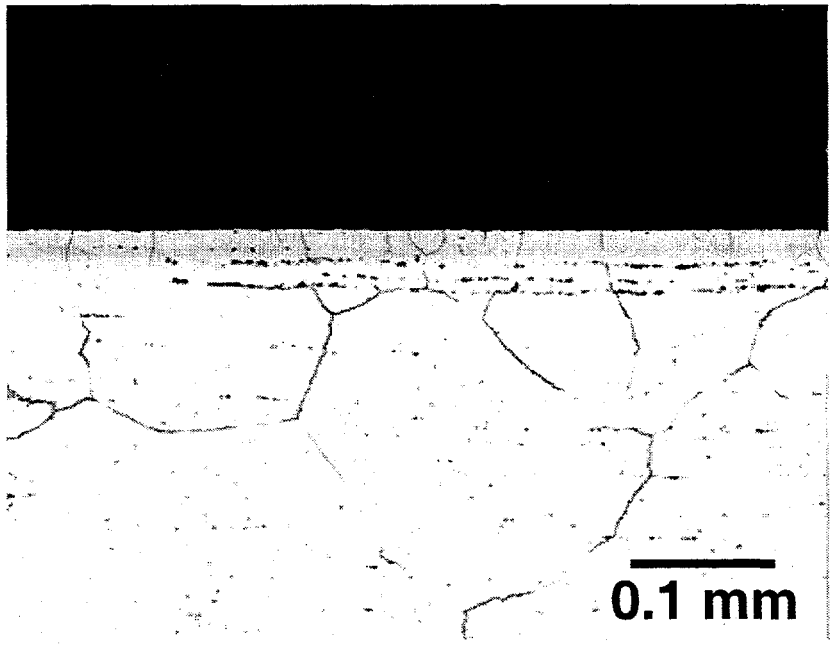

Fig. 8. Optical micrograph of the cross section of the Hastelloy™S sample with a Ni electrodeposited layer, after exposure to the process parameters of the sessile drop experiment (1270°C, 7 min, 750 mtorr Ar). The Ni has diffused into the substrate.

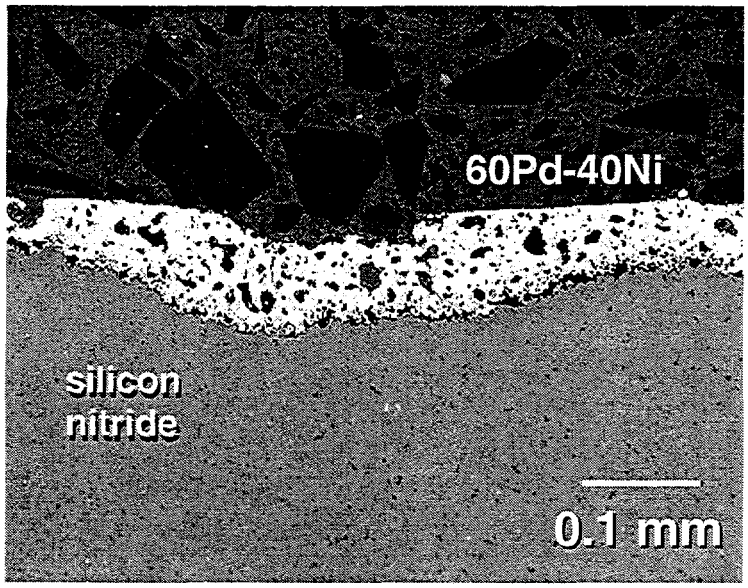

(a)

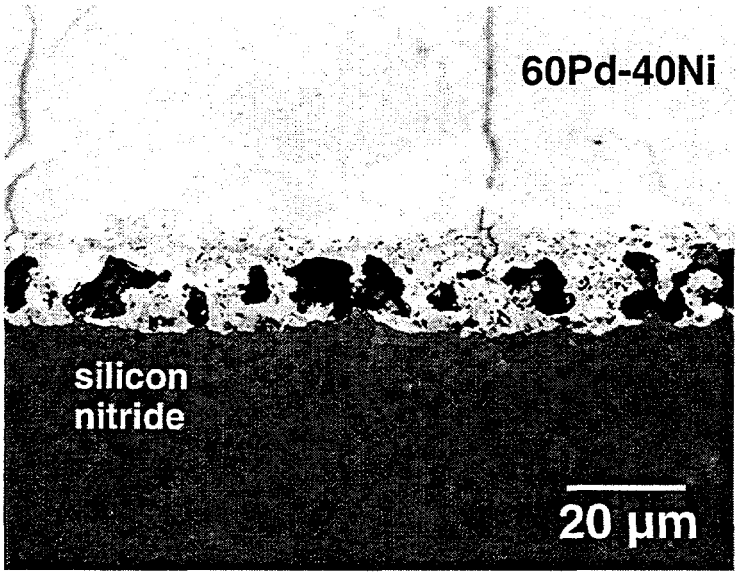

(b)

Fig. 9. (a) Optical micrograph of the cross section of the sessile drop of the 60Pd-40Ni alloy on AS-800 silicon nitride (1270°C, 7 min, 750 mtorr Ar). (b) A higher magnification of the interface region shows void formation and cracking within the filler metal.

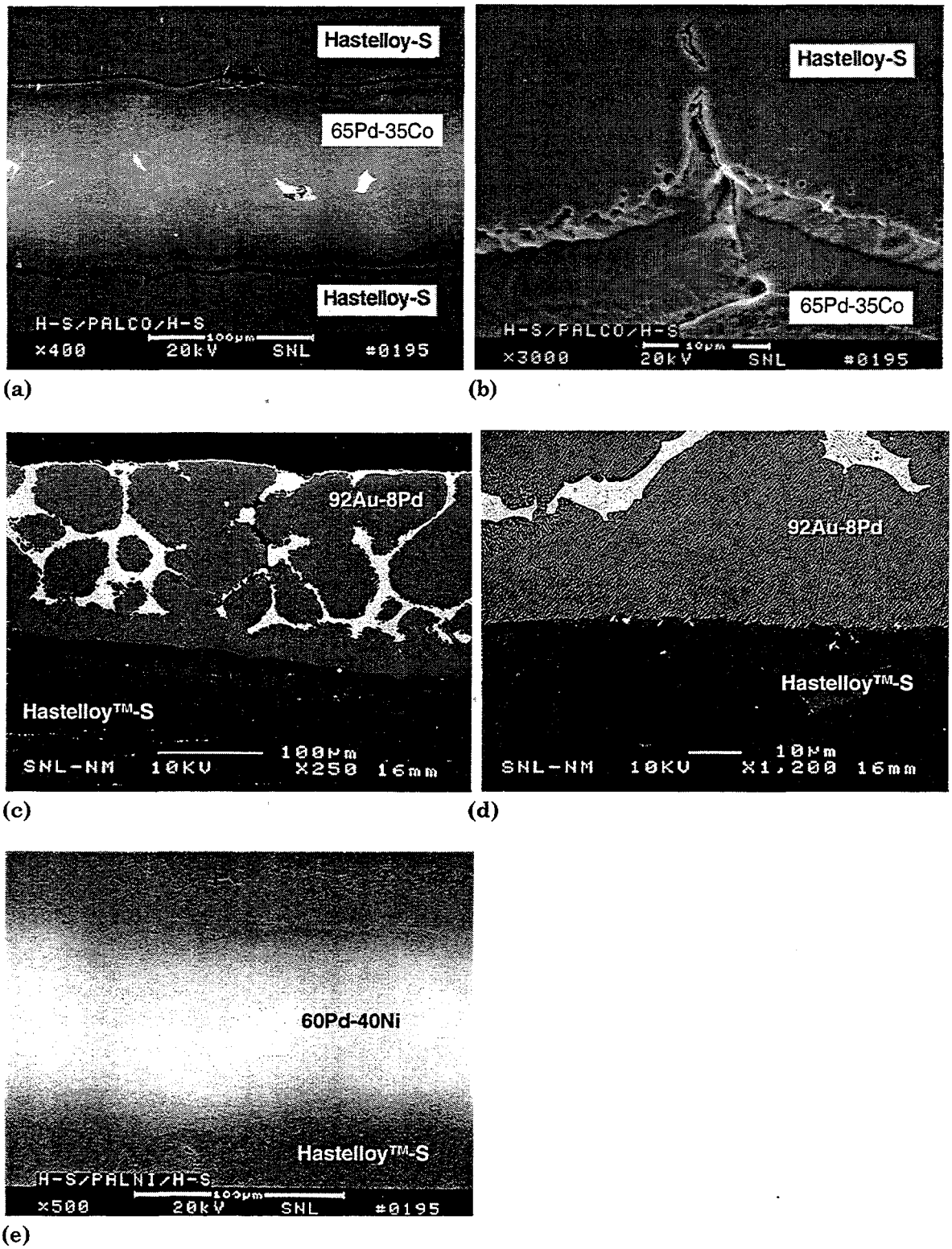

Fig. 10. SEM (SE image) micrographs of the braze joints showing the braze alloy/Hastelloy™-S base metal interfaces (a) 65Pd-35Co, low magnification; (b) 65Pd-35Co, high magnification, (c) 92Au-8Pd, low magnification; (d) 92Au-8Pd, high magnification; and (e) 60Pd-40Ni, low magnification only.

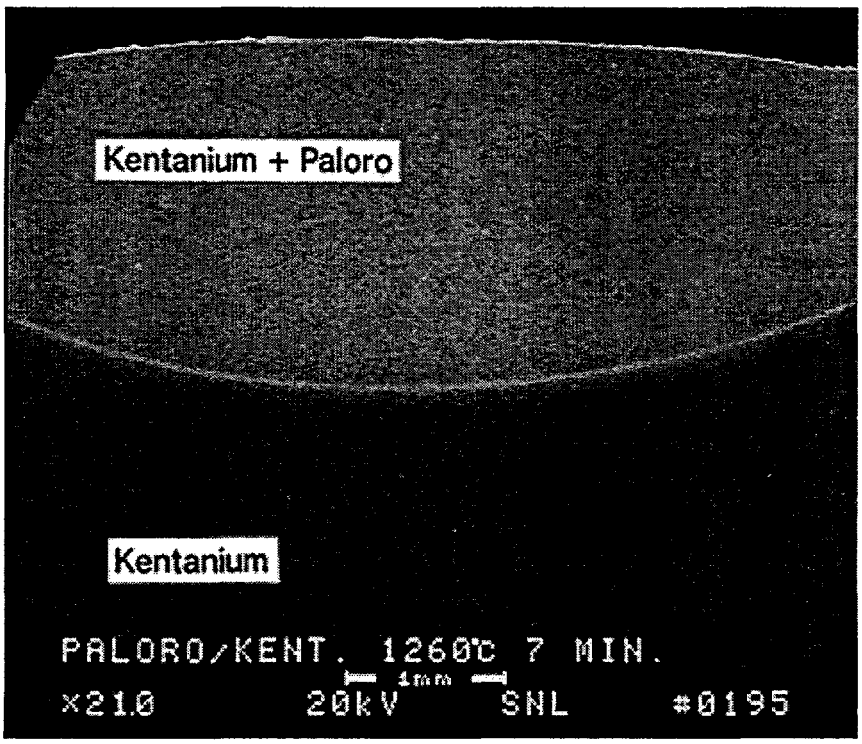

(a)

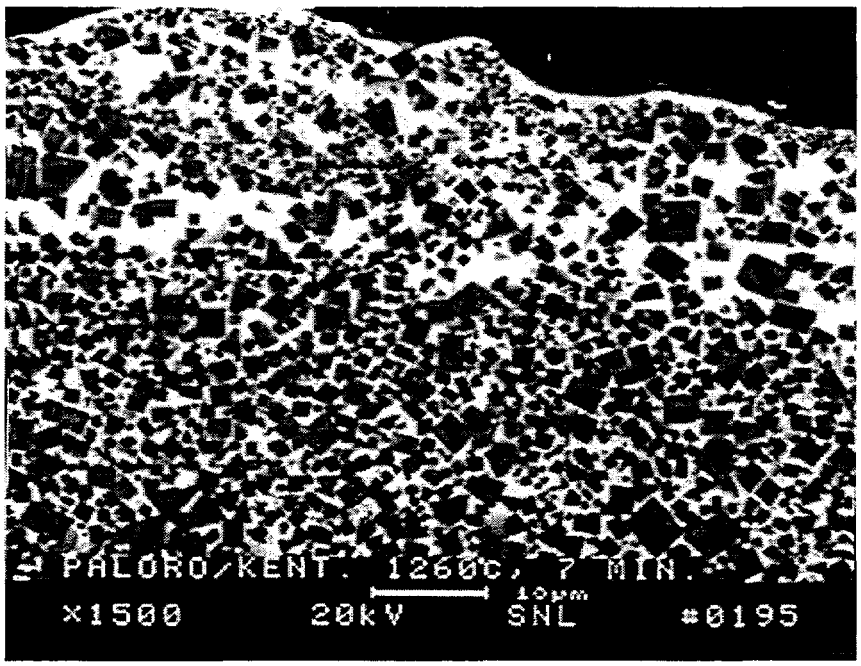

(b)

Fig. 11. SEM micrographs of a cross section of the wetting sample taken at the surface of the Kentanium™ on which the 92Au-8Pd alloy had been wetted. (a) An apparent diffusion zone extend from the surface on which the 92Au-8Pd alloy had been deposited into the bulk Kentanium™ material. At the surface (b), there is no appreciable thickness of braze alloy, suggesting that the braze alloy had fully diffused into the substrate structure, through the Ni-Mo matrix phase.

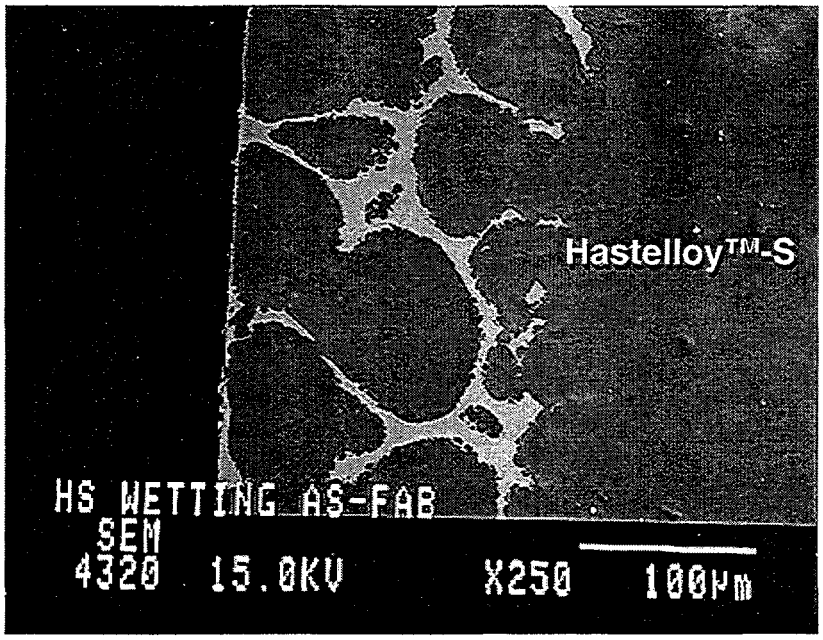

(a)

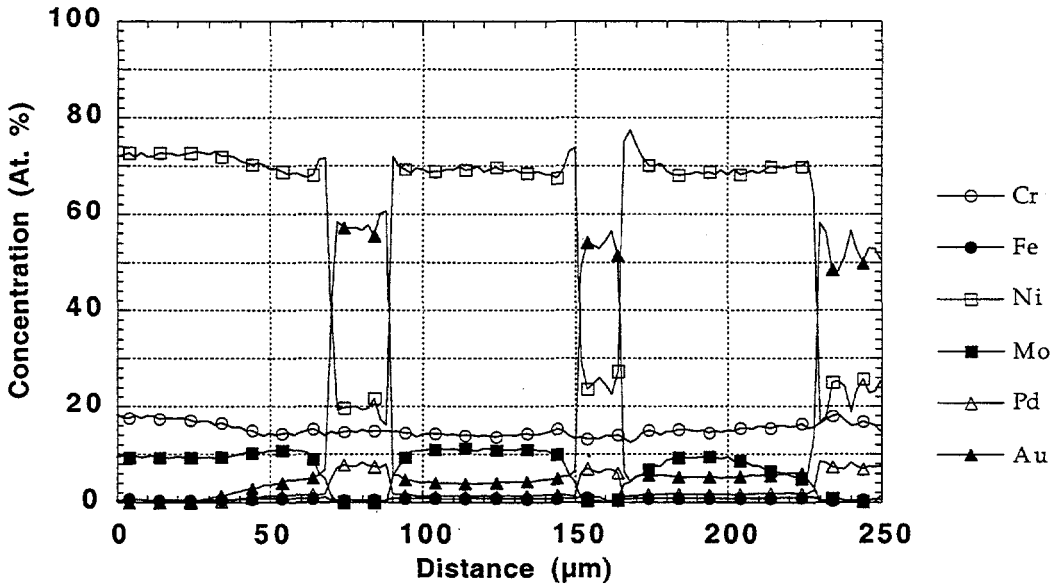

(b)

Fig. 12. (a) SEM (SE image) of the Hastelloy™-S/92Au-8Pd wetting sample (Phase V, vacuum processing) in the as-fabricated condition. (b) EMPA trace (base metal: Cr, Fe, Ni, and Mo; braze alloy: Au, Pd) across the near-surface region shown in (a). The trace in (b) is representative of ten traces that were made in that area.

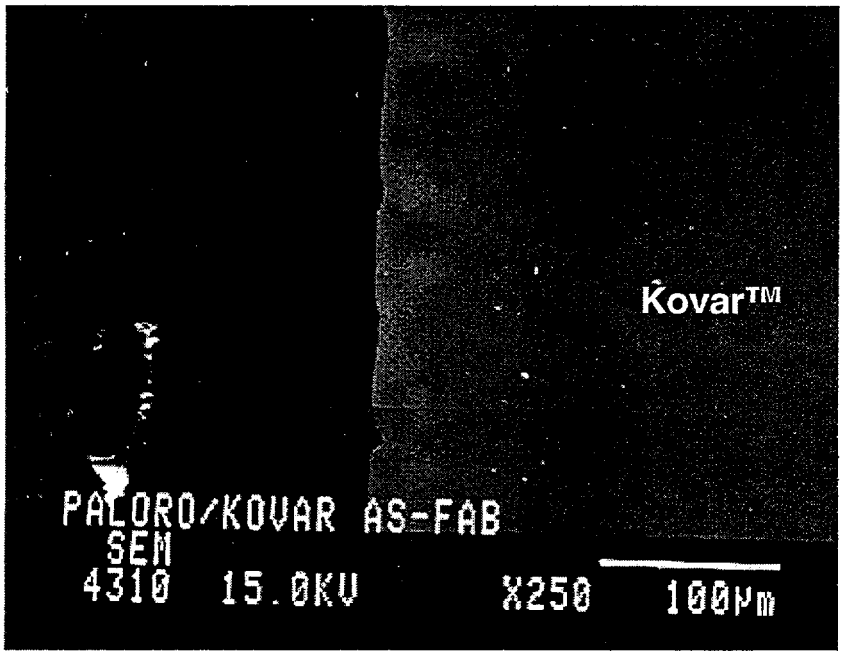

(a)

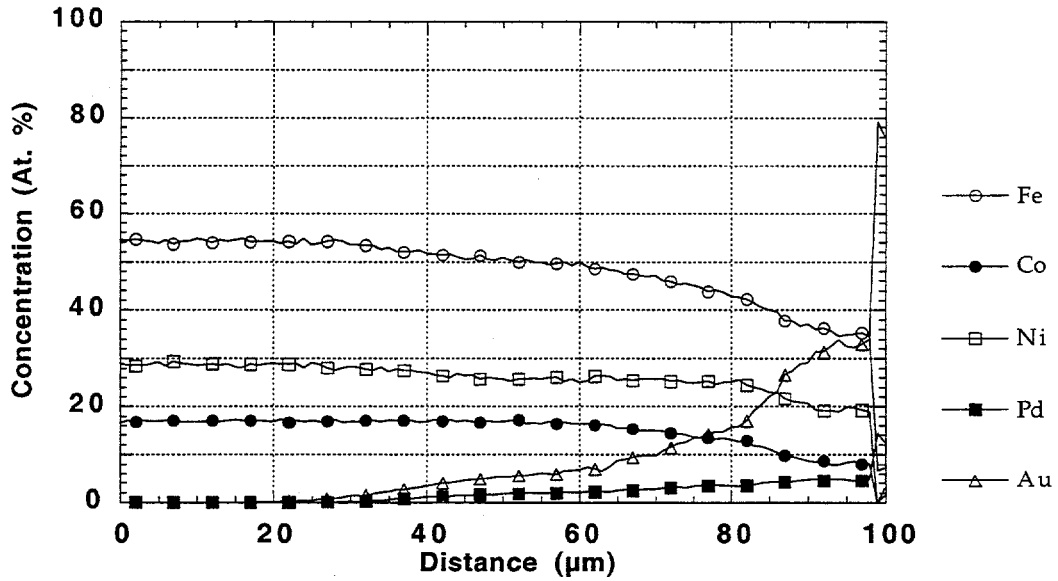

(b)

Fig. 13. (a) SEM (SE image) of the Kovar™ /92Au-8Pd wetting sample (Phase V, vacuum processing) in the as-fabricated condition. (b) EMPA trace (base metal: Co, Fe, and Ni; braze alloy: Au, Pd) across the near-surface region shown in (a). The trace in (b) is representative of ten traces that were made in that area.

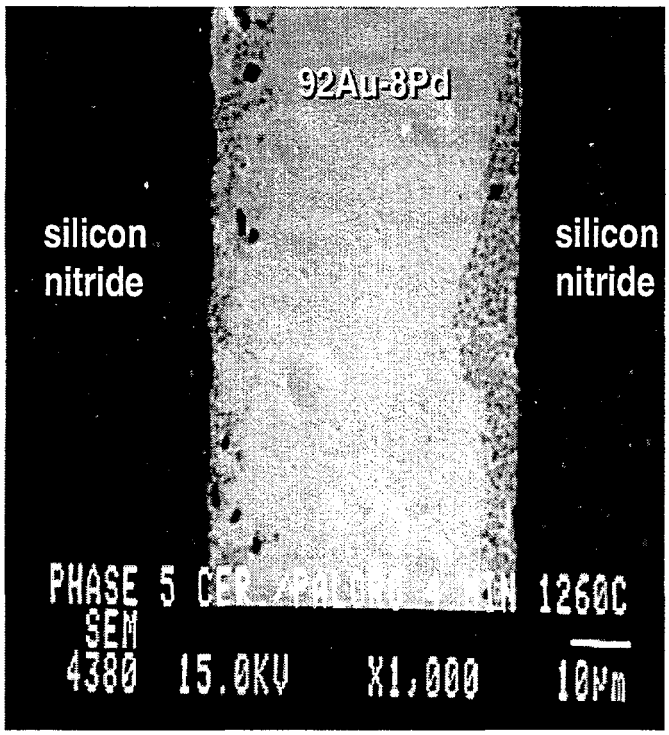

(a)

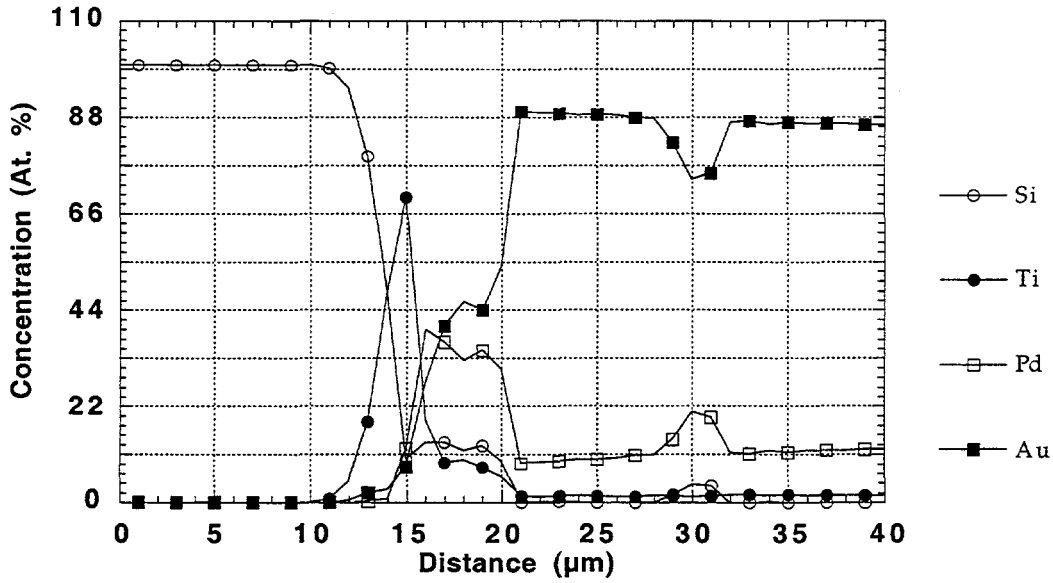

(b)

Fig. 14. (a) SEM (SE image) of the AS-800/92Au-8Pd four-point bend bar sample (1260°C, 4 min hold time, vacuum processing) in the as-fabricated condition. (b) EMPA trace (base metal: Si, and Ti; braze alloy: Au, Pd) across the near-surface region shown in (a). The trace in (b) is representative of ten traces that were made in that area.

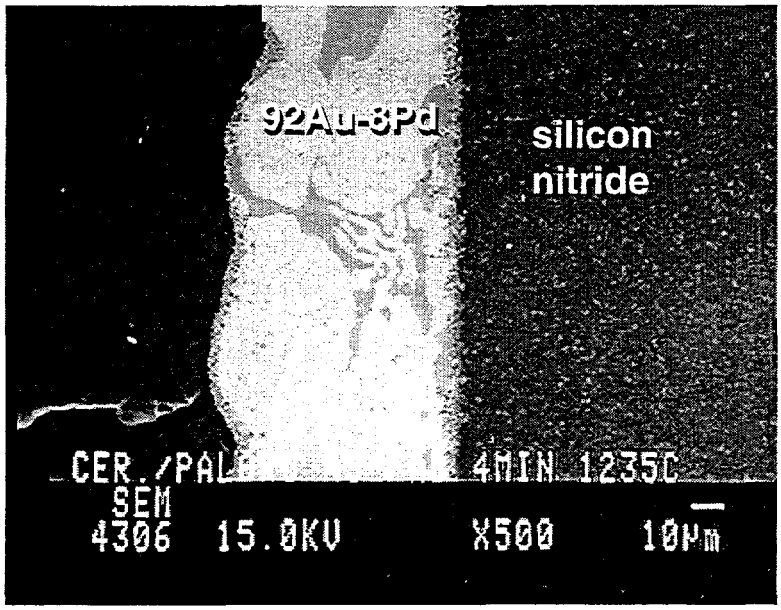

(a)

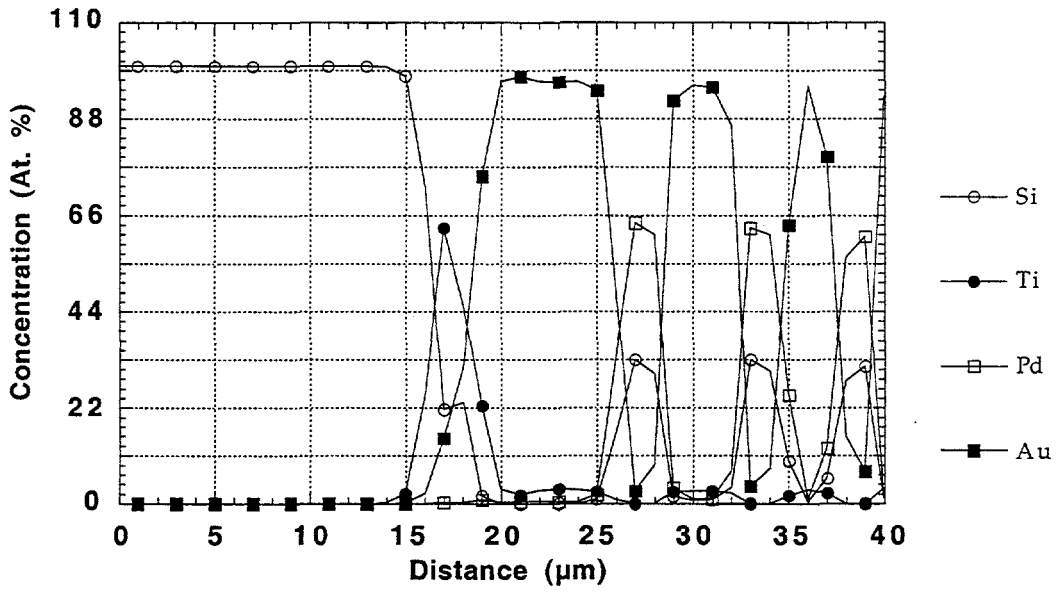

(b)

Fig. 15. (a) SEM (SE image) of the AS-800/92Au-8Pd wetting sample (1235°C, 4 min hold time, vacuum processing) in the as-fabricated condition. (b) EMPA trace (base metal: Si, and Ti; braze alloy: Au, Pd) across the near-surface region as illustrated in (a). The trace in (b) is representative of ten traces that were made in that area.

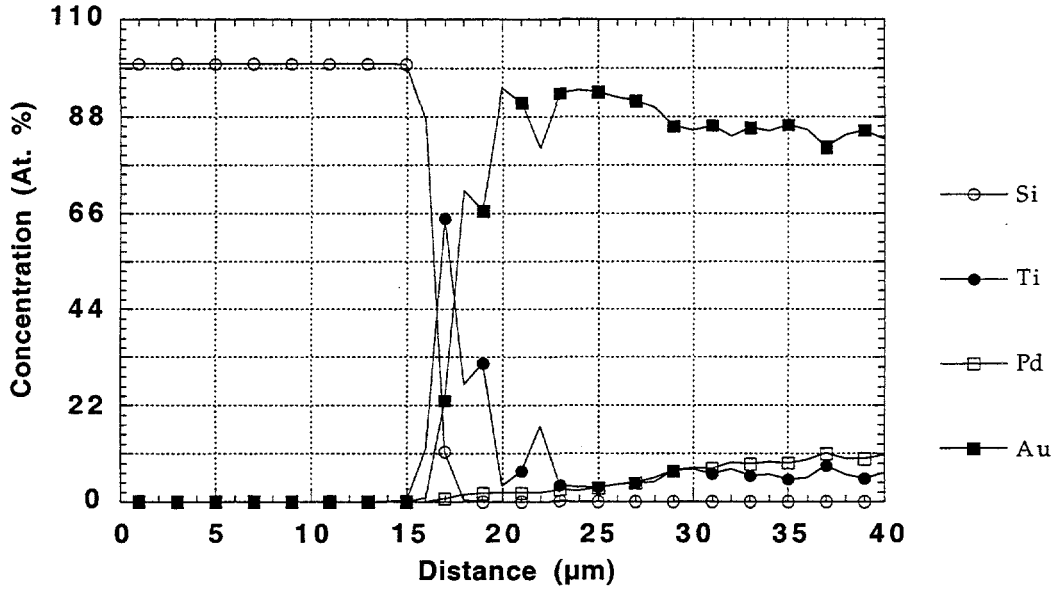

Fig. 16. EMPA trace of the AS-800/92Au-8Pd four-point bend bar sample (1215°C, 4 min hold time, vacuum processing) in the as-fabricated condition (base metal: Si, and Ti; braze alloy: Au, Pd). The trace is representative of ten traces that were made in that area.

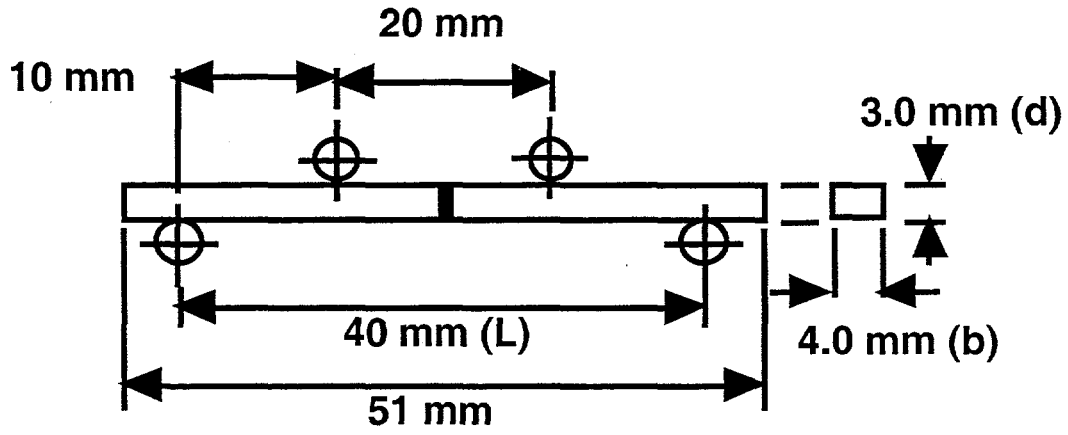

Fig. 17. Specimen geometry for the four-point bend experiment as per ASTM C1161-90, Specimen B.

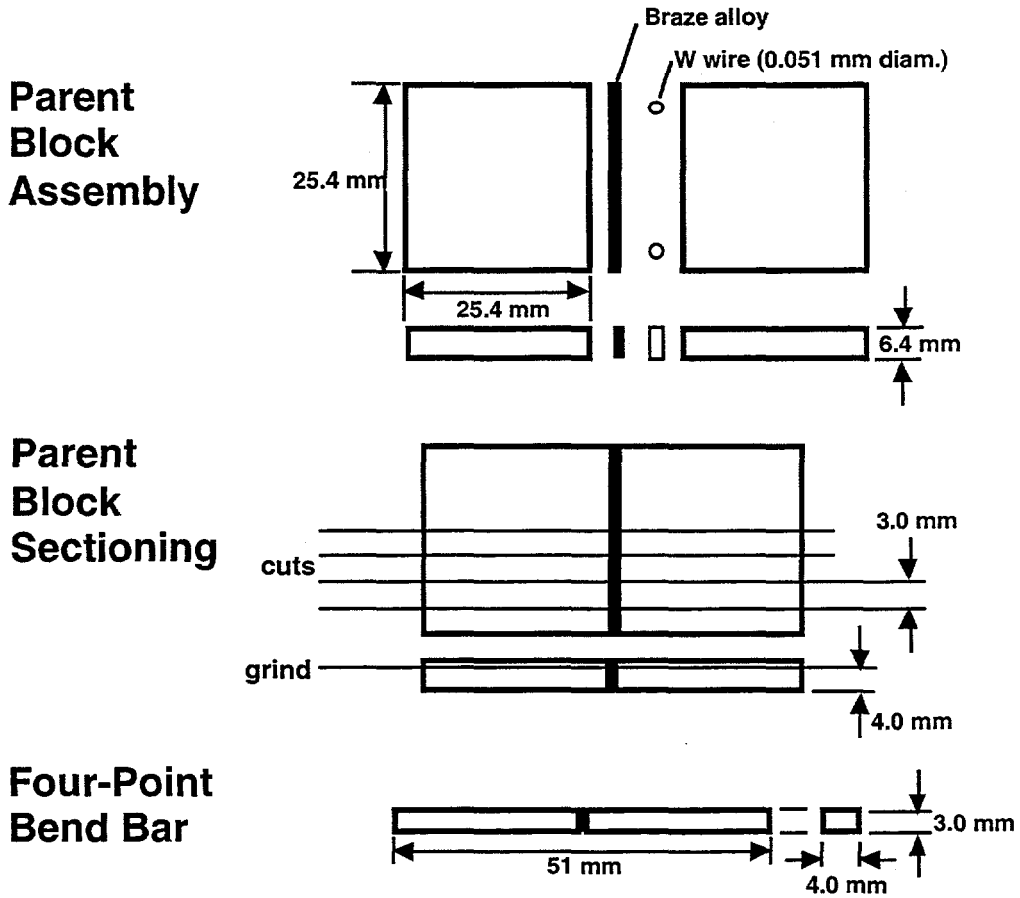

Fig. 18. Four-point bend test specimen fabrication from the parent block starting configuration. The braze alloy gap thickness was maintained at 51 μm by the placement of similar diameter, W wires within each of the gaps.

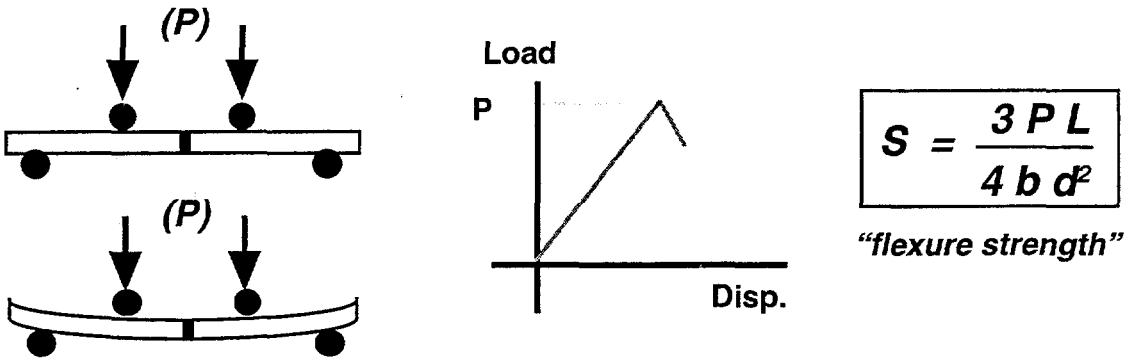

Fig. 19. Four-point bend testing procedure per ASTM C1161-90.

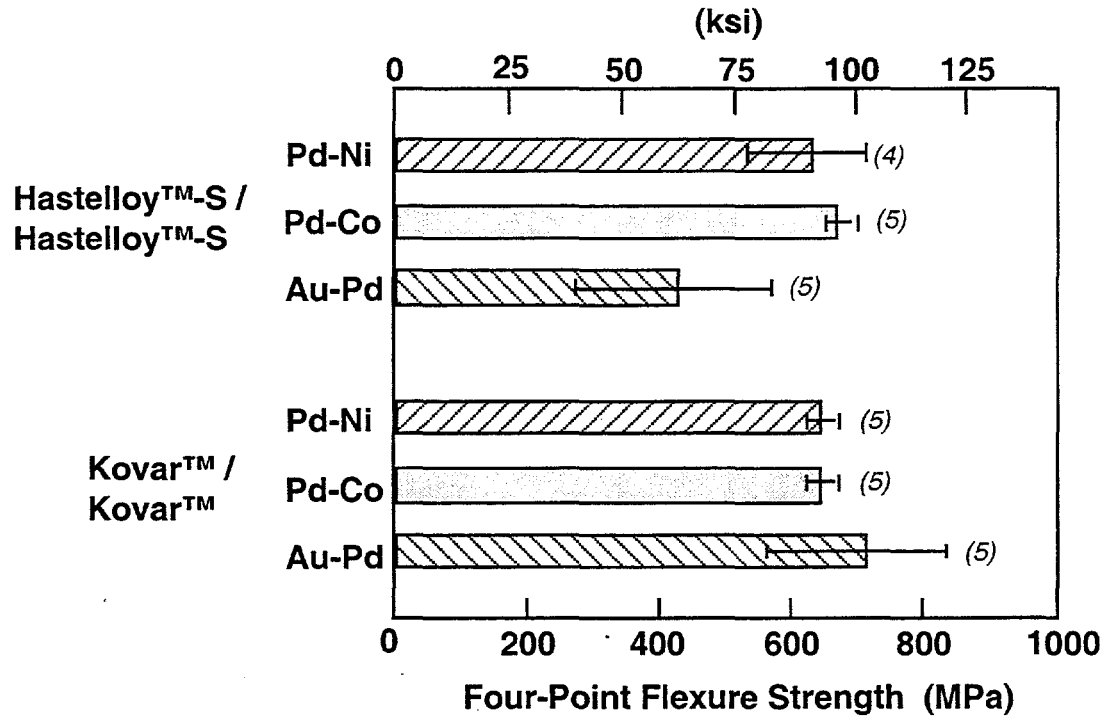

Fig. 20. Room temperature, four-point bend strengths of Hastelloy™-S / Hastelloy™-S couples and Kovar™ / Kovar™ joints using the 60Pd-40Ni, 65Pd-35Co, and 92Au-8Pd braze alloys, under the respective Phase V conditions, in vacuum. The number in parentheses is the number of tests.

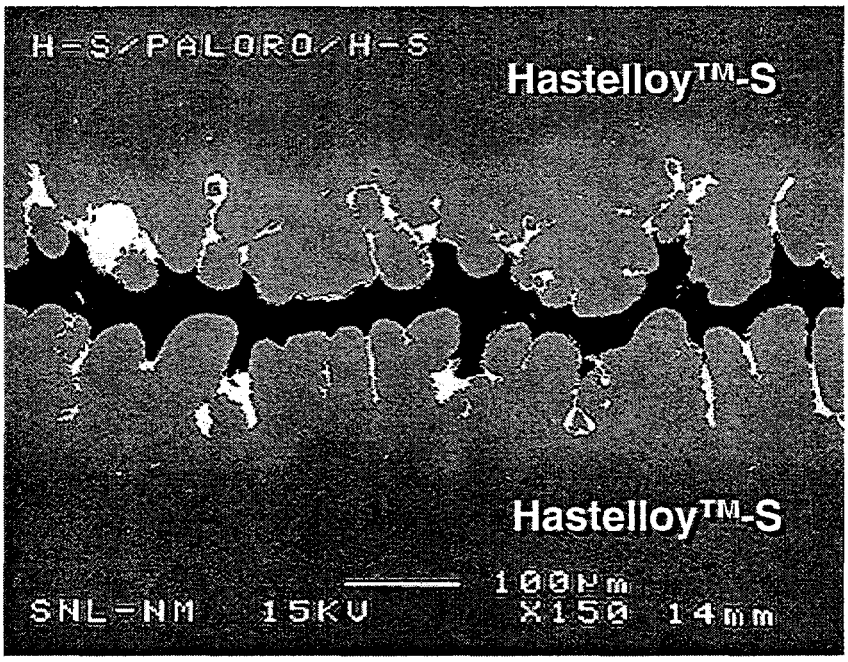

Fig. 21. SEM micrograph (BSE image) of the braze joint from a Hastelloy™-S/Hastelloy™-S four-point bend sample (Phase V, vacuum) made with the 92Au-8Pd filler metal. Gaps were intermittently observed in the braze joint.

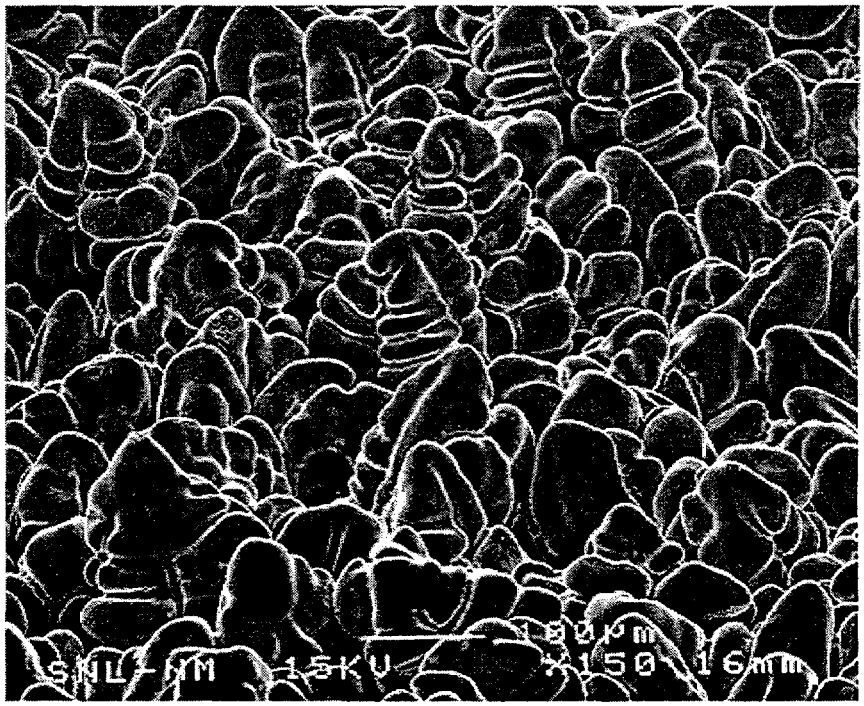

Fig. 22. SEM micrograph of the fracture surface from a Hastelloy™-S/Hastelloy™-S four-point bend sample (Phase V, vacuum) made with the 92Au-8Pd filler metal. The region exemplifies base metal dissolution.

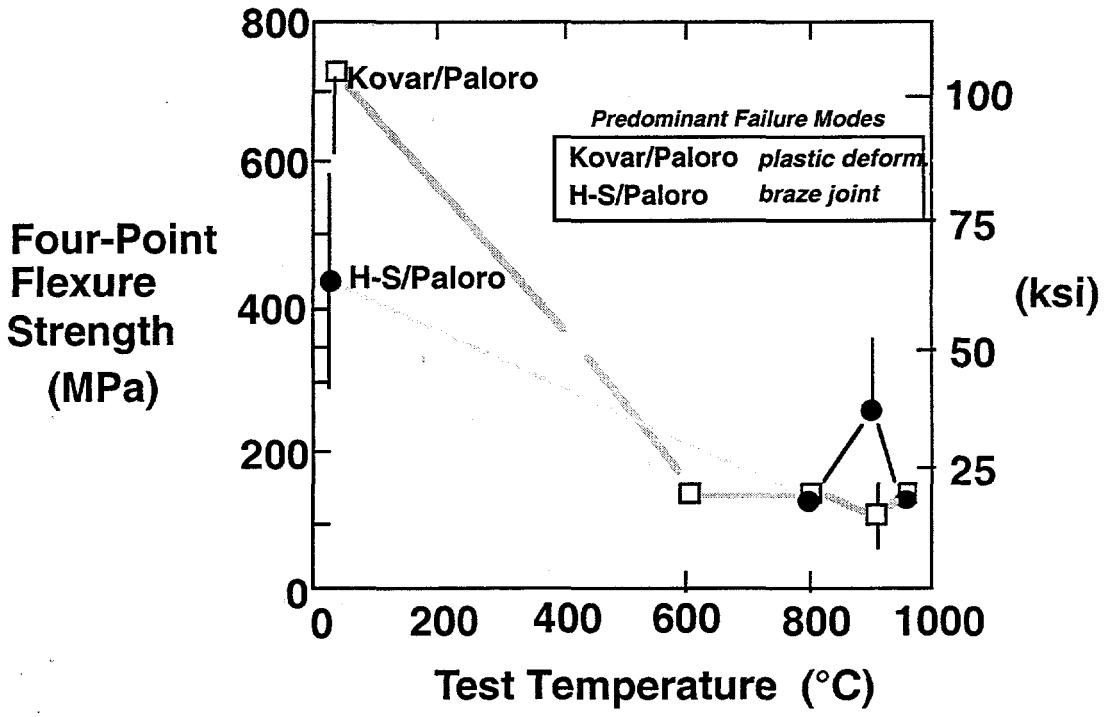

Fig. 23. Four-point flexure strength as a function of test temperature for the Kovar™/Kovar™ and Hastelloy™-S/Hastelloy™-S couples.

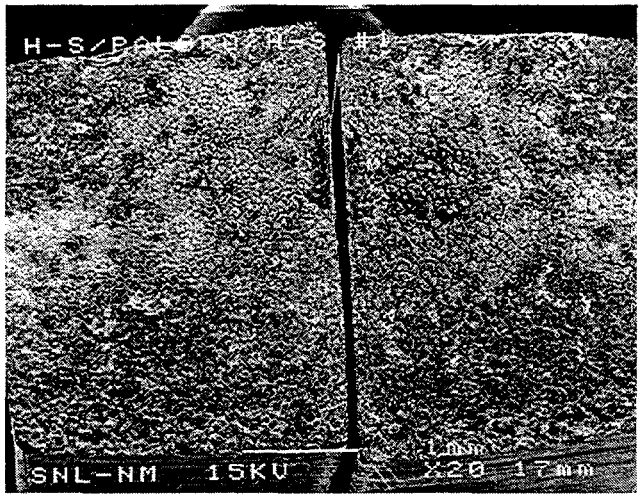

(a)

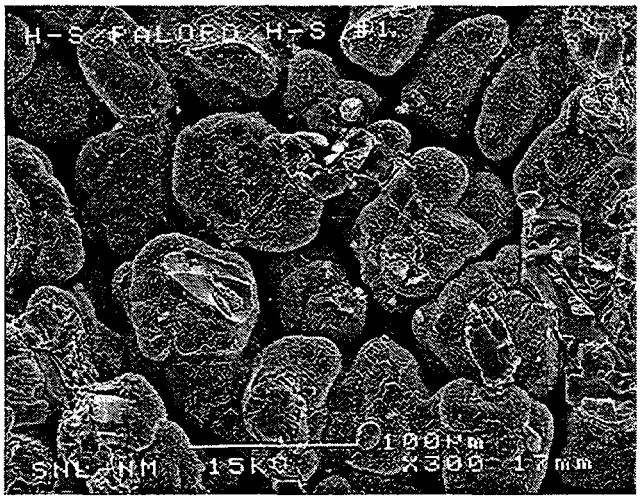

(b)

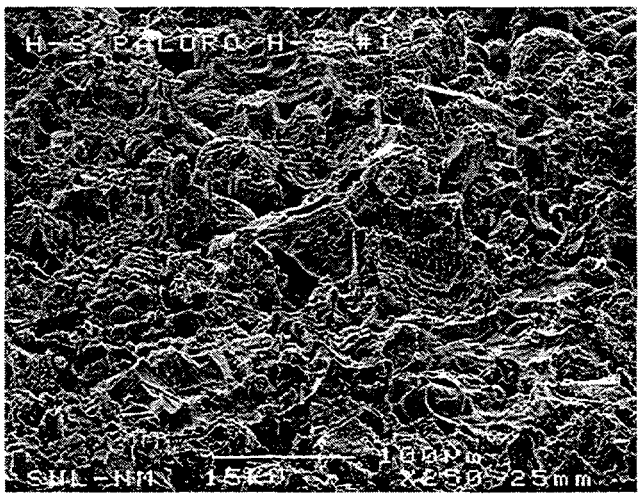

(c)

Fig. 24. (a) SEM micrograph of the fracture surfaces of a Hastelloy™-S/Hastelloy™-S couple brazed with the 92Au-8Pd alloy and tested at 950°C. Two morphologies were identified and are shown in the SEM micrographs in (b) and (c).

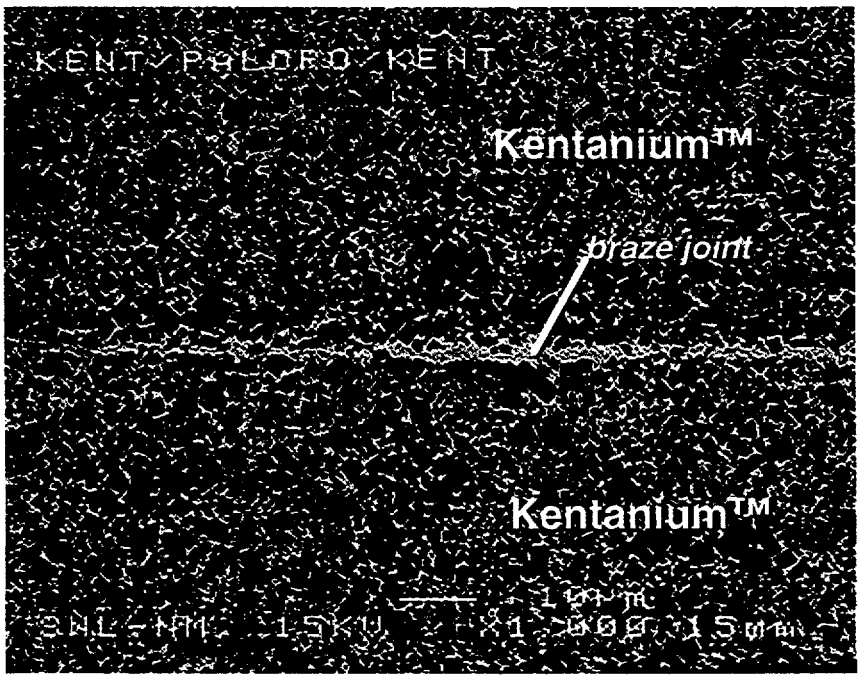

(a)

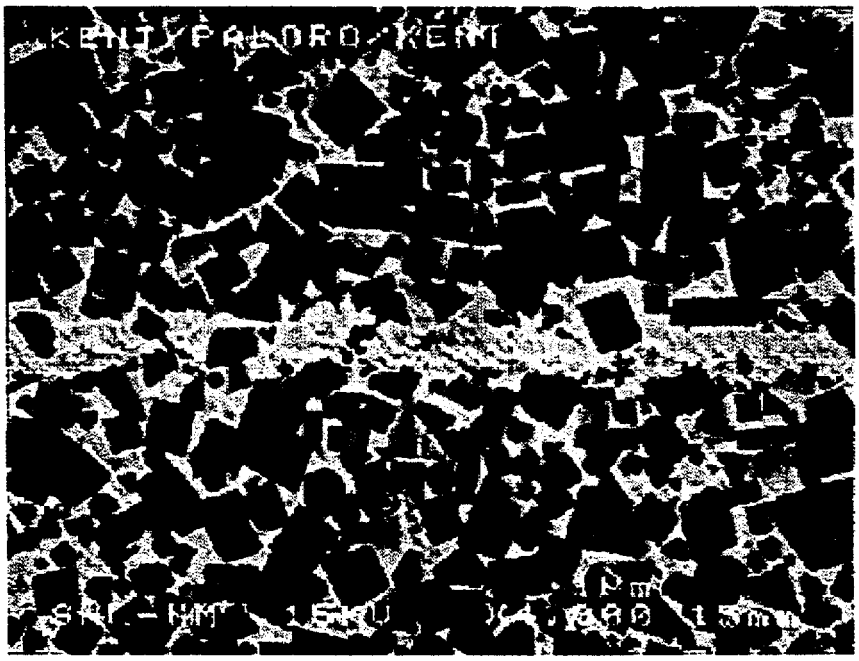

(b)

Fig. 25. SEM micrographs of the cross sectional view through the Au-Pd braze joint of a Kentanium™/Kentanium™ couple (untested) following fabrication under Phase V furnace cycle and vacuum conditions: (a) low magnification and (b) high magnification.

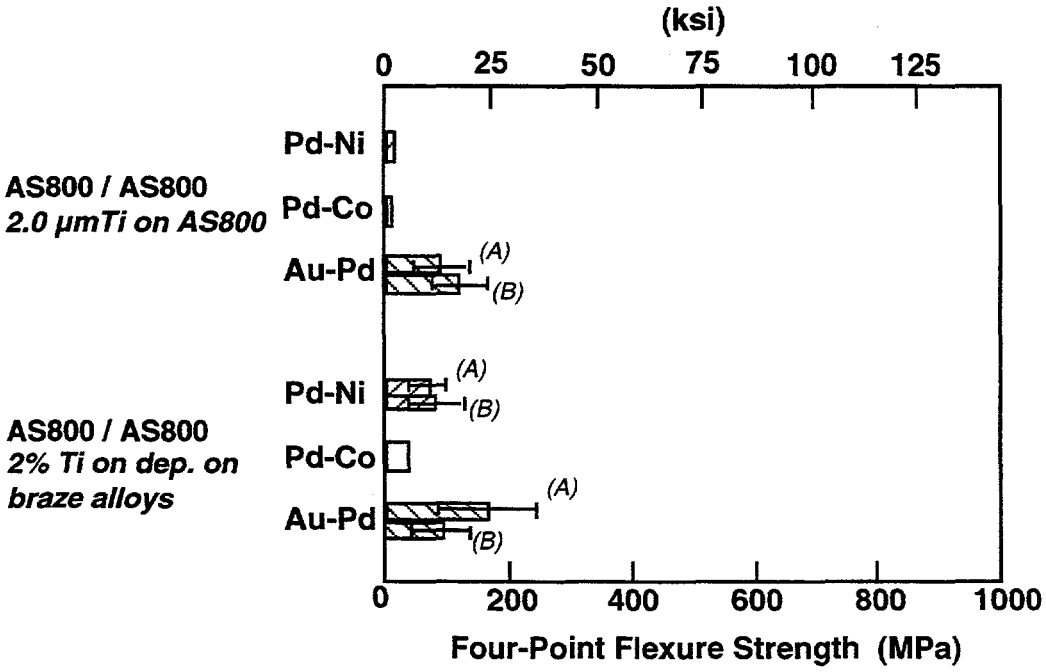

Fig. 26. Four-point bend strengths of AS-800/AS-800 silicon nitride joints fabricated with each of the three filler metals under conditions of (1) 2.0 μm Ti on the silicon nitride, Phase V, vacuum for the Au-Pd and Phase III, Ar for the Pd-Ni and Pd-Co alloys and (2) deposition of 2 wt.% Ti on the filler metal foils, using Phase III, Ar furnace conditions.

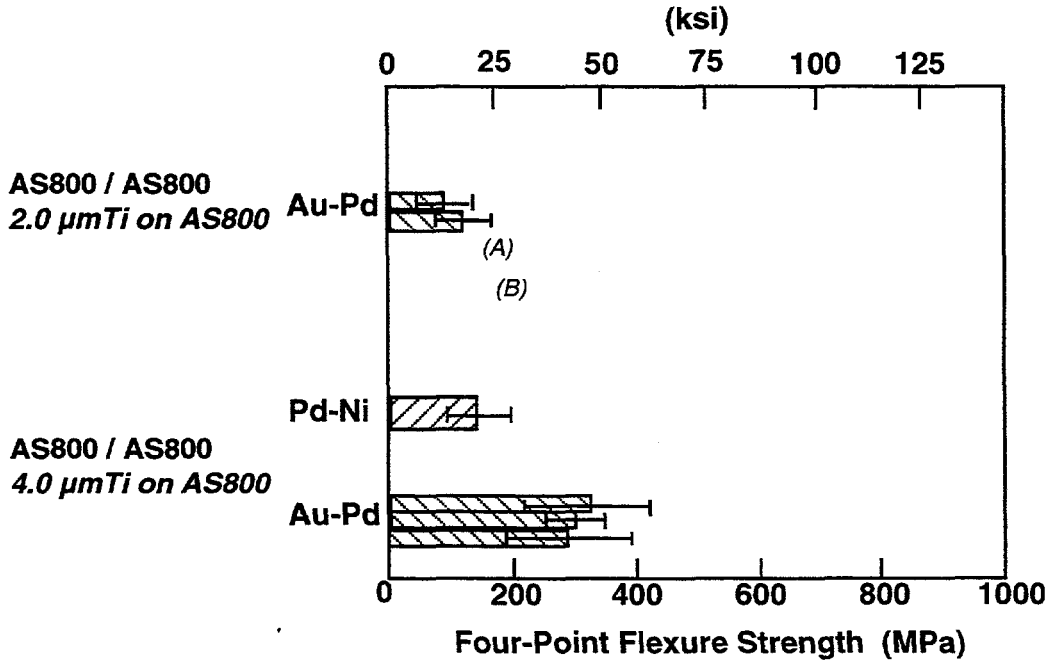

Fig. 27. Four-point bend strengths of AS-800/AS-800 silicon nitride joints fabricated with Au-Pd filler metal under conditions of 2.0 μm Ti and 4.0 μm Ti on the silicon nitride, using Phase V, vacuum conditions. Also included are the strength data for the Pd-Ni alloy with 4.0 μm Ti on the AS-800 silicon nitride, using the Phase V, vacuum conditions.

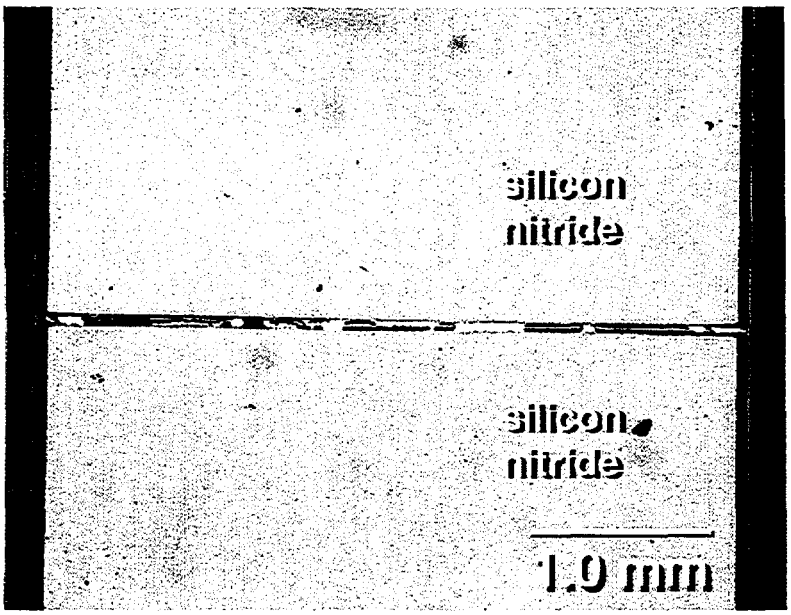

(a)

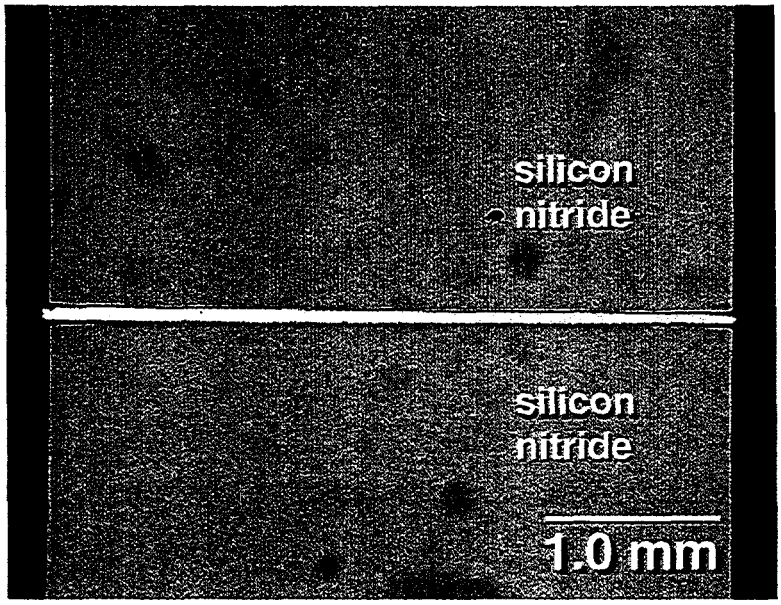

(b)

Fig. 28. Optical micrographs of the cross sections of untested, Au-Pd braze joints between AS-800 base materials with (a) 2.0 μm Ti coating and (b) the 4.0 μm Ti coating. Both samples were processed under Phase V, vacuum conditions.

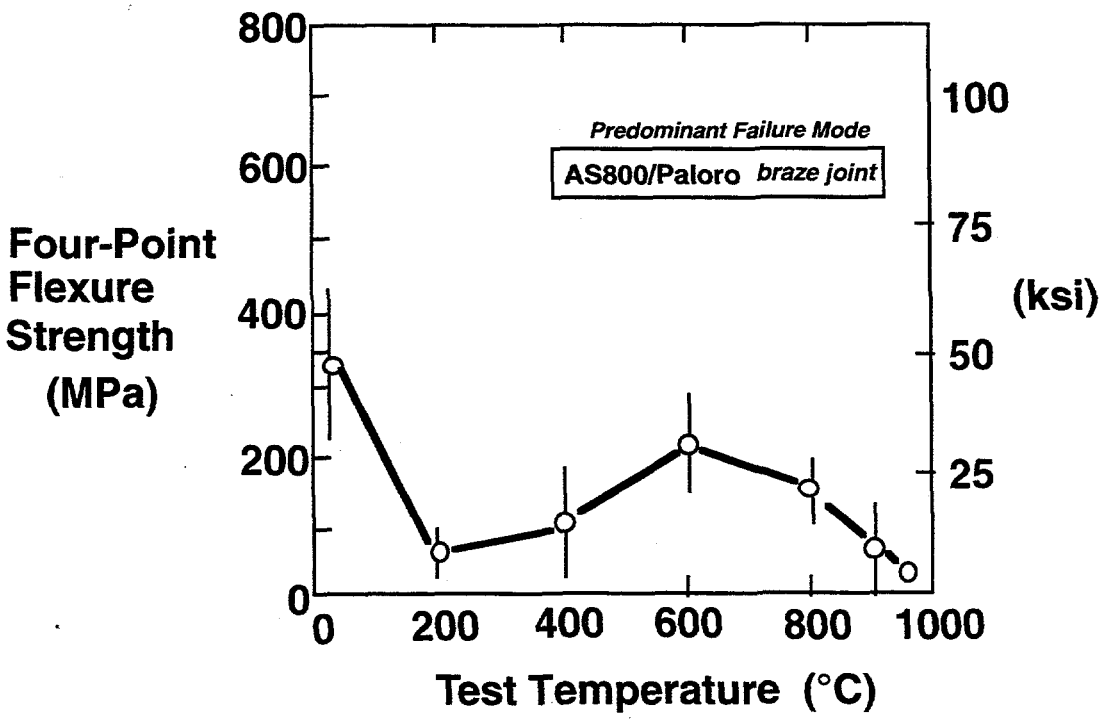

Fig. 29. Four-point bend strength of AS-800 (4.0 μm Ti) / AS-800 (4.0 μm Ti) braze joints tested at elevated temperatures.

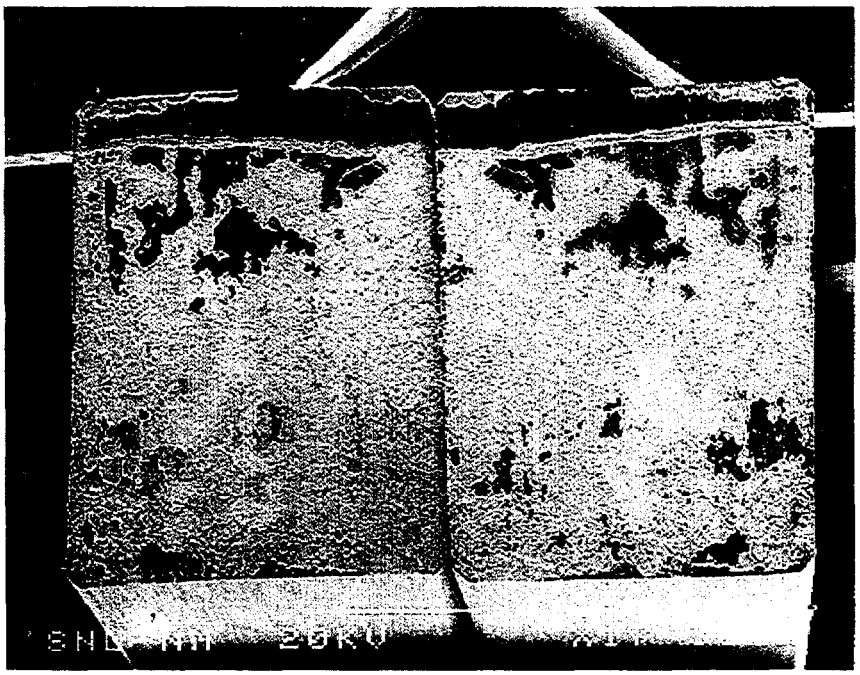

(a)

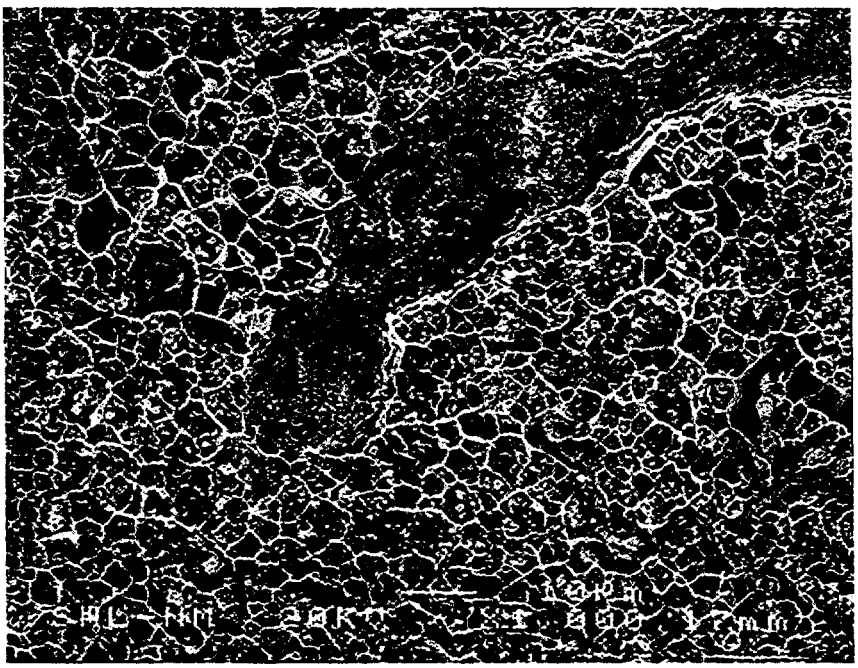

(b)

Fig. 30. Low magnification (a) and high magnification (b) SEM micrographs of an AS-800/Au-Pd/AS-800 four point bend sample after testing at 600°C. The surfaces are covered with regions of microvoid coalescence and plastic deformation within the braze alloy.

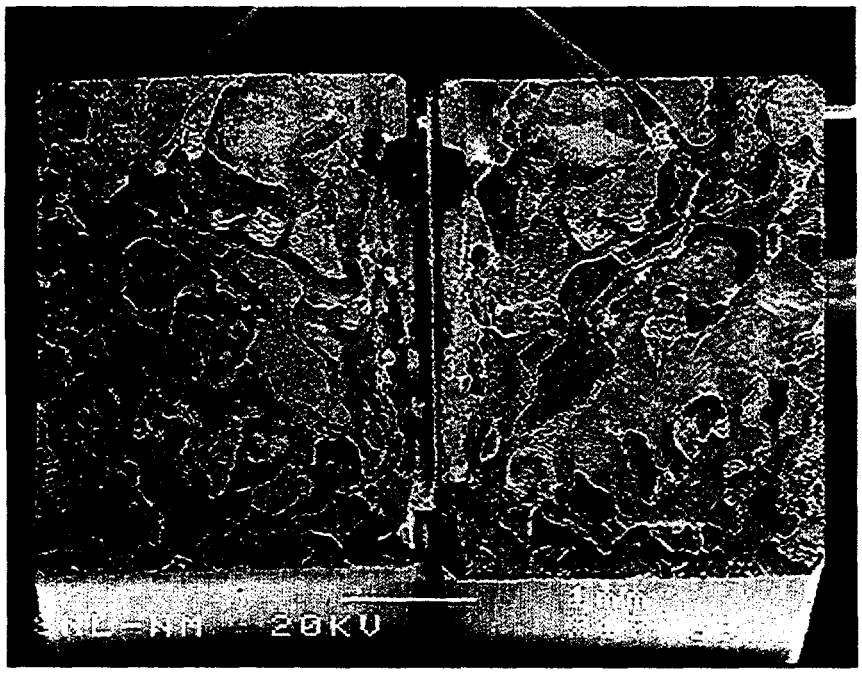

(a)

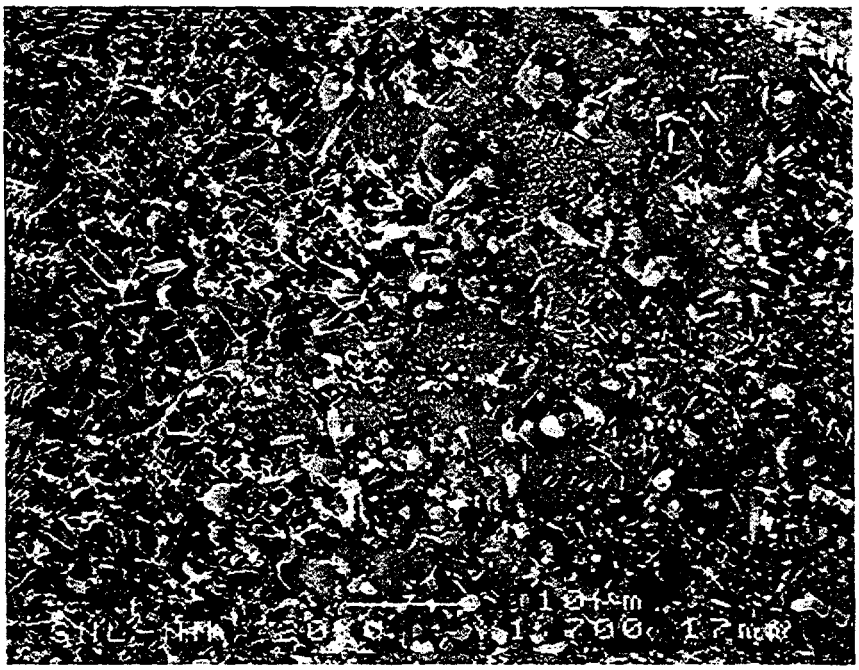

(b)

Fig. 31. Low magnification (a) and high magnification (b) SEM micrographs of an AS-800/Au-Pd/AS-800 four point bend sample after testing at 950°C. The fracture path exhibited no preference for either side of the gap, jumping between the two sides, resulting in the general morphology seen in a).

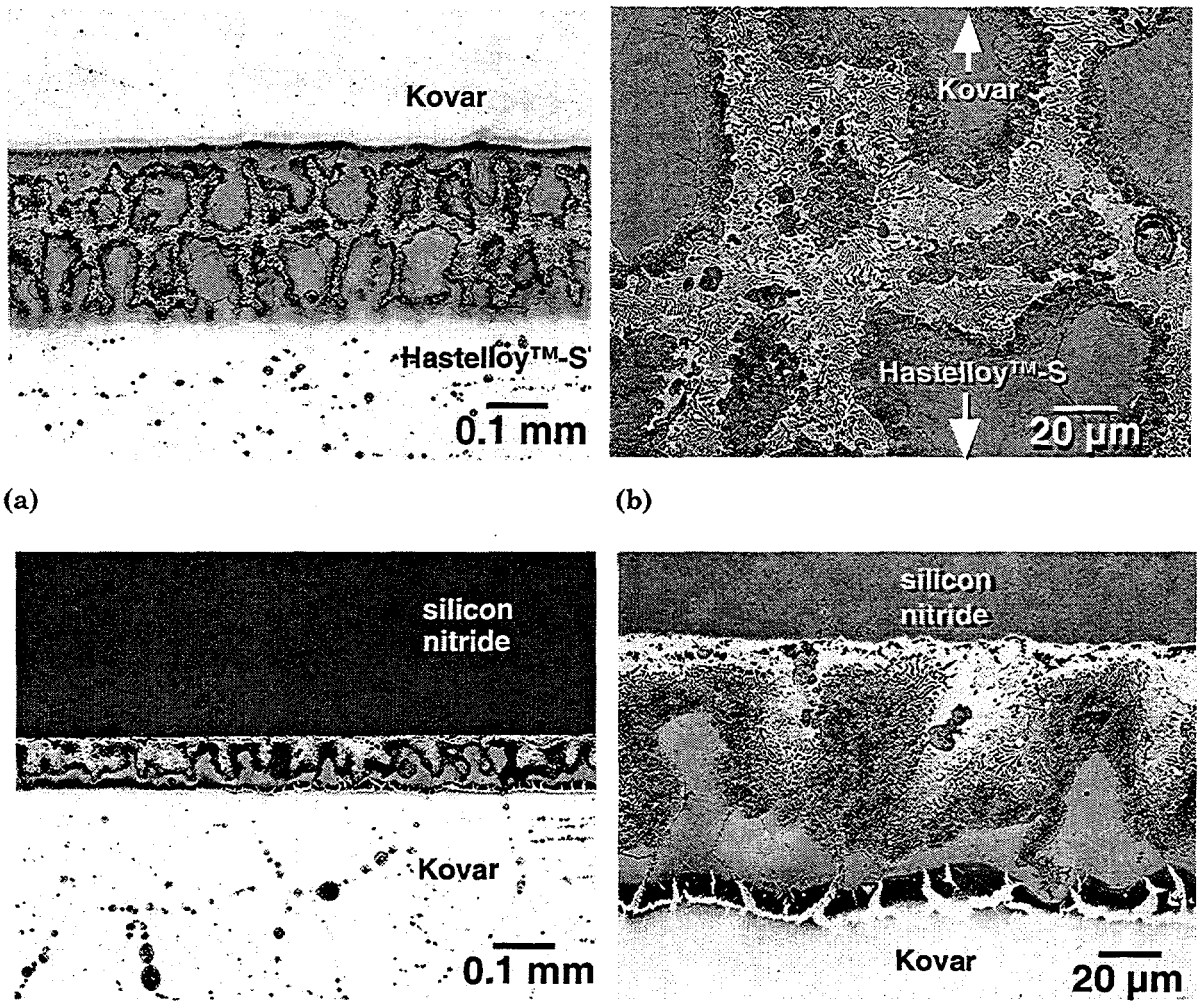

Fig. 32. Optical micrographs (etched to reveal the interlayer features) of the Hastelloy™-S/Kovar™/silicon nitride joint made with the Au-Pd braze alloy, 3.18 mm thick Kovar™ interlayer, and the modified Phase V furnace cycle: (a) Hastelloy™-S/Kovar™ joint, low magnification; (b) Hastelloy™-S/Kovar™ joint, high magnification; (c) Kovar™/AS-800 joint, low magnification; and (d) Kovar™/AS-800 joint, high magnification.

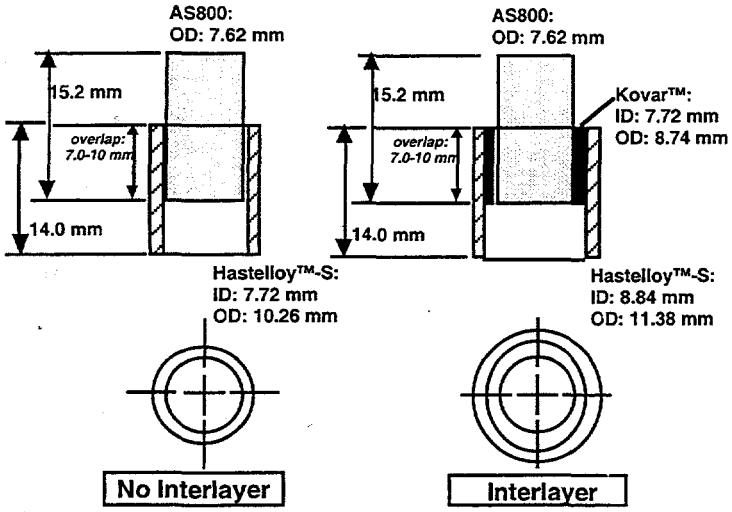

Fig. 33. Dimensions of the two versions of the Hastelloy™-S sleeve, the Kovar™ interlayer (the Kentanium™ material was not used in this study), and the AS-800 silicon nitride plug.

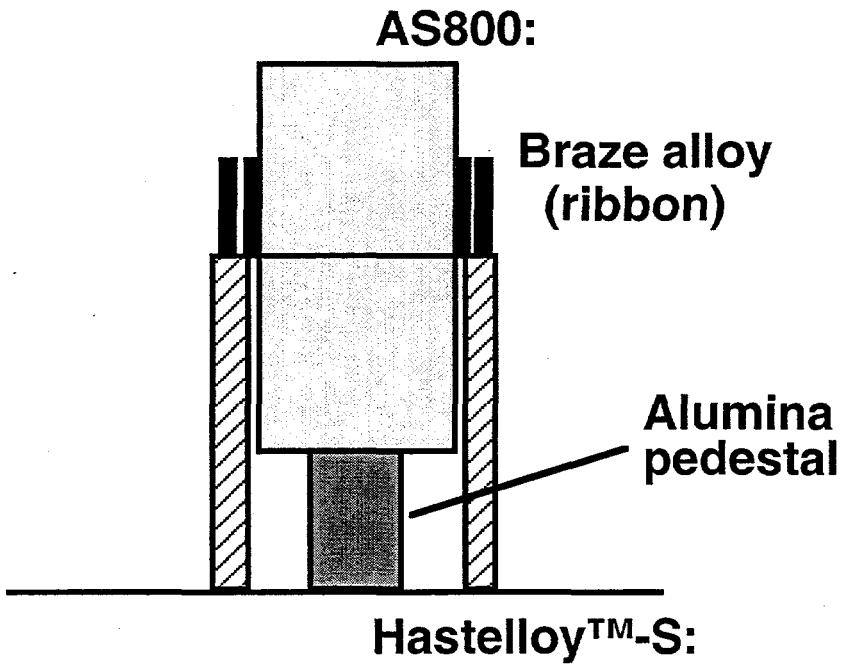

Fig. 34. Schematic diagram of the set-up of the Hastelloy™-S/AS-800 silicon nitride plug-in-ring cylinder assembly for brazing.

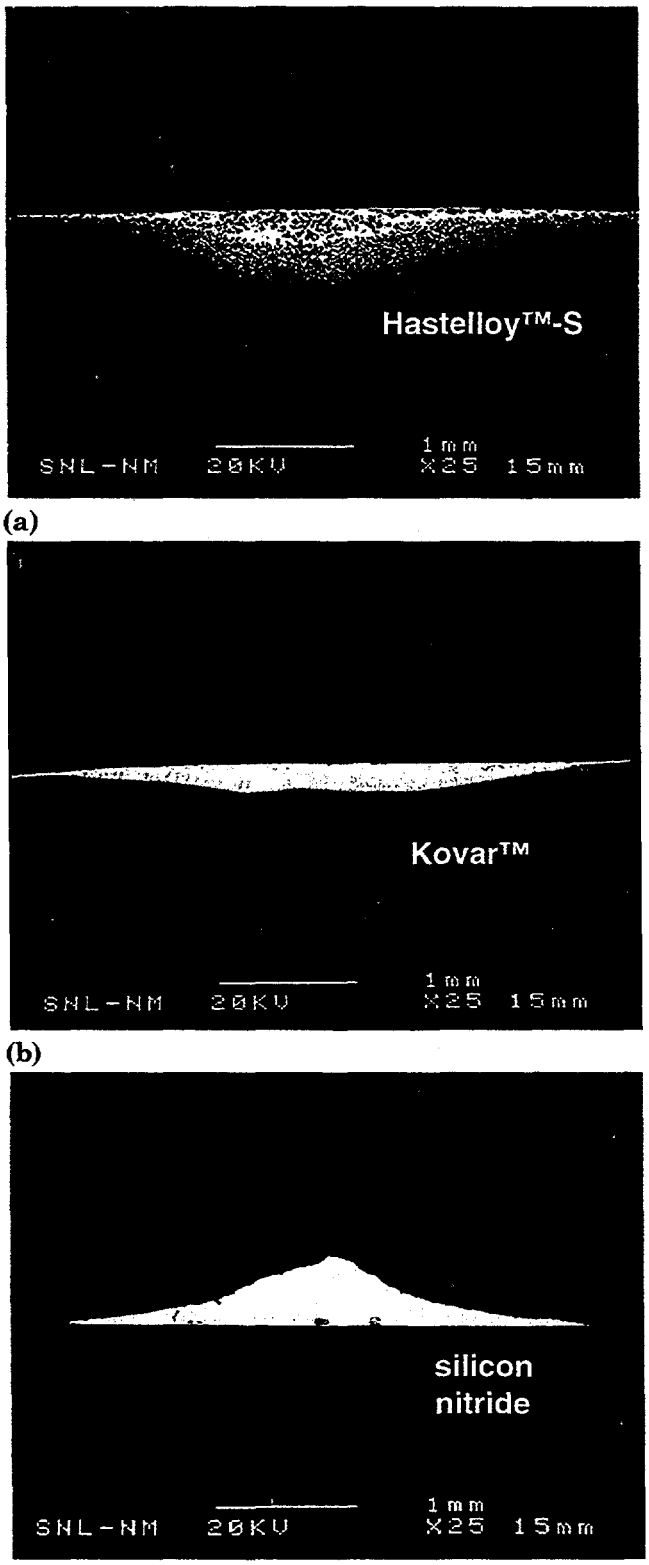

Fig. 35. SEM micrographs of the wetting samples of (a) Hastelloy™-S, (b) Kovar™, and (c) AS-800 silicon nitride (4.0 μm Ti) with Au-Pd, using the Phase V furnace cycle with a brazing condition of 1200°C, 4 min in vacuum.

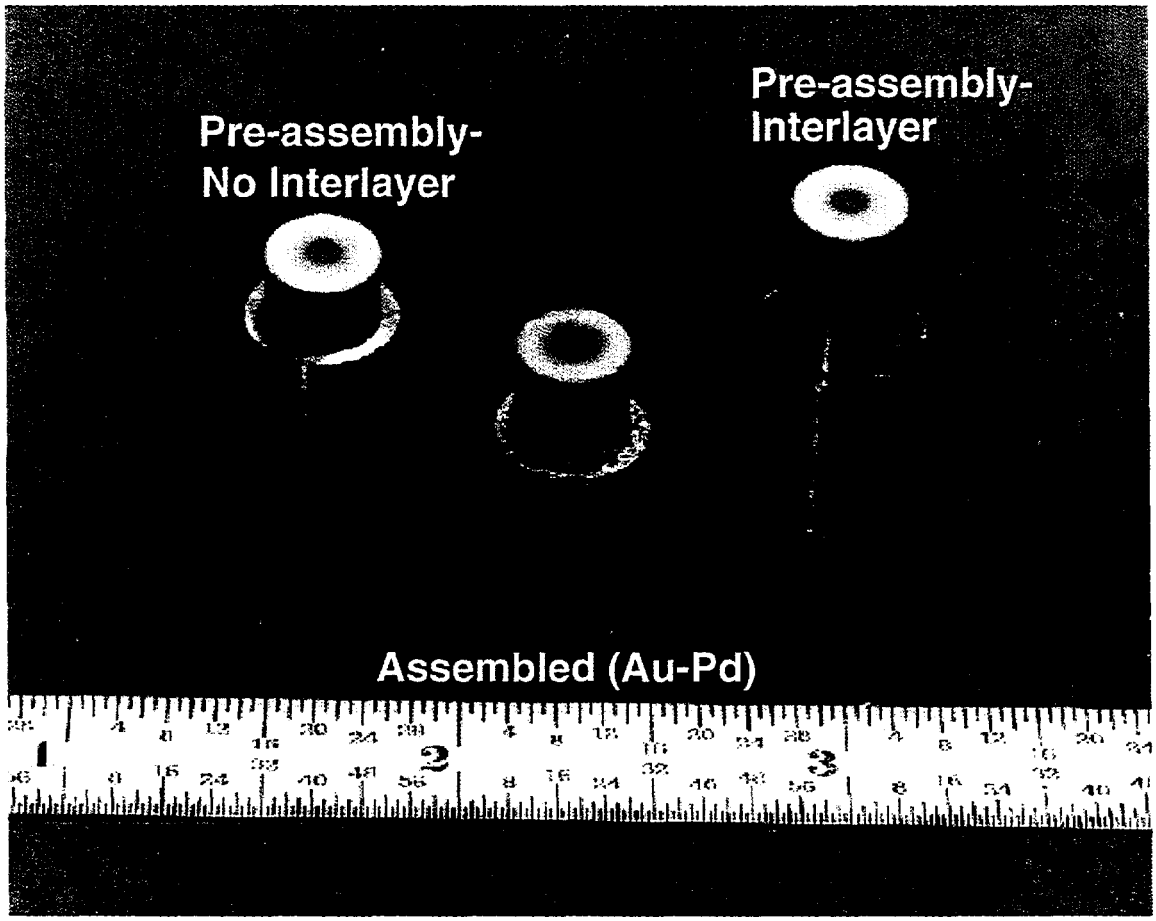

Fig. 36. Ring-in-plug test geometry: specimen set-ups both with and without the interlayer as well as a completed specimen (center).

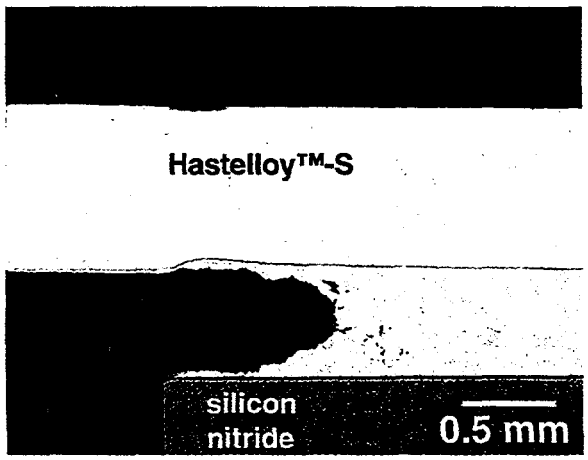

(a)

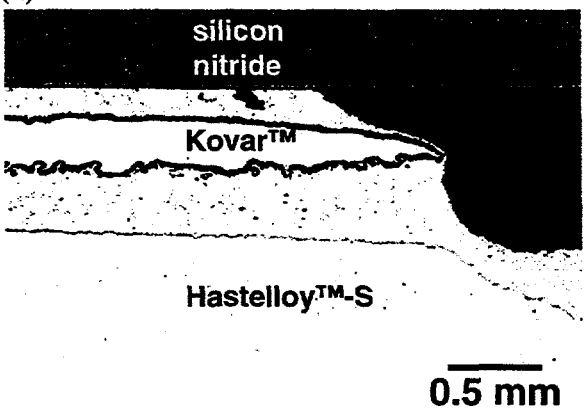

(b)

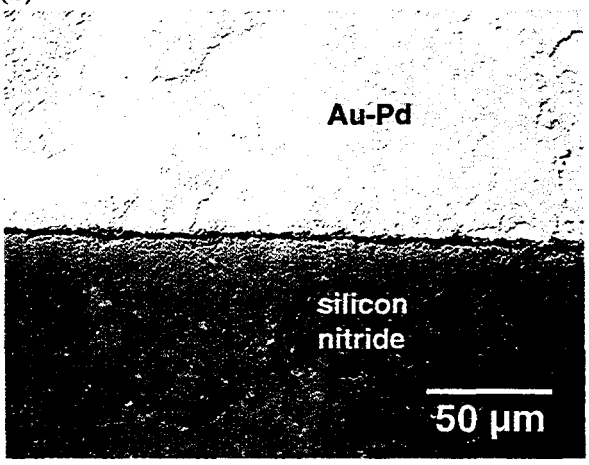

(c)

Fig. 37. Optical micrographs of the cross section of a plug-in-ring specimen (having the Kovar™ interlayer) that was processed at 1175°C for 4 min. The view in Fig. 37(a) is that of Hastelloy™-S sleeve and the silicon nitride; the start of the Kovar™ interlayer is just out of view. (b) View showing the eroded Kovar™ interlayer. (c) Braze alloy/AS-800 silicon nitride interface showing excellent wetting.

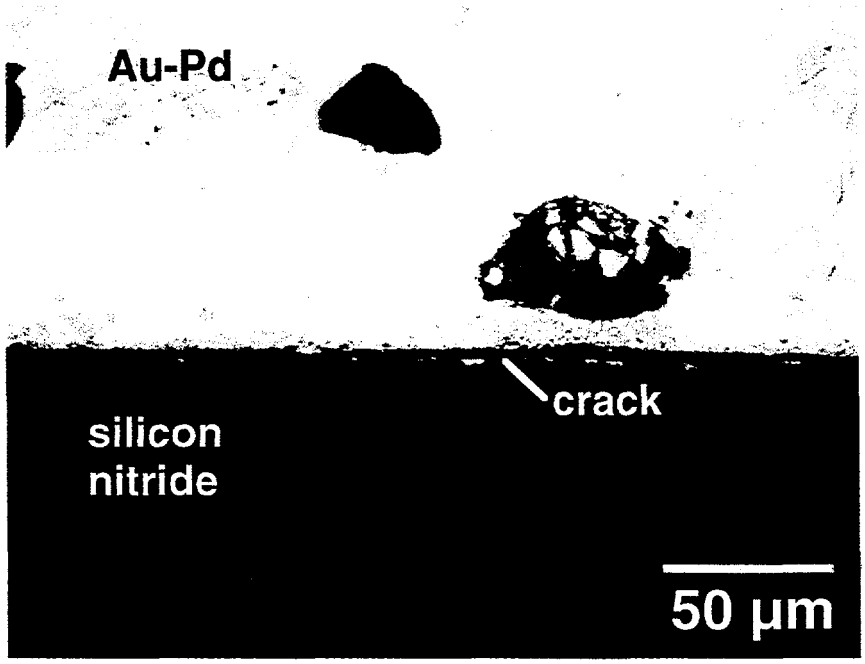

Fig. 38. Optical micrograph of the Hastelloy™-S/silicon nitride plug-in-ring braze joint fabricated at 1175°C for 4 min in vacuum after mechanical testing.

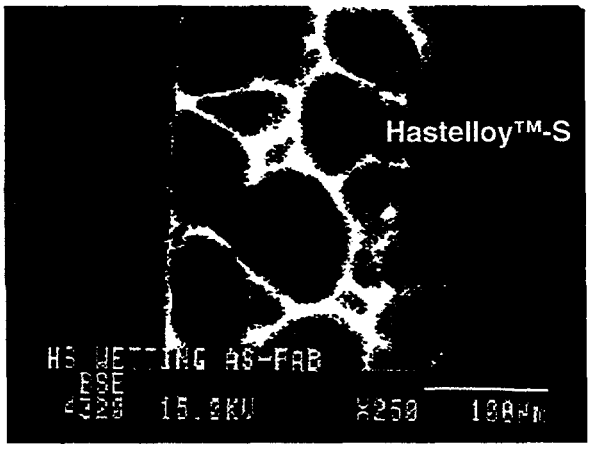

(a)

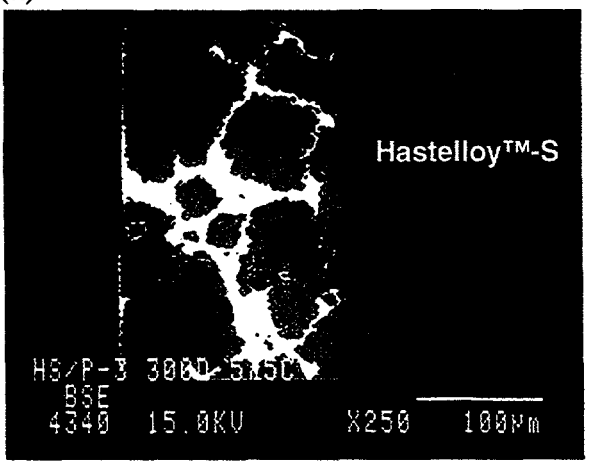

(b)

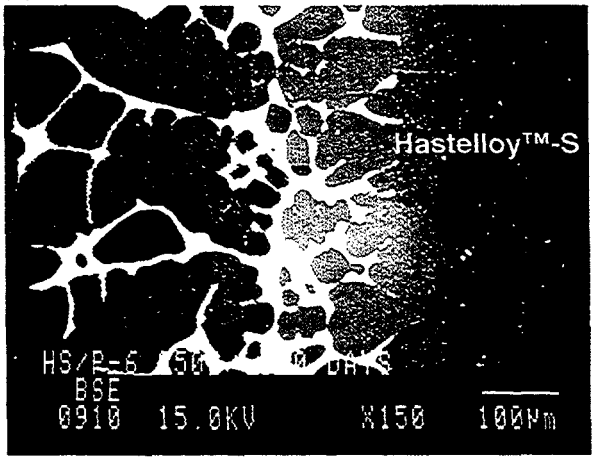

(c)

Fig. 39. SEM micrographs (BSE image) of the near-surface region of Hastelloy™-S/Au-Pd aging specimens in (a) the as-fabricated condition, (b) 575°C, 300 days, and (c) 950°C, 300 days.

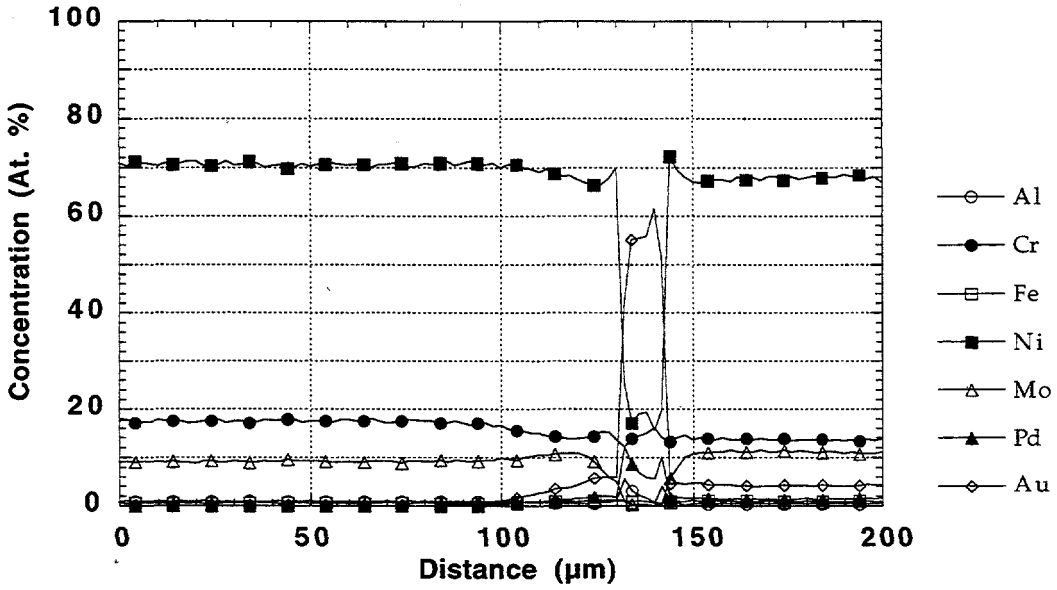

Fig. 40. Representative electron microprobe (EMPA) trace across the reaction zone between the 92Au-8Pd braze alloy and the Hastelloy™-S sample aged at 575°C for 300 days.

(a)

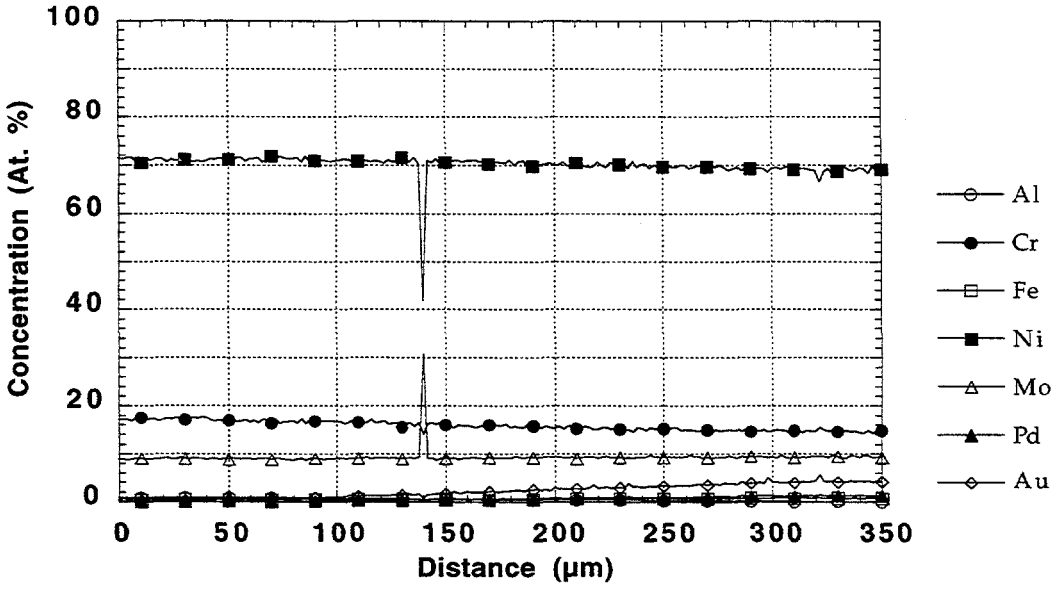

(b)

Fig. 41. (a) SEM (BSE image) micrograph of the bulk Hastelloy™-S sample after aging at 950°C for 300 days, showing the formation of a grain boundary phase (bright features). (b) Electron microprobe trace across the aged Hastelloy™-S sample show the grain boundary particles are comprised of Ni, Cr, and Mo, but at different levels than the grains.

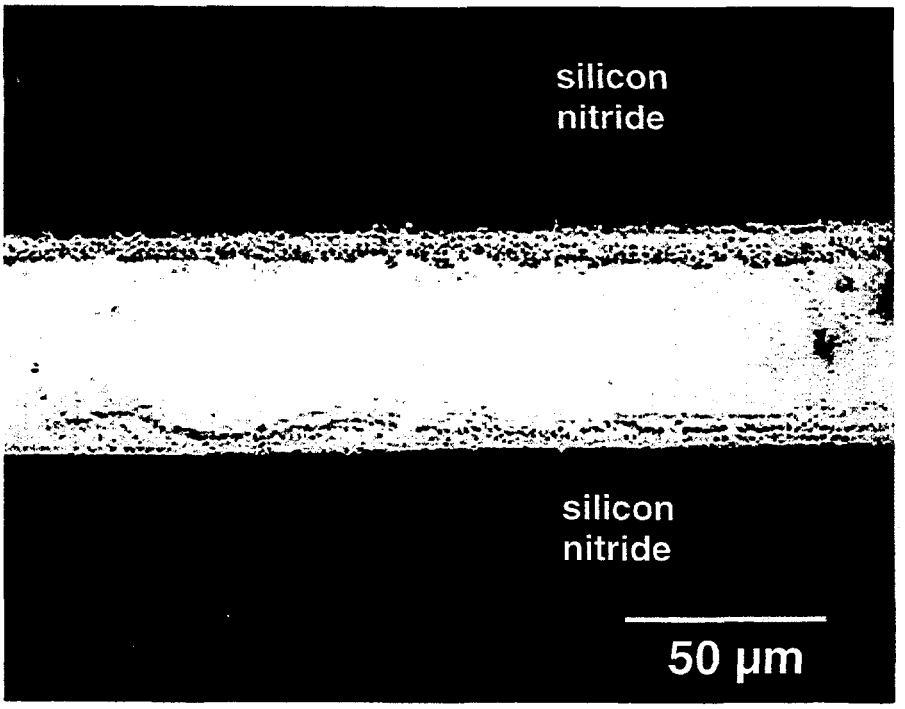

Fig. 42. Optical micrograph of a cross section of an AS-800/AS-800 braze joint following aging at 950°C for 200 days.

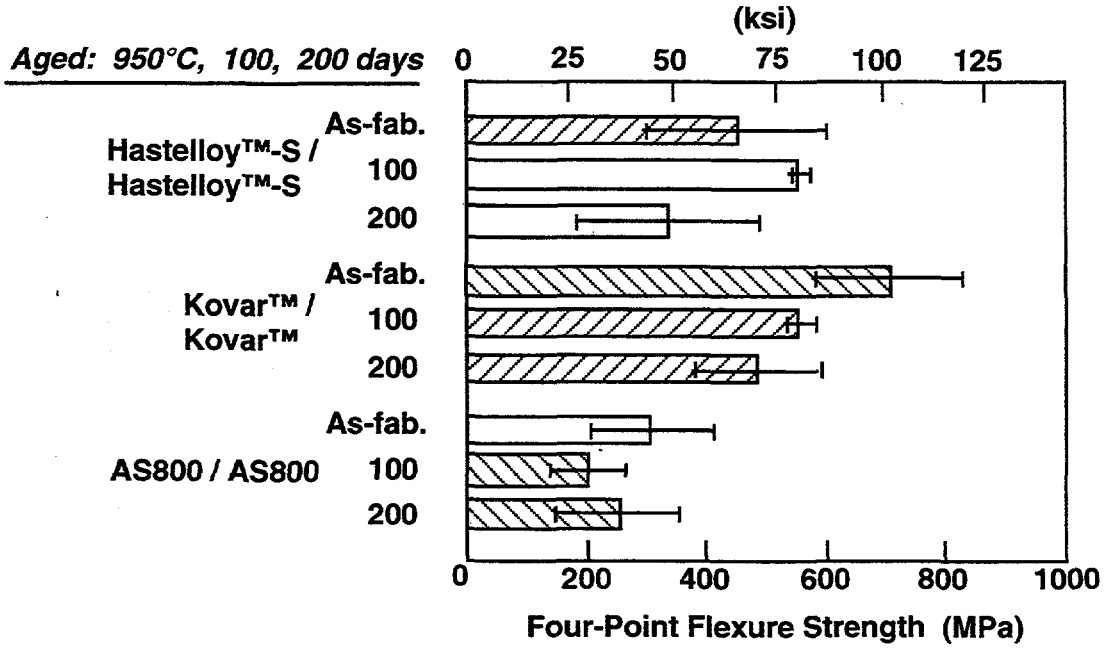

Fig. 43. Four-point bend data for as-fabricated samples and specimens that were aged at 950°C for 100 and 200 days. The materials systems were: Hastelloy™-S/Hastelloy™-S, Kovar™/Kovar™, and AS-800/AS-800 brazed with Au-Pd under the Phase V process in vacuum.

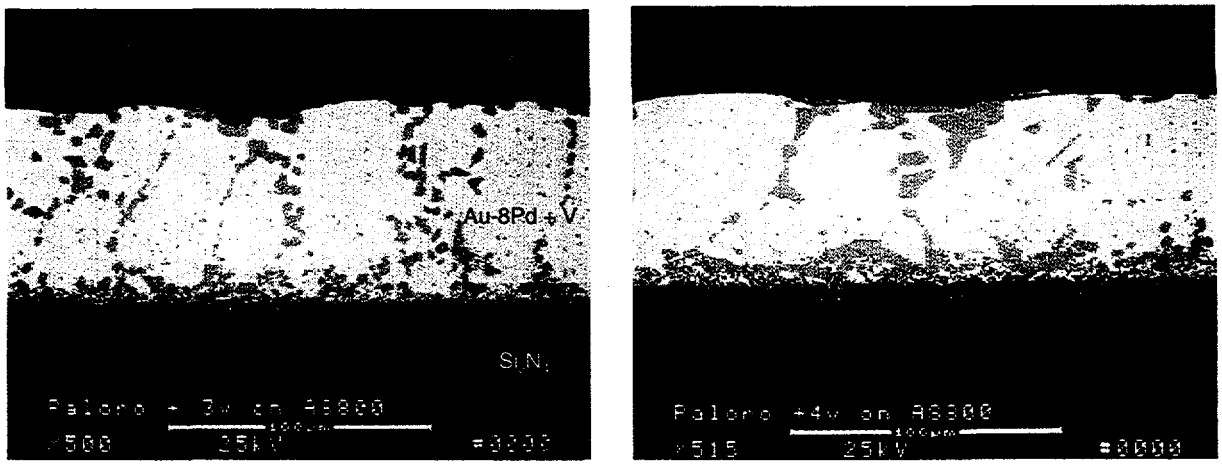

(a) (b)

Fig. 44. SEM images of (a) Au-8Pd-3V and (b) Au-8Pd-4V on AS-800 Si_3N_4.

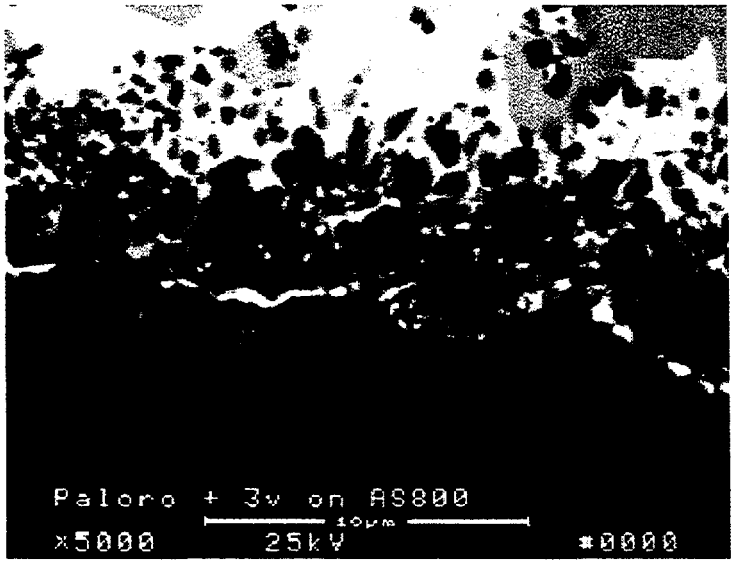

Fig. 45. SEM image of the Au-8Pd-3V alloy and AS-800 Si_3N_4 braze interface.

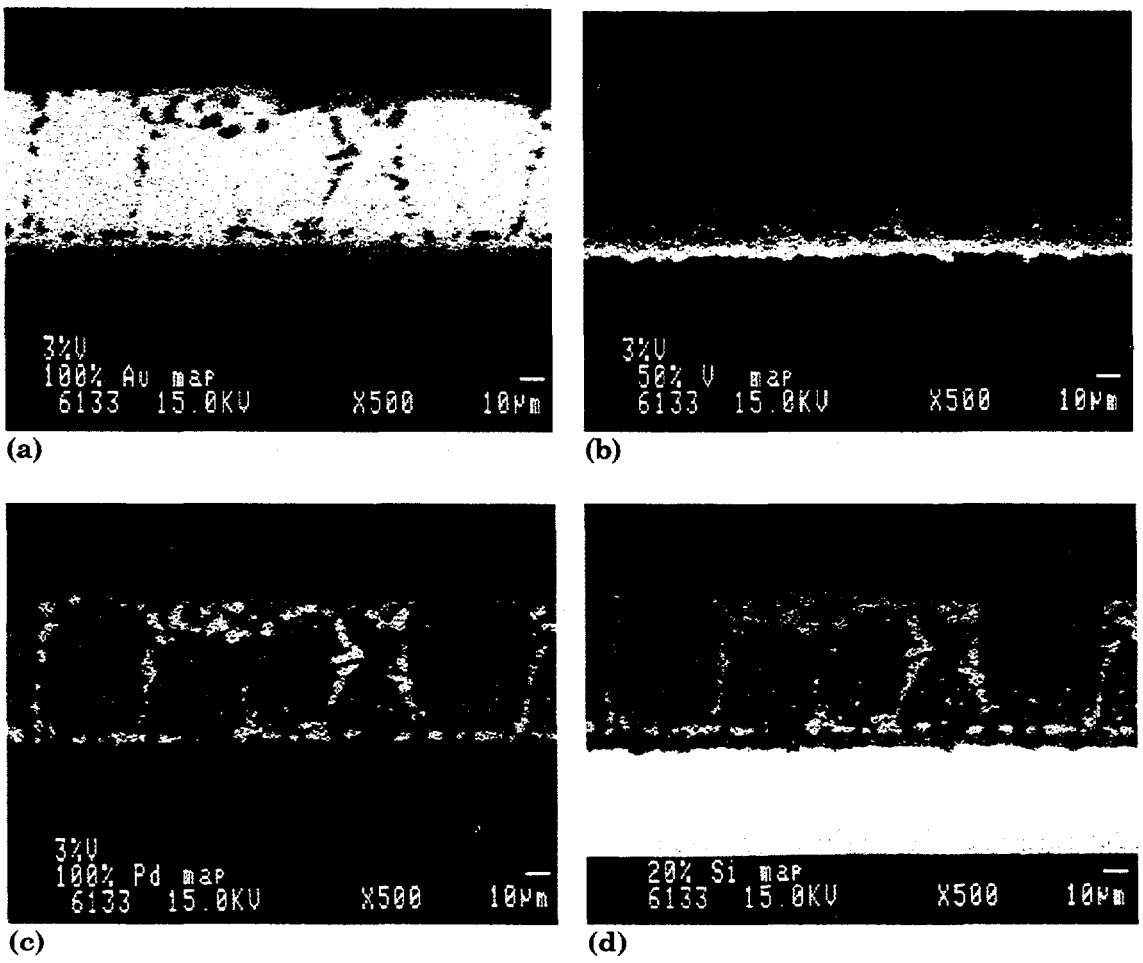

Fig. 46. Elemental maps of Au-8Pd-3V on AS-800 Si_3N_4, (a) Au, (b) V, (c) Pd, and (d) Si.

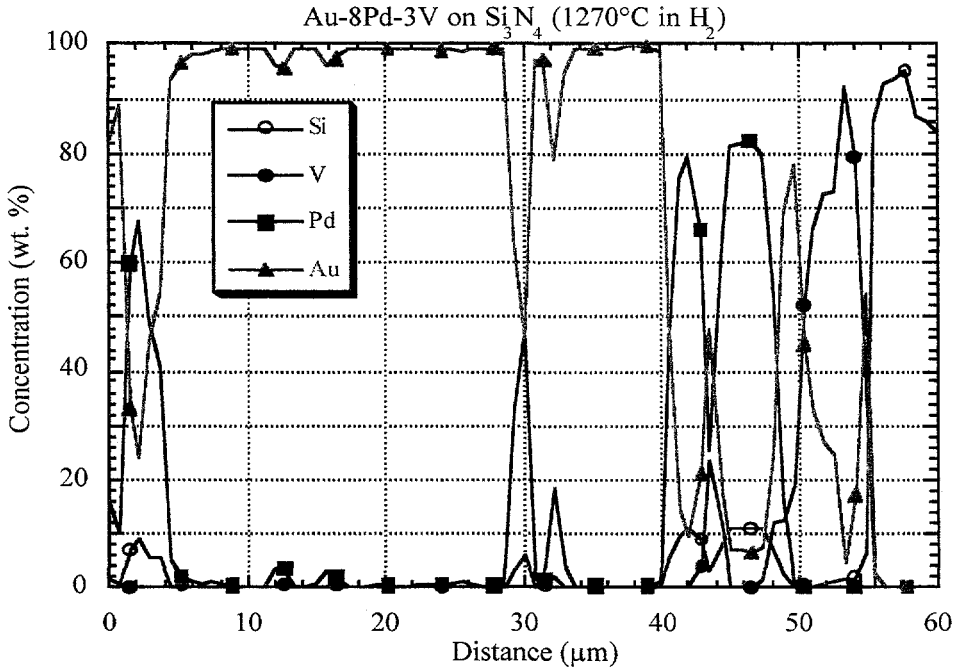

Fig. 47. Elemental traces across an Au-8Pd-3V / AS-800 Si_3N_4 interface, braze alloy on the left (~5 to 40 μm), braze Si_3N_4 reaction layer (~40 to 55 μm) and Si_3N_4 (55 to 60 μm).

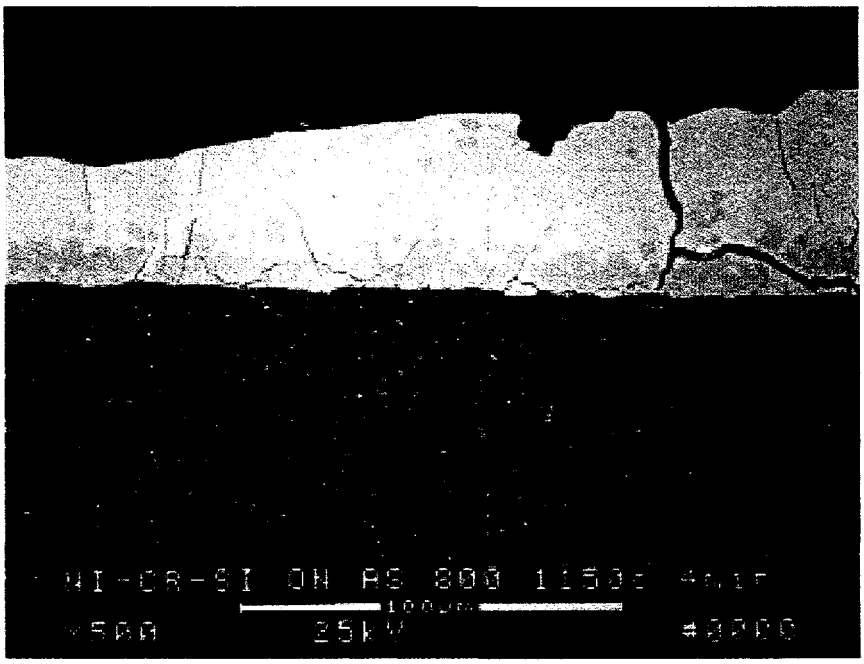

Fig. 48. SEM image of Ni-19Cr-10Si on AS-800 Si_3N_4.

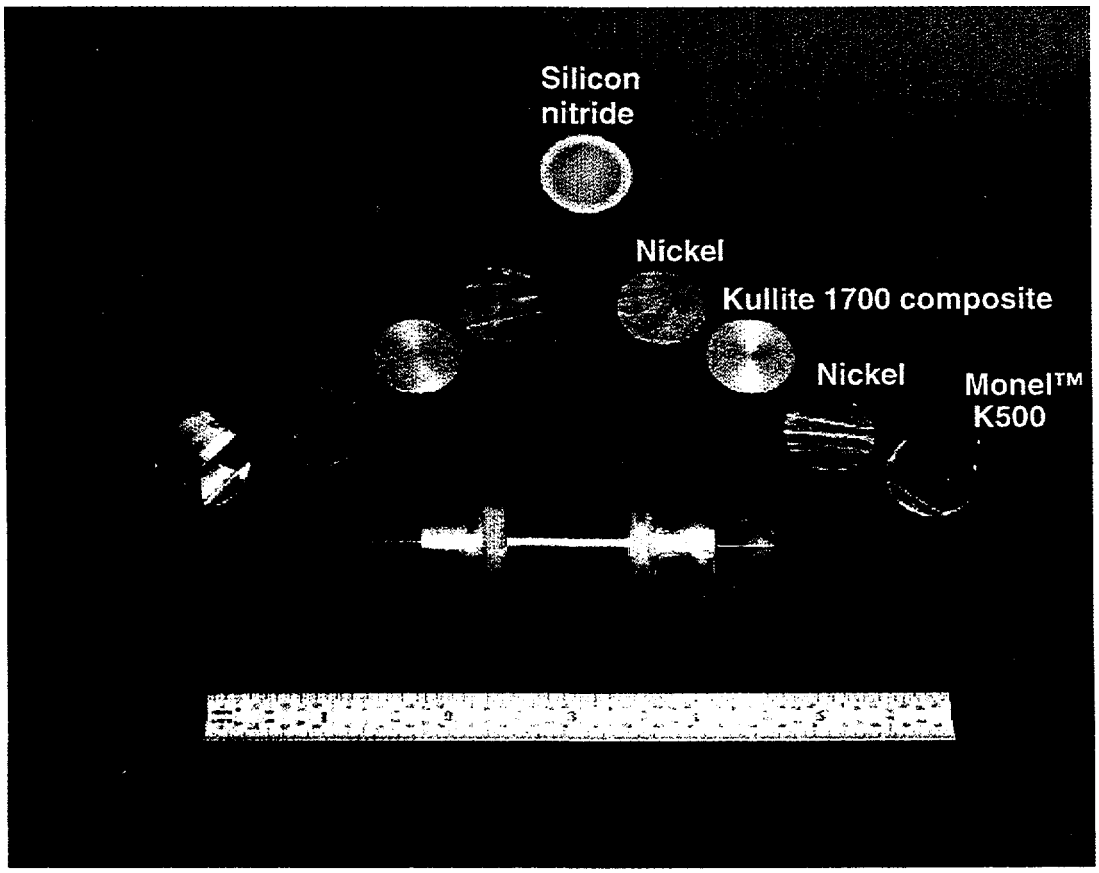

Fig. 49. Monel™ K500 to AS-800 silicon nitride (20.3 mm diameter) axle assembly. The segments (and thicknesses) on either side of the silicon nitride (middle) were: K500 - 12.7 mm, Nickel - 0.76 mm, Kullite 1700 - 3.18 mm, Nickel - 0.76 mm, and the AS-800 - 25.4 mm.

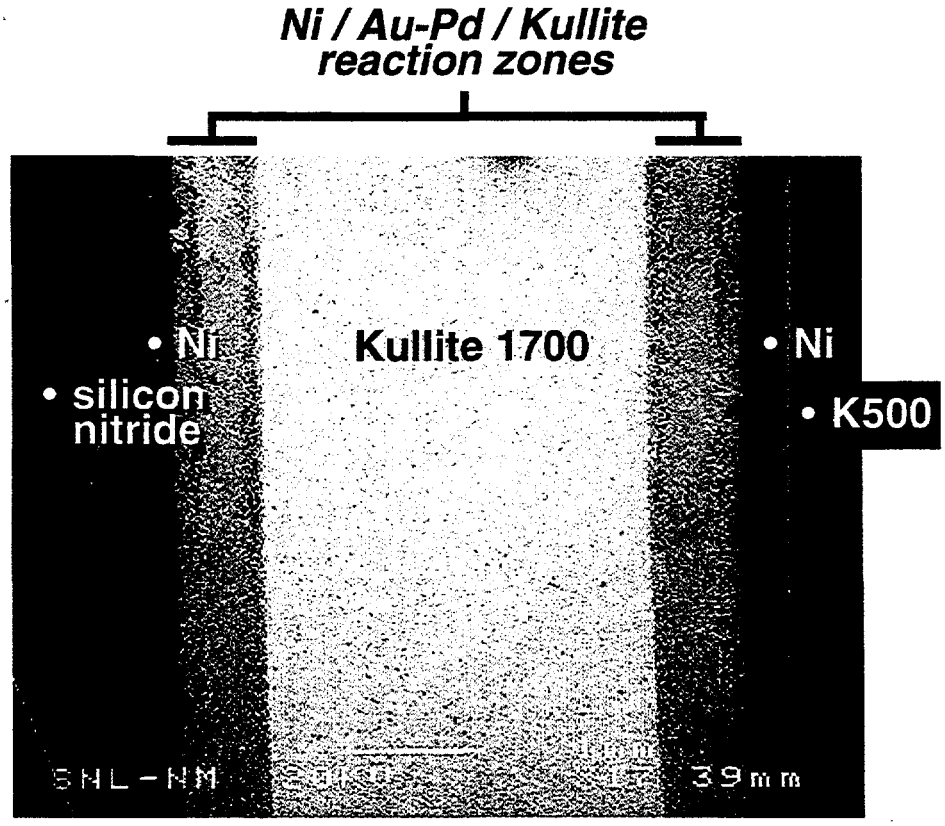

(a)

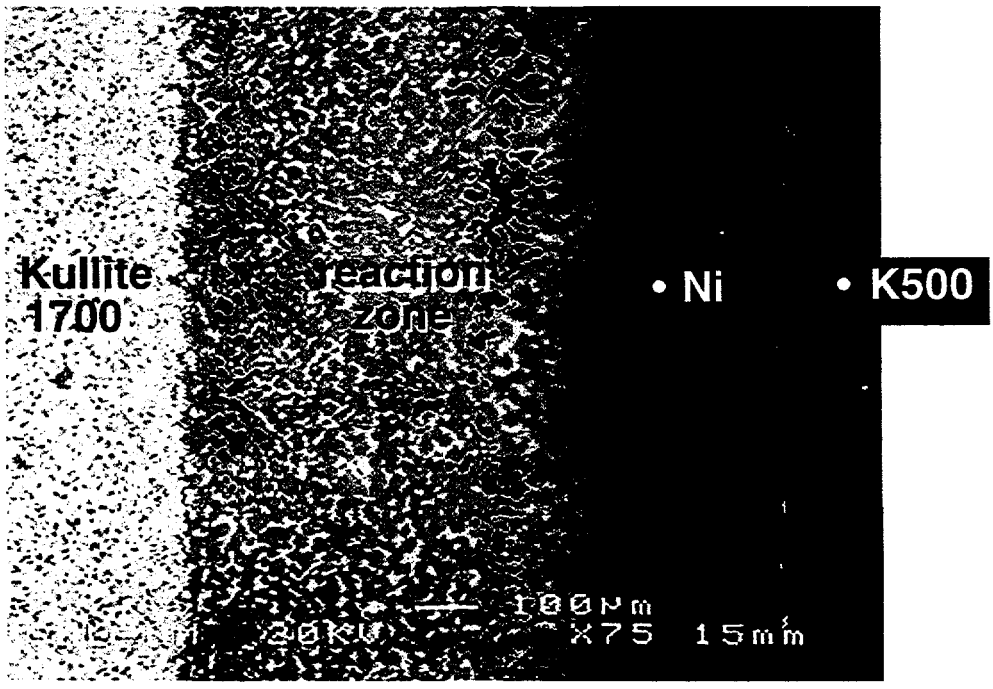

(b)

Fig. 50. (a) Low magnification SEM micrograph of the joint region between the K500 metal alloy and the AS-800 silicon nitride, showing the Ni interlayers to either side of the Kullite composite. (b) High magnification SEM micrograph of the joint region between the Ni interlayer and the Kullite.

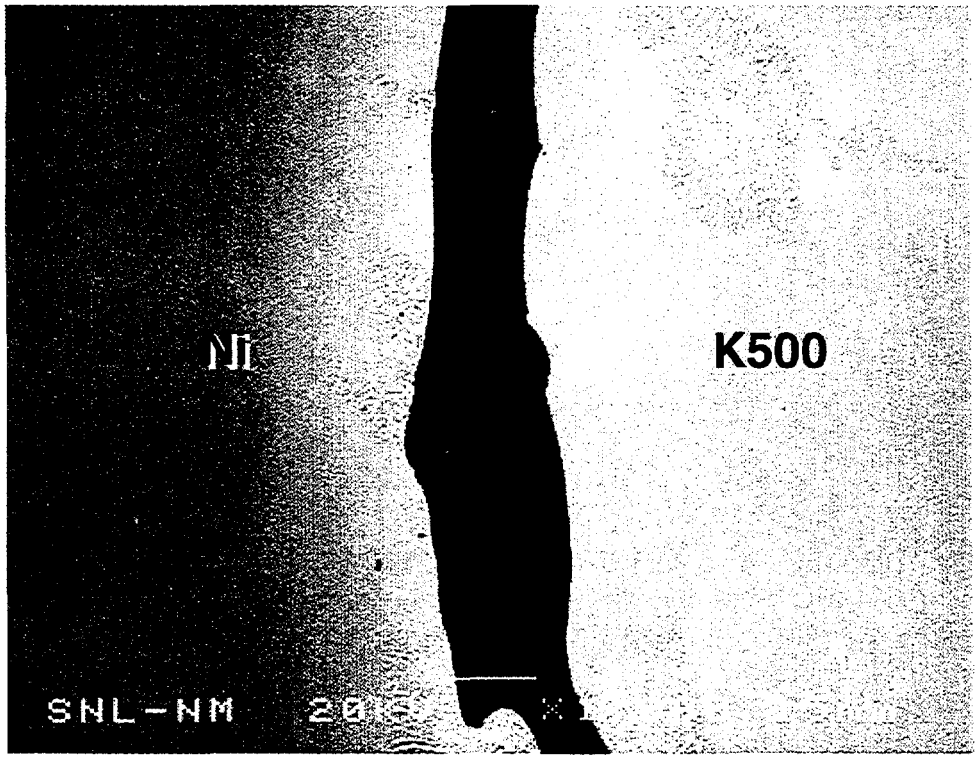

(a)

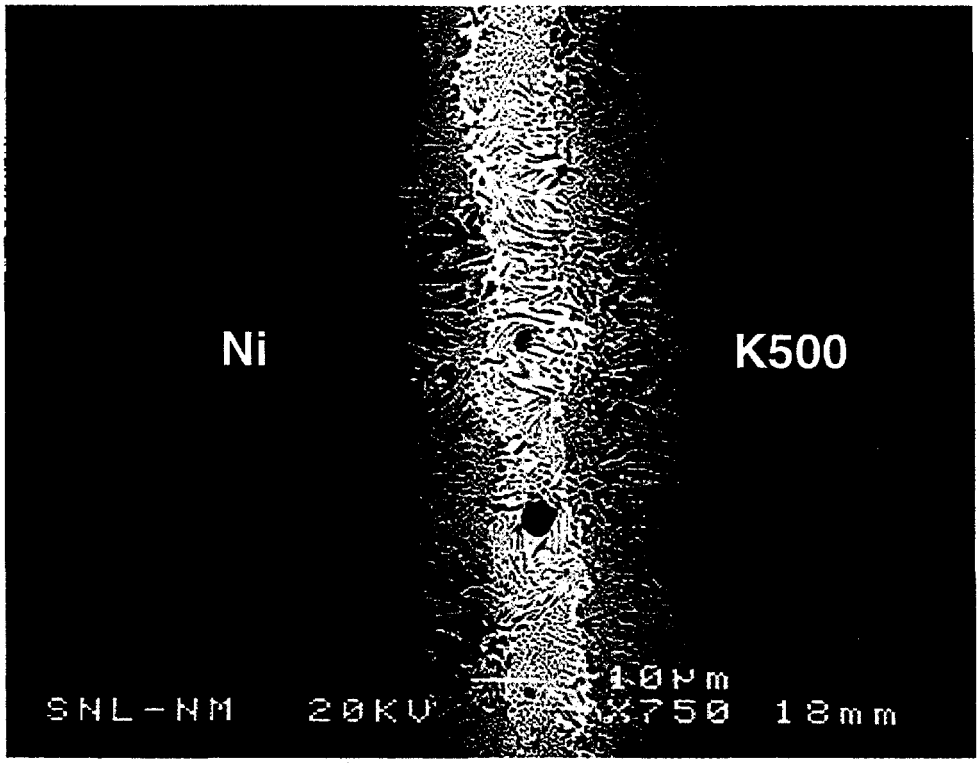

(b)

Fig. 51. SEM micrographs of the K500/Ni interface after assembly of the K500/AS-800 unit at 1200°C for 4 min.: (a) case in which braze alloy was present, (b) dissolution of the braze alloy into both the Ni and K500 left a void in the joint.

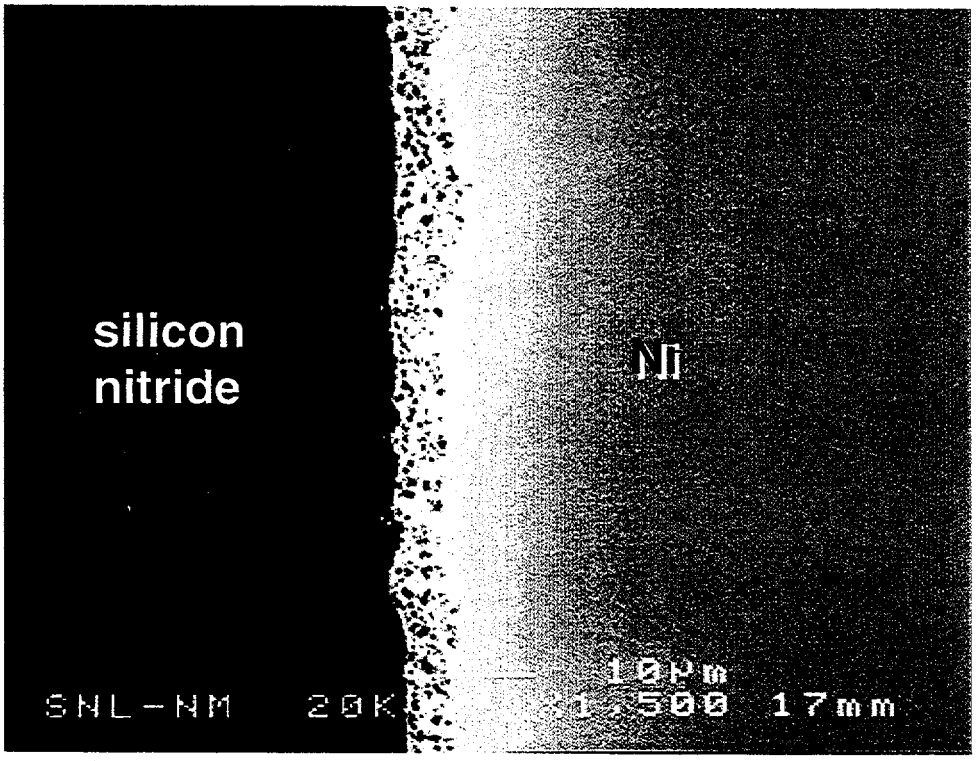

Fig. 52. SEM micrograph of the AS-800/Ni interface after assembly at 1200°C for 4 min.

Chapter 3. Braze and Interlayer Properties

I. Introduction

Due to the large thermal expansion mismatch between the AS-800 silicon nitride and structural alloys used in the turbine industry, residual stresses in the ceramic following brazing depend critically on the ability of the braze alloy to accommodate thermal mismatch strains. As such, the creep and tensile properties of the various braze alloys used in this project were measured as input for FEA calculations of residual stresses in the AS-800 material following brazing.

The first section of this chapter presents a summary of the mechanical properties of braze alloys studied during the project. The next section of this chapter discusses oxidation studies conducted on braze alloys and interlayer materials used in the project. The final section of this chapter includes two additional physical measurements obtained during the project: (1) thermal expansion for Paloro ABA alloy and (2) dynamic modulus data for the Palni braze alloy.

II. Creep and Tensile Properties of Braze Alloys

A. General Information - Mechanical Test Methods

All of the braze alloys used in this study were procured in the form of 1/8 in diameter wire (in straight lengths) from WESGO, Inc.[i] Table 1 shows the vendor-supplied chemical analyses. Miniature tensile test samples were machined to the dimensions shown in Fig. 1. Following machining, samples of all materials were annealed as shown in Table 2. Two types of annealing furnaces were used. For the Palco, Palni and Paloro alloys, a Centorr furnace was run with a hydrogen atmosphere, followed by a furnace cooldown. In the case of the Paloro ABA alloy, samples were encapsulated in quartz tubes, along with a Ta sheet getter. An overpressure of 100 Torr Argon was used in the tubes. The tubes were annealed in a tube furnace, followed by water quenching.

The majority of mechanical tests was performed on a servohydraulic test machine, equipped with a 156 kN actuator and an MTS Testar operating system.[ii] A smaller number of creep tests run at low stress (<30 MPa) and high temperature (550-850°C) conditions used a second MTS testing machine, with the actuator disconnected and direct load applied using a can of Pb shot. Due to the miniature test sample configuration and high temperature conditions, strain was measured across circumferential grooves located on the sample grips using a high temperature platform type extensometer constructed of Inconel 601 alloy, and connected to a ±0.5 inch LVDT. The effective gage length was obtained for the sample design shown in Fig. 1 by running a room temperature tensile test, and collecting data with both the high temperature extensometer and an MTS clip-on extensometer, with a 12.5 mm gage. By virtue of using the clip-on extensometer, it was possible to obtain the effective gage length (l_{eff}) of the sample by analyzing post-yield data for the tensile test by means of graphical analysis and statistical averaging. Effective gage lengths were measured as follows:

a. Palni Alloy, Test Palni06 (strain rate = 3.79×10^{-5} s^{-1}), l_{eff} = 19.295 ± 0.036 mm.
b. Palni Alloy, Test Palni09 (strain rate = 8.33×10^{-4} s^{-1}), l_{eff} = 19.316 ± 0.076 mm.
c. Paloro Alloy, Test Paloro26 (strain rate = 8.33×10^{-4} s^{-1}), l_{eff} = 23.095 ± 0.024 mm.
d. Paloro Alloy, Test Paloro28 (strain rate = 8.33×10^{-4} s^{-1}), l_{eff} = 23.166 ± 0.028 mm
e. Paloro ABA Alloy, Test Paloro49 (strain rate = 8.33×10^{-4} s^{-1}), l_{eff} = 21.037 ±0.521 mm

[i] WESGO, Inc., Belmont, CA.

[ii] MTS, Inc., Minneapolis, MN.

Table 1. Chemical composition (in wt.%) of the braze alloys which were included in the bulk mechanical properties investigation. All analyses shown were provided by WESGO, Inc.

Alloy	Au	Ag	Al	Cd	Co	Cu	Fe	In	Mg	Ni	Pb	Pd	Pt	Si	Zn
Palco (Lot #72065)	----	0.003	0.0002	0.0004	35.42 *	0.003	0.001	------	0.0001	0.06	0.0007	64.58	0.005	0.001	0.0004
Palni (Lot #72127)	0.001	0.001	0.0003	---------	---------	0.001	0.005	0.001	0.0002	40.58*	<0.001	59.42	0.02	0.002	0.0001

Alloy	Au	Ag	Cr	Cu	Fe	Mg	Ni	Pb	Pd	Pt	Si	V	Zn
Paloro (Lot #72131)	91.29	0.002	-----	0.003	0.001	<0.0001	------	0.001	8.71*	--------	<0.001	-----	<0.0001
Paloro ABA (Lot #77816)	90.39	0.002	0.002	0.002	0.001	<0.0001	0.003	-------	7.60*	0.01	0.002	2.01	----------

* Balance (i.e., determined by difference).

Table 2. Summary of annealing conditions used for the various braze alloys included in the mechanical properties study.

Alloy	Annealing Conditions	Resulting Grain Size
Palco	20°C/min. to 900°C, hold 15 min at 900°C, ramp 10°C/min to 1000°C, hold 30 min at 1000°C, furnace cool , dry hydrogen	ASTM#4
Palni	same as Palco alloy	ASTM#5
Paloro	60 min at 810°C, furnace cool, dry hydrogen atmosphere.	ASTM #3
Paloro ABA	samples encapsulated under 100 Torr Argon w/Ta getter, samples annealed 60 min at 1000°C, water quenched.	ASTM #4-5

Thus, the following values of l_{eff} were used to obtain strain data from the LVDT displacement data:

Palco and Palni alloys - l_{eff} = 19.306 mm = 0.760 in
Paloro ABA alloy - l_{eff} = 21.037 mm = 0.828 in
Paloro alloy - l_{eff} = 23.131 mm = 0.911 in

As might be expected, l_{eff} appears to have some dependence on the yield strength of the material being tested. The "gage length" of the sample appears to increase to include a progressively larger portion of the radius transition area as the yield stress decreases for a given alloy. Thus, the alloys with lower yield stresses tended to have larger values of l_{eff} - e.g., Paloro alloy. On the other hand, the Palni alloy - with a relatively high yield strength - has a value of l_{eff} just slightly above that of the nominal reduced gage section on the sample drawing (0.750 in). These trends are consistent with previous investigations conducted with the same test sample design.[1]

A.1 Tensile Test Methods

Constant true strain rate tests were run using the MTS Testar servohydraulic frame, operated in the "Playback" mode. Based on a given value of l_{eff}, a displacement versus time profile was calculated that would produce the desired true strain rate. Tensile tests were run at two different true strain rates: $8.33 \times 10^{-4} s^{-1}$, and $3.79 \times 10^{-5} s^{-1}$. All samples were heated in air with an optical furnace; samples were held at the test temperature for 30 min prior to testing.

A.2 Creep Testing Procedures

All of the creep tests were run under constant load conditions, with the vast majority run to fracture. All samples were heated in air with an optical furnace and soaked for 30 min at the test temperature before applying the creep load. For samples tested at high temperatures (550-850°C) and low stress levels (up to 30 MPa), the load was achieved by direct application of a static load at the beginning of the test. Tests run at the higher stress levels were run using the MTS frame actuator, operating in load control with a loading rate of 41.5 N/s, resulting in an approximate stress ramp rate of 13.6 MPa/s at the beginning of the test. For the case of Palni alloy, it was determined that somewhat faster loading rates were needed; this information is included in the Palni creep test summary (see Table 3).

Because the creep tests were all run using constant load conditions, but constitutive models for creep are generally based on true stress and true minimum strain rates, a protocol was followed to obtain true stress/minimum strain rate conditions. For purposes of the following discussion, please see Table 3. The true strain rate and true stress shown for a given test are calculated using the standard formulas for conversion from the engineering quantities in the following manner: the engineering strain interval (minimum and maximum) over which the minimum creep rate is observed is noted on the strain-time plot, and the average of these strain values - the "Eng. Strain @ Min. Strain Rate" is calculated. The values of True Stress and True Strain for a given creep test are then calculated using the Engineering Stress and (Engineering) Minimum Strain Rate quantities tabulated for a given test.

B. Results

B.1 Palni Alloy

Constant load tensile creep data were obtained for Palni alloy over the temperature range 250-850°C. A summary of the creep tests run is presented in Table 3. As discussed in the following section, the data appear to fall into two groupings, based on minimum creep rate correlations: a high temperature regime is observed from 650-950°C, followed by a low temperature creep regime at 250-550°C. Both regimes were well fit by a standard power law creep equation.

Table 3. Summary of creep tests run on Palni alloy. "Load rate" refers to the rate at which load was applied at the beginning of the creep test for tests run on the MTS frame. "Direct" denotes direct loading using fixed weight, full load application at the beginning of the creep test.

Test ID	Temp. (°C)	Eng Stress (MPa)	Min. Eng Str.Rate (s^{-1})	Load Rate (MPa/s)	Fracture Strain	Rupture Time (s)	Eng. Strain @ Min.Rate	True Stress (MPa)	True Min. Str.Rate (s^{-1})
22	250	499.68		14.			see Note 1		
9a	250	550.29	6.005e-9	85.	*not to fracture*		0.169	643.22	5.137e-9
36	250	585.07	7.235e-9	88.	*not to fracture*		0.232	720.64	5.874e-9
35	250	603.07		14.	0.327	43	see Note 2		
23	350	500.07	1.821e-7	14.	0.249	354400	0.230	614.99	1.481e-7
24	350	540.12	5.735e-7	14.	0.312	141390	0.272	686.87	4.510e-7
25	350	580.15	2.045e-6	14.	0.421	40676	0.384	802.66	1.478e-6
20a	450	300.15	6.616e-8	14.	0.0581	538180	0.0189	305.84	6.493e-8
28	450	330.10	3.468e-7	15.	0.0763	126110	0.0468	345.54	3.313e-7
27	450	359.98	3.780e-7	14.	0.0977	107460	0.0801	388.80	3.500e-7
26	450	410.10	3.005e-6	14.	0.148	17534	0.132	464.37	2.654e-6
37	450	460.01	6.483e-5	46.	0.212	1113	0.183	543.99	5.483e-5
30	550	220.20	3.065e-7	15.	0.0540	78184	0.00837	222.04	3.040e-7
29	550	280.05	2.585e-6	14.	0.0573	17881	0.0228	286.42	2.527e-6
31	550	319.92	1.644e-5	14.	0.0731	2974	0.0482	335.35	1.568e-5
34	650	109.94	4.994e-7	14.	0.230	41612	0.00628	110.63	4.963e-7
33	650	140.05	6.394e-7	14.	0.158	37049	0.00722	141.06	6.349e-7
32	650	179.97	3.086e-6	14.	0.0662	4364	0.00621	181.09	3.067e-6
06	750	50.02	1.274e-6	15.	0.290	55312	0.00750	50.39	1.265e-6
05	750	99.98	5.670e-6	13.	0.193	6312	0.00549	100.53	5.635e-6
04	750	150.13	2.980e-5	16.	0.117	811	0.00657	151.12	2.961e-5
03	850	20.00	5.321e-7	direct	0.255	375070	0.132	22.63	4.702e-7
08	850	39.99	1.075e-5	direct	0.372	12657	0.0123	40.49	1.062e-5
07	850	60.06	3.177e-5	13.	0.383	2913	0.00936	60.63	3.148e-5
02	950	12.00	5.950e-8	direct	*not to fracture*		0.115	13.38	5.337e-8
01	950	20.00	1.232e-5	direct	0.573	26429	0.0604	21.21	1.162e-5

Note 1: Sample crept for 5×10^5 seconds, which was insufficient time to reach the minimum strain rate.
Note 2: Substantial necking and fracture occurred prior to attaining desired stress level and min. creep rate.

The shape of the creep curves for Palni at the various temperatures deserves mention. Fig. 2 shows the strain-time record obtained for the two tests run at 250°C. Note that both tests show significant amounts of strain upon loading, followed by a transition to second stage creep at the minimum creep rate. The amount of strain upon loading is proportional to the applied stress of the creep test. Similar behavior is observed at 350°C (Fig. 3). The two higher stress tests went to fracture, and those complete creep curves suggest three-stage creep curves with somewhat limited tertiary regime. The same general shape of the creep curve (three-stage, limited tertiary regime) applies for the 450°C tests, as shown in Fig. 4.

The tests run at 550°C show somewhat transitional behavior, as shown in Fig. 5. The lowest stress test, run at 220.2 MPa, exhibits a small primary regime, followed by a limited second stage and finally a well-pronounced tertiary regime. Taken as a group, these three tests run at 550°C show the average lowest strain to fracture of any of the test temperatures studied.

At 650°C and above, the creep curves exhibit an inverted shape; this is consistent with the trends in the stress dependence of the creep process as discussed below. The 650°C creep tests, shown in Fig. 6, are representative of this behavior. All of the tests run at 750°C, plotted in Fig. 7, clearly follow this trend as well. The two higher stress tests run at 850°C (see Fig. 8) are consistent with this trend, while the test run at 20 MPa/850°C exhibits classical three-stage behavior. It is not apparent why this creep curve does not exhibit inverted behavior. Finally, at 950°C, the two curves plotted in Fig. 9 show quite different behavior. The 20 MPa/950°C test exhibits the inverted shape, while the 12 MPa/950°C test shows a continuously decreasing strain rate. Metallographic cross sections of Palni oxidation specimens run at 950°C for comparable lengths of time suggest that internal oxidation is probably affecting the 12 MPa/950°C test, leading to a net decrease in the creep rate as internal oxidation affects the entire specimen cross section. Because the microstructure of the 12 MPa/950°C test is so different from the other specimens, we have not included it in the creep correlations discussed below.

B.1.1 Minimum Creep Rate Correlations for Palni Alloy

A variety of data groupings was attempted for the Palni data set. Based on the apparent stress exponent behavior, and the quality of fit parameters (r^2) obtained from the multivariable linear regression analysis, two power law creep regimes were identified: (1) a high temperature regime, extending from 650-950°C and (2) a lower temperature regime including the 250-550°C data. These data groupings are rather consistent with the shapes of creep curves discussed above.

B.1.1a High Temperature Creep Correlation (650 - 950°C)

The true minimum creep rate data as a function of true stress for Palni tests run from 650 through 950°C are plotted in Fig. 10. As indicated above, the 12 MPa/950°C test is considered anomalous due to internal oxidation and is not included in the data analysis. The best fit for true minimum creep rate ($\dot{\varepsilon}_{min}$) as a function of true stress (σ) and absolute temperature T (Kelvin) in this temperature range is as follows:

$$\dot{\varepsilon}_{min}\ (s^{-1}) = 114.16\ (\sigma(MPa))^{3.41}\ \exp(-65{,}151/RT) \qquad (1)$$

with r^2=0.936. The fit to the data is also shown in Fig. 10. It is interesting to note that the activation energy for creep (Q_{creep}) in this temperature range (65.2 kcal/mole) is quite close to the generally accepted values (68-70 kcal/mole) of activation energy for self-diffusion in pure nickel.[2] The stress exponent, n = 3.41, is consistent with the observation of inverted creep curves in this temperature range, and suggests Class I solid solution strengthening due to the atomic size mismatch between palladium and nickel. The relatively low exponent also contributes to an increase in the strain to fracture at these temperatures, relative to the strain to fracture data observed at 550°C (see Table 3). This is also consistent with Class I solid solution behavior.[1]

B.1.1b Low Temperature Creep Correlation (250 - 550°C)

The true minimum creep rate data as a function of true stress for tests run from 250 through 550°C are plotted in Fig. 11. A casual inspection of this data suggests that the stress exponent in this temperature range is significantly higher than at the higher temperatures. The following best fit to the 250-550°C data was obtained by means of multivariable linear regression analysis:

$$\dot{\varepsilon}_{min}\ (s^{-1}) = 1.49 \times 10^{-14}\ (\sigma(MPa))^{7.27}\ \exp(-36{,}605/RT) \qquad (2)$$

with r^2=0.906. The lines shown in Fig. 11 are based on the fit shown in Eq. 2 above. Note that Q_{creep} in this temperature range (36.6 kcal/mole) is about 56% of the value observed at the higher temperatures; this is consistent with what appears to be a transition to dislocation climb-controlled creep at the lower temperatures. The increase in stress exponent at these lower temperatures is also consistent with the transition to climb-controlled behavior from solute-controlled creep at the higher temperatures.

B.1.2 Tensile Test Results for Palni Alloy

A limited number of constant true strain rate tensile tests was run for the Palni alloy at two strain rates: $8.33 \times 10^{-4} s^{-1}$ and $3.79 \times 10^{-5} s^{-1}$. The results for these tests are shown in Table 4. The complete plot of tests run at $3.79 \times 10^{-5} s^{-1}$ is shown in Fig. 12a. Note that this alloy appears to go through a ductility minimum at the intermediate temperatures of 550-750°C, followed by a return to relatively high ductility at 850°C. Although fewer tests were run at $8.33 \times 10^{-4} s^{-1}$, the stress strain curve plot shown in Fig. 12(b) also indicates a ductility minimum at 550°C. All of the tensile data suggest that work hardening is important in Palni alloy at temperatures up to ~550°C. Summary plots of yield stress and maximum true stress as a function of temperature are shown in Fig. 13. Note that significant strain rate sensitivity is not apparent for this data set until the temperature has increased to ~450°C.

B.1.3 Discussion - Results for the Palni Alloy

The creep strength of the Palni alloy at lower temperatures is quite substantial. For example, the 100 hr creep strength of Palni at 350°C is 500 MPa (72.5 ksi). This high strength at low temperatures makes Palni somewhat undesirable for use in joints to silicon nitride because the high creep strength will not accommodate thermal expansion mismatch across the braze joint.

B.2 Palco Alloy

A limited number of creep tests was run at elevated temperatures (750-950°C) for the Palco alloy. This was done because of a cost viewpoint, along with the information obtained from isothermal oxidation data in air (see section III, below), which showed that Palni was more oxidation resistant in air than Palco at 900°C.

B.2.1 750-950°C Constant Load Creep Tests - Palco Alloy

The results of the eight creep tests performed on Palco alloy are presented in Table 5. The data indicate that the strain to fracture increases as temperature is increased. Strain-time records for these tests are shown in Figures 14, 15 and 16. The minimum true strain rate as a function of true stress is shown in Fig. 17. Using multivariable linear regression analysis, the data were fit to the standard power law equation:

$$\dot{\varepsilon}_{min}\ (s^{-1}) = 7.37 \times 10^{3}\ (\sigma(MPa)^{3.65})\ \exp(-76{,}226/RT), \quad r^2 = 0.958 \qquad (3)$$

Table 4. Constant true strain rate tensile tests performed on annealed Palni alloy. The "Work-Hardening Slope" refers to the average slope of the stress-strain curve between e = 0.01 to 0.03. "Measured Modulus" refers to the apparent modulus measured from the elastic portion of the stress-strain curve - it is always less than the Dynamic Modulus measured by acoustic methods (see Section VI.B of this chapter).

Test ID#	Temp (°C)	True Strain Rate (s^{-1})	Measured Modulus (MPa)	0.2% Yield Stress (MPa)	W-H Slope	Max. True Stress (MPa)	SUTS (MPa)	Uniform Strain	Fracture Strain
Palni 9	23	3.79e-5	83630.	387.20	2594.80	914.66	673.20	0.3065	0.3162
Palni 10	250	3.79e-5	47850.	392.50	1737.20	845.00	638.85	0.2797	0.2988
Palni 11	450	3.79e-5	95510.	320.11	1696.60	630.26	482.56	0.2670	0.2782
Palni 12	550	3.79e-5	43740.	291.56	1413.20	373.06	348.71	0.0675	0.0802
Palni 13	650	3.79e-5	50940.	249.00	169.70	253.40	247.51	0.0235	0.0896
Palni 14	750	3.79e-5	57870.	179.16	0.00	180.16	179.74	0.0023	0.1314
Palni 15	850	3.79e-5	31790.	89.910	0.00	96.02	95.93	0.0009	0.3477
Palni 16	23	8.33e-4	97770.	391.75	2590.80	922.20	679.16	0.3059	0.3312
Palni 17	550	8.33e-4	54920.	319.85	1797.70	509.70	431.68	0.1661	0.1836
Palni 18	850	8.33e-4	51430.	168.15	0.00	170.16	170.06	0.0006	0.2831

Table 5. Constant load creep tests performed on annealed Palco alloy.

Test ID	Temp. (°C)	Eng Stress (MPa)	Min. Eng Str.Rate (s^{-1})	Fracture Strain	Rupture Time (s)	Eng. Strain @ Min.Rate	True Stress (MPa)	True Min. Str.Rate (s^{-1})
06	750.00	50.01	6.556e-07	0.1397	56340.	0.0038	50.20	6.531e-07
05	750.00	100.07	4.432e-06	0.0635	3249.	0.0038	100.45	4.415e-06
04	750.00	150.10	5.790e-05	0.0601	572.	0.0107	151.71	5.729e-05
03	850.00	20.00	8.007e-07	0.1997	106900.	0.0061	20.13	7.954e-07
08	850.00	40.05	9.293e-06	0.2412	10920.	0.0165	40.71	9.142e-06
07	850.00	60.04	2.694e-05	0.2134	2576.	0.0054	60.37	2.680e-05
02	950.00	12.00	1.729e-06	0.3807	161800.	0.0789	12.95	1.603e-06
01	950.00	20.00	1.301e-05	0.2997	16750.	0.0248	20.50	1.301e-05

The stress exponent value obtained (3.65) suggests that this alloy behaves in this temperature range as a Class I solid solution alloy (n~3); this is consistent with the shape of all the Palco creep curves we obtained - see, for example the data obtained at 850 and 950°C in Figures 15 and 16. The only Palco test that shows a slight deviation from the inverted creep curve shape is the 150 MPa/750°C, where it is possible that some primary strain (about 0.004) was caused by the relatively high applied stress in this test. Following the initial primary strain, the 150 MPa/750°C test exhibits an inverted shape identical to the other Palco creep curves.

B.3 Paloro Alloy

B.3.1 Elevated Temperature Tensile Tests

A summary of the yield stress, tensile stress and ductility data obtained from the tensile tests is shown in Table 6. The true stress-strain plots for all tests run at a constant true strain rate of $8.33 \times 10^{-4} s^{-1}$ are shown in Fig. 18(a). As expected, both the yield and tensile strengths have a strong temperature dependence. The strain to fracture increases as a function of temperature - with the noticeable exception of the 550°C test. The true stress-strain plots for the $3.79 \times 10^{-5} s^{-1}$ tensile tests are shown in Fig. 18(b). The temperature dependence of the yield stress is shown in Fig. 19a; note that the data from both strain rates had to be combined onto one trend curve due to problems with the data acquisition at the beginning of tests run at 450, 550 and 650°C at the strain rate of $8.33 \times 10^{-4} s^{-1}$. The maximum true stress (true stress equivalent of UTS) is plotted as a function of temperature in Fig. 19(b). Note that while the effect of strain rate on tensile strength is small at 250°C, the effect is more pronounced at both 450 and 650°C.

B.3.2 Elevated Temperature Creep Tests

All of the Paloro creep tests were run under constant load conditions, with the vast majority run to fracture. A summary of these results is shown in Table 7. The engineering strain-time records are shown for the various temperatures in Figures 20 through 26. At both 250 and 350°C, the amount of strain observed upon initial loading is proportional to the applied stress for a particular test (see Figures 20 and 21). This strain upon loading is not significant at 450°C or higher temperatures. However, all of the tests from 250-450°C, and the higher stress tests at 550°C shown in Fig. 23 have creep curves that exhibit classical three-stage creep behavior - that is, primary and secondary, followed by the tertiary creep stage prior to fracture. At the lower stresses at 550°C, and the higher temperatures (650-850°C), the creep curves exhibit secondary behavior at the beginning of the test. That is, there is no well-defined primary stage of the creep curve, only a secondary stage, followed by the tertiary stage. This type of behavior could signify a change in creep mechanism. The size difference between Au and Pd is not very large (Ω_{sf} for Au-Pd is -14.20% - see ref. 3) and thus one would expect this alloy to exhibit Class II or "metal" type creep behavior,[4] rather than the characteristics of a Class I solid solution alloy.

B.3.3 Minimum Creep Rate Correlations for Paloro Alloy

A variety of data groupings was attempted for the Paloro creep tests. Based on the shape of the creep curves discussed above, and the quality of fit parameters (r^2) obtained from the multivariable linear regression analysis, two creep regimes were identified: (1) a high temperature regime, including the two lower stresses studied at 550°C, and all the 650-850°C data and (2) a lower temperature regime including the 250-450°C tests, and the high stress tests run at 550°C.

B.3.3a Low Temperature Creep Correlation (250 - 550°C

As discussed above, this regime includes all of the tests that exhibit the classical three-stage creep curve - i.e., all of the 250-450°C tests, along with the three higher stress tests run at 550°C. The true minimum creep rate data as a function of true stress for these tests are plotted in Fig. 27. The

Table 6. Summary of tensile tests run on annealed Paloro alloy. Note that all tests were run at a constant true strain rate as indicated in the third column. Note: the Uniform and Fracture strain are in units of engineering strain, while the last column is in units of true strain.

Sample ID#	Temp. (°C)	$\dot{\varepsilon}$ (s^{-1})	Yield Stress (MPa)	UTS (MPa)	Uniform Strain	Fracture Strain	Max. True Stress (MPa)	True Uniform Strain
9	250	3.79e-5	52.30	150.23	0.200	0.258**	181.86	0.182
2	450	3.79e-5	48.65	92.61	0.214	0.260	112.75	0.194
11	650	3.79e-5	31.13	37.86	0.219	0.348	45.94	0.198
26	23	8.33e-4	59.36	216.74	0.219	0.266**	264.64	0.198
27	23	8.33e-4	63.47	213.60	0.212	0.258**	259.38	0.192
8	250	8.33e-4	50.99	161.27	0.197	0.246**	193.78	0.180
4	450	8.33e-4	*	122.46	0.312	0.338	161.58	0.272
5	550	8.33e-4	*	78.86	0.263	0.338	100.13	0.233
6	650	8.33e-4	*	62.04	0.364	0.421	84.77	0.310
7	750	8.33e-4	32.29	40.86	0.297	0.484	53.04	0.260

* Yield stress not available for these tests.
** Sharply defined neck formed in these tests; test concluded just prior to actual fracture of the sample.

Table 7. Summary of elevated temperature creep tests run on annealed Paloro alloy. Note: values of e_f marked with a star indicate that no rupture occurred and the number shown under e_f is the eng. strain recorded at the end of the test.

Sample ID #	Temp. (°C)	Eng. Stress (MPa)	$\dot{e}_{min}$ (s^{-1})	e at $\dot{e}_{min}$	e_f	t_r (sec)	True Stress (MPa)	$\dot{\varepsilon}_{min}$ (s^{-1})
3	850	3.10	1.24e-07	0.023	0.028*		3.17	1.21e-07
10	850	5.89	3.51e-06	0.062	0.549*		6.25	3.31e-06
16	850	9.69	1.54e-05	0.056	0.549*		10.23	1.46e-05
40	750	4.93	1.34e-07	0.089	0.150*		5.37	1.23e-07
15	750	9.89	1.44e-06	0.110	0.475	2.044e+05	9.99	1.24e-06
18	750	19.75	3.14e-05	0.082	0.517	1.044e+04	21.37	2.90e-05
13	750	39.89	7.30e-04	0.156	0.550	4.275e+02	46.11	6.32e-04
33	650	7.83	6.64e-08	0.038	0.049*		8.12	6.40e-08
21	650	14.66	8.41e-07	0.070	0.465	3.184e+05	15.69	7.86e-07
19	650	30.03	2.61e-05	0.082	0.313	8.573e+03	32.49	2.41e-05
12	650	49.99	1.45e-04	0.155	0.428	1.873e+03	57.73	1.25e-04
39	550	19.90	1.94e-07	0.038	0.278	8.303e+05	20.67	1.87e-07
14	550	29.84	5.47e-07	0.053	0.229	3.244e+05	31.42	5.20e-07
34	550	54.98	1.65e-05	0.142	0.394	1.562e+04	62.80	1.44e-05
20	550	74.99	1.82e-04	0.179	0.441	1.464e+03	88.43	1.54e-04
17	550	90.07	4.99e-04	0.182	0.340	3.785e+02	107.2	4.22e-05
27	450	50.53	9.10e-08	0.055	0.204	1.980e+05	53.30	8.62e-08
22	450	90.06	6.57e-05	0.141	0.277	2.516e+03	106.4	5.56e-05
29	450	124.9	1.28e-03	0.206	0.311	1.368e+02	150.7	1.06e-03
32	350	75.00	1.19e-07	0.070	0.116*		80.23	1.11e-07
23	350	110.0	2.92e-06	0.124	0.213	3.199e+04	123.7	2.59e-06
31	350	130.1	1.66e-05	0.165	0.236	5.674e+03	151.6	1.43e-05
35	350	140.4	1.03e-04	0.208	0.277	7.432e+01	169.6	1.03e-04
25	250	110.1	6.09e-08	0.061	0.062*		116.7	5.74e-08
38	250	110.2	9.24e-09	0.084	0.087*		119.4	8.53e-09
37	250	135.0	3.25e-07	0.176	0.228	2.264e+05	158.8	2.76e-07
24	250	160.3	2.82e-04	0.176	0.232	1.914e+02	188.4	2.40e-04

upward slope of the trend line at each temperature suggests that these data are in a power-law breakdown regime. This also suggests the use of the Garofalo sinh equation

$$\dot{\varepsilon}_{min}\ (s^{-1}) = A\ [\sinh(\alpha\ \sigma(MPa)]^{n'}\ \exp(-Q_{cr}/RT) \qquad (4)$$

as an appropriate representation of minimum strain rate as a function of stress and temperature.[5] The following best fit to the data was obtained by means of multivariable linear regression analysis:

$$\dot{\varepsilon}_{min}\ (s^{-1}) = 47.01\ [\sinh(0.0352\ \sigma(MPa)]^{2.70}\ \exp\text{-}(32{,}445/RT) \qquad (5)$$

In the above equation, the activation energy for creep (Q_{cr}) is 32,445 cal/mole, and R has units of 1.987 cal/mole/K. The quality of fit parameter (r^2) for this fit to the data is 0.905, this maximum value was obtained as a result of iterating on the values of α. This fit is shown in comparison to the data in Fig. 27. A second comparison of the data and fit is shown in Fig. 28, where the temperature effect on strain rate has been normalized by multiplying the left hand side of Eq. 4 by $\exp(Q_{cr}/RT)$.

It should be noted that the effective stress exponent, n_{eff}, for the Garofalo sinh equation depends on the instantaneous value of $\alpha\sigma$. By taking the natural log of both sides of Eq. 4 and then differentiating, it can be shown that

$$n_{eff} = n'\ (\alpha\sigma\ \coth(\alpha\sigma)) \qquad (6)$$

The ratio n_{eff}/n' is plotted as a function of $\alpha\sigma$ in Fig. 29. Clearly, at low values of $\alpha\sigma$, the value of n_{eff} is equal to n'. However, as $\alpha\sigma$ goes >>1, the value of n_{eff} increases linearly with $\alpha\sigma$, since $\coth(\alpha\sigma)$ tends to 1. For example, near the low end of $\alpha\sigma$ where the fit applies - $\alpha\sigma$ equal to 1.76 where σ=50 MPa - the value of n_{eff} is equal to 5.0. Conversely, the highest value of σ studied is equal to 188 MPa, leading to a value of n_{eff} equal to 17.9.

B.3.3b High Temperature Creep Correlation (550 - 850°C)

The true minimum creep rate data as a function of true stress for Paloro tests run from 650 through 850°C, and at the two low stress tests run at 550°C, are plotted in Fig. 30. A standard power law equation gives the best fit for true minimum strain rate ($\dot{\varepsilon}_{min}$) in this temperature range as follows:

$$\dot{\varepsilon}_{min}\ (s^{-1}) = 0.9932\ [\sigma(MPa)]^{3.918}\ \exp(-45{,}327/RT) \qquad (7)$$

The quality of fit parameter (r^2) for the fit shown in Eq. 7 is equal to 0.991. A comparison of the power law fit and the creep data is shown in Fig. 30.

B.3.4 Discussion - Results for the Paloro Alloy

The transition in the shape of the creep curves was found to be coincident with the transition from the hyperbolic sinh equation to the high temperature power law creep equation. The shift in the activation energy for creep is quite pronounced between the two creep regimes (see eqs. 5 and 7). At the higher temperatures, the creep activation energy of 45.3 kcal/mole is comparable to the generally accepted value of the activation energy for self-diffusion in gold (42.3 kcal/mole).[2] This, along with the value of stress exponent (3.92), suggest that the high temperature creep of Paloro is consistent with a classical volume diffusion-controlled creep mechanism. On the other hand, the low temperature correlation given in Eq. 5 suggests that creep in Paloro at low temperatures is controlled by the diffusion along dislocation cores, because the creep activation energy (32.4 kcal/mole) is roughly 77% of the activation energy for self-diffusion in gold.

The creep strength of the Paloro alloy is clearly much lower than that of either the Palco or Palni alloys discussed earlier in this report. The relatively low creep strength exhibited by the Paloro alloy is probably not a liability for the silicon nitride joining application because of the need for the

braze alloy to be able to accommodate relatively large amounts of thermal mismatch strain across the braze joint.

B.4 Paloro ABA Alloy[iii]

B.4.1 Elevated Temperature Tensile Tests

A summary of the yield stress, tensile stress and ductility data obtained from the tensile tests run on Paloro ABA alloy is shown in Table 8. The true stress-strain plots for all tests run at a constant true strain rate of 8.33×10^{-4} s^{-1} are shown in Fig. 31(a). The strain to fracture decreases slightly as a function of temperature from 23 up to 450°C, followed by a relative minimum at 650°C. The true stress-strain plots for the 3.79×10^{-5} s^{-1} tensile tests are shown in Fig. 31(b). These tests show an even greater tendency for decrease in strain to fracture - and uniform strain - than the tests run at the faster strain rate. This suggests a greater tendency to void-induced cavitation and/or intergranular fracture in Paloro ABA alloy at higher temperatures.

B.4.2 Elevated Temperature Creep Tests

Although the testing matrix for this alloy is incomplete, the preliminary data are included for completeness, as well as to permit a comparison of creep strength relative to the conventional Paloro alloy. The creep tests performed to date are shown in Table 9. The strain-time records of these tests (not shown) have also exhibited the expected inverted shape that was observed with the Paloro alloy, and is indicative of Class I solid solution alloys. In general, the strain to fracture in Paloro ABA is lower than in the creep tests for Paloro alloy.

The creep tests over the temperature range 550-850°C have been completed, and have been analyzed based on the conventional power law equation. The following power law fit has been found to provide an excellent fit to the data (r^2=0.949) over this temperature range:

$$\dot{\varepsilon}_{min}\ (s^{-1}) = 2.6218\ [\sigma(MPa)]^{3.462}\ \exp(-50{,}363/RT) \qquad (8)$$

The stress exponent (3.462) observed for this alloy is also consistent with the idea that the Paloro ABA alloy exhibits Class I solid solution alloy behavior. A comparison of the data and the fit given by Eq. 8 is shown in Fig. 32. By comparison to the high temperature power law fit to the conventional Paloro alloy, the slightly higher activation energy for creep in Paloro ABA alloy (50.36 kcal/mole vs. 45.33 kcal/mole for the conventional Paloro alloy) is also consistent with the idea that a relatively high melting point alloying addition (2 wt.% Vanadium) has been added to the conventional Paloro composition.

C. Comparison of Properties: Paloro ABA Alloy vs. Conventional Paloro Alloy

Examination of the tensile properties for Paloro and Paloro ABA alloys indicates that the addition of 2 wt.% V to the conventional Paloro alloy produces significant strengthening effects. This is illustrated in Fig. 33, where the yield stress and maximum true stress (i.e., the true stress equivalent of UTS) for both alloys - obtained at a strain rate of 8.33×10^{-4} s^{-1} - are illustrated. The increase in yield stress for Paloro ABA relative to the conventional alloy is approximately a factor of 2-2.5 over the entire temperature range studied (23-750°C). By comparison, the increase in maximum true stress for Paloro ABA is most pronounced at room temperature (23°C) and decreases gradually as the temperature is increased.

A comparison of the strain time data for the two alloys at 750°C indicates that Paloro ABA has higher creep strength at high temperatures than the conventional Paloro alloy. Strain-time data for the two alloys are shown in Fig. 34. Clearly, both the minimum creep rate and time to fracture

[iii] Nominally 90Au-8Pd-2V (wt%).

Table 8. Summary of tensile tests run on annealed Paloro ABA alloy. Note that all tests were run at a constant true strain rate as indicated in the third column. Note: the Uniform and Fracture strain are in units of engineering strain, while the last column is in units of true strain.

Sample ID#	Temp. (°C)	$\dot{\varepsilon}$ (s^{-1})	Yield Stress (MPa)	UTS (MPa)	Uniform Strain	Fracture Strain	Max. True Stress (MPa)	True Uniform Strain
51	250	3.79e-5	131.10	287.73	0.2824	0.3156	368.97	0.2743
52	450	3.79e-5	103.31	175.04	0.1044	0.1116	193.32	0.0993
53	650	3.79e-5	87.805	89.473	0.0037	0.0707	89.80	0.0683
49	23	8.33e-4	137.47	343.07	0.2929	0.3243	443.55	0.2809
50	250	8.33e-4	118.14	284.82	0.2713	0.3067	362.09	0.2400
46	450	8.33e-4	111.82	235.90	0.2403	0.2564	292.60	0.2154
47	650	8.33e-4	109.14	122.05	0.0362	0.0737	126.47	0.0355
48	750	8.33e-4	80.256	80.096	0.0646	0.1595	85.27	0.0626

Table 9. Preliminary creep test results for annealed Paloro ABA alloy.

Test File	Temp. (°C)	Eng Stress (MPa)	$\dot{e}_{min}$ (s^{-1})	e @ $\dot{e}_{min}$	e_{fr}	Rupture Time (seconds)	σ (MPa)	$\dot{e}_{min}$ (s^{-1})
Paloro62*	850	4.000	2.4729e-08	0.00071	0.0275	5.3914e+05	4.029	2.455e-08
Paloro61	850	6.000	2.9983e-07	0.02037	0.1612	2.0630e+05	6.122	2.938e-07
Paloro60	850	12.000	3.4400e-06	0.03747	0.3940	4.8359e+04	12.450	3.316e-06
Paloro54	750	5.000	5.4741e-09	0.00814	*Not to Fracture*		14.486	5.430e-09
Paloro56	750	10.000	2.3820e-07	0.02622	0.1225	3.5102e+05	10.260	2.321e-07
Paloro55	750	20.000	1.6320e-06	0.02290	0.2106	6.5946e+04	20.458	1.596e-06
Paloro57	650	20.000	1.8104e-07	0.01182	0.1791	4.3748e+05	20.236	1.789e-07
Paloro58	650	30.000	5.7850e-07	0.00825	0.1651	1.0021e+05	30.247	5.785e-07
Paloro64	650	58.102	2.3460e-06	0.00314	0.0875	8.1247e+03	58.285	2.339e-06
Paloro59	550	30.000	2.2242e-08	0.01578	*Not to Fracture*		130.473	2.190e-08
Paloro68	550	69.970	1.8963e-07	0.00658	0.0285	9.6501e+04	70.430	1.884e-07
Paloro65	550	70.136	2.2997e-07	0.00778	0.0250	8.4925e+04	70.682	2.282e-07
Paloro66*	450	99.799	3.6620e-09	0.00460	0.0080	7.5200e+05	100.260	3.645e-09
Paloro68	450	150.030	3.3396e-07	0.05920	0.0627	1.5070e+04	158.910	3.153e-07
Paloro63	350	150.000	5.1743e-10	0.00220	*Not to Fracture*		150.330	5.160e-10
Paloro69	350	239.940	3.9630e-08	0.17790	0.1797	1.1663e+05	282.630	3.364e-08

* Fractured in threads of the sample.

are higher for the case of the Paloro ABA alloy. Note, however, that the strain to fracture for Paloro ABA is consistently lower than for the conventional Paloro alloy.

These results suggest that residual stresses resulting from metal/ceramic brazing with Paloro ABA alloy will be somewhat higher than with the conventional Paloro alloy. However, the tensile strength of the Paloro ABA alloy is still substantially less than that of the Palni alloy (see Fig. 13), and undoubtedly compares well with virtually any other alloy with similar melting point range.

D. Mechanical Properties Comparisons with Other Braze Alloys

It is interesting to compare the tensile yield and maximum true stress obtained for Paloro with other braze alloys. A comparison of the 0.2% offset yield stress for Paloro, along with the Nioro (82Au-18Ni), Cusil (72Ag-28Cu) and Cusil ABA (62.2Ag-36.2Cu-1.6Ti) braze alloys is shown in Fig. 35. As is evident from this graph, the stress required for plastic flow is significantly less for Paloro than the other three braze alloys. A similar conclusion can be obtained from comparing the maximum true stress for all four alloys, as shown in Fig. 36. In the latter figure, it should be noted that the data for Cusil and Cusil ABA alloys were obtained in compression, and because the tests were run to only ε=0.16, it is possible that the maximum true strain obtained in tension for these alloys could be slightly higher if the uniform strain for these alloys are in excess of ε=0.16. Similar comparisons with the Palni (60Pd-40Ni) braze alloy show that Paloro is substantially weaker than the Palni alloy.

The fact that the stresses required for plastic flow in Paloro are quite low is relevant to the use of this alloy in metal/ceramic joining applications. Because the thermal expansion mismatch between silicon nitride and nickel base alloys is quite large, an easily deformed braze alloy facilitates the accommodation of those mismatch strains. As a result, given similar braze alloy melting points, one would expect the peak stresses in such a joint brazed with Paloro alloy to be significantly less than that of the Palni braze alloy.

E. Summary - Mechanical Properties of Braze Alloys

Palni alloy. Constant load tensile creep tests were run on Palni alloy at temperatures ranging from 250-950°C. The shapes of the creep curves, along with trends in the minimum creep rate data, indicate two distinct regimes of power-law creep: (a) at high temperatures, 650-950°C, inverted creep curves suggest Class I power law creep with a stress exponent (n) of 3.41 and an activation energy (Q_{creep}) of 65.2 kcal/mole, (b) at intermediate and lower temperatures (250-550°C), three-stage creep curves with n = 7.27 and Q_{creep} = 36.6 kcal/mole are observed. The latter set of parameters suggest a return to climb-controlled creep at the lower temperatures from solid solution strengthening at high temperatures.

Palco alloy. The creep properties of Palco alloy were studied over the limited temperature range of 650-850°C. The data were well fit to a conventional power law creep equation with a stress exponent of 3.65 and an activation energy (Q_{creep}) of 76.23 kcal/mole.

Paloro alloy. Constant load tensile creep tests were conducted at temperatures ranging from 250-850°C. Based on minimum strain rate correlations obtained from the data and changes in the shape of the creep curves, two distinct creep regimes are observed: (a) a low temperature creep regime (250-550°C) which is characterized by the Garofalo sinh equation, with an activation energy of 32.4 kcal/mole and (b) a high temperature creep regime (550-850°C) well fit by a power law equation with n= 3.92 and an activation energy of 45.3 kcal/mole. Constant true strain rate tensile tests were also run, from room temperature to 750°C. These results, as well as the creep results, suggest that the stresses required for deformation in Paloro are significantly lower than observed with other braze alloys. This fact, along with Paloro's excellent oxidation resistance, suggest that it is a good candidate alloy for use in metal/ceramic brazing to the AS-800 silicon nitride material.

Paloro ABA alloy. Constant true strain rate tensile tests have been completed for this alloy; the creep test matrix at lower temperatures (250-450°C) is still incomplete. The elevated temperature

creep properties of Paloro ABA are well characterized by a power law creep equation with n=3.46 and an activation energy of 50.64 kcal/mole. The tensile data indicate that Paloro ABA alloy is stronger than conventional Paloro alloy at elevated temperatures.

III. Oxidation Properties of Braze Alloys and Interlayer Materials

Static air oxidation tests were run on both candidate interlayer materials and braze alloys. All oxidation tests were run in static air using a Thermolyne Type 15 box furnace equipped with a 4 x 4 x 12 inch hot zone. Prior to testing, samples were solvent cleaned and weighed using a Metler M5 balance, capable of resolving approximately 2 μg. The samples were hung from alumina ceramic boats, and were inserted into the furnace at the desired oxidation temperature. A standard run cycle of 20 hr was used, followed by a furnace cool to room temperature. The samples were then re-weighed, and sent though another furnace cycle. Total run times of 100 hr or 200 hr were typically used, although some samples were pulled at 1/2 the maximum run time and cross sectioned for comparison purposes. All samples were longitudinally cross sectioned following the run to obtain evidence of oxide scales and/or internal oxidation.

A. Oxidation Test Results - Braze Alloys

A.1 Oxidation of Palco and Palni Alloys

Wire samples measuring 0.019 inches in diameter were used to compare the oxidation properties of the Palco and Palni alloys. Samples of both alloys measuring approximately 2 inches in length were hung across an alumina boat, and oxidized repeatedly through the 20 hr oxidation cycles described above at both 900 and 1000°C. The weight gain for Palco alloy is shown in Fig. 37; weight gain data obtained at 600°C for a separate SNL project are included for completeness. The solid lines shown in Fig. 37 are a parabolic rate equation fit to the oxidation data. We express the parabolic rate constant, k^2, for Palco as an Arrhenius expression:

$$k^2\ (g^2/cm^4\text{-hr}) = 4.893 \times 10^{-3}\ \exp(-21{,}299/RT) \qquad (9)$$

The data set for Palco was used to obtain the expression for k^2 in Eq. (9), and a correlation coefficient (r^2) of 0.913 was obtained for all three temperatures. The expression for k^2 permits prediction of the normalized weight gain (NWG) at a particular temperature as follows:

$$NWG\ (g/cm^2) = (k^2\ time(hr))^{1/2} \qquad (10)$$

While the parabolic rate fit works well at 600°C, it is clearly inadequate to describe the oxidation behavior of Palco alloy at 1000°C. As will be discussed below, this is due to a transition in oxidation behavior from external scale formation to internal oxidation.

Oxidation results for the Palni alloy are shown in Fig. 38, along with a parabolic fit to the oxidation data:

$$k^2\ (g^2/cm^4\text{-hr}) = 1.2431\ \exp(-37{,}390/RT) \qquad (11)$$

The data set for Palni at 900 and 1000°C produced a correlation coefficient (r^2) of 0.980. Clearly, the parabolic rate expression fits the Palni oxidation data set better than the data set for Palco alloy.

Metallographic cross sections were obtained for the 200 hr samples of Palni and Palco alloys at both temperatures. Figure 39 shows the cross sections for the 200 hr samples run at 900°C. At this temperature, the Palco alloy (Fig. 39(a)) exhibits both external scale formation, which appears to be quite porous, coupled with extensive internal oxidation. By comparison, the Palni alloy (Fig. 39(b))

exhibits what appears to be a denser, more adherent oxide scale, along with relatively limited internal oxidation. The samples oxidized at 1000°C are shown in Fig. 40. Interestingly enough, there is very little difference in the appearance of the 1000°C Palco alloy (Fig. 40(a)) relative to the 900°C sample (Fig. 39(a)). This is reasonably consistent with the weight gain data for Palco at these two temperatures - where there is relatively little difference in the 900 vs. 1000°C curves, and both curves suggest that oxidation in the wire sample geometry has been saturated by 80-100 hr. On the other hand, the 1000°C Palni sample shows a dramatic difference in microstructure relative to the 900°C sample. While internal oxidation is limited in Palni alloy at 900°C, it is extensive and throughout the sample at 1000°C. These results suggests that the external oxide scale in Palni is somewhat protective at 900°C, but by 1000°C provides no protection.

On the basis of the oxidation results, the superior oxidation performance of Palni relative to Palco at 900°C led to the elimination of Palco as a candidate alloy in this study. Further mechanical properties work was carried out on with the Palni alloy but only a limited amount of mechanical properties data was generated for the Palco alloy.

A.2 Oxidation of Paloro and Paloro ABA Alloys

Strip samples measuring approximately 1 in long by 1/2 in wide by 0.003 in thick were used to evaluate the oxidation behavior of Paloro and Paloro ABA alloys. The results for Paloro alloy, shown in Fig. 41, indicate virtually no observable weight gain following 200 hr oxidation at either 900 or 1000°C. This is understandable in view of the high Au content (92 wt.%) of this alloy, and suggests that the 8% Pd addition plays no role in the oxidation behavior.

The oxidation behavior of Paloro ABA was quite different from that of the conventional Paloro alloy. Tests run at both 900 and 1000°C showed significant weight loss, as shown in Fig. 42. Following the oxidation runs, the samples were metallographically cross sectioned and subjected to electron microprobe analysis. Backscattered electron micrographs of samples oxidized at both temperatures are shown in Fig. 43. The results of the microprobe analysis for both 900 and 1000°C samples indicate the following: (1) A significant amount of the remaining V in the alloy has segregated into large oxide inclusions that appear to be close to the stoichiometry of V_2O_5 and/or VO_2, and (2) only about 0.25 wt.% V remains in the bulk alloy. The microprobe results suggest a hypothesis about oxidation of Paloro ABA alloy: the V addition diffuses to the surface, reacting with oxygen gas to form volatile vanadium oxides, producing the observed weight loss. It should be noted that none of the vanadium oxide inclusions observed in Fig. 43 intersect the surface, suggesting that they would probably volatilize if they were exposed to the atmosphere under oxidizing conditions at elevated temperatures. See, for example, the void near the surface in Fig. 43(a) that apparently at one time contained one of the coarse vanadium oxide particles.

These results suggest that braze joints made with Paloro ABA alloy will need to be coated for oxidation resistance. One possible approach could be to pack chromize or aluminize the material in order to form a protective oxide coating for the braze joint when exposed to oxidizing conditions.

B. Oxidation Test Results - Interlayer Materials

B.1 Kentanium Gr162B

Four air oxidation tests were run on Kentanium Grade 162B material: samples were run at 900 and 1000°C for either 100 or 200 hr total exposure time. Normalized weight gain data obtained from strips of the Kentanium Grade 162B at 900 and 1000°C are shown in Fig. 44. Note that while the two samples run at 900°C exhibit reasonably consistent data, the 100 hr sample at 1000°C shows somewhat higher oxidation rates relative to the 200 hr sample. Micrographs showing the cross sections of the 1000°C samples are shown in Fig. 45. The oxidation scale appears to be in two bands: an outer scale that appears to be free of inclusions, along with an inner scale with large number of inclusions. It would appear that the inner scale is the result of internal oxidation. Longer term oxidation in Kentanium Grade 162B at 1000°C appears to proceed primarily by means of internal oxidation - i.e., the external scale is not protective. By comparison, the samples oxidized at 900°C are shown in Fig. 46. In this case, there is only a limited amount of internal oxidation apparent. This suggests that either the external scale is protective at 900°C, or else the diffusion processes that lead to the rapid internal oxidation processes at 1000°C are much diminished.

B.2 Comparison of Kentanium Gr162B Oxidation with Kovar Alloy

A previous survey of the oxidation of Kovar alloy[6] determined that the oxidation of this alloy in air at temperatures from 750 to 1100°C can be represented by a parabolic rate equation. These predictions are included so that a comparison can be drawn with the Kentanium Grade 162B interlayer material.

The data of Pask,[7] Piscitelli et al.,[8] and Abendroth[9] were used to determine that a single equation can be used to represent the parabolic rate constant for oxidation of Kovar alloy over the temperature range 750-1100°C as follows:

$$k^2\ (g^2/cm^4\text{-hr}) = 1.843 \times 10^4 \exp(-52{,}232/RT) \qquad (12)$$

Both Piscitelli et. al. and Abendroth found that the dominant oxide species present at these high temperatures is the spinel (Fe, Co, Ni)$_3$O$_4$, which is presumably a protective scale. This correlation can be used to obtain a prediction for the normalized weight gain (NWG) of Kovar alloy as a function of time:

$$NWG\ (g/cm^2) = (k^2\ time(hr))^{1/2} \qquad (13)$$

We have used the correlation given in Eq. 13 to construct a prediction for the oxidation of Kovar alloy at 900 and 1000°C; this prediction is plotted in Fig. 47 along with the 200 hr data for Kentanium Grade 162B at these temperatures. Clearly, the Kovar alloy is expected to oxidize at a much faster rate at both temperatures relative to the Grade 162B composite.

These results suggest the Kentanium Grade 162B composite would be preferred over Kovar alloy with respect to oxidation properties. However, other materials compatibility issues with respect to brazing tended to favor the use of Kovar as an interlayer material.

IV. Other Physical Properties

A. Thermal Expansion of Paloro ABA Alloy, and Comparison with Published Data for Palco Alloy

Thermal expansion of the Paloro ABA alloy was determined over the temperature range 23-1000°C. The 1/8 in diameter sample had a length of 25.46 mm (1.002 in), and was run using a Netzsch dilatometer, run with silica pushrods. The data was referenced to a 94% alumina standard. The expansion data for this material can be fit to the following polynomial:

$$dL/L\ (\%) = -0.043394 + (1.4433e\text{-}3 * T(°C)) + (1.0543e\text{-}7 * T^2) \qquad (14)$$

with a high correlation factor. This fit to the dilatation data is plotted in Fig. 48, along with the thermal expansion data for a 64Pd-36Co alloy (nominal composition corresponding to the Palco braze alloy) obtained from the literature.[10] The Palco data over the range 20-693°C were fit to the following second order polynomial:

$$dL/L\ (\%) = -0.039988 + (1.3337e\text{-}3 * T(°C)) + (2.5664e\text{-}8 * T^2) \qquad (15)$$

Note that the leading constant in both of the above polynomial expressions has been arbitrarily adjusted so that dL/L = 0 at 30°C. The results in Fig. 48 indicate that the Palco alloy has a slightly lower coefficient of thermal expansion than the Paloro ABA alloy. This can be rationalized in light of the relatively high CTE for pure Au relative to pure Pd.

B. Dynamic Moduli Data for Palni Alloy

Dynamic modulus measurements were performed for the Palni alloy over the temperature range 23-900°C by J. H. Gieske, SNL Dept. 9752. The dynamic modulus experiments involve

measurement of both longitudinal and shear ultrasonic wave velocities as a function of temperature. In order to compute Young's Modulus (E), Shear Modulus (G), and Poisson's Ratio (ν), it is necessary to assume isotropic elastic behavior. A summary of the data is shown in Table 10. Based on these data, this alloy appears to have a magnetic transition point of approximately 240°C - as evidenced by the relative maximum in the ultrasonic shear wave velocity at this temperature. It is not clear why the moduli increase above 600°C. The following sixth order polynomials were obtained as representations of E, G and ν as a function of temperature:

$$E\ (GPa) = 21.4 + 0.0186\ T(°C) - 9.98e\text{-}5\ T^2 + 5.15e\text{-}7\ T^3 - 1.51e\text{-}9\ T^4 + 1.90e\text{-}12\ T^5 - 8.40e\text{-}16\ T^6 \quad (16)$$

$$G\ (GPa) = 53.88 + 0.05048\ T(°C) - 2.627e\text{-}4\ T^2 + 1.462e\text{-}6\ T^3 - 4.42e\text{-}9\ T^4 + 5.648e\text{-}12\ T^5 - 2.503e\text{-}15\ T^6 \quad (17)$$

$$\nu = 0.3711 - 1.275e\text{-}4\ T(°C) + 5.965e\text{-}7\ T^2 - 4.787e\text{-}9\ T^3 + 1.574e\text{-}11\ T^4 - 2.027e\text{-}14\ T^5 + 8.928e\text{-}18\ T^6 \quad (18)$$

Table 10. Dynamic moduli data for Palni (60Pd-40Ni) alloy. The moduli are calculated from the longitudinal and the shear ultrasonic velocities. The magnetic transition point is approximately 240°C.

Temperature (°C)	Longitudinal Wave Velocity (mm/μsec)	Shear Wave Velocity (mm/μsec)	Young's Modulus (GPa)	Shear Modulus (GPa)	Poisson's Ratio
23	5.0981	2.3077	150.24	54.88	0.369
50	5.0327	2.3183	152.68	55.90	0.366
100	4.9838	2.3508	156.16	57.38	0.361
150	4.9742	2.3815	158.97	58.63	0.356
200	4.9677	2.3992	161.31	59.73	0.350
250	4.9513	2.4012	162.97	60.56	0.346
300	4.9263	2.3903	163.59	60.95	0.342
350	4.9017	2.3717	162.94	60.79	0.340
400	4.8884	2.3512	160.99	60.03	0.341
450	4.8952	2.3332	157.98	58.79	0.344
500	4.9256	2.3200	154.46	57.30	0.348
550	4.9773	2.3117	151.15	55.90	0.352
600	5.0414	2.3058	148.90	54.95	0.355
650	5.1050	2.2987	148.43	54.74	0.356
700	5.1531	2.2871	150.14	55.45	0.354
750	5.1740	2.2695	153.74	56.99	0.349
800	5.1646	2.2498	157.89	58.78	0.343
850	5.1380	2.2399	159.69	59.56	0.341
900	5.1320	2.2637	154.21	57.18	0.349

V. Summary

Creep and tensile properties of the braze alloys used in this project were measured for use in Finite Element Analysis (FEA) stress predictions. Two creep regimes were observed for the Palni alloy; a low to intermediate temperature regime (~250-550°C) and a high temperature regime (~650-950°C). The data for this alloy fit a power law creep in both regimes. The stress exponents and the activation energies from a power law fit to the data in each regime suggest a transition from dislocation climb controlled creep at lower temperatures to solid solution strengthening controlled creep at the higher temperatures. The Paloro alloy also exhibited two distinct creep regimes; the low temperature regime (250-550°C) data fit the Garofalo sinh equation and the high temperature regime (550-850°C) fit a power law equation. Oxidation behavior of the braze alloys and interlayer materials was measured to aid in the selection of the best materials for use in metal/ceramic brazing. Because of the superior oxidation resistance of the Paloro alloy relative to the Palni and Palco alloys, and its promising creep behavior relative to other commonly used braze alloys, its coefficient of thermal expansion and modulus measurements were also measured, along with those for Paloro ABA. Weight losses measured for Paloro ABA during oxidation measurements and microstructural evaluations suggested that the vanadium in this braze alloy was reacting with oxygen to form volatile oxides. Oxidation tests on the two candidate interlayer materials, Kentanium Gr162B and a Kovar alloy showed that Kentanium has better oxidation resistance.

VI. REFERENCES

1. J. J. Stephens and F. A. Greulich, "Elevated Temperature Creep and Fracture Properties of the 62Cu-35Au-3Ni Alloy," Metall. Trans. A, 26A, 1471-1482 (June, 1995).
2. J. Askill, Tracer Diffusion Data for Metals, Alloys, and Simple Oxides, New York: IFI/Plenum, pp. 35-36, (1970).
3. H. W. King, "Qualitative Size-Factors for Metallic Solid Solutions," J. Mater, Sci., 1, 79-90 (1966).
4. W. R. Cannon and O. D. Sherby, "High Temperature Creep Behavior of Class I and Class II Solid Solution Alloys," Metall. Trans., 1, 1030-1032 (1970).
5. F. Garofalo, Fundamentals of Creep and Creep-Rupture in Metals. New York: The MacMillan Company, pp. 50-52, 100-101, (1965).
6. J. J. Stephens, F. A. Greulich and L. C. Beavis, "High Temperature Grain Growth and Oxidation of Fe-29Ni-17Co (Kovar™) Alloy Leads," pp. 79-112 in Low Thermal Expansion Alloys and Composites. Edited by J. J. Stephens and D. R. Frear, TMS, Warrendale, PA (1994).
7. J. A. Pask, "New Techniques in Glass-to-Metal Sealing," Proceedings of the I. R. E. - Waves and Electrons Section, 36, 286-289 (February, 1948).
8. R. A. Piscitelli, S. K. Rhee and F. N. Bradley, "Oxidation of Fe-29Ni-17Co Alloy," J. Electrochem. Soc.: Solid State Sci. Tech., 123, #6, 929-933 (June, 1976).
9. R. P. Abendroth, "Oxide Formation and Adherence on an Iron-Cobalt-Nickel Glass Sealing Alloy," Mater. Res. Stand., 5, 459-466 (September, 1965).
10. Y. S. Touloukian, R. K. Kirby, R. E. Taylor and P. D. Desai, Thermal Expansion - Metallic Elements and Alloys. New York: IFI/Plenum, Vol. 12, pp. 752-753 (1976).

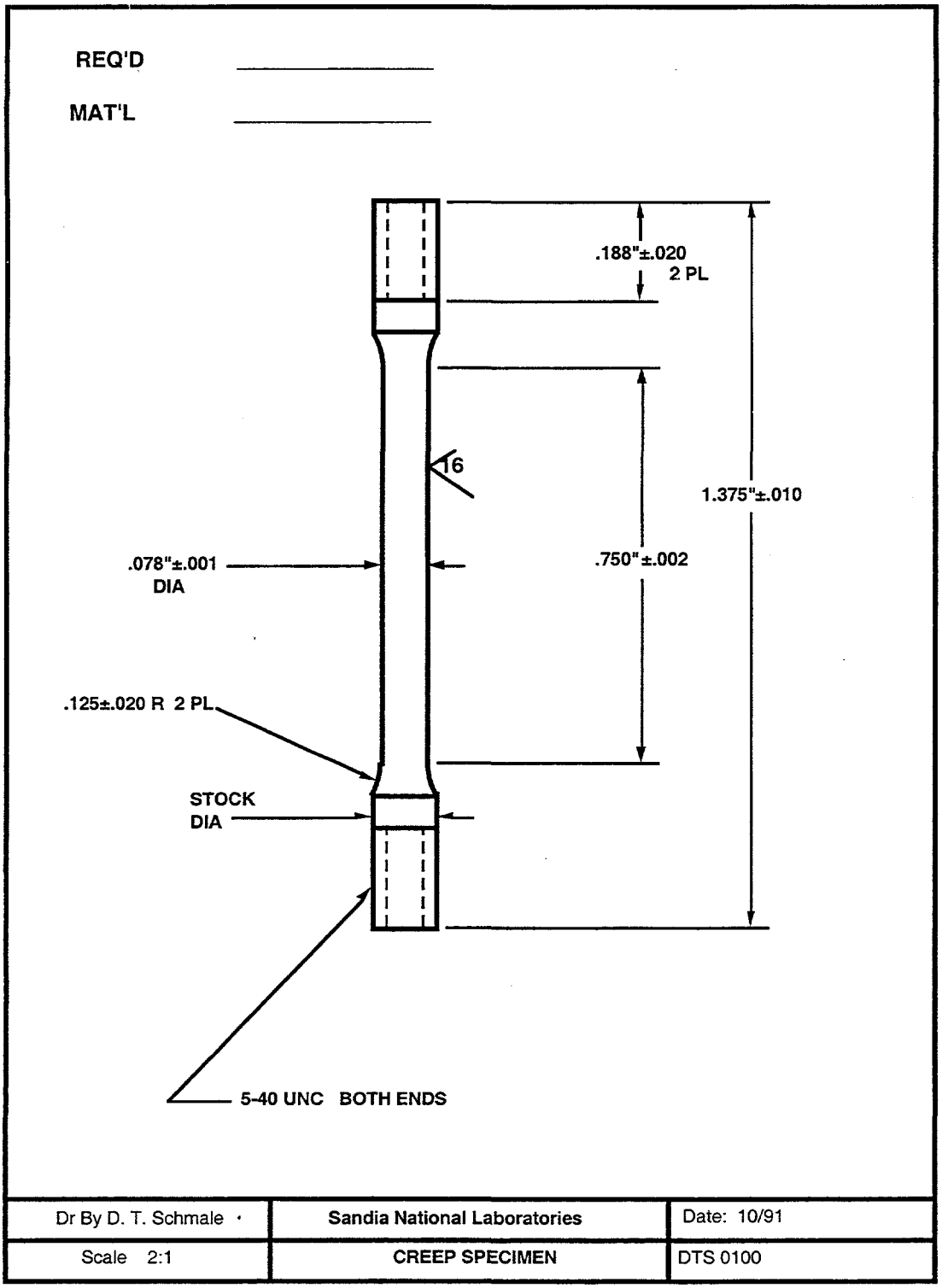

Fig. 1. Mechanical test specimen design used to study the high temperature creep and tensile properties of braze alloys. The (nominal) stock material diameter was 0.125 inches.

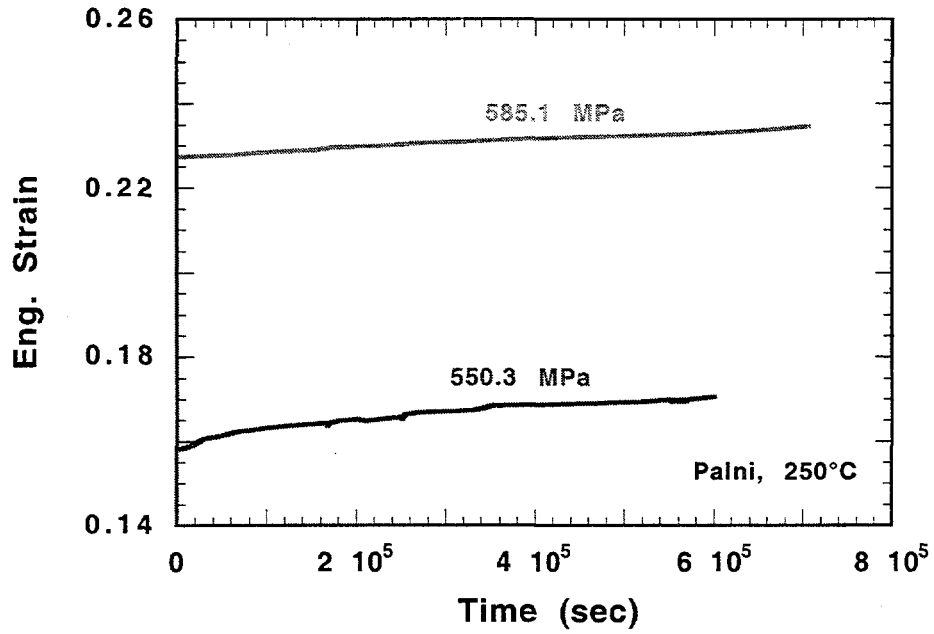

Fig. 2. Creep test strain-time plot for 250°C tests performed on annealed Palni alloy.

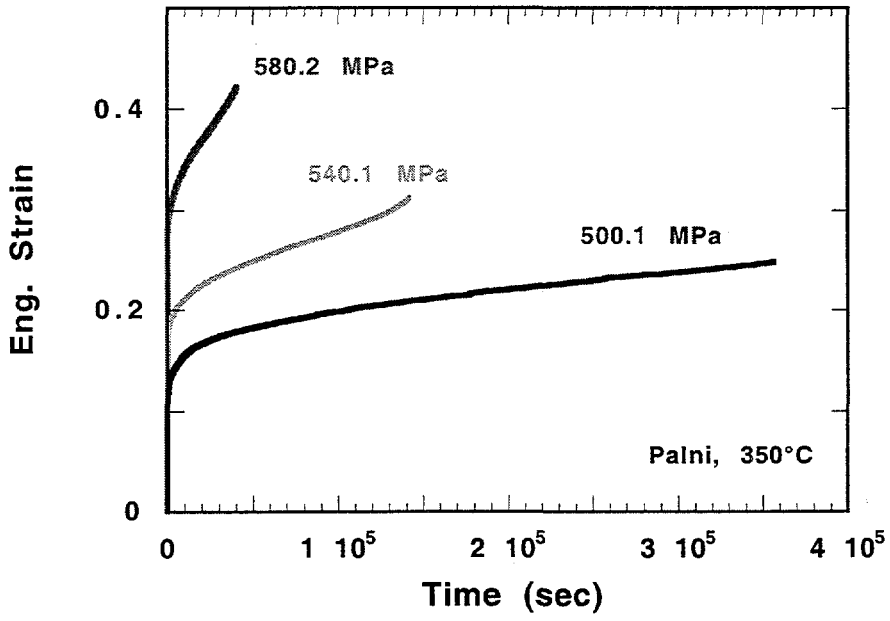

Fig. 3. Creep test strain-time plot for 350°C tests performed on annealed Palni alloy.

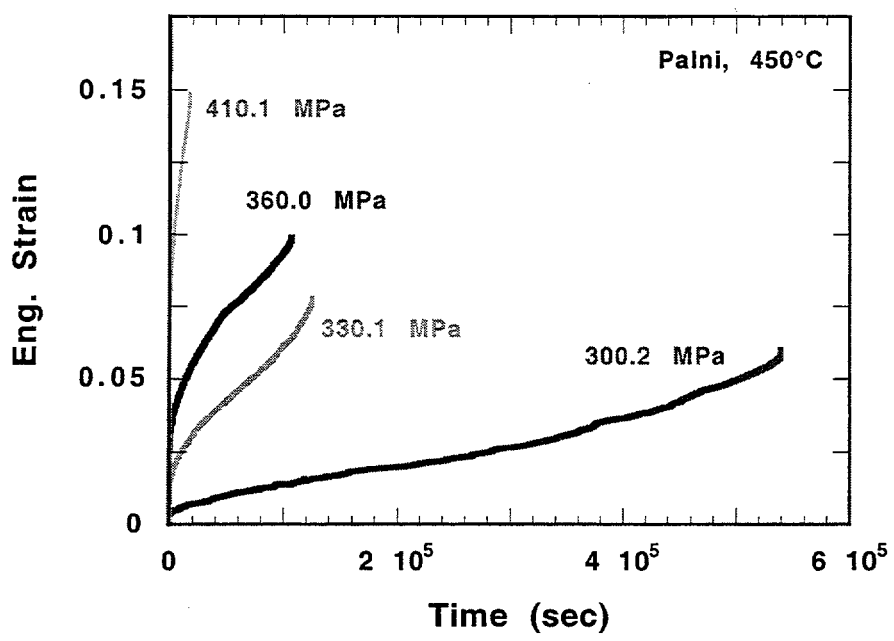

Fig. 4. Creep test strain-time plot (long-term data) for 450°C tests performed on annealed Palni alloy.

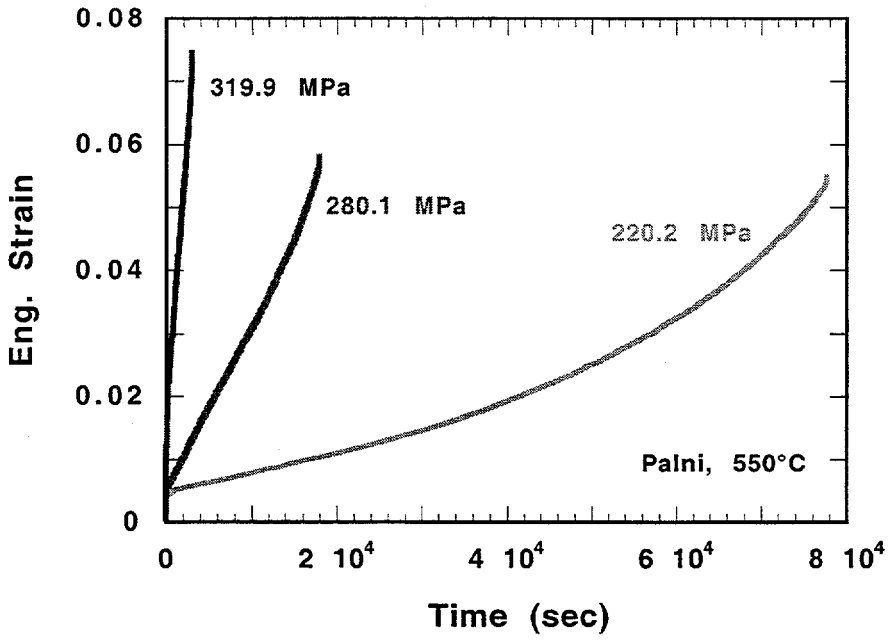

Fig. 5. Creep test strain-time plot for 550°C tests performed on annealed Palni alloy.

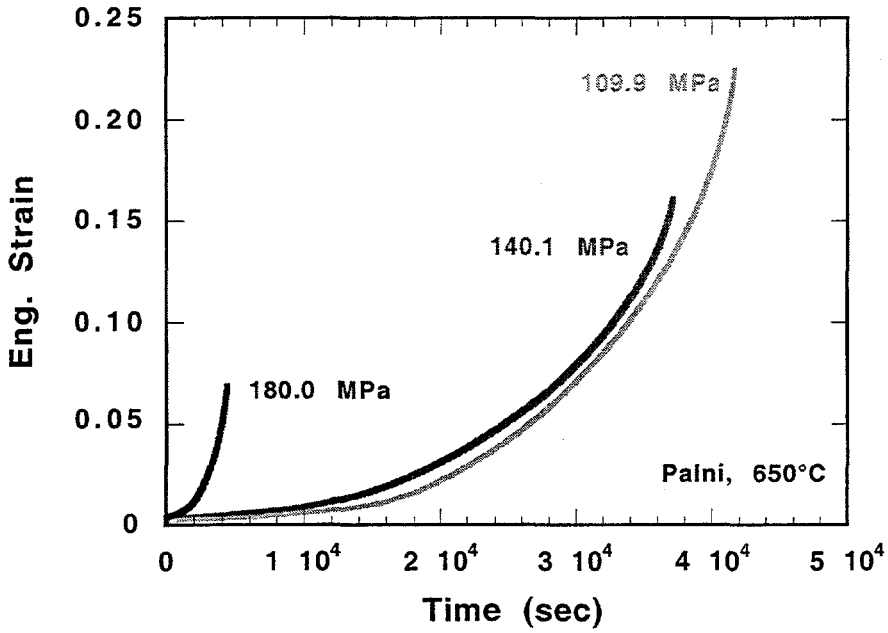

Fig. 6. Creep test strain-time plot for 650°C tests performed on annealed Palni alloy.

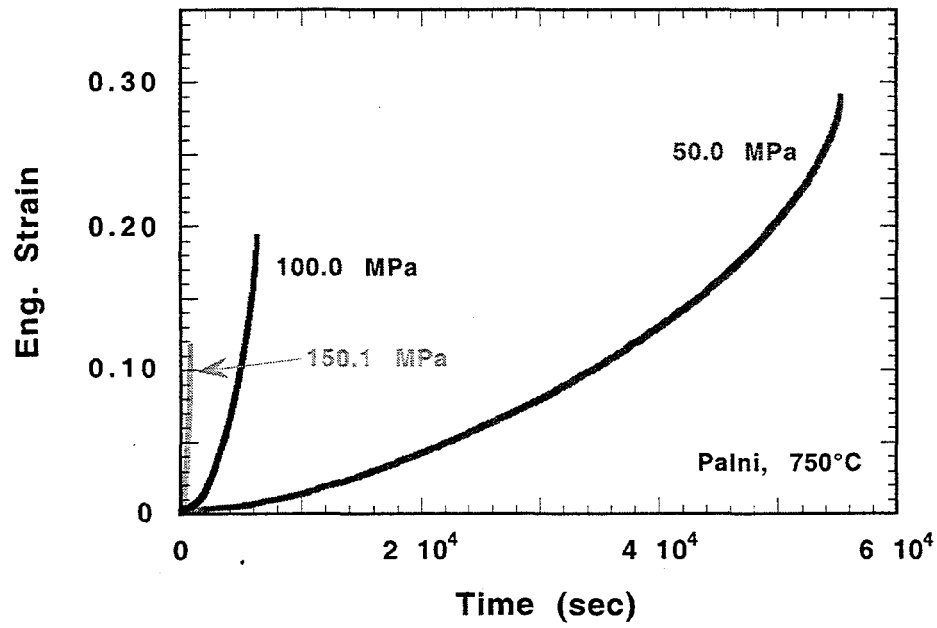

Fig. 7. Creep test strain-time plot for 750°C (long-term data) tests performed on annealed Palni alloy.

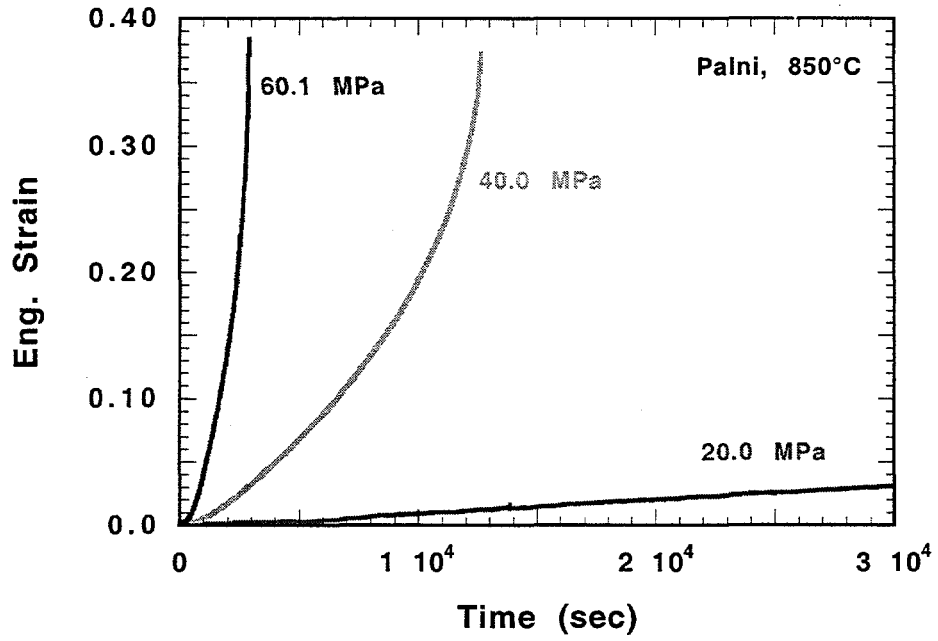

(a)

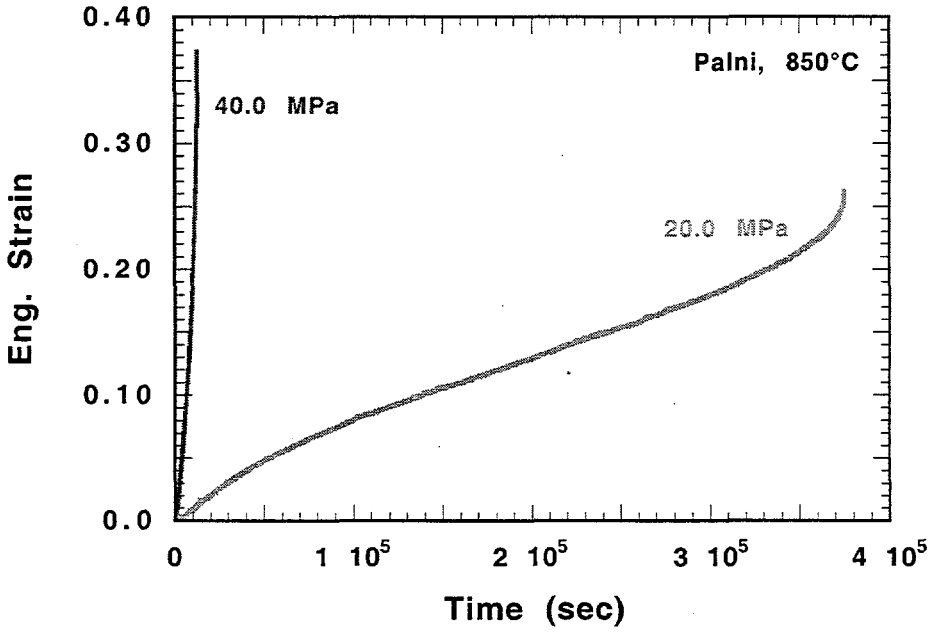

(b)

Fig. 8. Creep test strain-time plot for 850°C tests performed on annealed Palni alloy. (a) Short-term creep data. (b) Long-term creep data.

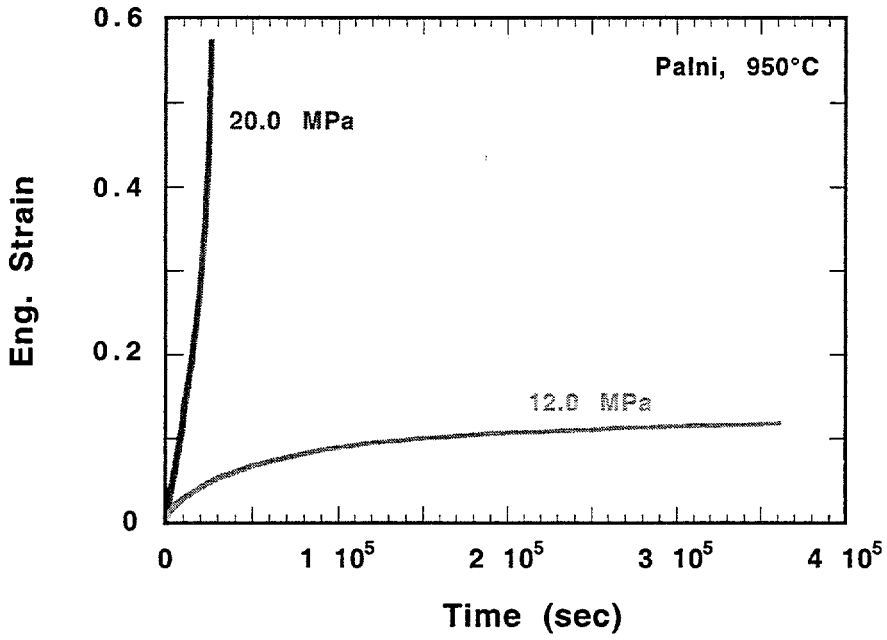

Fig. 9. Creep test strain-time plot for 950°C tests performed on annealed Palni alloy.

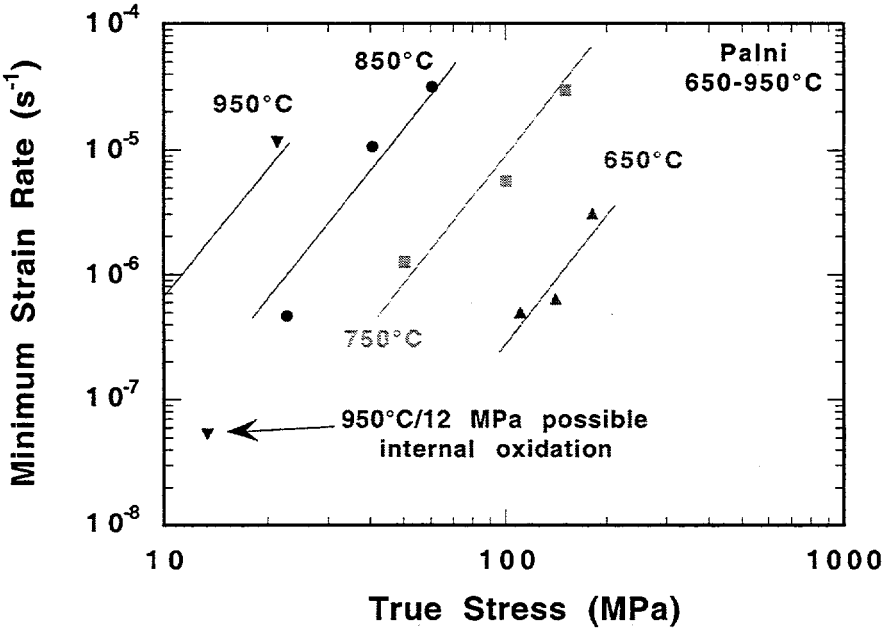

Fig. 10. Minimum strain rate as a function of true stress for annealed Palni alloy: 650-950°C tests. The trend lines shown are based on the high temperature power law fit discussed in the text. Note that the 12 MPa/950°C test has an unusually low creep rate due to internal oxidation.

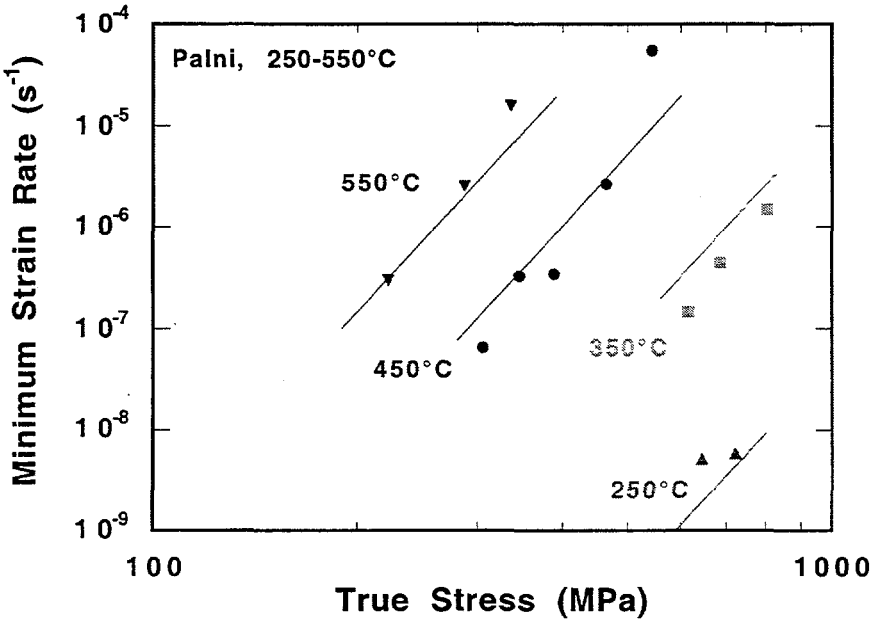

Fig. 11. Minimum strain rate as a function of true stress for annealed Palni alloy: 250-550°C tests. The trend lines shown are based on the low temperature power law fit discussed in the text.

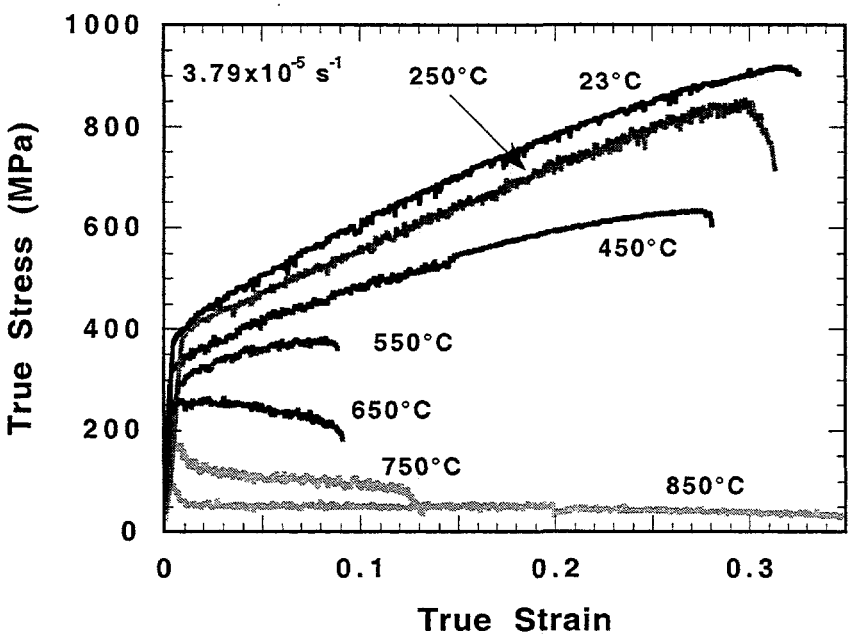

(a)

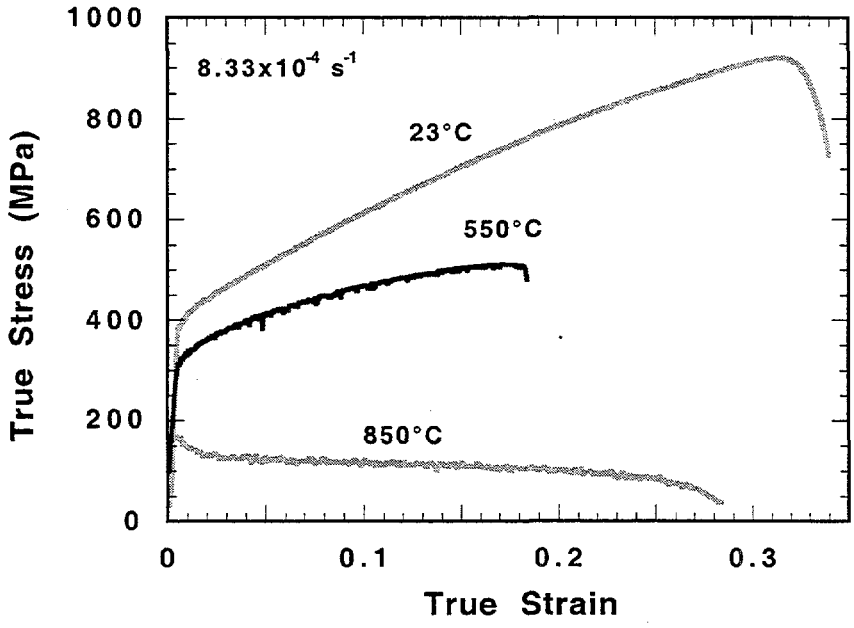

(b)

Fig. 12. Constant true strain rate tensile curves for Palni alloy. (a) Tests run at a constant true strain rate of 3.79 x 10^{-5} s^{-1}. (b) Tests run at a constant true strain rate of 8.33 x 10^{-4} s^{-1}.

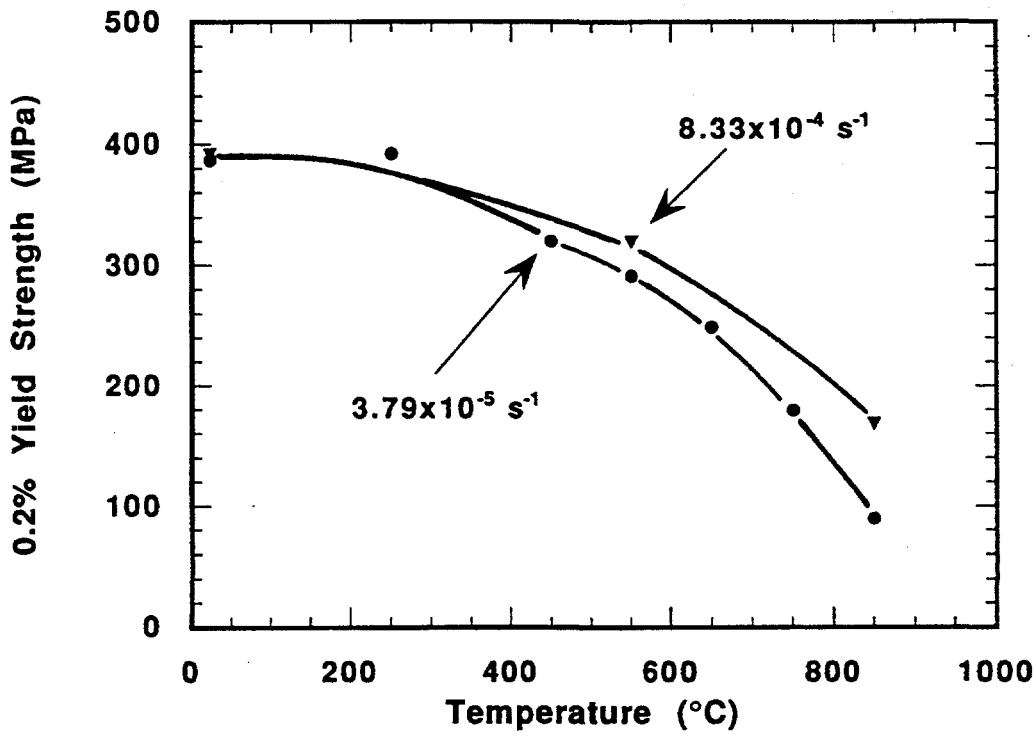

(a)

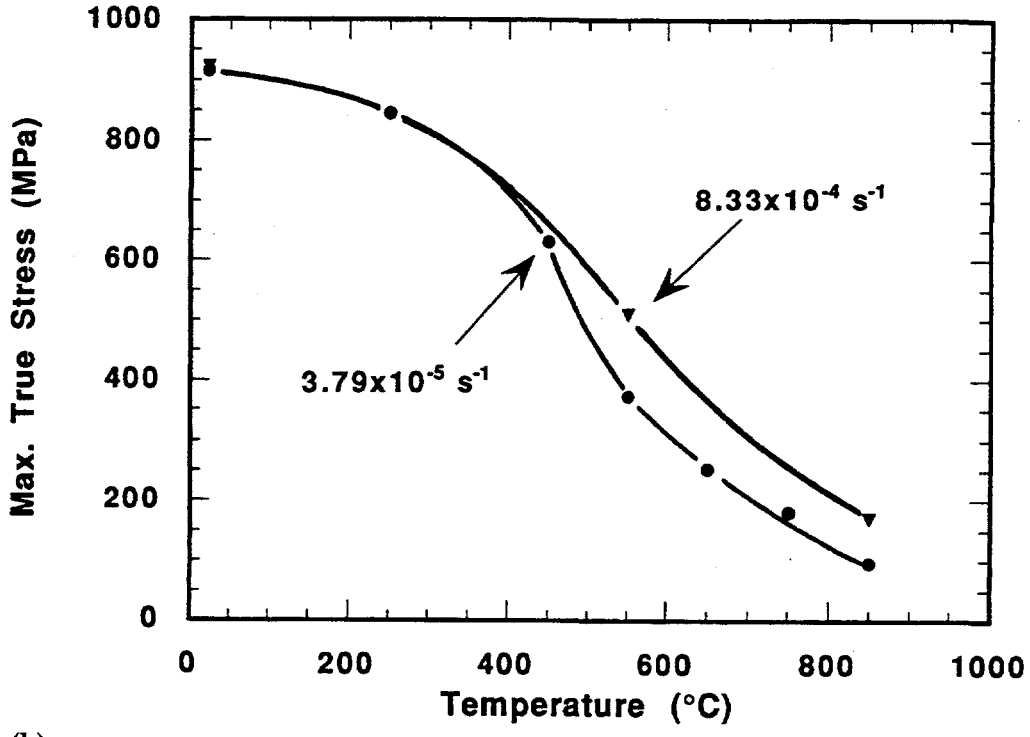

(b)

Fig. 13. Summary plots for Palni alloy tensile properties as a function of temperature. (a) 0.2% Offset Yield Stress as a function of temperature. (b) Maximum true tensile stress as a function of temperature.

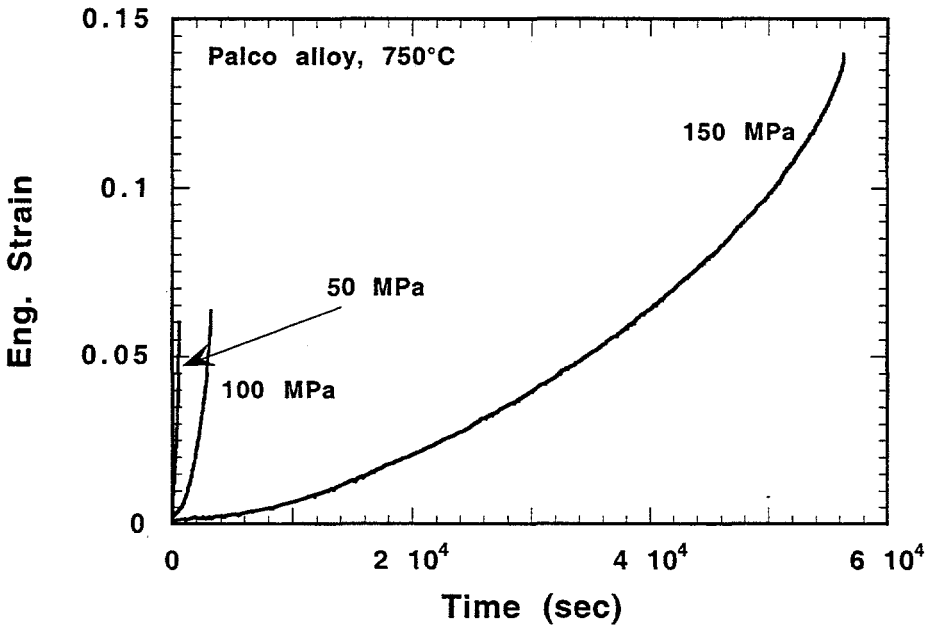

Fig. 14. Strain-time record for annealed Palco alloy tests at 750°C.

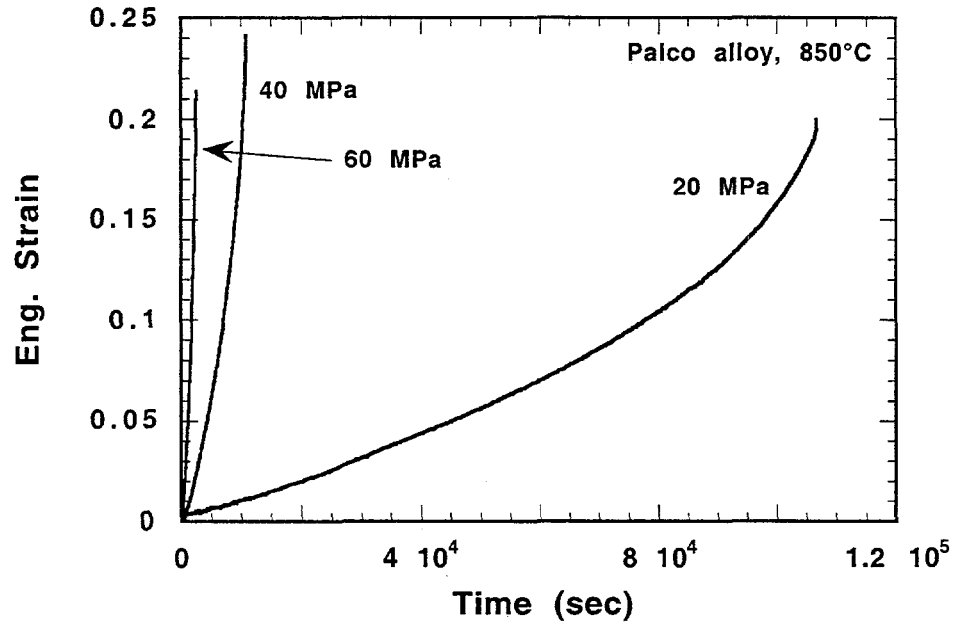

Fig. 15. Strain-time record for annealed Palco alloy tests at 850°C.

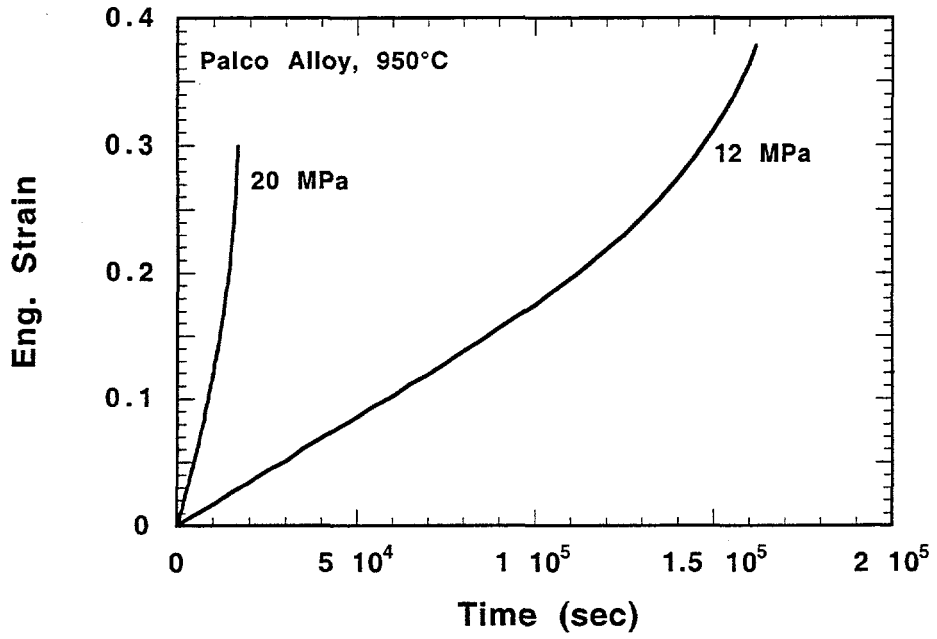

Fig. 16. Strain-time record for annealed Palco alloy tests at 950°C.

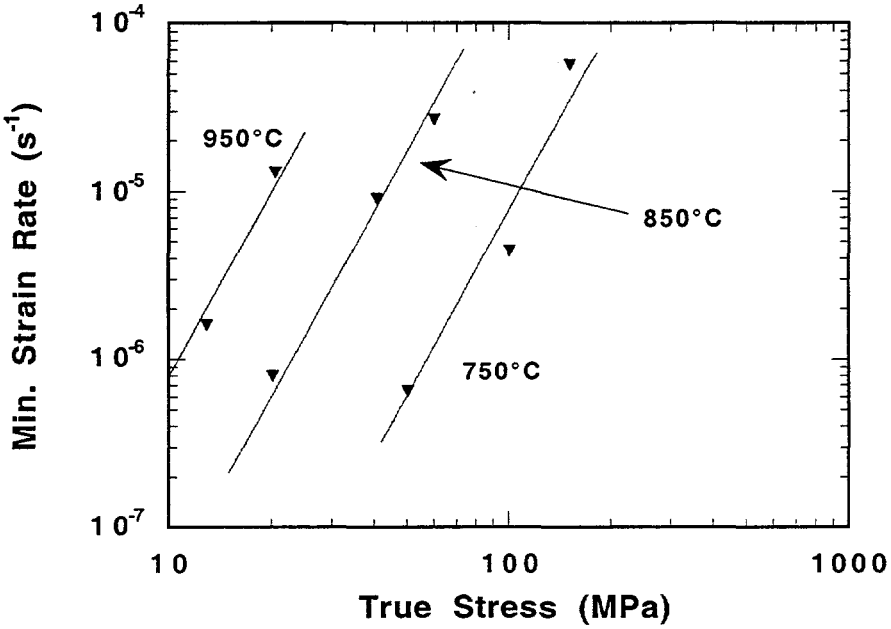

Fig. 17. Minimum true strain rate as a function of true stress for annealed Palco alloy. The trend lines shown are based on the power law equation discussed in the text.

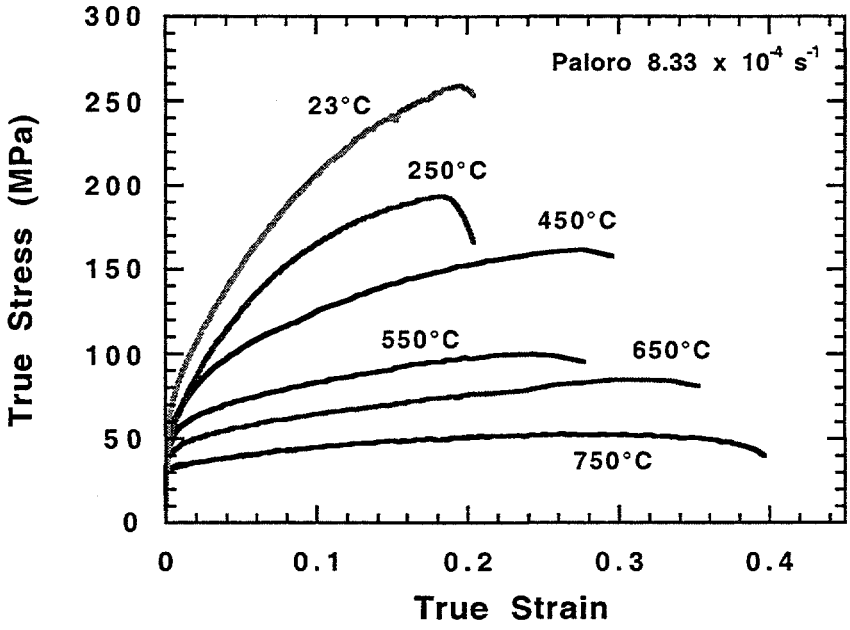

(a)

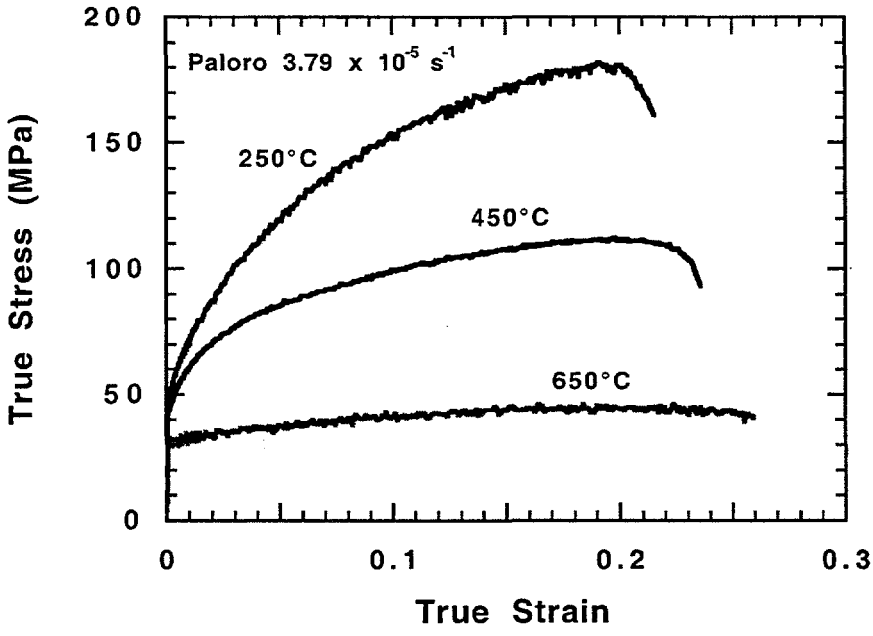

(b)

Fig. 18. Stress-strain curves for annealed Paloro alloy. (a) Tests run at a true strain rate of 8.33 x 10^{-4} s^{-1}. (b) Tests run at a true strain rate of 3.79 x 10^{-5} s^{-1}.

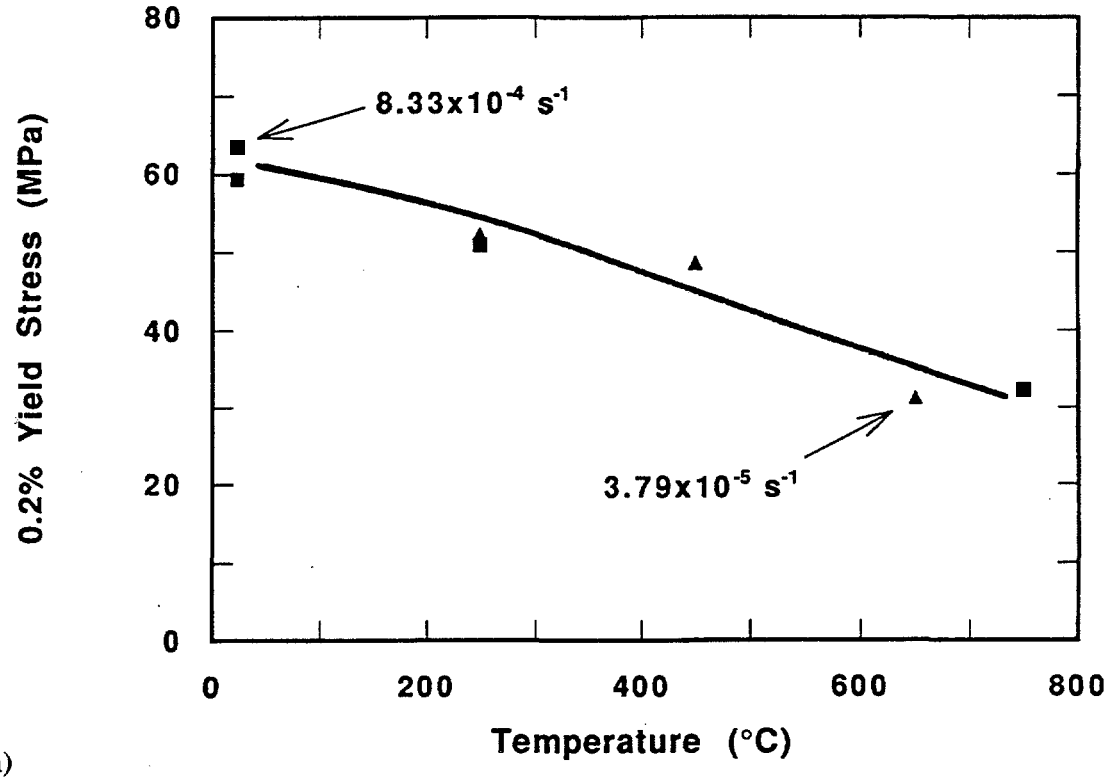

(a)

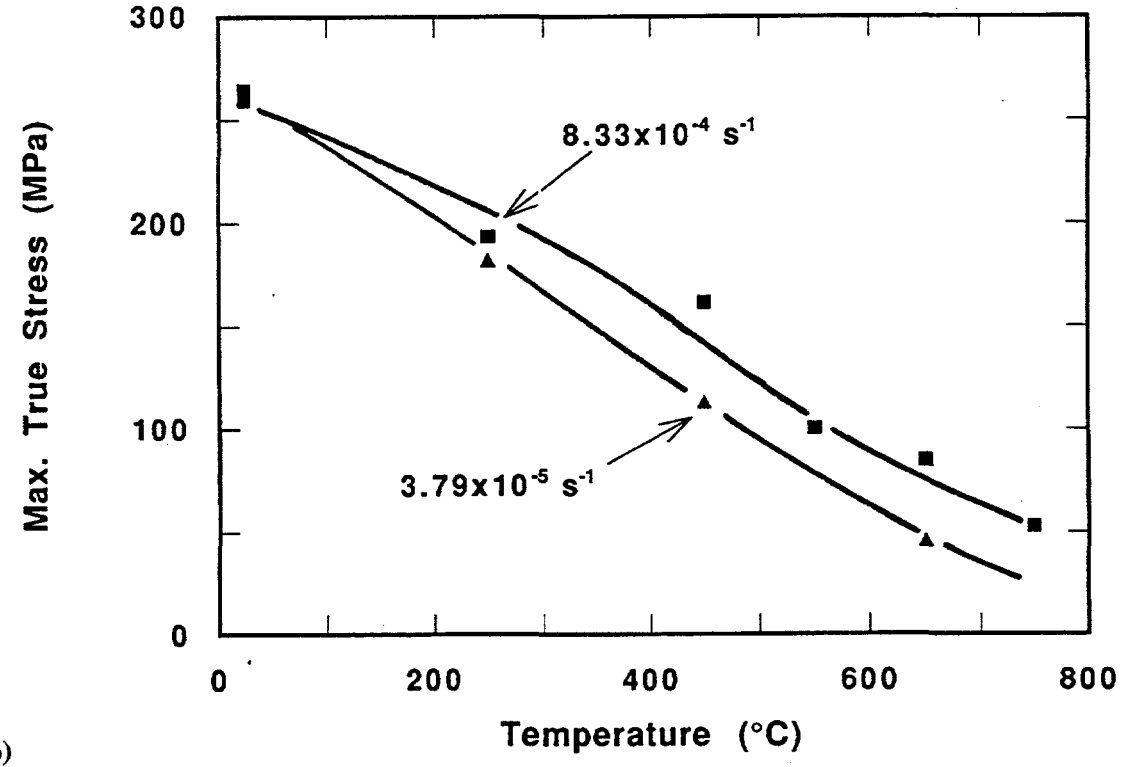

(b)

Fig. 19. Tensile trend curves for annealed Paloro alloy. (a) 0.2% Offset Yield Stress as a function of temperature. (b) Maximum true stress (true stress equivalent of UTS) as a function of temperature.

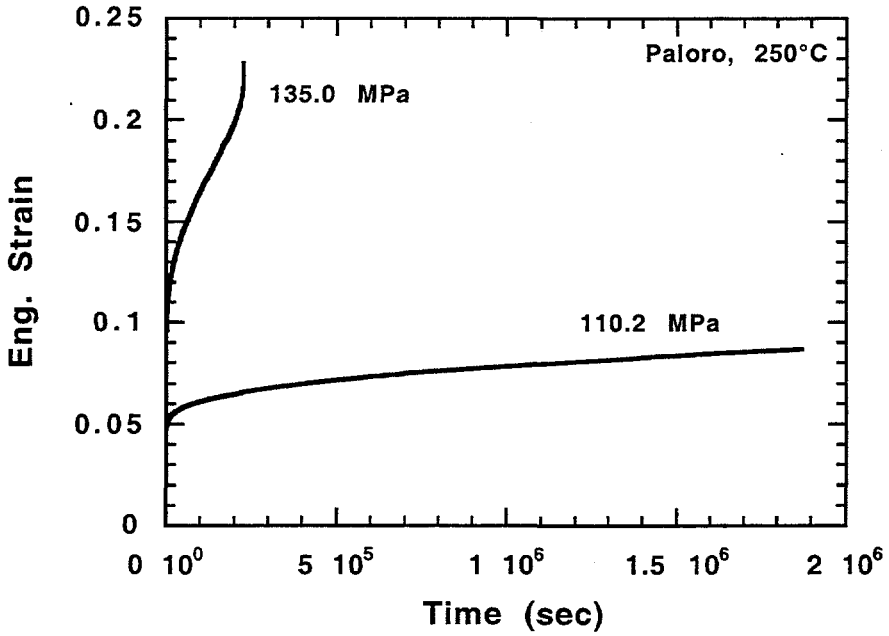

Fig. 20. Strain-time record (long-term creep data) for annealed Paloro alloy at 250°C.

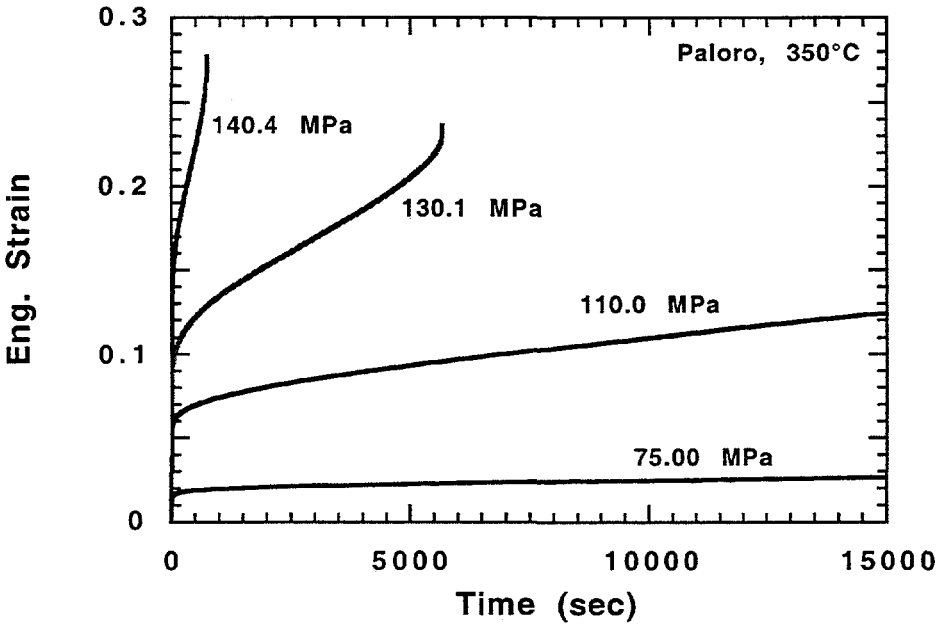

Fig. 21. Strain-time record (short-term creep data) for annealed Paloro alloy at 350°C.

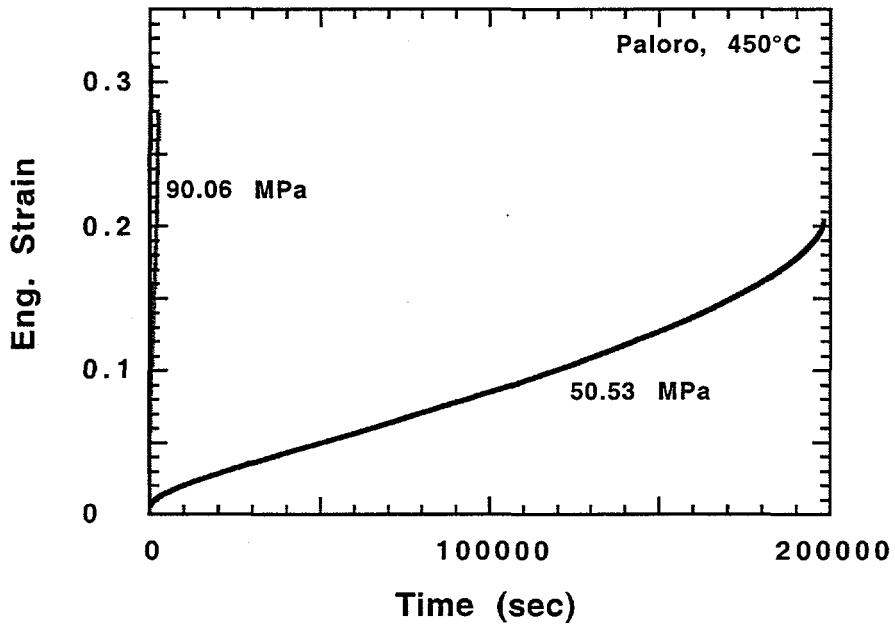

Fig. 22. Strain-time record (long-term creep data) for annealed Paloro alloy at 450°C.

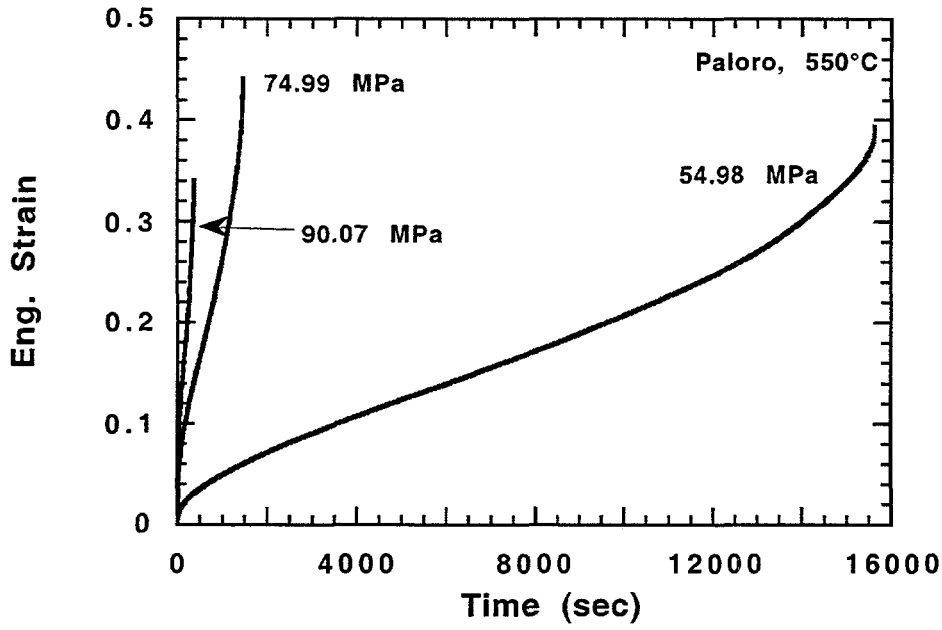

(a)

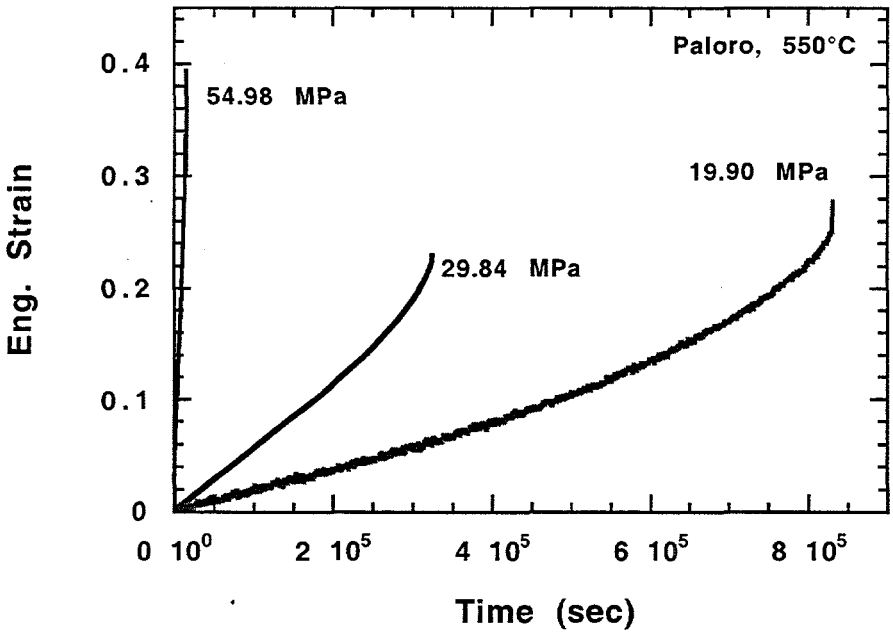

(b)

Fig. 23. Strain-time records for annealed Paloro alloy at 550°C. (a) Short-term creep data. (b) Long-term creep data.

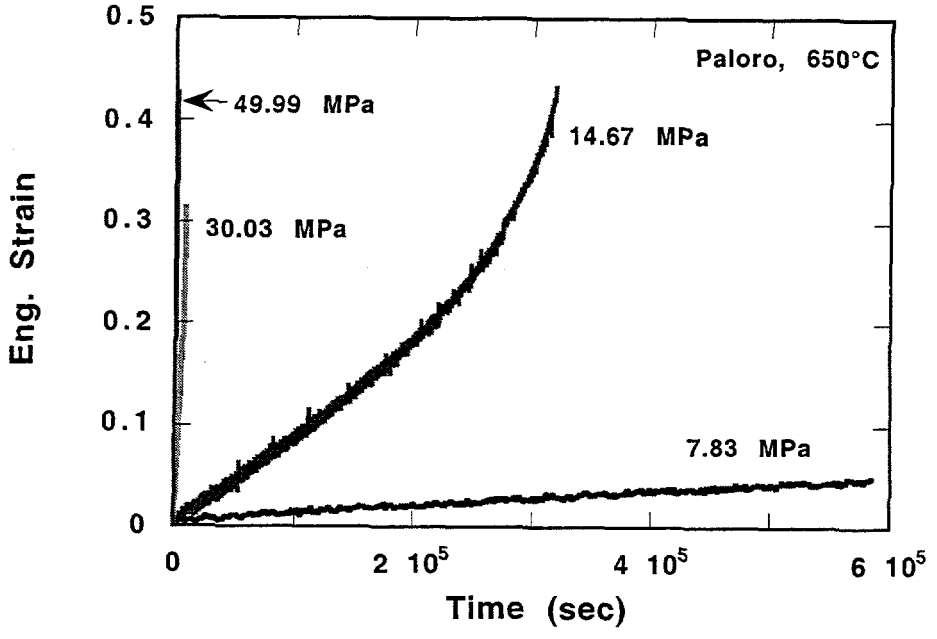

Fig. 24. Strain-time record (long-term creep data) for annealed Paloro alloy at 650°C.

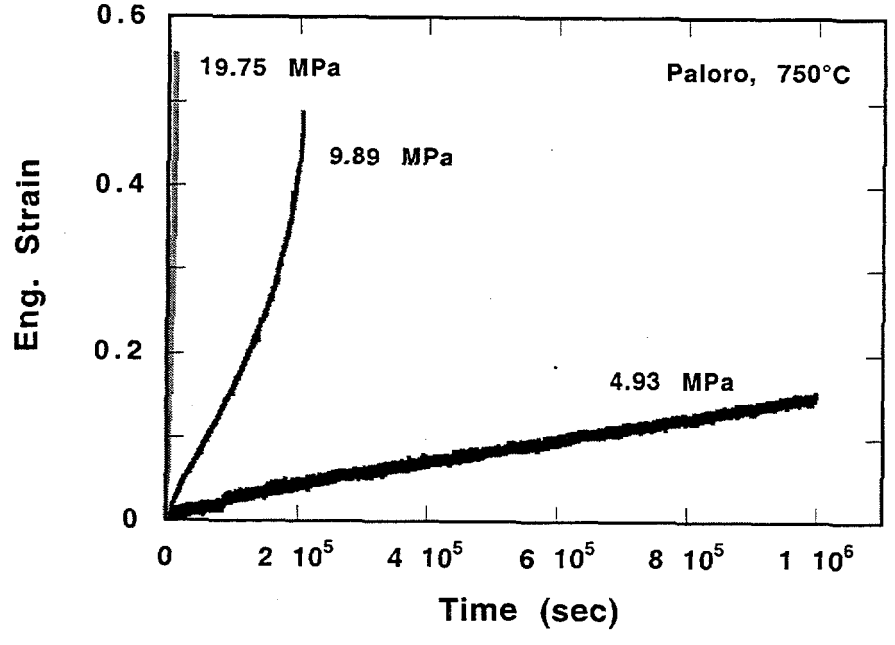

Fig. 25. Strain-time record (long-term creep data) for annealed Paloro alloy at 750°C.

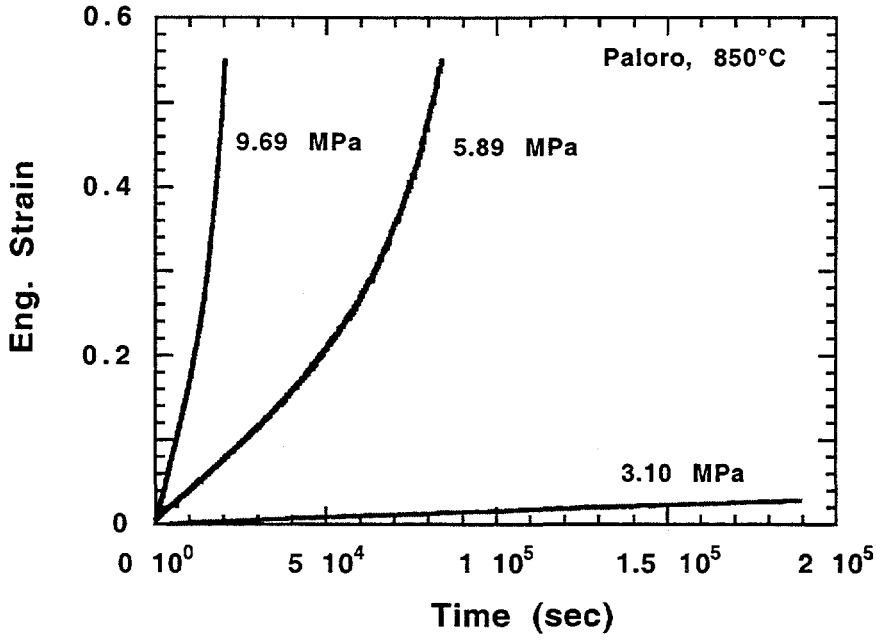

Fig. 26. Strain-time record for annealed Paloro alloy - creep tests at 850°C.

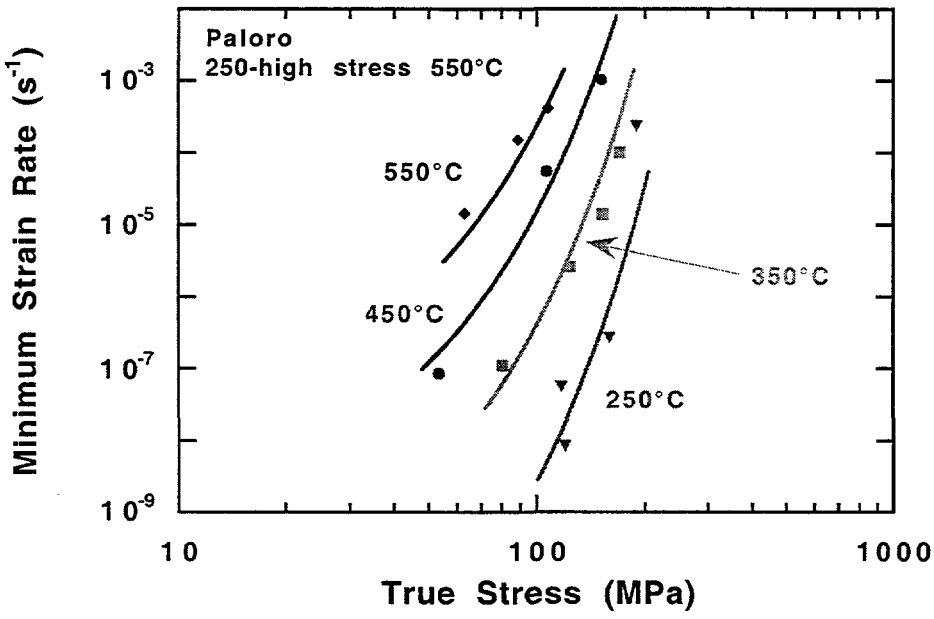

Fig. 27. Minimum strain rate as a function of true stress for annealed Paloro alloy, including data from 250-450°C, and the high stress data at 550°C. The trend line is the fit obtained with the Garofalo sinh equation discussed in the text.

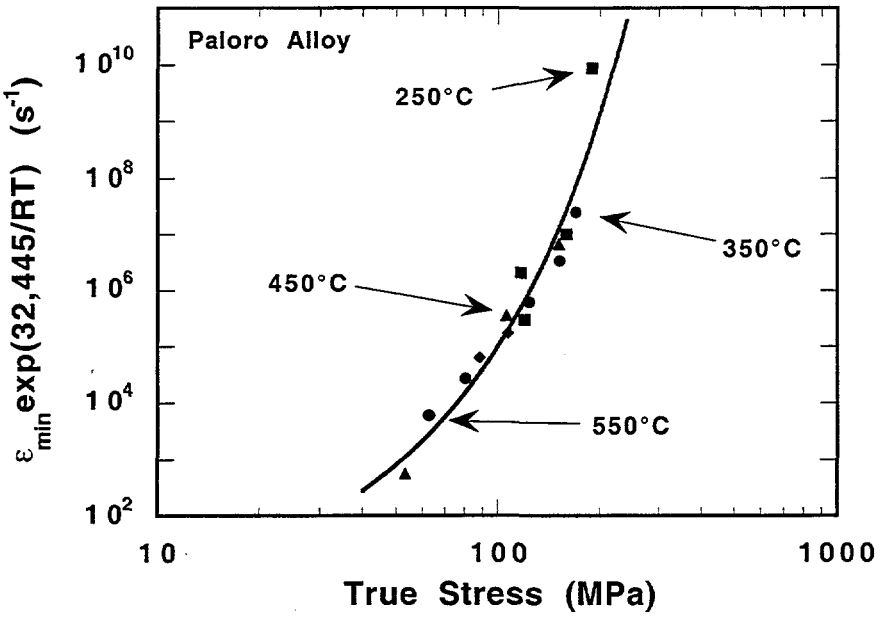

Fig. 28. Zener-Holloman plot of the low temperature data set for annealed Paloro alloy, including data from 250-450°C, and the high stress data at 550°C. The trend line is the fit obtained with the Garofalo sinh equation discussed in the text.

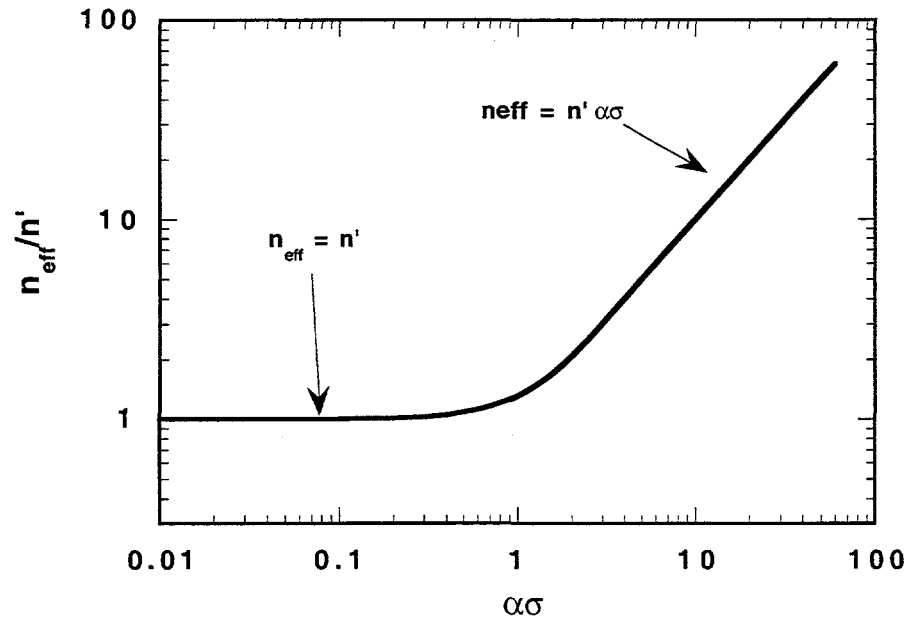

Fig. 29. Plot of n_{eff} as a function of ασ for the Garofalo sinh equation. This plot indicates that power law breakdown begins to occur close to where ασ ~ 1.

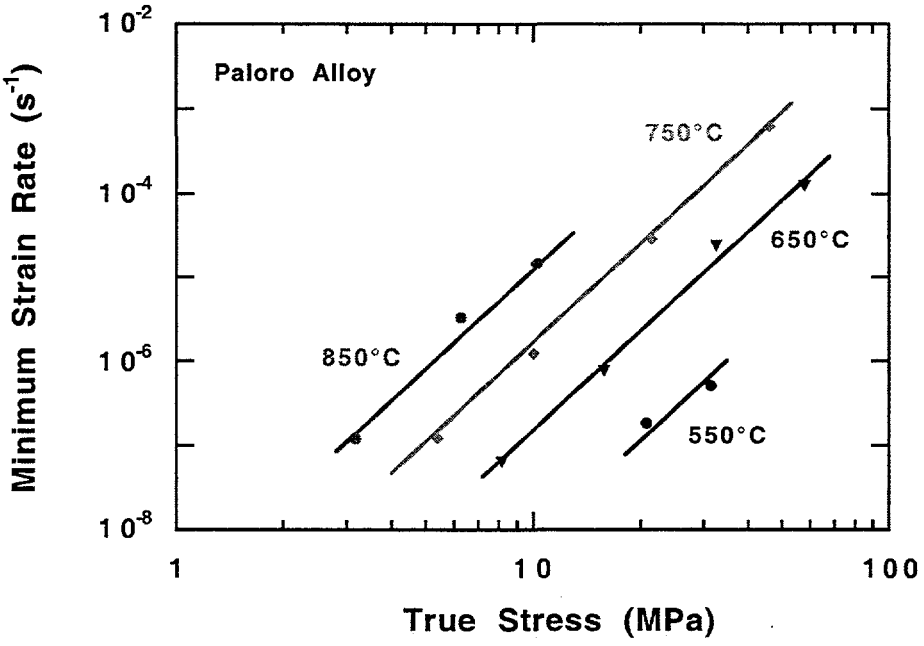

Fig. 30. Minimum strain rate as a function of true stress for annealed Paloro alloy, including low stress data at 550°C and 650-850°C data. The trend lines indicate the fit obtained with the power law equation discussed in the text.

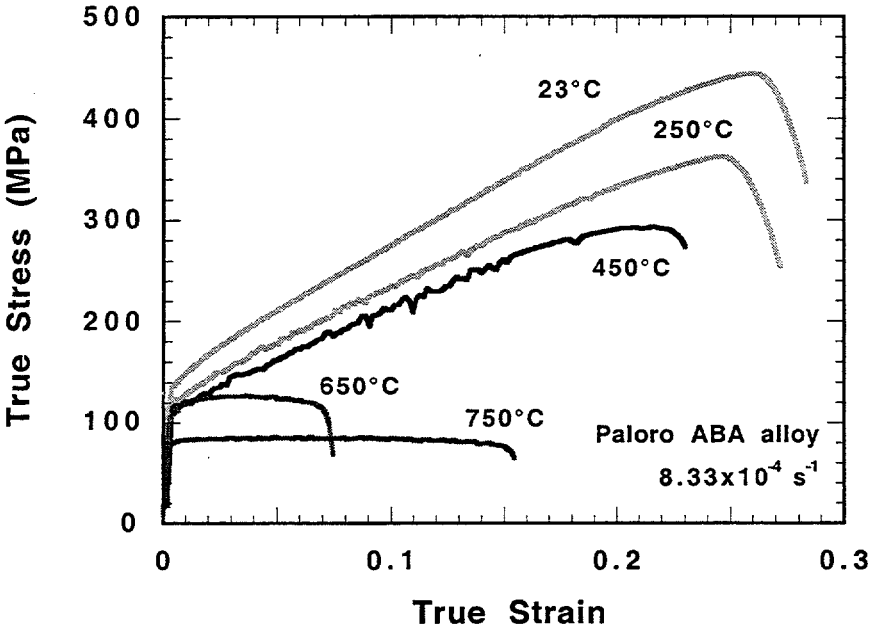

(a)

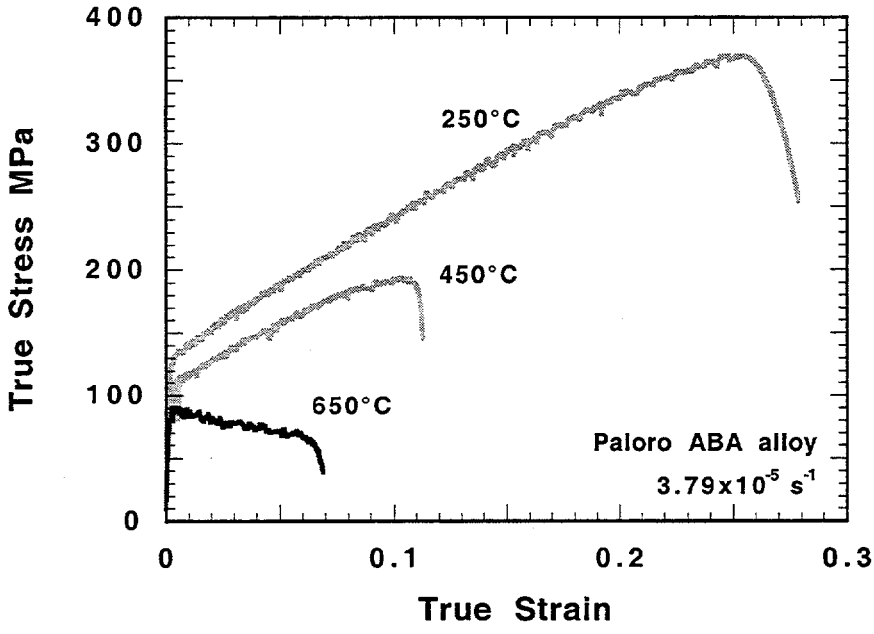

(b)

Fig. 31. Elevated temperature tensile tests run on Paloro ABA alloy. (a) Tests run at 8.33 x 10^{-4} s^{-1}. (b) Tests run at 3.79 x 10^{-5} s^{-1}.

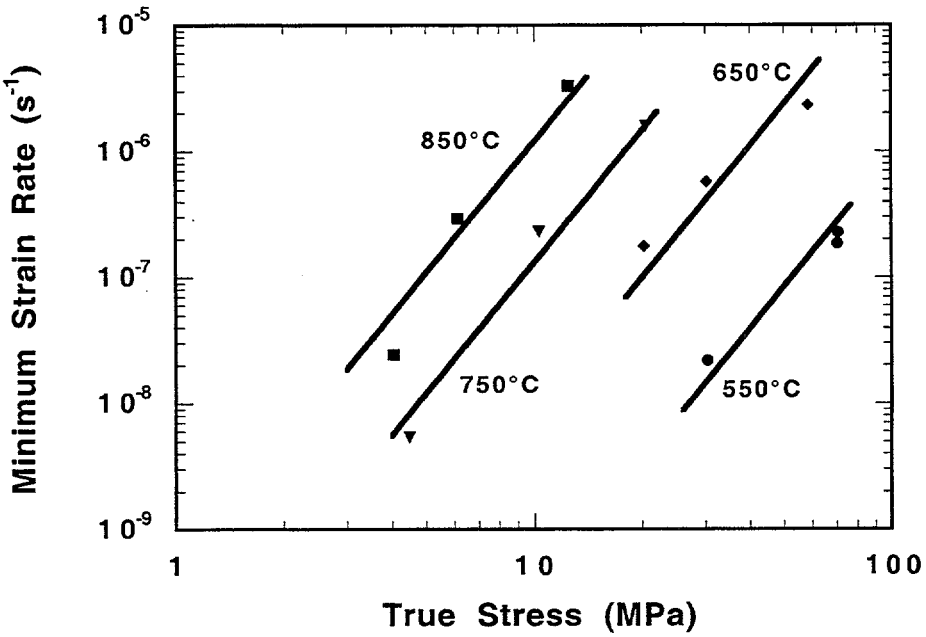

Fig. 32. Elevated temperature creep properties summary for Paloro ABA alloy. Data covers tests run in the temperature range 550-850°C.

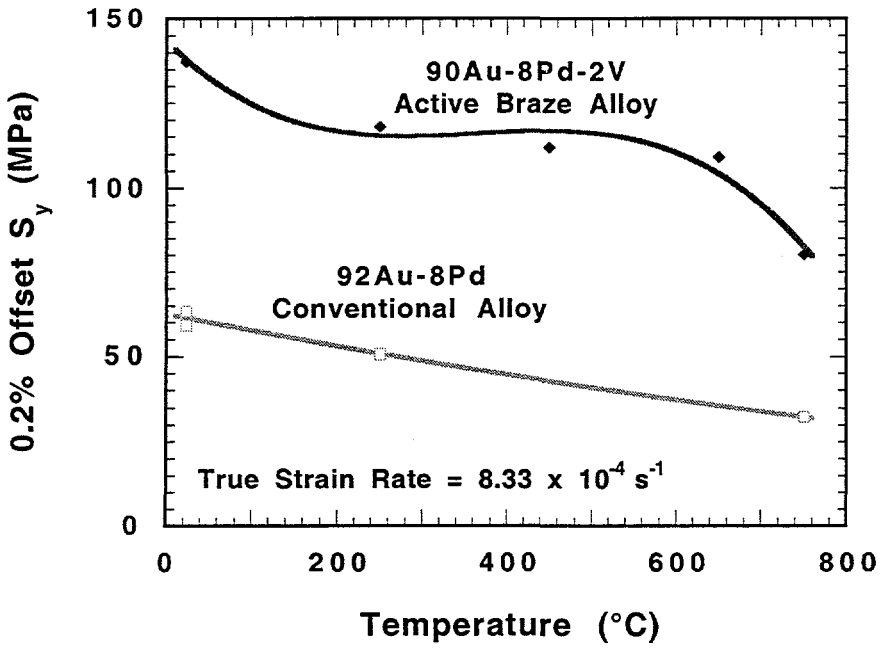

(a)

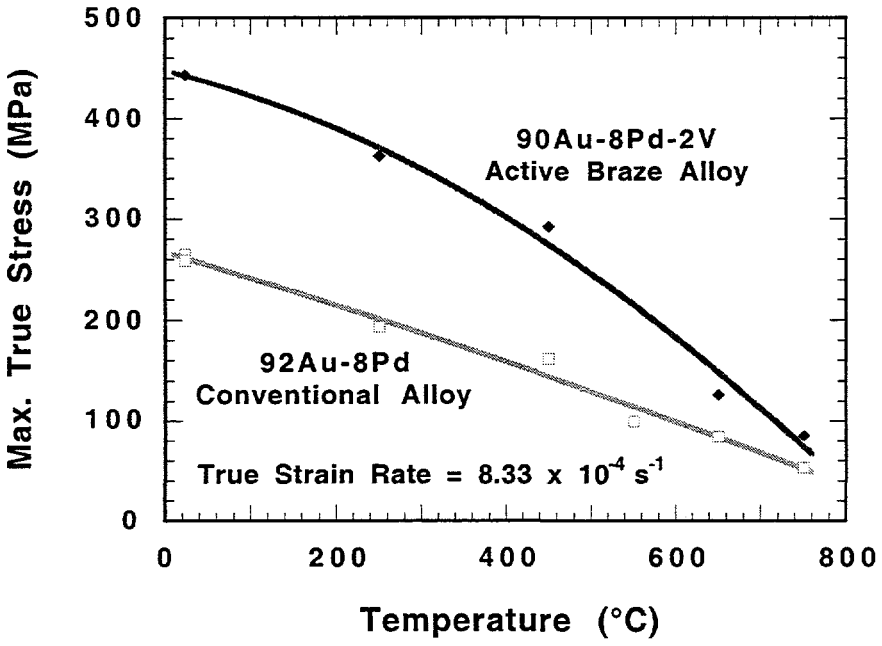

(b)

Fig. 33. Comparison of Paloro ABA and conventional Paloro alloy tensile properties as a function of temperature. (a) Yield stress. (b) Maximum true stress.

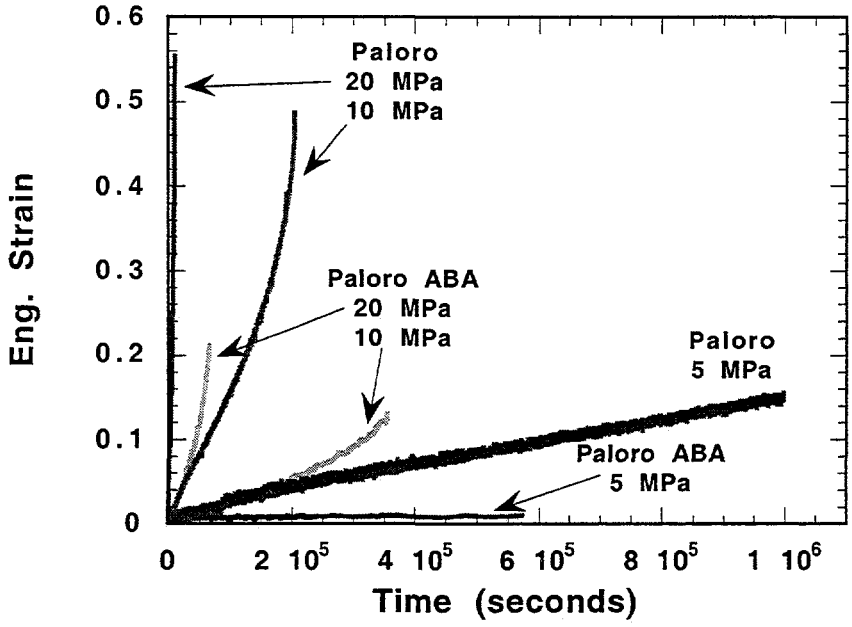

Fig. 34. Comparison of strain-time creep data at 750°C for Paloro ABA and conventional Paloro alloy.

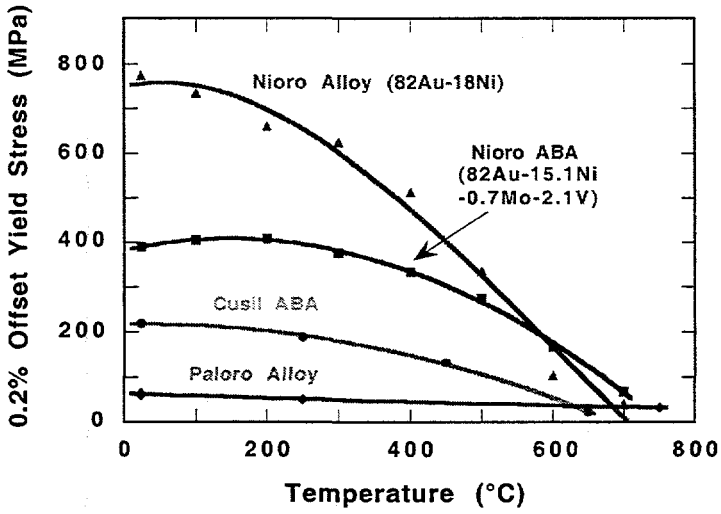

Fig. 35 Comparison of 0.2% offset Yield Strength as a function of temperature for four braze alloys. Note that the Cusil and Cusil ABA data were generated on compression samples, while the Nioro and Paloro data were generated on miniature tension samples as shown in Fig. 1.

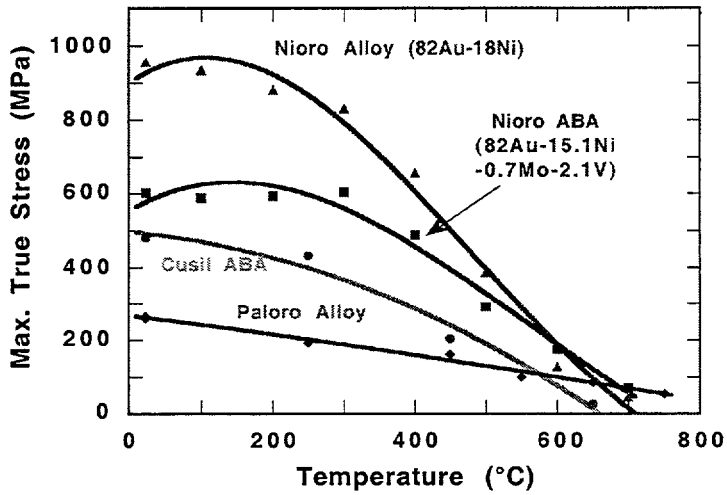

Fig. 36 Comparison of maximum true stress as a function of temperature for four braze alloys (same samples as discussed in Fig. 35).

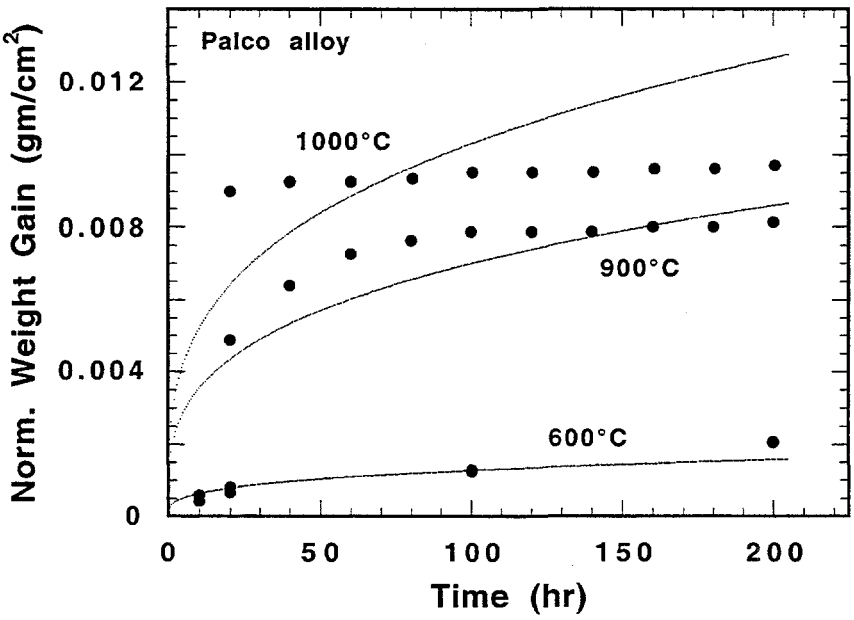

Fig. 37. Oxidation behavior of Palco alloy at 600, 900 and 1000°C. The trend curves are fits to the parabolic oxidation equation discussed in the text.

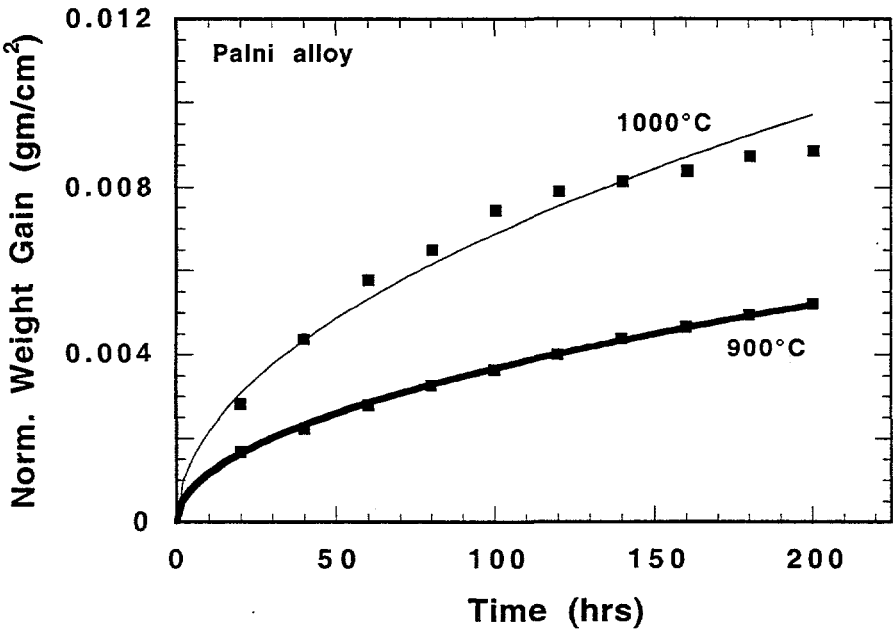

Fig. 38. Oxidation of Palni alloy at 900 and 1000°C. The trend curves are fits to the parabolic oxidation equation discussed in the text.

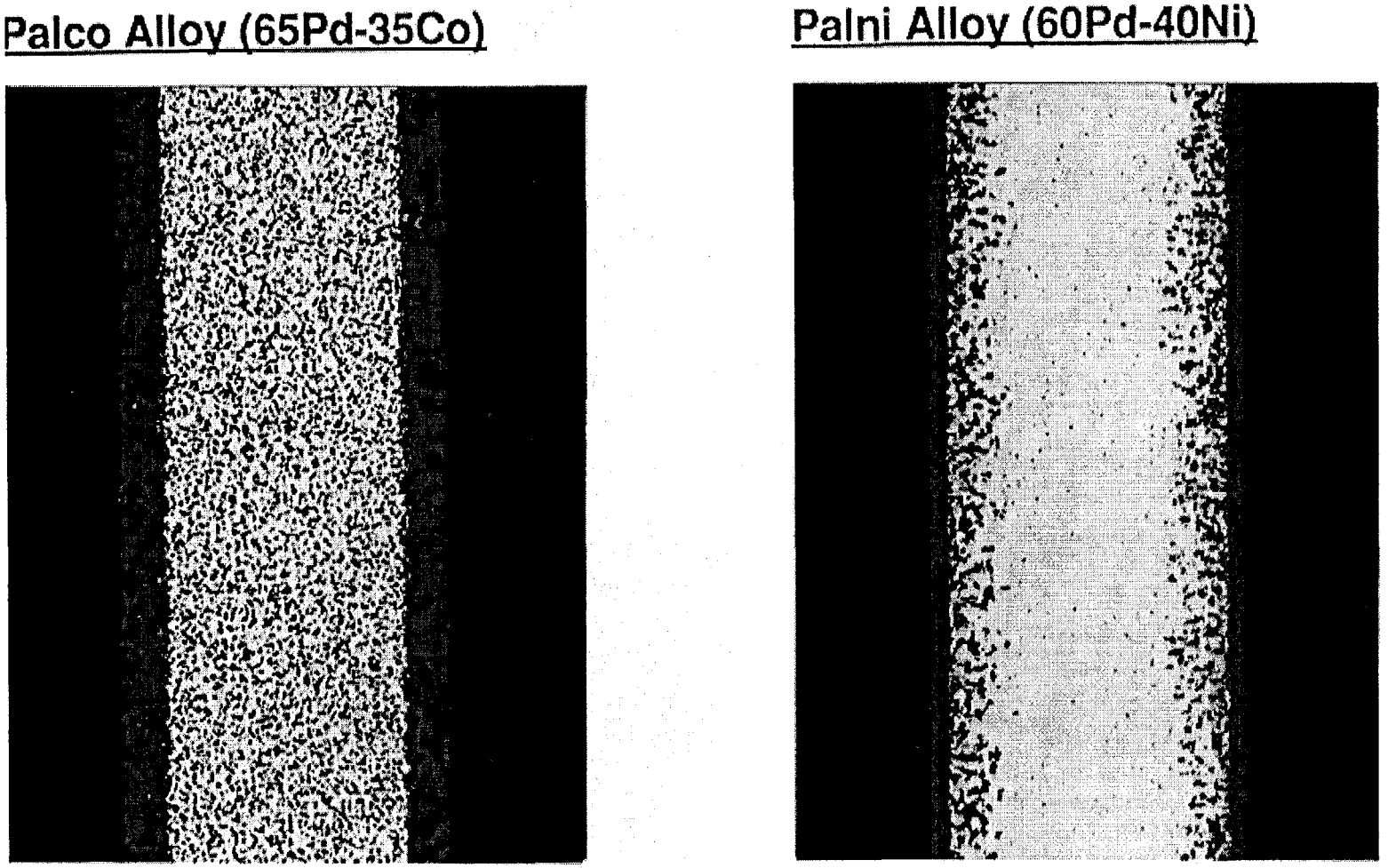

(a) (b)

Fig. 39. Micrographs comparing oxidation of Palco and Palni alloys after 200 hr at 900°C. (a) Palco alloy. (b) Palni alloy. (Note: same magnification scale as Fig. 40)

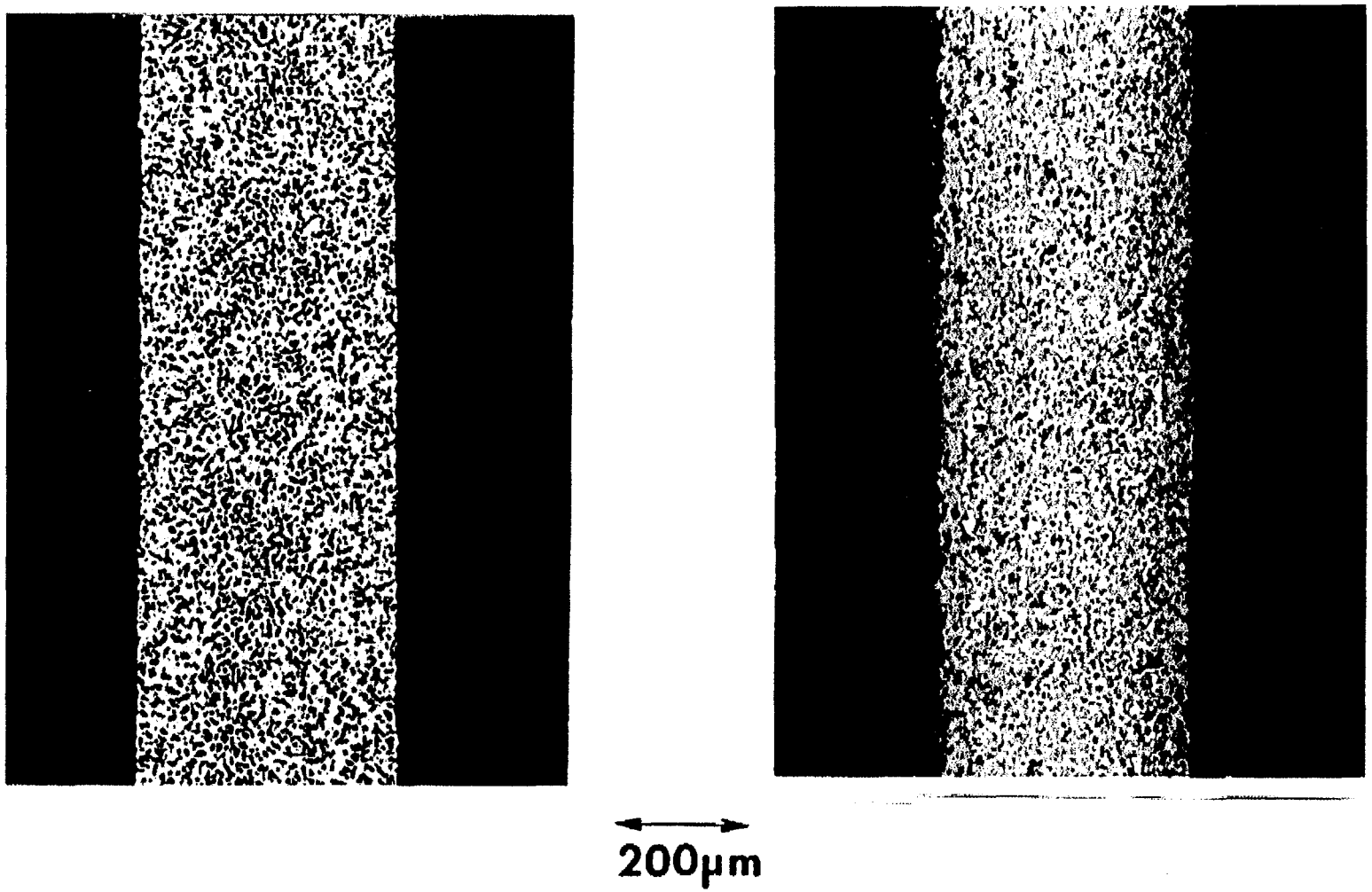

Fig. 40. Micrographs comparing oxidation of Palco and Palni alloys after 200 hr at 1000°C. (a) Palco alloy. (b) Palni alloy.

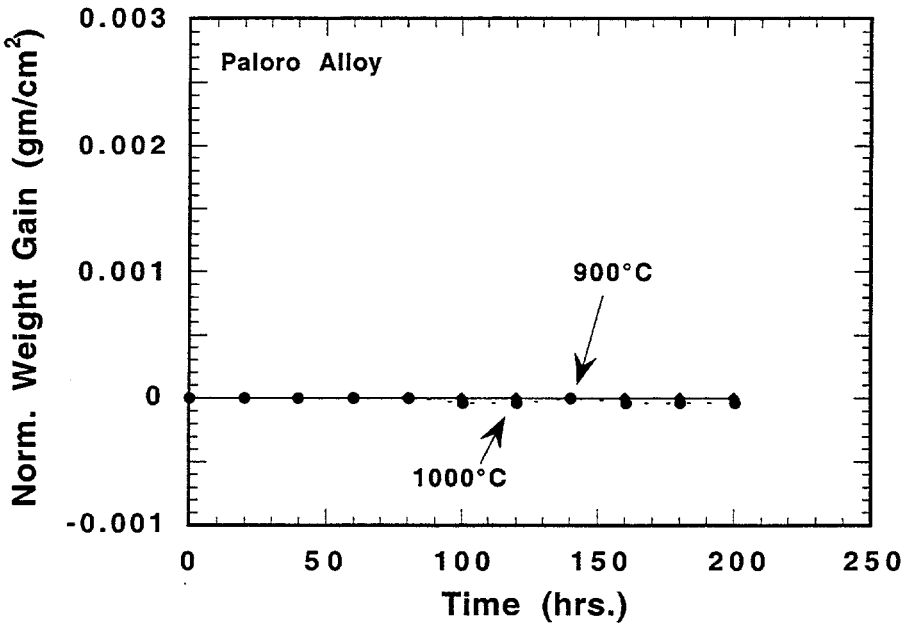

Fig. 41. Oxidation behavior of Paloro alloy. Very low weight gains were observed at both 900 and 1000°C.

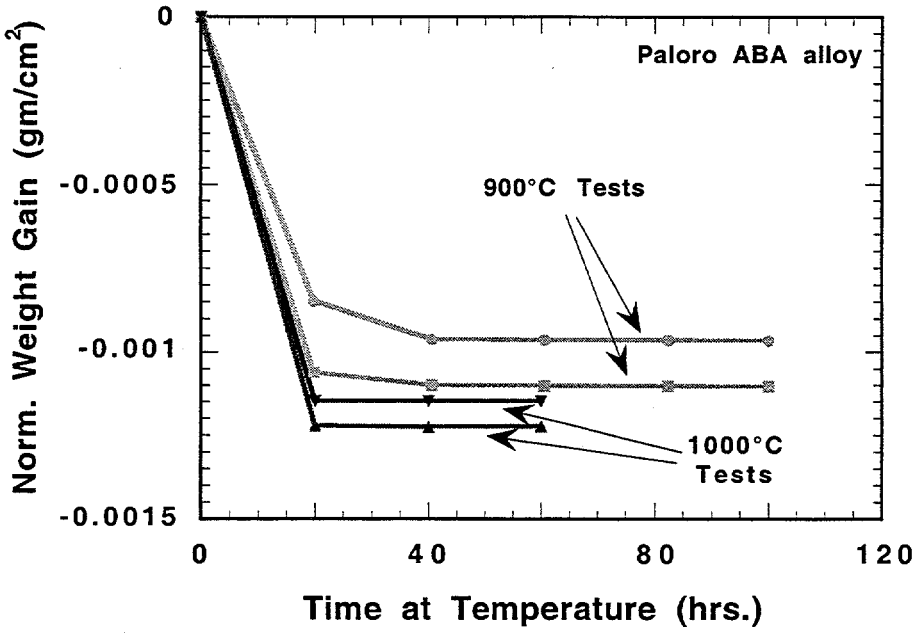

Fig. 42. Oxidation behavior of Paloro ABA alloy. In general, weight loss was observed, this is rationalized via migration of vanadium to the surface, and formation of volatile vanadium oxide species.

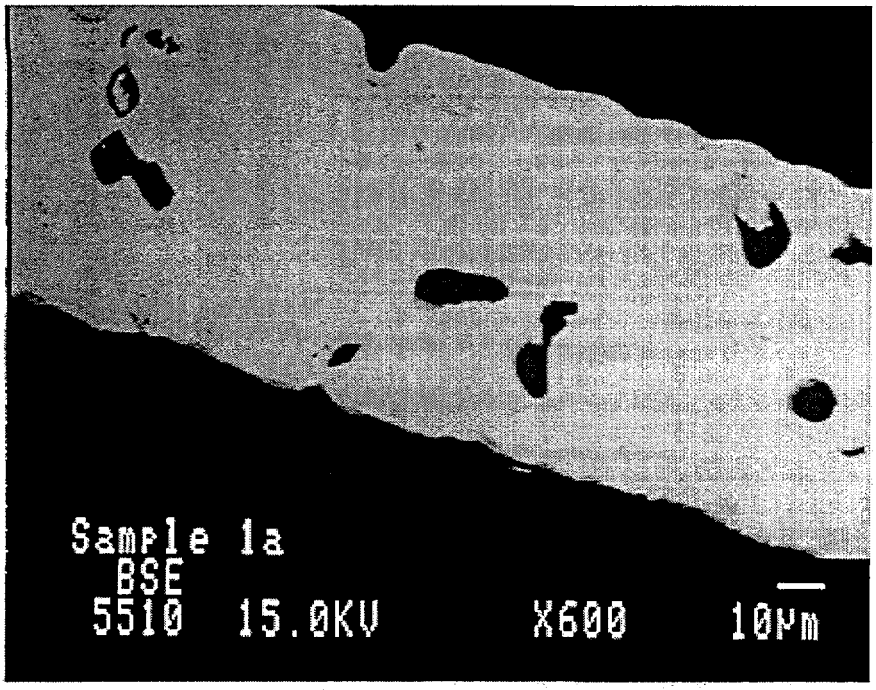

(a)

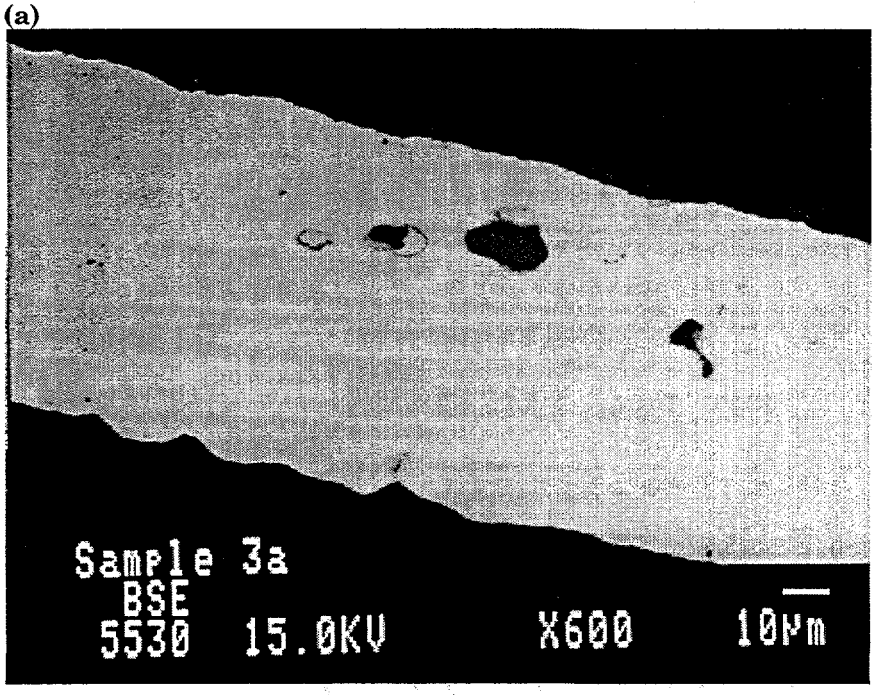

(b)

Fig. 43. Backscattered electron micrographs of Paloro ABA strip oxidized in air (a) 100 hr at 900°C. (b) 60 hr at 1000°C. In (a), note the area near the top surface of sample that apparently contained a vanadium oxide particle. Also, note that the density of vanadium oxide particles is higher in the 900°C sample than the 1000°C sample.

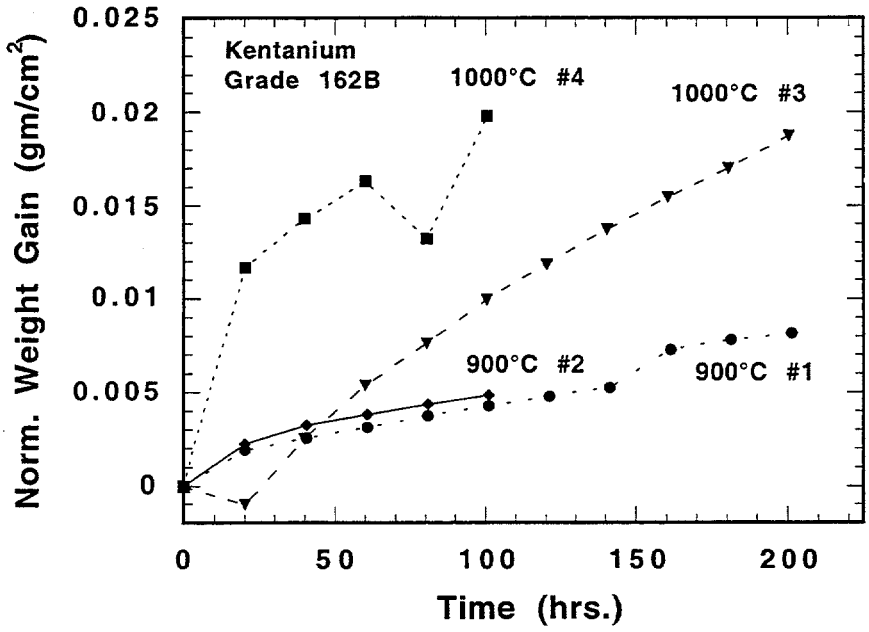

Fig. 44. Oxidation behavior of Kentanium Grade 162B material in air at 900 and 1000°C.

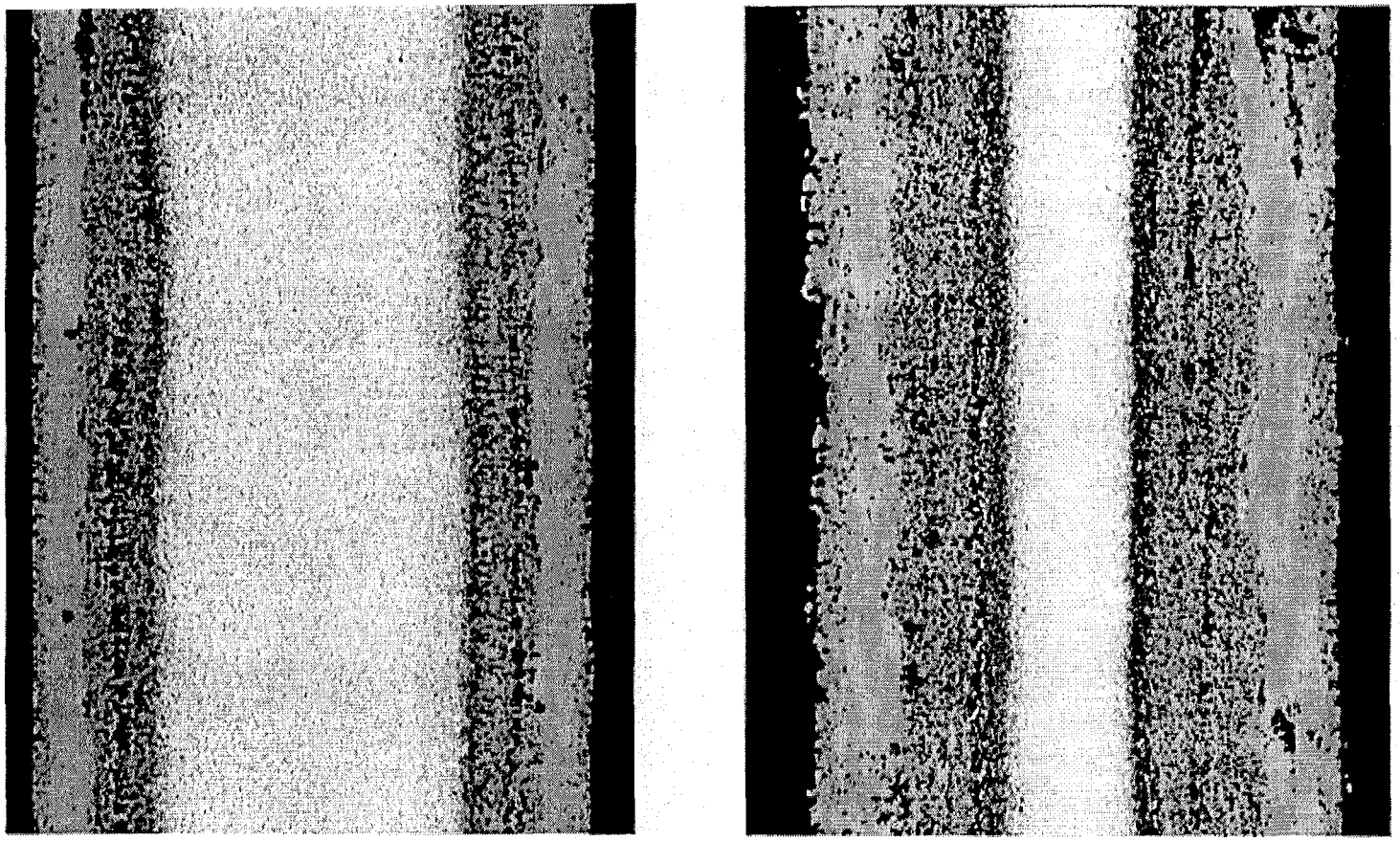

(a) (b)

Fig. 45. Samples of Kentanium Grade 162B oxidized in air at 1000°C. (a) Sample run for 100 hr at 1000°C. (b) Sample run for 200 hr at 1000°C. Note: same scale as in Fig. 46.

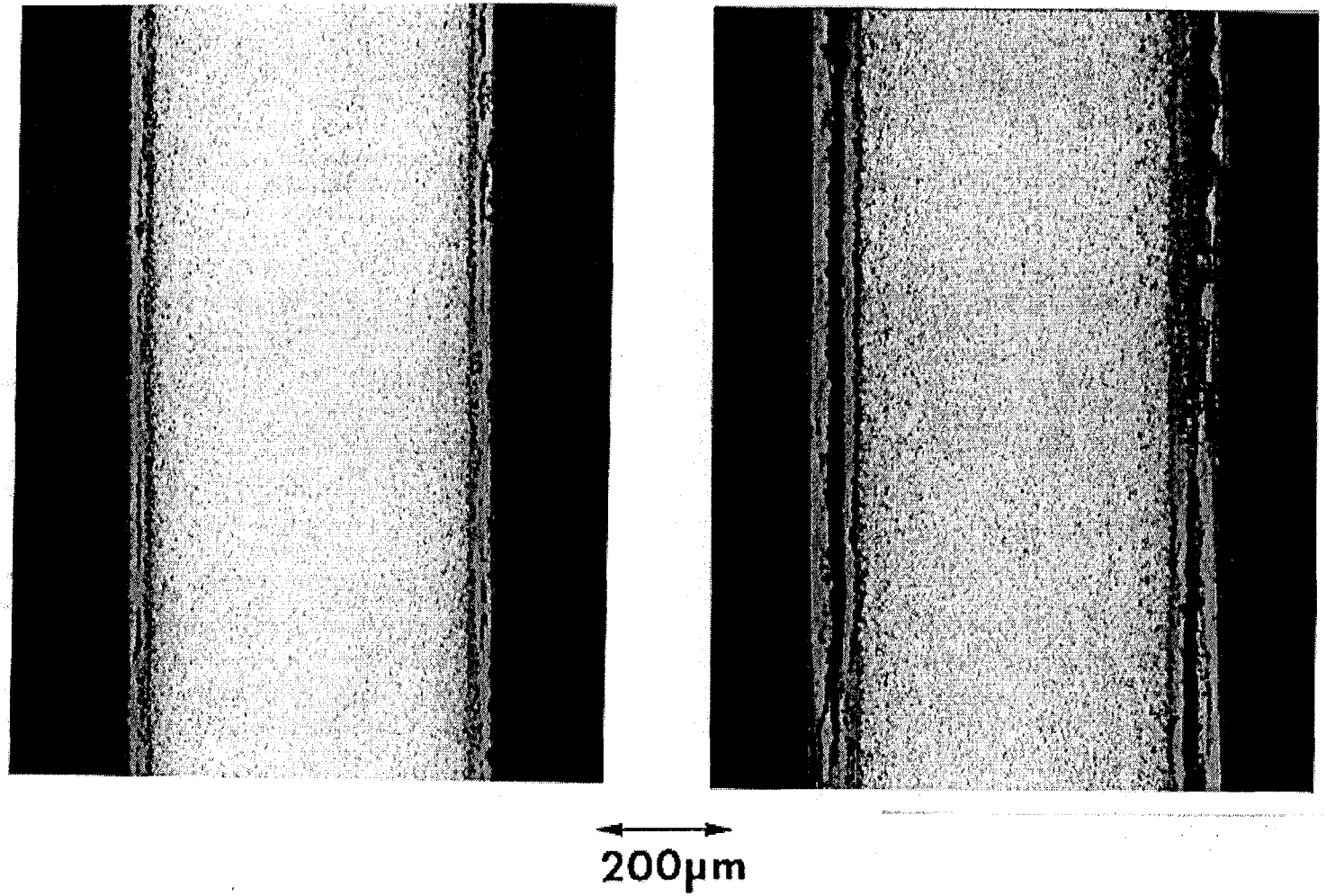

Fig. 46. Samples of Kentanium Grade 162B oxidized in air at 900°C. (a) Sample run for 100 hr at 900°C. (b) Sample run for 200 hr at 900°C.

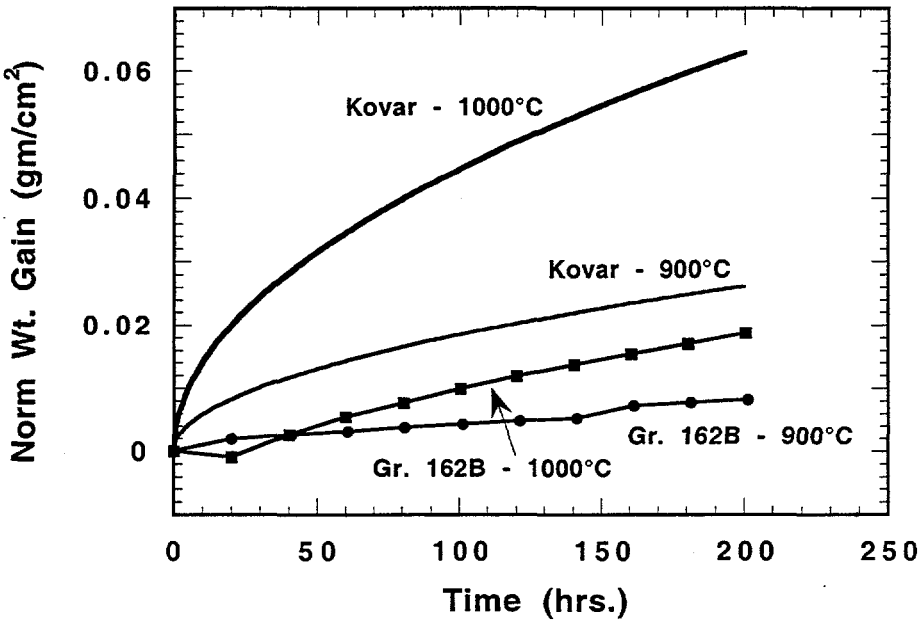

Fig. 47. Comparison of the predicted oxidation weight gain behavior of Kovar alloy with data obtained in this study for Kentanium Grade 162B at 900 and 1000°C.

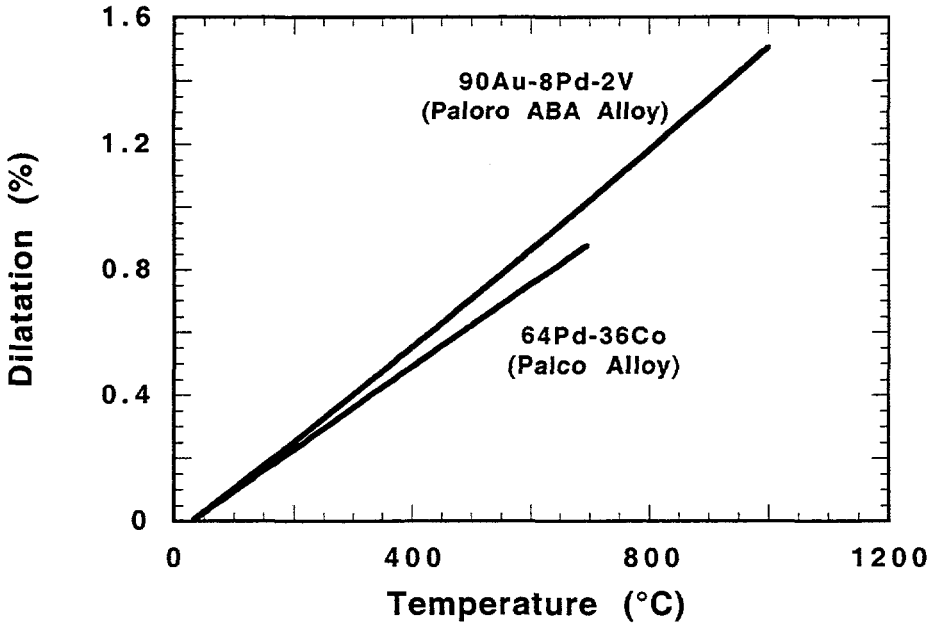

Fig. 48. Comparison of thermal expansion generated for Paloro ABA w/existing data from the literature for the 64Pd-36Co (Palco) alloy. Note: the data have been arbitrarily set so that dL/L = 0 at 30°C.

Chapter 4. Finite Element Analysis of Metal-to-Ceramic Brazing

I. Introduction

During metal to ceramic brazing undesirable residual stresses can be generated in the ceramic or in the braze joint due to differential thermal contraction of the materials. As the braze and use temperatures are increased, the stresses caused by differential thermal contraction will also increase and may either cause the joint to fail during manufacture or prematurely during use. Residual stresses generated during brazing will be affected by both the braze joint materials and the braze joint geometry. One approach that has been used to reduce the residual stress levels is to add layers of material between the ceramic and the metal that help to isolate the ceramic from the metal.[1-3]

Finite element analyses were performed to characterize the residual stress state that is generated during the brazing of silicon nitride (Si_3N_4) to Monel K-500 with a Cusil* (Copper-Silver) or Cusil-ABA† (Copper-Silver-Titanium) braze and during the brazing of silicon nitride to Hastelloy-S with a Nioro‡ (Nickel-Gold) braze. The Nioro braze material was used because it is the highest temperature braze material (950°C liquidus) that had been adequately characterized prior to these analyses. A variety of joint geometries was evaluated. In the first series of analyses, axisymmetric silicon nitride rods and metal rods were joined at their ends with a 0.005 in (127 μm) thick layer of braze alloy. In the second series of analyses, single interlayers were added to the braze joint and evaluated. In the third series of analyses, more complex composite interlayers were evaluated because researchers at AlliedSignal have recently had success brazing an AS-800 silicon nitride rod to a Monel K-500 rod with a Cusil-ABA braze and a composite interlayer constructed using nickel and molybdenum or tungsten. In the final series of analyses, the brazing of a silicon nitride post to a metal sleeve was evaluated. A variety of post and sleeve geometries and the effects of a Kovar interlayer were investigated. Results from all of these analyses are documented in this section.

II. Material Behavior

The material parameters used in these analyses are summarized in Tables 1 through 3. The AS-800 and GN-10 silicon nitride was modeled as linear elastic materials. The base and interlayer metals were all modeled as temperature-dependent, elastic-plastic materials. The braze alloys were modeled using a viscoplastic model that was recently developed specifically for braze alloys (Neilsen et al., 1996).[4]

The braze alloys were characterized by both uniaxial compression/tension tests in which the material was subjected to a constant strain rate and the resulting stress history was recorded, and creep tests in which the material was subjected to a constant stress and the resulting strain history was recorded.[5-7] Typical uniaxial compression/tension test results for the braze alloys are shown in Figures 1 through 3. These uniaxial compression/tension experiments were simulated by subjecting an axisymmetric finite element model of a test specimen to a variety of temperatures and loading rates. Results from these analyses indicated that the viscoplastic model used for the braze alloys captures the changes in response due to changes in strain rate and temperature. Note that Cusil-ABA has a higher room-temperature yield strength than Cusil and that Nioro has a significantly higher room temperature yield strength than either Cusil or Cusil-ABA. As the yield strength of the braze alloy increases, the residual stresses generated during brazing are also expected to increase.

---

* Wesgo, Belmont, CA.

† Wesgo, Belmont, CA.

‡ Wesgo, Belmont, CA.

Table 1. Silicon nitride material parameters.

AS-800 Silicon Nitride - Linear Elastic	
Elastic Modulus (psi)	45.0×10^6
Poisson's Ratio	0.28
Flexural Strength (psi)	120.0×10^3
Thermal Expansion Coefficient (1/°C)	2.88×10^{-6}
GN-10 Silicon Nitride - Linear Elastic	
Elastic Modulus (psi)	45.0×10^6
Poisson's Ratio	0.30
Tensile Strength (psi)	92.2×10^3
Thermal Exp. Coeff. (1/°C)	3.30×10^{-6}

Table 2. Base and interlayer metal material parameters.

Monel K-500 - Elastic-Plastic		
Temperature (°C)	20	1000
Poisson's Ratio	0.30	
Yield Strength (psi)	90.0×10^3	60.0×10^3
Hardening Modulus (psi)	1.3×10^6	1.3×10^6
Thermal Exp. Coeff. (1/°C)	13.68×10^{-6}	
Nickel - Elastic-Plastic		
Temperature (°C)	20	1000
Elastic Modulus (psi)	21.5×10^6	
Poisson's Ratio	0.30	
Yield Strength (psi)	25.0×10^3	10.0×10^3
Hardening Modulus (psi)	70.0×10^3	28.0×10^3
Thermal Exp. Coeff. (1/°C)	16.0×10^{-6}	
Molybdenum - Elastic-Plastic		
Temperature (°C)	20	1000
Elastic Modulus (psi)	46.0×10^6	40.0×10^6
Poisson's Ratio	0.324	
Yield Strength (psi)	90.0×10^3	60.0×10^3
Hardening Modulus (psi)	2.3×10^6	2.0×10^6
Thermal Exp. Coeff. (1/°C)	5.4×10^{-6}	
Tungsten - Elastic-Plastic		
Temperature (°C)	20	1000
Elastic Modulus (psi)	50.0×10^6	40.0×10^6
Poisson's Ratio	0.280	
Yield Strength (psi)	130.0×10^3	90.0×10^3
Hardening Modulus (psi)	2.5×10^6	2.0×10^6
Thermal Exp. Coeff. (1/°C)	4.6×10^{-6}	

Table 2. Base and interlayer metal material parameters (cont).

Hastelloy-S - Elastic-Plastic		
Temperature (°C)	20	1000
Elastic Modulus (psi)	29.0×10^6	
Poisson's Ratio	0.300	
Yield Strength (psi)	60.0×10^3	39.2×10^3
Hardening Modulus (psi)	120.0×10^3	80.0×10^3
Thermal Exp. Coeff. (1/°C)	15.5×10^{-6}	
Kovar - Elastic-Plastic		
Temperature (°C)	20	1000
Elastic Modulus (psi)	20.0×10^6	
Poisson's Ratio	0.317	
Yield Strength (psi)	60.0×10^3	25.3×10^3
Hardening Modulus (psi)	100.0×10^3	60.0×10^3
Thermal Exp. Coeff. (1/°C) 20-1000°C	12.15×10^{-6}	

Table 3. Braze material parameters.

Cusil Braze - Viscoplastic					
Temperature (°C)	20	250	450	650	780
Thermal Strain	0.0	0.00420	0.00801	0.01195	0.01474
Shear Modulus (psi)	3.10×10^6	1.22×10^6	0.79×10^6	0.41×10^6	8.78×10^4
Bulk Modulus (psi)	10.28×10^6	4.24×10^6	2.83×10^6	1.64×10^6	4.28×10^5
Flow Rate - ln(f)	-59.04	-43.16	-16.23	-8.262	-6.312
Sinh Exponent	15.0	11.36	3.611	2.653	1.833
Iso. Hardening (psi^{A+1})	2.90×10^5	1.74×10^5	1.74×10^4	0.0	0.0
Iso. Recovery (1/psi-sec)	0.0				
Flow Stress (psi)	5800.0				
Hardening Exponent - A	0.80				
Cusil-ABA Braze - Viscoplastic					
Temperature (°C)	20	250	450	650	780
Thermal Strain	0.0	0.00446	0.00834	0.0122	0.0147
Shear Modulus (psi)	4.98×10^6	4.44×10^6	4.10×10^6	3.52×10^6	2.92×10^6
Bulk Modulus (psi)	16.5×10^6	15.7×10^6	15.0×10^6	14.7×10^6	14.5×10^6
Flow Rate - ln(f)	-59.89	-56.61	-13.88	-7.65	-5.23
Sinh Exponent	24.0	22.5	2.59	1.69	1.13
Iso. Hardening (psi^{A+1})	1.08×10^{12}	7.05×10^{11}	2.58×10^{10}	1.94×10^7	5.38×10^6
Iso. Recovery (1/psi-sec)	0.0	6.9×10^{-12}	1.43×10^{-7}	1.98×10^{-5}	3.89×10^{-5}
Flow Stress (psi)	7250.0				
Hardening Exponent - A	1.746				
Nioro Braze - Viscoplastic					
Temperature (°C)	20	400	500	1020	
Thermal Strain	0.0	0.00676	0.00854	0.01780	
Shear Modulus (psi)	5.77×10^6	4.35×10^6	2.63×10^6	0.52×10^6	
Bulk Modulus (psi)	20.2×10^6	16.7×10^6	10.0×10^6	4.0×10^6	
Flow Rate - ln(f)	-22.03	-17.43	-12.80	0.400	
Sinh Exponent	2.224	2.224	2.224	2.224	
Iso. Hardening (psi^{A+1})	3.31×10^4	100.0	0.0	0.0	
Iso. Recovery (1/psi-sec)	0.0				
Flow Stress (psi)	15,950.0				
Hardening Exponent - A	0.0				

III. Brazing Simulations

A. Braze Alloy and Base Metal Variations

The initial brazing simulations were performed using axisymmetric rods of silicon nitride and a metal brazed with Cusil, Cusil-ABA, or Nioro. The metals were either candidate structural metals or candidate interlayer materials. These rods were brazed together at their ends using a 0.005 in thick braze layer as shown in Fig. 4. The assemblies were assumed stress free at the solidus temperature for the braze and cooled to room temperature in 1 hr. All of the analyses were performed using the finite element code JAC-2D.[8] The parameter of interest was the maximum tensile stress.

In the first analysis, a Monel K-500 rod was brazed to an AS-800 silicon nitride rod with Cusil. The assembly was initially stress-free and at a temperature of 780°C. The assembly was cooled to room temperature in one hr and the resulting stresses were studied. Results from this analysis indicated that a maximum tensile stress of only 24,510 psi (169 MPa) would be generated in the silicon nitride during the brazing process (Fig. 5). This maximum tensile stress is located near the outer surface of the silicon nitride rod and is oriented in a direction parallel to the axis of the rod.

The next five analyses were identical to the first analysis except the base metal and/or the braze alloy was modified. The assemblies were all initially stress-free at the solidus temperature for the braze which is 780°C for Cusil and Cusil-ABA and 950°C for Nioro. The assemblies were cooled to room temperature in one hr and the resulting stresses were studied. Results from these analyses are summarized in Table 4. The stress distributions generated by all of these analyses are similar to the distribution generated during the first analysis (Fig. 5). The maximum principal stress in the silicon nitride is located near the outer surface of the rod and oriented in a direction parallel to the axis of the rod.

The use of nickel in place of Monel K-500 had a small effect on the residual tensile stress level generated in the silicon nitride (Table 4). The maximum principal stress in the silicon nitride decreased to 16,080 psi (111 MPa) when molybdenum was used in place of the Monel K-500. When the braze alloy was changed from Cusil to Cusil-ABA, the maximum tensile stress in the AS-800 dramatically increased to 58,500 psi (403 MPa). The highest residual stresses were generated when a Hastelloy-S rod was brazed to the AS-800 with Nioro. In summary, these results indicate that, as expected, base metal and braze alloy changes can have a dramatic effect of the residual stress levels generated in the AS-800 ceramic during the brazing process.

Table 4. Effect of braze and base metal variations on the residual stress generated in AS-800 silicon nitride during brazing.

Analysis	Base Metal	Braze Alloy	Max. Tensile Stress in AS-800 (psi)
1	Monel K-500	Cusil	24,510
2	Nickel	Cusil	26,670
3	Molybdenum	Cusil	16,080
4	Monel K-500	CusilABA	58,500
5	Hastelloy-S	Nioro	90,490
6	Kovar	Nioro	58,050

B. Effect of Single Interlayers

In the next series of brazing simulations, the effects of placing a single interlayer between the base metal and the AS-800 silicon nitride were investigated. A variety of interlayer thicknesses and materials were used in these simulations.

In the first interlayer analysis, a molybdenum interlayer was brazed between an AS-800 silicon nitride rod and a Monel K-500 rod with Cusil (Fig. 6). A braze layer thickness of 0.005 in was used between all layers. The molybdenum layer had a thickness of 0.120 in (3.1 mm). The assembly was initially stress-free and at a temperature of 780°C. The assembly was cooled to room temperature in one hr and the resulting stresses were studied. Results from this analysis indicated that a maximum tensile stress of 33,170 psi (229 MPa) would be generated in the silicon nitride during the brazing process (Fig. 7). This maximum tensile stress is significantly higher than the maximum tensile stress of 24,510 psi (169 MPa) that was generated in the first analysis when interlayers were not used. Thus, the addition of a 0.120 in thick molybdenum interlayer is not beneficial.

The next series of analyses was identical to the previous analysis except the interlayer thickness was varied from 0.005 to 0.480 in (12.2 mm). Results from these analyses are summarized in Table 5. These results show that the use of a molybdenum interlayer with a thickness less than approximately 0.30 in is not beneficial but that the use of an interlayer with a thickness greater than approximately 0.30 in will be beneficial. With increases in interlayer thickness the residual stress value appears to be approaching the value of 16,080 psi obtained in Analysis 3 in which AS-800 was brazed directly to molybdenum. This means that, as expected, if the interlayer thickness is large enough the AS-800 will not be affected by the base metal but will behave as if it were only brazed to the interlayer.

Table 5. Effect of molybdenum interlayer thickness on the residual stress generated during Monel K-500 to AS-800 silicon nitride brazing with Cusil.

Analysis	Molybdenum Interlayer Thickness (inch)	Maximum Tensile Stress in the AS-800 (psi)
1	0.000	24,510
7	0.005	28,100
8	0.020	31,210
9	0.040	32,880
10	0.120	33,170
11	0.240	26,940
12	0.480	17,940

The next series of analyses was identical to the previous series of analyses except the interlayer material was changed from molybdenum to nickel. Results from these analyses are summarized in Table 6. These results show that the use of a nickel interlayer with a thickness less than approximately 0.31 in (7.9 mm) provides a minimal reduction in the residual tensile stress. The use of a nickel interlayer with a thickness greater than approximately 0.31 in will not be beneficial. Note that with increases in interlayer thickness the residual maximum tensile stress value appears to be approaching the value of 26,670 psi obtained in Analysis 2 in which AS-800 was brazed directly to nickel.

In the next interlayer analyses, a Kovar interlayer was brazed between a Hastelloy-S rod and an AS-800 silicon nitride rod with Nioro. The assembly had the same geometry as the

previous interlayer analyses (Fig. 6). A braze layer thickness of 0.005 in was used between all layers. The Kovar interlayer had a thickness between 0.005 in and 0.480 in. The assembly was initially stress-free and at a temperature of 950°C. The assembly was cooled to room temperature in one hr and the resulting stresses were studied. Results from these analyses are summarized in Table 7. These results show that the use of a Kovar interlayer with a thickness greater than 0.005 in and less than approximately 0.16 in (4.1 mm) is not beneficial. The maximum tensile stress generated during Analysis 19 is probably lower than the maximum tensile stress generated during Analysis 5 because there are two braze layers (a total braze alloy thickness of 0.010 in) between the Hastelloy-S and the AS-800 in Analysis 19 and only one braze layer (a total braze alloy thickness of 0.005 in) between the Hastelloy-S and the AS-800 in Analysis 5. The use of a Kovar interlayer with a thickness greater than approximately 0.16 in is beneficial. Note that with increases in interlayer thickness the residual stress value appears to be rapidly approaching the value of 58,050 psi obtained in Analysis 6 in which AS-800 was brazed directly to Kovar.

Table 6. Effect of nickel interlayer thickness on the residual stress generated during Monel K-500 to AS-800 silicon nitride brazing with Cusil.

Analysis	Nickel Interlayer Thickness (inch)	Maximum Tensile Stress in the AS-800 (psi)
1	0.000	24,510
13	0.005	22,900
14	0.020	22,540
15	0.040	23,000
16	0.120	23,940
17	0.240	23,950
18	0.480	25,760

Table 7. Effect of Kovar interlayer thickness on the residual stress generated during Hastelloy-S to AS-800 silicon nitride brazing with Nioro.

Analysis	Kovar Interlayer Thickness (inch)	Maximum Tensile Stress in the AS-800 (psi)
5	0.000	90,490
19	0.005	83,230
20	0.020	96,630
21	0.040	107,100
22	0.120	97,590
23	0.240	77,880
24	0.480	62,790

In summary, these analyses indicate that the use of a single molybdenum interlayer between the Monel K-500 and AS-800 was beneficial when the interlayer thickness was greater than 0.30 in. The use of a nickel interlayer between Monel K-500 and AS-800 was not very beneficial. The use of a Kovar interlayer between Hastelloy-S and AS-800 was beneficial when the interlayer thickness was greater than 0.16 in. The use of a 0.040 in thick Kovar interlayer caused the residual stresses in the AS-800 to increase significantly.

C. Composite Interlayers

In the next series of brazing simulations, the effects of placing composite interlayers between the base metal rod and the AS-800 silicon nitride rod were investigated. A variety of interlayer thicknesses and materials were used in these simulations.

In the first composite interlayer analysis, a nickel/molybdenum/nickel interlayer was brazed between a Monel K-500 rod and an AS-800 silicon nitride rod with Cusil (Fig. 8). A braze layer thickness of 0.005 in was used between all layers. The nickel layers had a thickness of 0.050 in and the molybdenum layer had a thickness of 0.125 in (3.2 mm).

The assembly was initially stress-free and at a temperature of 780°C. The assembly was cooled to room temperature in one hr and the resulting stresses were studied. Results from this analysis indicated that a maximum tensile stress of only 13,110 psi (90.4 MPa) would be generated in the silicon nitride during the brazing process (Fig. 9). This maximum tensile stress is significantly lower than the maximum tensile stress of 24,510 psi (169 MPa) that was generated in the first analysis when the AS-800 rod was brazed to the Monel K-500 rod without any interlayer materials. Like the previous analyses, this maximum tensile stress was located near the outer surface of the AS-800 rod and was oriented in a direction parallel to the rod axis. Unlike the previous analysis this maximum tensile stress occurred during the cooling process at a temperature of 235°C (Fig. 10). The maximum residual tensile stress in the AS-800 after the brazing operation was completed and the assembly was at room temperature was only 12,850 psi (88.6 MPa).

The next series of analyses was identical to the previous analysis except the thickness of the nickel layers was varied. In these analyses, the nickel layer between the molybdenum and the Monel K-500 was given the same thickness as the nickel layer between the molybdenum and the AS-800 silicon nitride. The thickness of the nickel layers was varied from 0.0 to 0.120 in (3.1 mm). Results from these analyses are summarized in Table 8 and shown graphically in Fig. 11. In Fig. 11, the maximum principal stress in the AS-800 predicted by an analysis is plotted as a function of the nickel layer thickness used in that analysis. Results from these analyses show that the maximum tensile stress in the AS-800 was minimized when a nickel layer thickness of 0.050 in (1.3 mm) was used. The next series of analyses was identical to the previous series except the thickness of the molybdenum layers was also varied. The thickness of the molybdenum layers was varied from 0.075 to 0.250 in. Results from these analyses are summarized in Table 9 and shown graphically in Fig. 12. These results clearly show that the tensile stress in the AS-800 can be reduced by increasing the thickness of the molybdenum layer and by using nickel layers with a thickness of approximately 0.050 in.

The next series of analyses were similar to the previous analysis with a composite interlayer except that tungsten was used in place of molybdenum. The purpose of these analyses was to characterize the effects that this material change would have on the residual stresses generated in the AS-800. In these analyses, the thickness of the nickel layers was varied from 0.020 to 0.120 in. The tungsten layer was given a thickness of 0.125 inches in all of these analyses.

Results from these analyses are summarized in Table 10. Results from the previous Analyses 27 through 31 with a composite Ni/Mo/Ni interlayer are included in Table 10 for ease of comparison with the current results. A comparison of results from these analyses with the previous analyses shows that the stresses caused by brazing are lower when the tungsten is used in place of molybdenum. With the composite Ni/W/Ni interlayer, tensile stresses in the AS-800 were minimized at 11,300 ksi when a nickel layer thickness of 0.050 in was used.

Table 8. Effect of nickel layer thickness on the residual stress generated during Monel K-500 to AS-800 silicon nitride brazing with a composite Ni/Mo/Ni interlayer.

Analysis	Nickel Layer Thickness (inch)	Molybdenum Layer Thickness (inch)	Maximum Tensile Stress in the AS-800 (psi)
25	0.000	0.125	33,020
26	0.005	0.125	22,500
27	0.020	0.125	15,140
28	0.040	0.125	13,260
29	0.050	0.125	13,110
30	0.060	0.125	13,240
31	0.120	0.125	18,530

Table 9. Effect of nickel and molybdenum layer thicknesses on the residual stress generated during Monel K-500 to AS-800 silicon nitride brazing with a composite Ni/Mo/Ni interlayer.

Analysis	Nickel Layer Thickness (inch)	Molybdenum Layer Thickness (inch)	Maximum Tensile Stress in the AS-800 (psi)
1	0.000	0.0	24,510
32	0.005	0.0	22,900
33	0.020	0.0	22,540
34	0.040	0.0	23,000
35	0.050	0.0	23,290
36	0.120	0.0	24,310
37	0.005	0.075	23,990
38	0.020	0.075	17,570
39	0.040	0.075	15,560
40	0.050	0.075	15,350
41	0.060	0.075	15,530
42	0.120	0.075	19,930
43	0.005	0.250	16,960
44	0.020	0.250	9,823
45	0.030	0.250	8,606
46	0.040	0.250	8,526
47	0.050	0.250	8,734
48	0.060	0.250	9,140
49	0.120	0.250	18,440

D. Rod Diameter

The next series of analyses was similar to the previous analyses with a composite interlayer except the diameter of the rods was reduced from 0.800 to 0.500 in (20.3 to 12.7 mm). The purpose of these analyses was to characterize the effects of rod diameter on the residual stresses generated in the AS-800. In these analyses, the thickness of the nickel layers was varied from 0.020 to 0.050 in (0.51 to 1.3 mm). The molybdenum layer was given a thickness of 0.125 inches in all of these analyses.

Results from these analyses are summarized in Table 11. Results from the previous Analyses 27 through 30 with a 0.80 in diameter rod are included in Table 11 for ease of comparison with the current results. A comparison of results from these analyses with the previous analyses shows that the stresses caused by brazing are lower when the rod diameter is reduced. When a rod diameter of 0.5 in is used, the residual tensile stress in the AS-800 can be minimized by using a nickel layer thickness of 0.030 in. In the previous analyses with a 0.8 in diameter rod, the residual tensile stress in the AS-800 was minimized when a nickel thickness of 0.050 in was used. Thus, it appears that with either design the nickel layer thickness should be chosen to be approximately six percent of the rod diameter.

E. Sleeve Joints

The next series of brazing simulations was performed to characterize the residual stress state that would be generated during the brazing of a silicon nitride post into a metal sleeve. A variety of sleeve joint geometries was evaluated. A Nioro braze layer thickness of 0.002 in was used in all of these analyses. The assemblies were assumed stress free at the liquidus temperature for Nioro (950°C) and cooled to room temperature in 10 min or 1 hr. A cooling time of 10 min was used for most of these analyses to minimize the computational cost of the study; however, faster cooling produces slightly higher stresses. The resulting stress distributions were investigated. The first sleeve joint analysis was performed using the finite element model shown in Fig. 13. Results from this analysis indicated that a maximum tensile stress of 87,280 psi (602 MPa) would be generated in the ceramic if the assembly was cooled from a stress-free 950°C to room temperature in 10 min (Fig. 14). A maximum tensile stress of 82,880 psi (572 MPa) was generated when this model was cooled from a stress-free 950°C to room temperature in one hr. Thus slower cooling is beneficial.

The first analysis indicated that the tensile stress generated near the tapered corner at the bottom end of the ceramic post would be significantly smaller than the tensile stress generated near the top end of the braze joint (Fig. 14). Thus for the second sleeve joint analysis, the geometry of the silicon nitride post was modified so that it would be tapered near both ends of the braze joint as shown in Fig. 15. The assembly was again cooled from a stress-free temperature of 950°C to room temperature in 10 min. Results from this analysis indicated that a maximum tensile stress of 99,280 psi (685 MPa) would be generated in the ceramic during the cooling process (Fig. 16). Thus, this geometric modification is not beneficial. The residual tensile stress generated in the ceramic near the base of the silicon nitride post is still significantly smaller than the residual tensile stress generated near the top of the braze joint.

The third sleeve joint analysis was performed to investigate the effects of sleeve geometry modifications (Fig. 17). In this analysis, the top end of the Hastelloy-S sleeve was tapered to reduce its stiffness and to, hopefully, reduce the tensile stress that was being generated in the ceramic near the top end of the braze joint. The assembly was again cooled from a stress-free 950°C to room temperature in 10 min. Results from this analysis indicated that a maximum tensile stress of 73,090 psi (504 MPa) would be generated in the ceramic during the cooling process (Fig. 18). Thus, this geometric modification is beneficial.

Table 10. Effect of using a composite Ni/W/Ni interlayer instead of a Ni/Mo/Ni interlayer on the residual stress generated during Monel K-500 to AS-800 silicon nitride brazing.

Analysis	Nickel Layer Thickness (inch)	Composite Interlayer	Maximum Tensile Stress in the AS-800 (psi)
50	0.020	Ni/W/Ni	12,320
51	0.040	Ni/W/Ni	11,300
52	0.050	Ni/W/Ni	11,280
53	0.060	Ni/W/Ni	11,500
54	0.120	Ni/W/Ni	17,430
27	0.020	Ni/Mo/Ni	15,140
28	0.040	Ni/Mo/Ni	13,260
29	0.050	Ni/Mo/Ni	13,110
30	0.060	Ni/Mo/Ni	13,240
31	0.060	Ni/Mo/Ni	18,530

Table 11. Effect of rod diameter on the residual stress generated during Monel K-500 to AS-800 silicon nitride brazing with a composite nickel/molybdenum/ nickel interlayer, 0.125 inch molybdenum layer thickness.

Analysis	Nickel Layer Thickness (inch)	Rod Diameter (inch)	Maximum Tensile Stress in the AS-800 (psi)
55	0.020	0.5	8,870
56	0.030	0.5	8,280
57	0.040	0.5	8,378
58	0.050	0.5	12,850
27	0.020	0.8	15,140
28	0.040	0.8	13,260
29	0.050	0.8	13,110
30	0.060	0.8	13,240

The previous analyses indicated that the tensile stress generated near the bottom tapered end of the ceramic post would be significantly smaller than the tensile stress generated near the top end of the braze joint (Figures 14 and 16). Thus, in the fourth sleeve joint analysis, the assembly was modified so that the top end of the braze joint was geometrically very similar to the bottom end of the braze joint (Fig. 19). The assembly was again cooled from a stress-free 950°C to room temperature in 10 min. Results from this analysis indicated that a maximum tensile stress of only 51,010 psi (352 MPa) would be generated in the ceramic near the top end of the braze joint during the cooling process (Fig. 20). Thus, this geometric modification is very beneficial.

The fifth sleeve joint analysis was performed using the finite element model shown in Fig. 21. The primary purpose of this analysis was to determine what effect braze joint length has on the residual stress state in the ceramic. This model is identical to the model used in the previous analysis (Fig. 19) except that the braze joint length has been reduced from 0.31 to 0.11 in. The assembly was again cooled from a stress-free 950°C to room temperature in 10 min. Results from this analysis indicated that a maximum tensile stress of 22,670 psi (156 MPa) would be generated in the ceramic during the cooling process (Fig. 22). Thus, reductions in the braze joint length can

significantly reduce the residual tensile stress in the ceramic the amount of differential axial contraction that needs to be accommodated is less.

The sixth sleeve joint analysis was performed using the finite element model shown in Fig. 23. The purpose of this analysis was to determine what effect a movement of the braze joint from the side to the base of the silicon nitride post would have on the residual stress state in the ceramic. This braze joint used in this model has an inner diameter of 0.16 in, an outer diameter of 0.26 in, and a thickness of 0.002 in. The assembly was again cooled from a stress-free 950°C to room temperature in 10 min. Results from this analysis indicated that a maximum tensile stress of 80,620 psi (556 MPa) would be generated in the ceramic during the cooling process (Fig. 24). Thus, the maximum tensile stresses generated using this design are significantly higher than the maximum tensile stresses generated using the previous sleeve design with sleeve overlap.

The seventh and final sleeve joint analysis was performed using the finite element model shown in Fig. 25. The purpose of this analysis was to determine what effect the addition of an interlayer would have on the residual stress state in the ceramic. This model is similar to the model used in the first analysis (Fig. 13) except that in this model a 0.012 in thick Kovar interlayer has been added. The assembly was again cooled from a stress-free 950°C to room temperature in 10 min. Results from this analysis indicated that a maximum tensile stress of 88,350 psi (609 MPa) would be generated in the ceramic during the cooling process (Fig. 26). Recall that a maximum tensile stress of 87,280 psi (602 MPa) was generated using a similar geometry without an interlayer. Thus, the addition of a Kovar interlayer that is only 0.012 in thick is not beneficial. This result is consistent with the previous interlayer analyses on butt joints that showed that thin Kovar interlayers are not beneficial.

Results from the sleeve joint analyses are summarized in Table 12. These analyses indicated that modifications to the metal sleeve and silicon nitride post geometry would have a significant effect on the residual stress state generated during the brazing operation. For example, the predicted maximum tensile stress in the ceramic was reduced from 87,280 psi (602 MPa) with the original geometry to 22,670 psi (156 MPa) with a modified geometry. Addition of a 0.012 in thick Kovar interlayer had little effect on the predicted residual stress state.

Table 12. Effect of geometric modifications on the residual stress generated during sleeve joint brazing.

Analysis	Analysis Description	Maximum Tensile Stress in the AS-800 silicon nitride (psi)
59	Baseline - Cool to 20°C in 10 min. Cool to 20°C in 1 hour	87,280 82,880
60	Tapered GN-10 Post	99,280
61	Tapered Hastelloy-S Sleeve	.73,090
62	Tapered Post with Sleeve Overlap	51,010
63	Shorten Braze Length on #62 - Cool to 20°C in 10 min. Cool to 20°C in 1 hour	22,670 21,570
64	Base Support Design	80,620
65	Baseline with 0.012 inch Thick Kovar Interlayer	88,350

IV. Summary

Metal-to-ceramic brazing is being investigated for a variety of defense, automotive and aircraft applications. Two common types of joints are butt joints in which the end of a metal rod is brazed to the end of a ceramic rod, and sleeve joints in which a ceramic rod is brazed to the inside of a metal sleeve. Axisymmetric finite element models of braze joints between silicon nitride and a variety of metals were developed to study both butt joints and sleeve joints.

Results from the butt joint analyses indicated that the use of single interlayers could either increase or reduce the residual stress levels generated in the silicon nitride depending on the thickness of the interlayer. The use of a single molybdenum interlayer between the Monel K-500 and AS-800 was most effective when the interlayer thickness was greater than 0.30 in. The use of a nickel interlayer between Monel K-500 and AS-800 was not very beneficial. The use of a Kovar interlayer between Hastelloy-S and AS-800 was beneficial when the interlayer thickness was greater than 0.16 in. The use of a 0.040 in thick Kovar interlayer caused the residual stresses in the AS-800 to increase significantly.

The use of composite interlayers between the base metal and silicon nitride dramatically reduced the residual stress levels in the silicon nitride when certain layer thickness combinations were used. The residual tensile stress in the 0.800 in diameter AS-800 rod generated by AS-800 to Monel K-500 brazing was minimized when a composite Ni/Mo/Ni interlayer was used, the thickness of the molybdenum layer was made as large as possible and the two nickel layers were given a thickness of approximately 0.050 in. There appears to be a relationship between the optimum nickel layer thickness and the diameter of the rods that are being brazed together. For a 0.500 in diameter rod the optimum nickel layer thickness is approximately 0.030 in. Thus, for the two diameters that were analyzed, the optimum nickel layer thickness is approximately six percent of the rod diameter.

Results from the sleeve joint analyses indicated that modifications to the metal sleeve and silicon nitride post geometry could have a significant effect on the residual stress state generated during the brazing operation. Residual stresses in the sleeve joint were minimized when the joint length was minimized and the sleeve was designed to extend beyond both ends of the braze joint.

V. Acknowledgments

This study would not have been possible without the material data provided by John Stephens (1833) and the information and ideas provided by John and the other researchers working on this CRADA: Jill Glass (1833), Ron Loehman (1808), Mike Hosking (1833), Paul Vianco (1833), Sandy Monroe (1833), and Chuck Walker (1471).

VI. REFERENCES

1. Y. Zhou, Y., F. H. Bao, J. L. Ren, and T. H. North, "Interlayer Selection and Thermal Stresses in Brazed Si_3N_4-Steel Joints," Materials Science and Technology, Vol. 7, pp. 863-868, Sept. 1991.
2. J. H. Selverian, D. O'Neil, and S. Kang, "Ceramic-to-Metal Joints: Part I-Joint Design," Am. Ceram. Soc. Bull., Vol. 71, pp. 1403-1409, Sept. 1992.
3. J. H. Selverian, and S. Kang, "Ceramic-to-Metal Joints: Part II-Performance and Strength Prediction," Am. Ceram. Soc. Bull., Vol. 71, pp. 1511-1520, Oct. 1992.
4. M. K. Neilsen, S. N. Burchett, C. M. Stone, and J. J. Stephens, "A Viscoplastic Theory for Braze Alloys," SAND96-0984, Sandia National Laboratories, April 1996.
5. J. J. Stephens, S. N. Burchett, and W. B. Jones, "Stress Relaxation of Braze Joints," in **Advances in Electronic Packaging**, Edited by Chen, W.T., and Hiroyuki, A., EEP1-1, American Society of Mechanical Engineers, 1992.
6. J. J. Stephens, F. M. Hosking, and S. N. Burchett, "Creep Properties of the 62.2Ag-36.2Cu-1.6Ti Active Metal Braze Alloy," Presented at the Annual TMS Meeting, Denver, CO, Feb. 1993.
7. J. J. Stephens, and K. D. Hamann, "High Temperature Tensile Properties of the BAu-4 (82Au-18Ni) Braze Alloy," Presented at the Annual TMS Meeting, San Francisco, CA, Feb. 1994.
8. J. H. Biffle, "JAC - A Two-Dimensional Finite Element Computer Program for the Non-Linear Quasi-Static Response of Solids with the Conjugate Gradient Method," SAND81-0998, Sandia National Laboratories, April 1984.

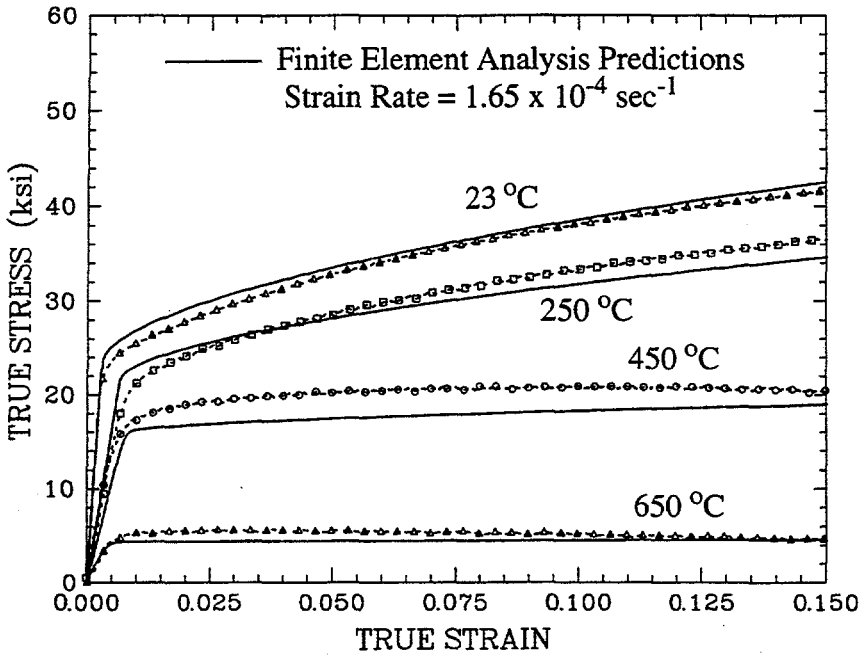

Fig. 1. Comparison of results from uniaxial compression experiments on Cusil[5] with finite element analysis predictions.

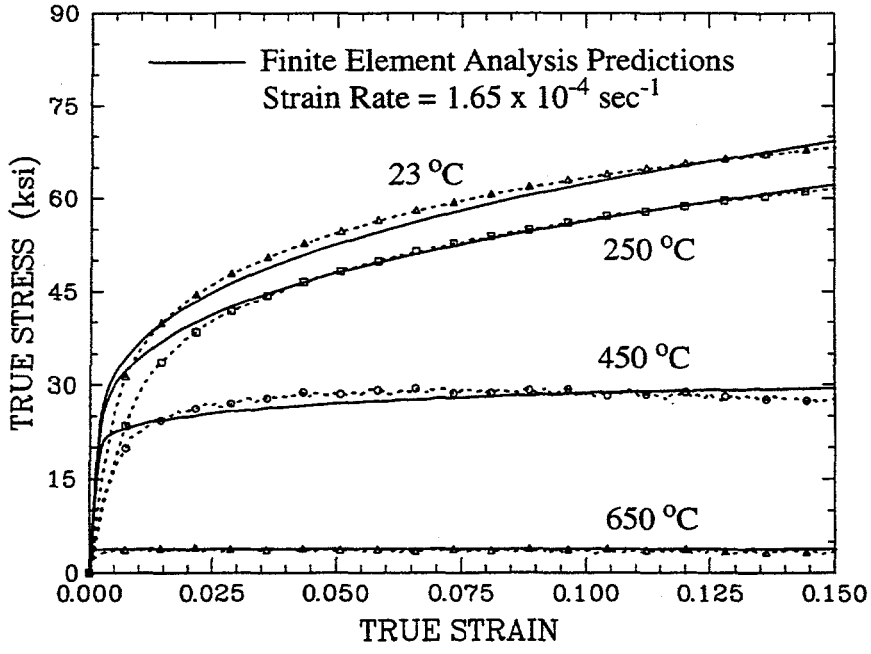

Fig. 2. Comparison of results from uniaxial compression experiments on CusilABA[6] with finite element analysis predictions.

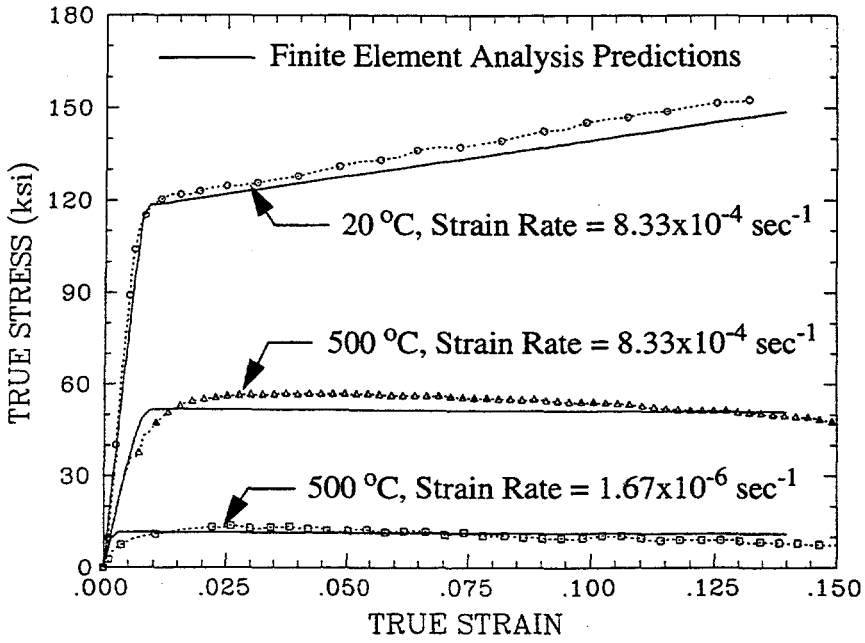

Fig. 3. Comparison of results from uniaxial tension experiments on Nioro[7] with finite element analysis predictions.

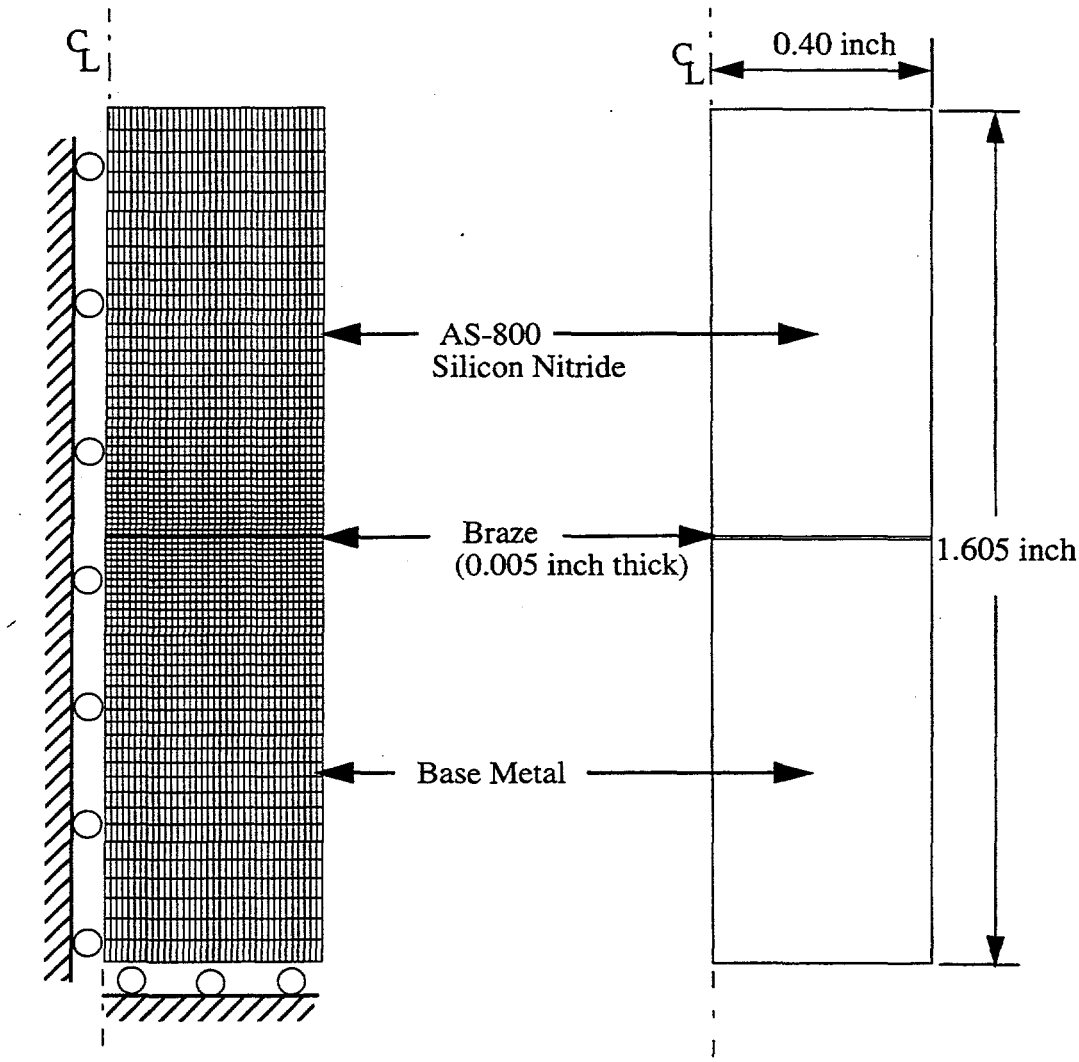

Fig. 4. Axisymmetric finite element model of end braze joint between two rods.

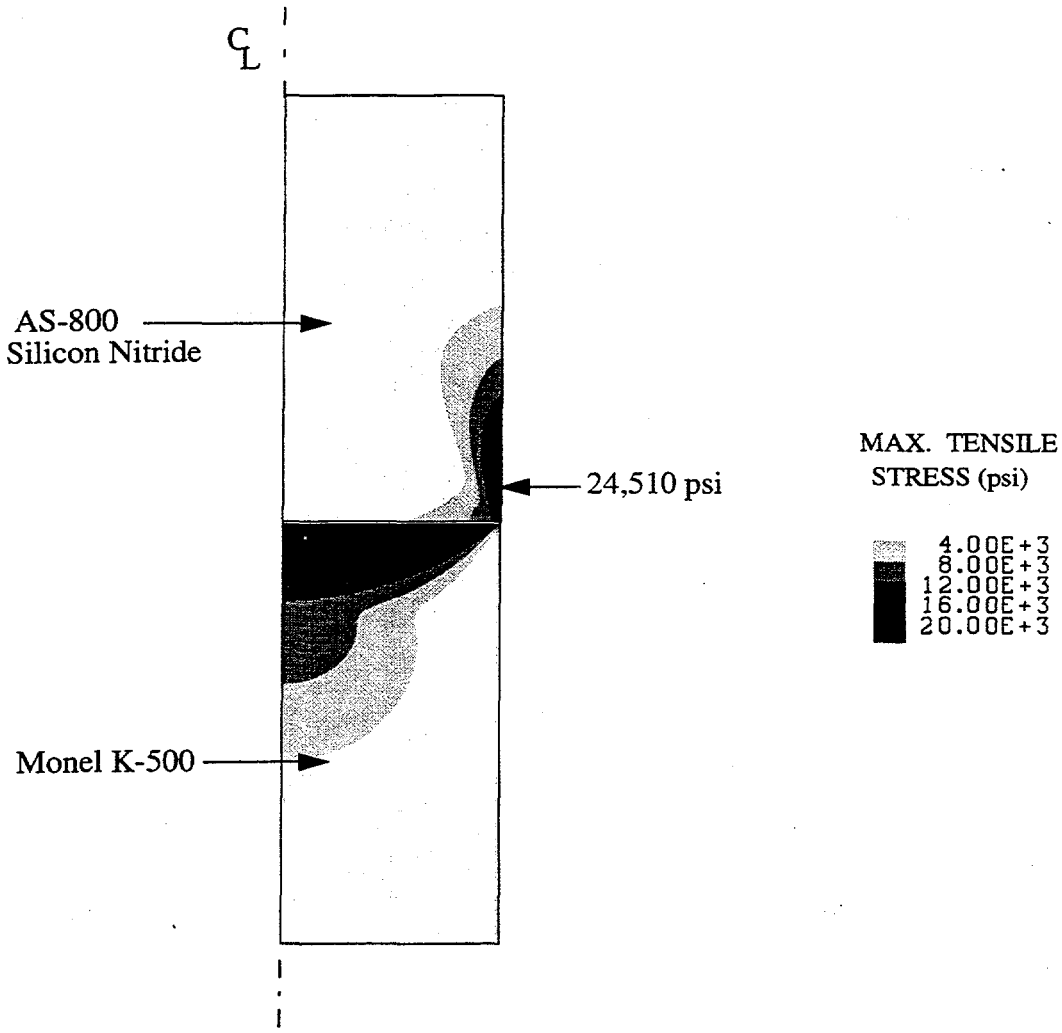

Fig. 5. Maximum tensile stress distribution generated during the brazing of a Monel K-500 rod to an AS-800 Si_3N_4 rod.

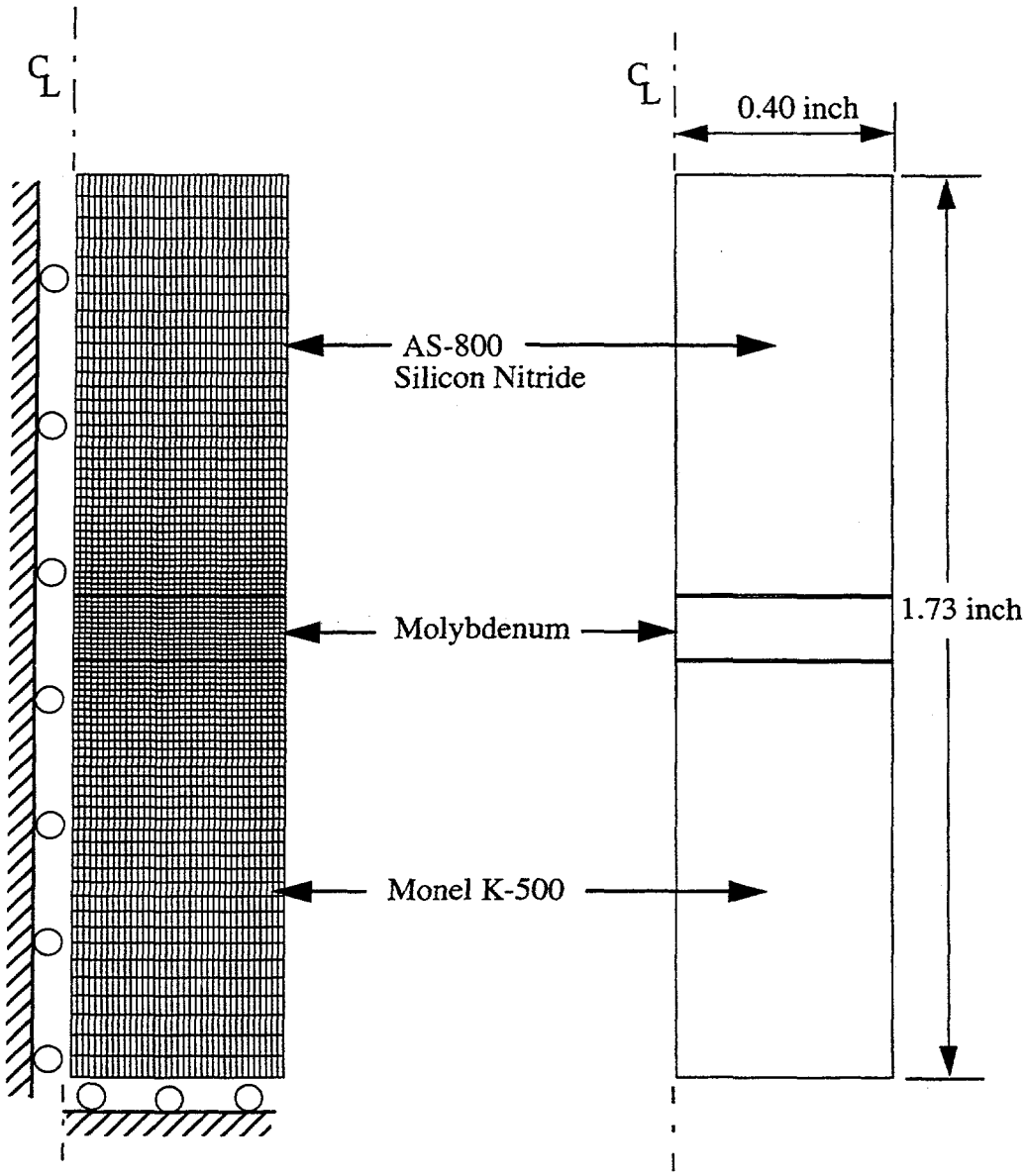

Fig. 6. Axisymmetric finite element model of end braze joint between a Monel K-500 rod and an AS-800 Si_3N_4 rod with a 0.120 inch molybdenum interlayer.

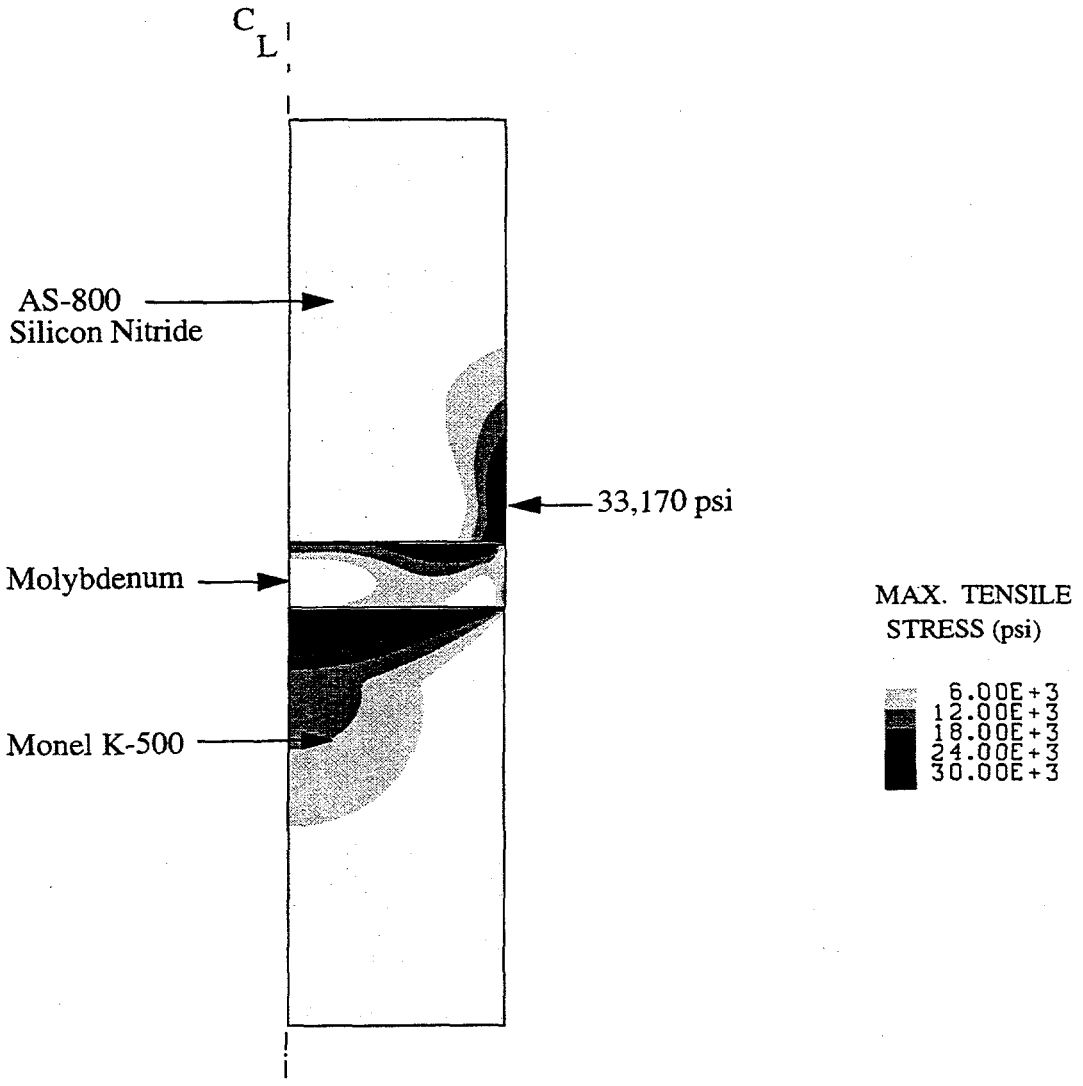

Fig. 7. Maximum tensile stress distribution generated during the brazing of a Monel K-500 rod to an AS-800 Si_3N_4 rod with a 0.120 inch molybdenum interlayer.

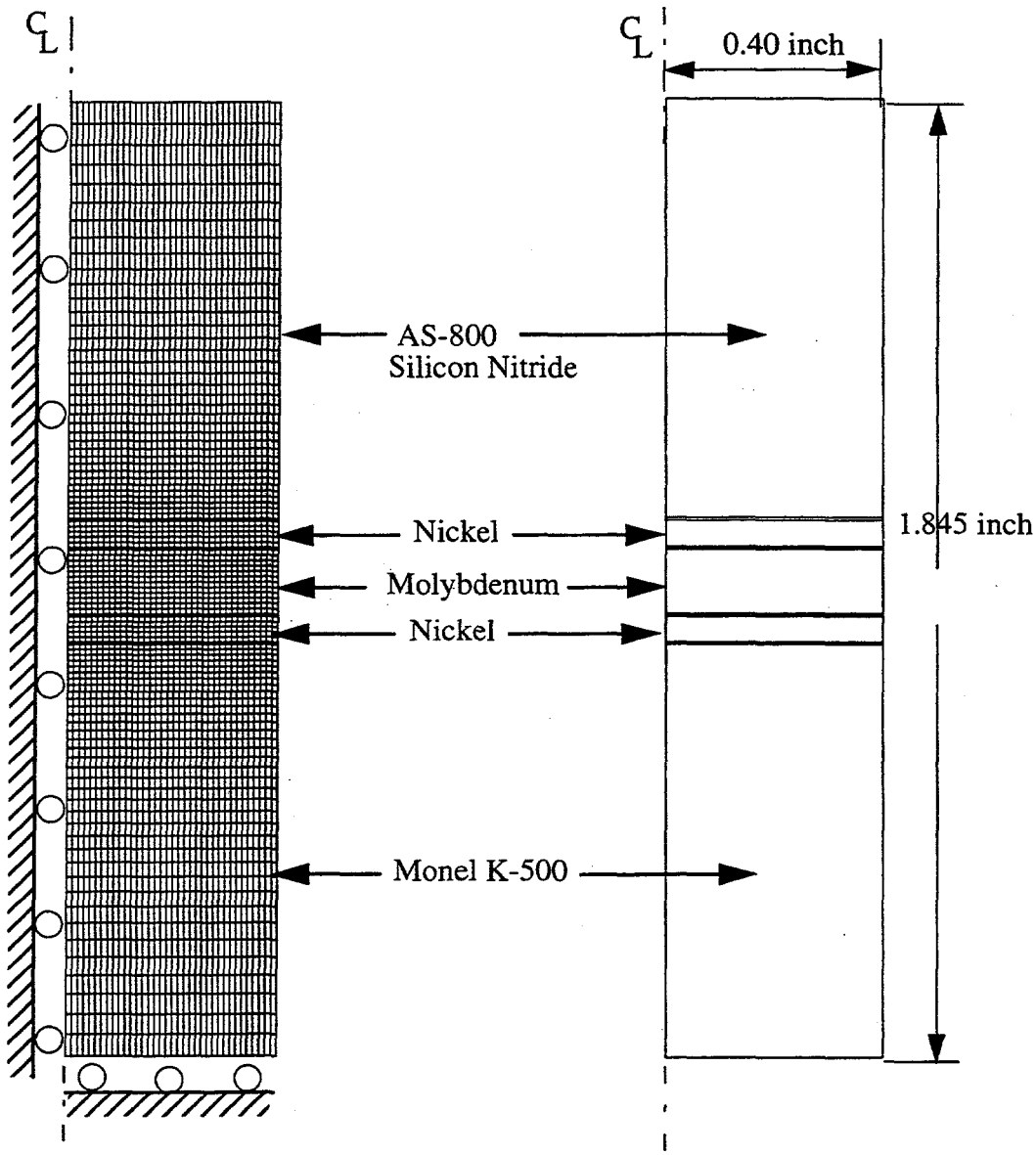

Fig. 8. Axisymmetric finite element model of an end braze joint between a Monel K-500 rod and an AS-800 Si_3N_4 rod with a nickel/molybdenum/nickel interlayer.

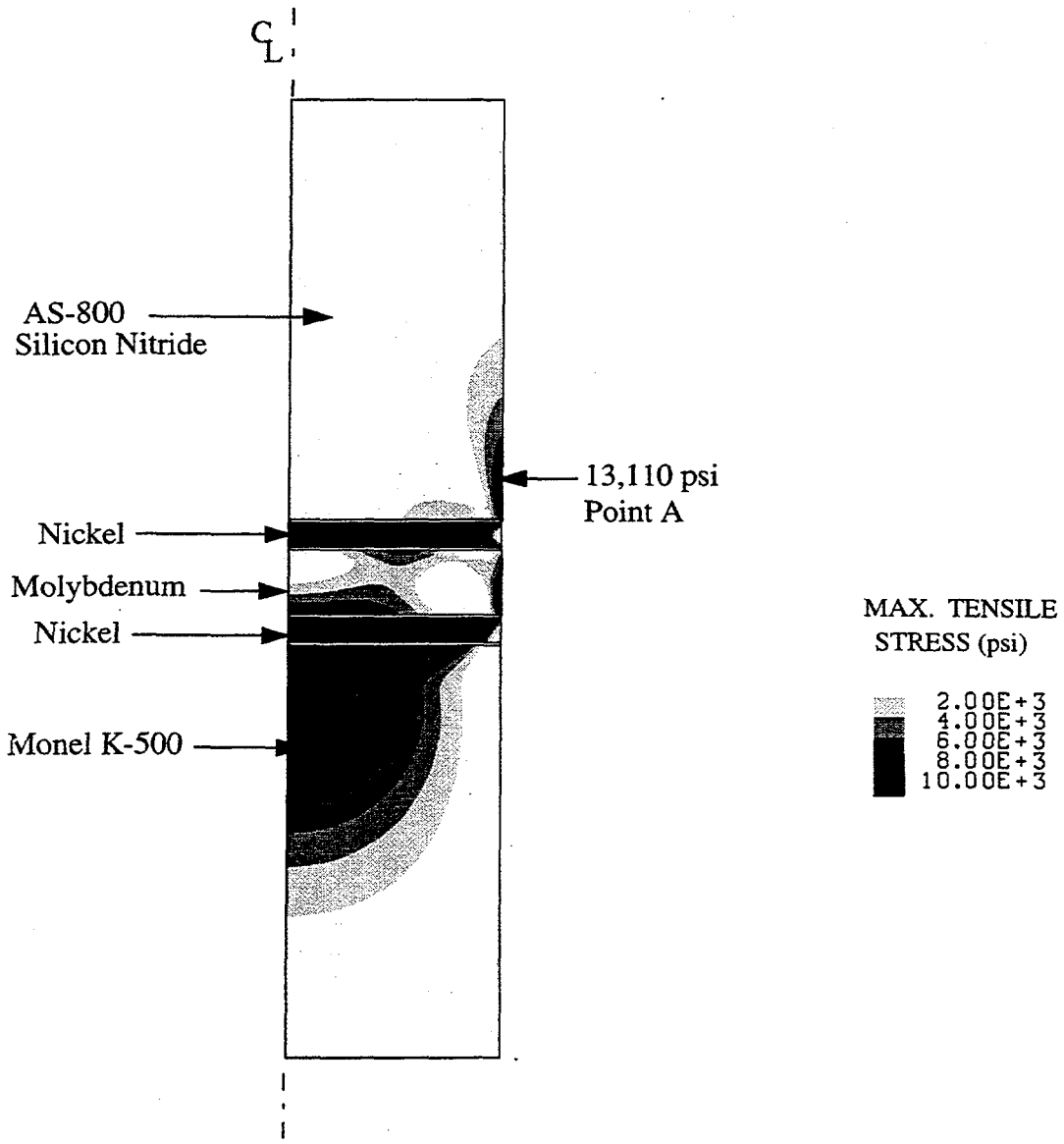

Fig. 9. Maximum tensile stress distribution generated during the brazing of a Monel K-500 rod to an AS-800 Si_3N_4 rod with a Ni/Mo/Ni interlayer.

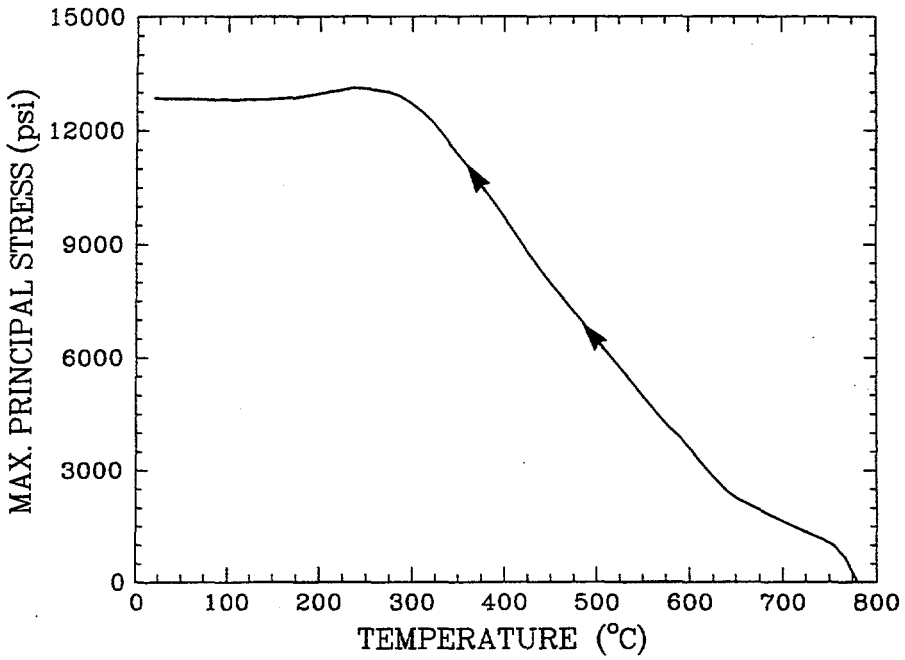

Fig. 10. Maximum tensile stress history at Point A (see Fig. 9) in the AS-800 Si_3N_4.

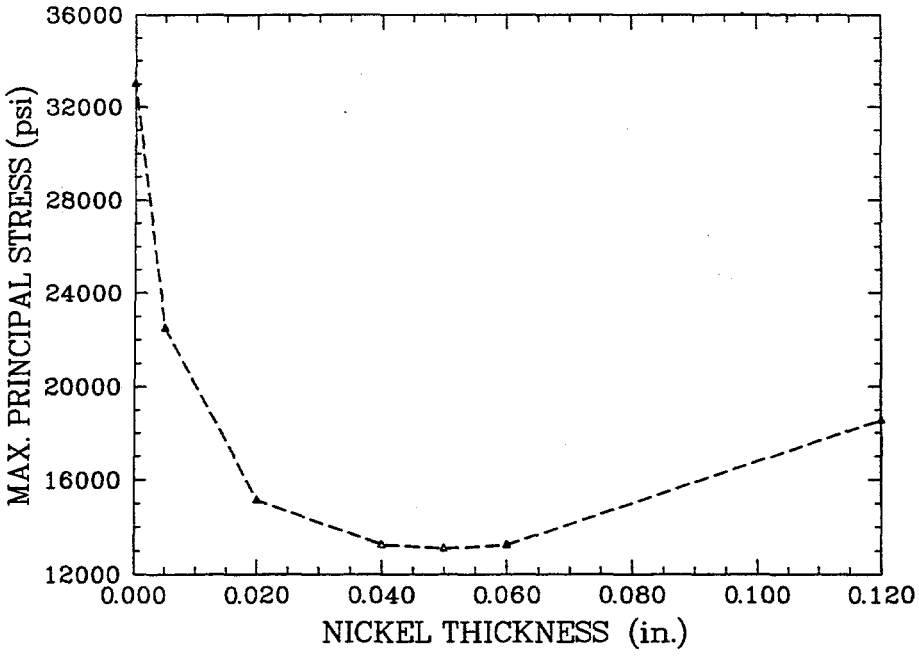

Fig. 11. Effect of nickel layer thickness on the maximum tensile stress generated in the Si_3N_4 during the brazing of a Monel K-500 rod to an AS-800 Si_3N_4 rod with a Ni/Mo/Ni interlayer.

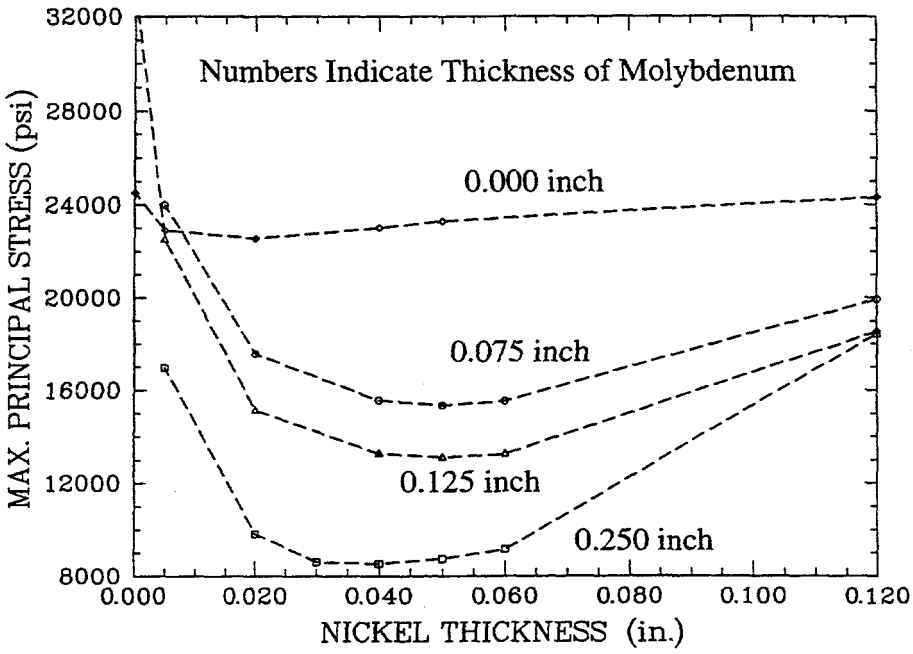

Fig. 12. Effect of molybdenum and nickel layer thickness on the maximum tensile stress generated in the AS-800 Si_3N_4 during the brazing simulations with a composite Ni/Mo/Ni interlayer.

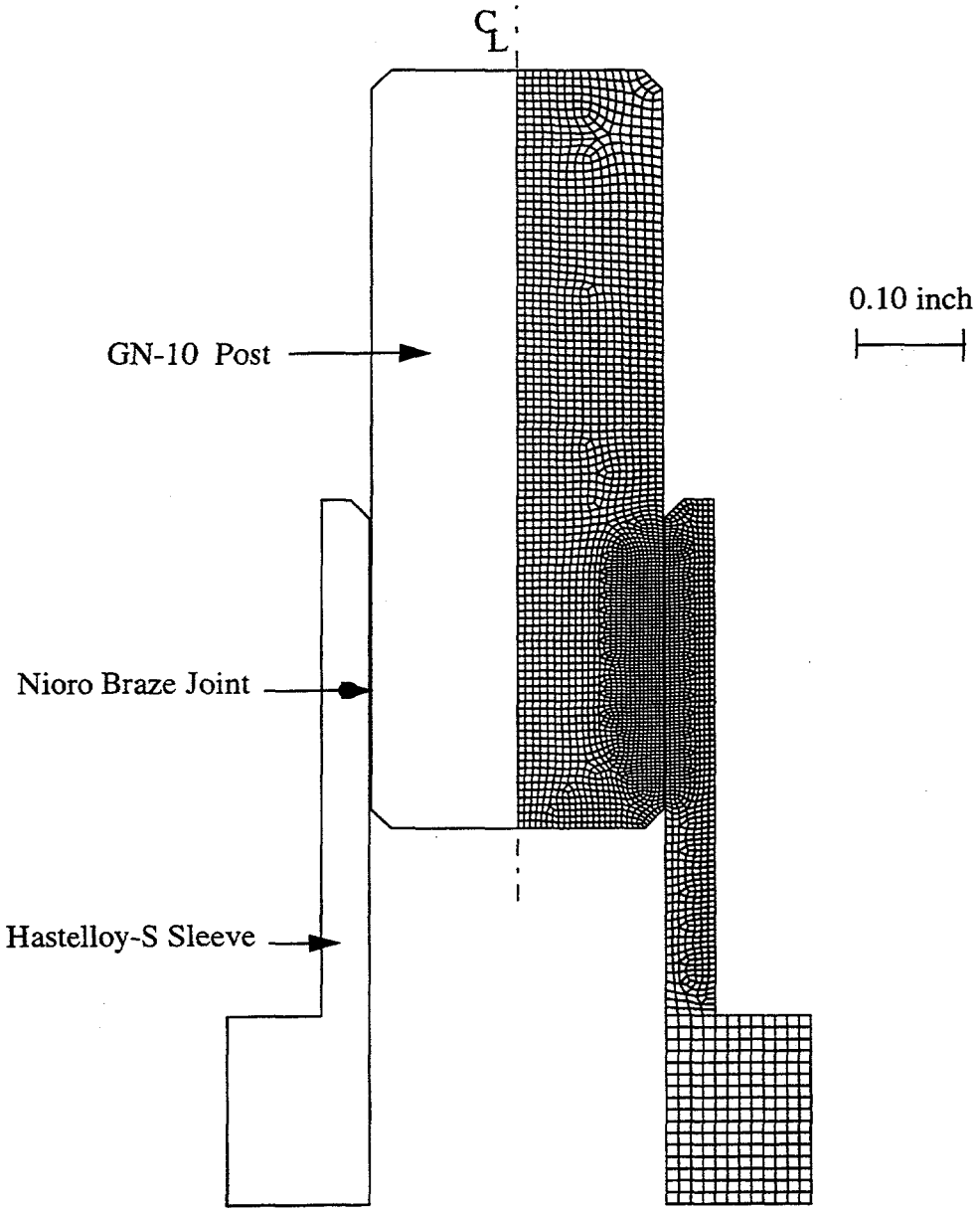

Fig. 13. Axisymmetric finite element model of the baseline sleeve braze joint.

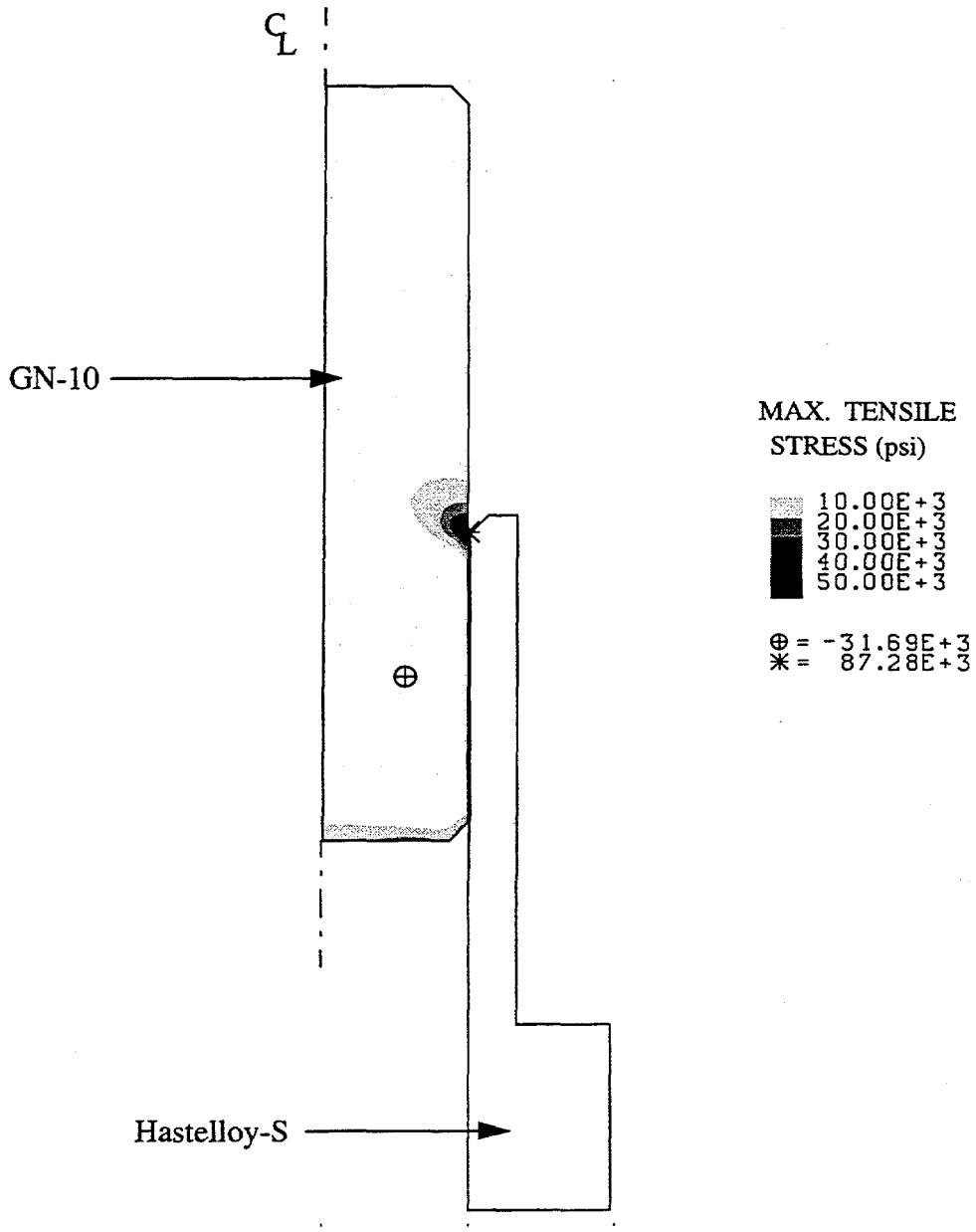

Fig. 14. Maximum tensile stress distribution generated during the brazing of a GN-10 Si_3N_4 post into a Hastelloy-S sleeve.

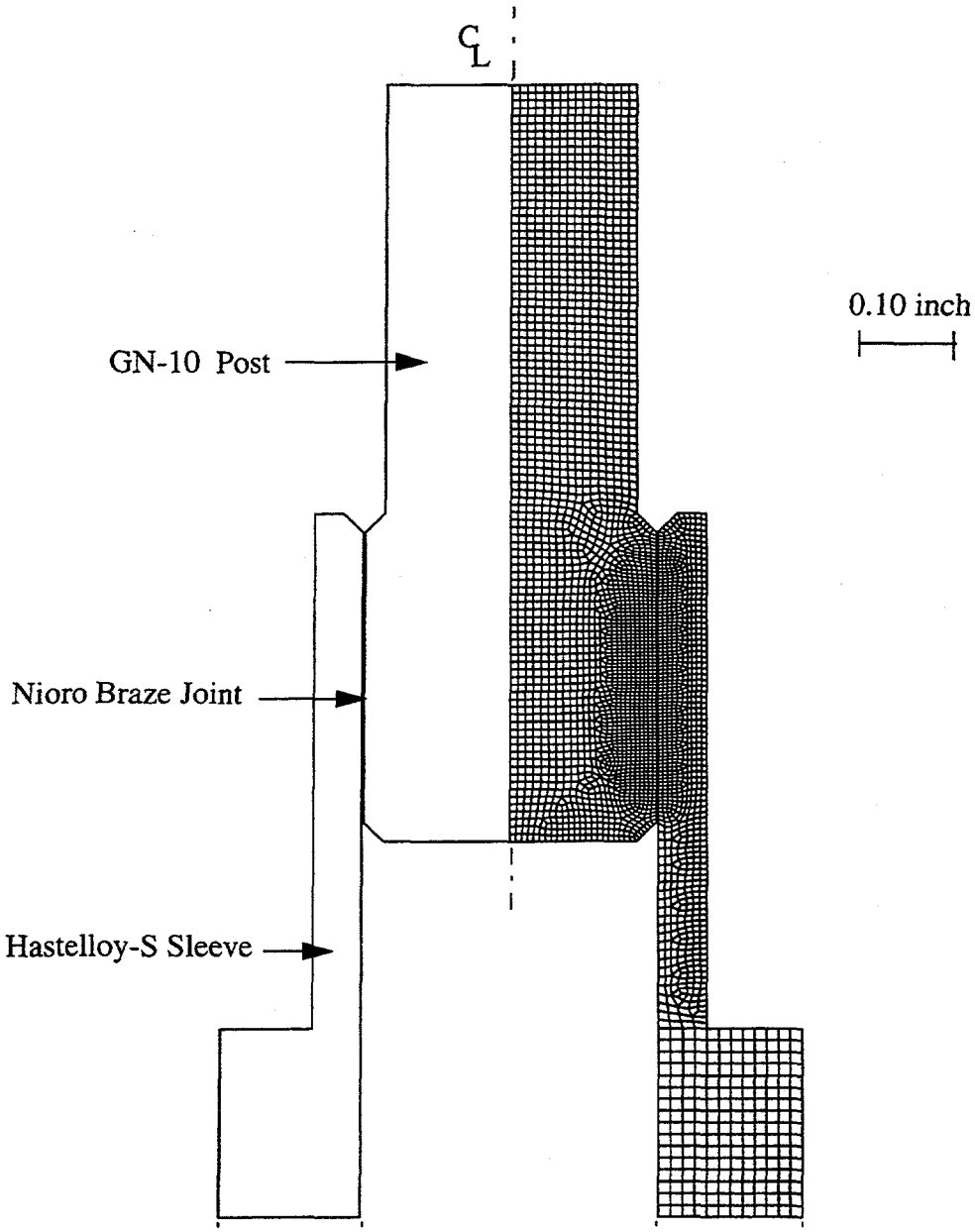

Fig. 15. Axisymmetric finite element model of a sleeve braze joint with a tapered GN-10 Si_3N_4 post.

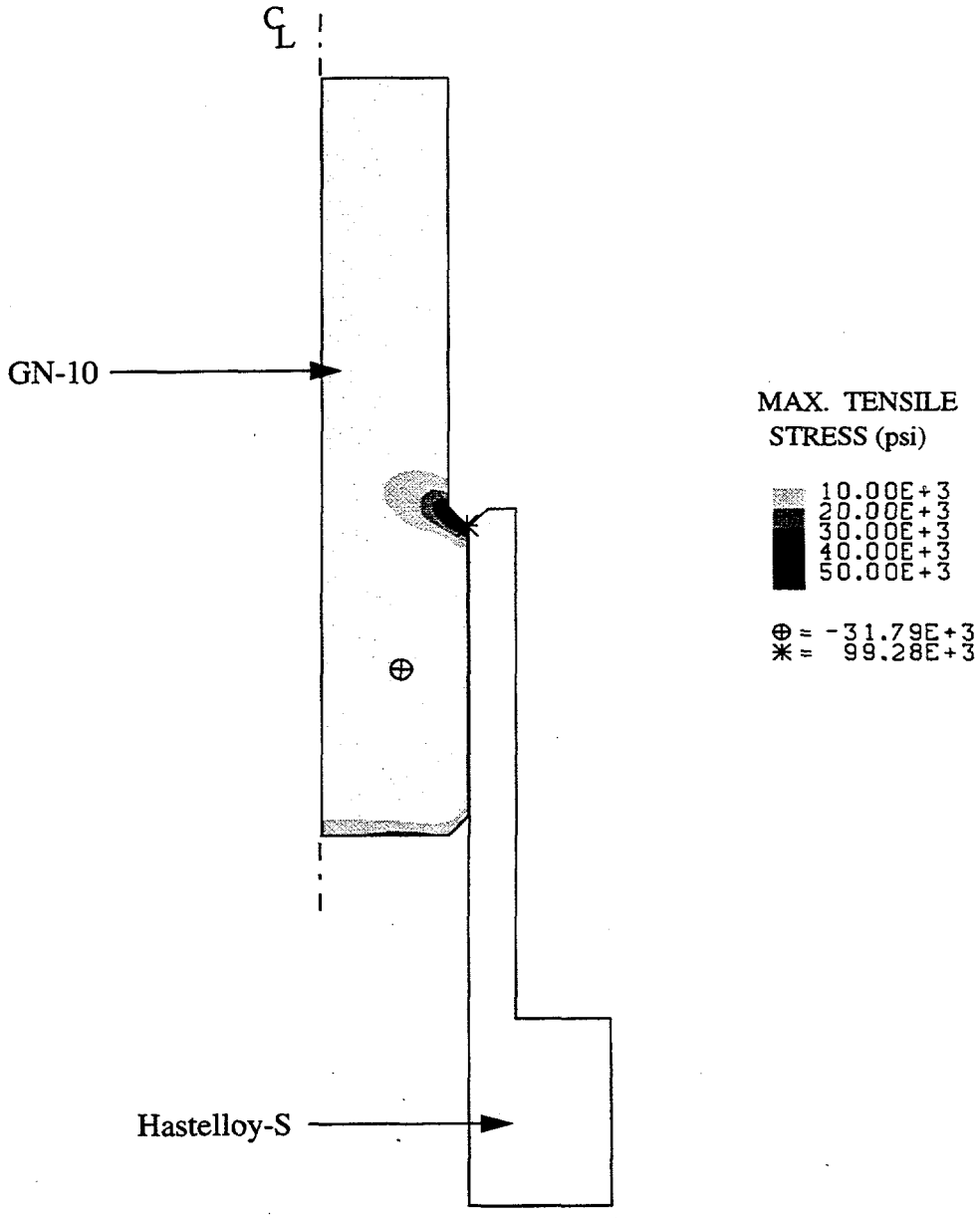

Fig. 16. Maximum tensile stress distribution generated during the brazing of a tapered GN-10 Si_3N_4 post into a Hastelloy-S sleeve.

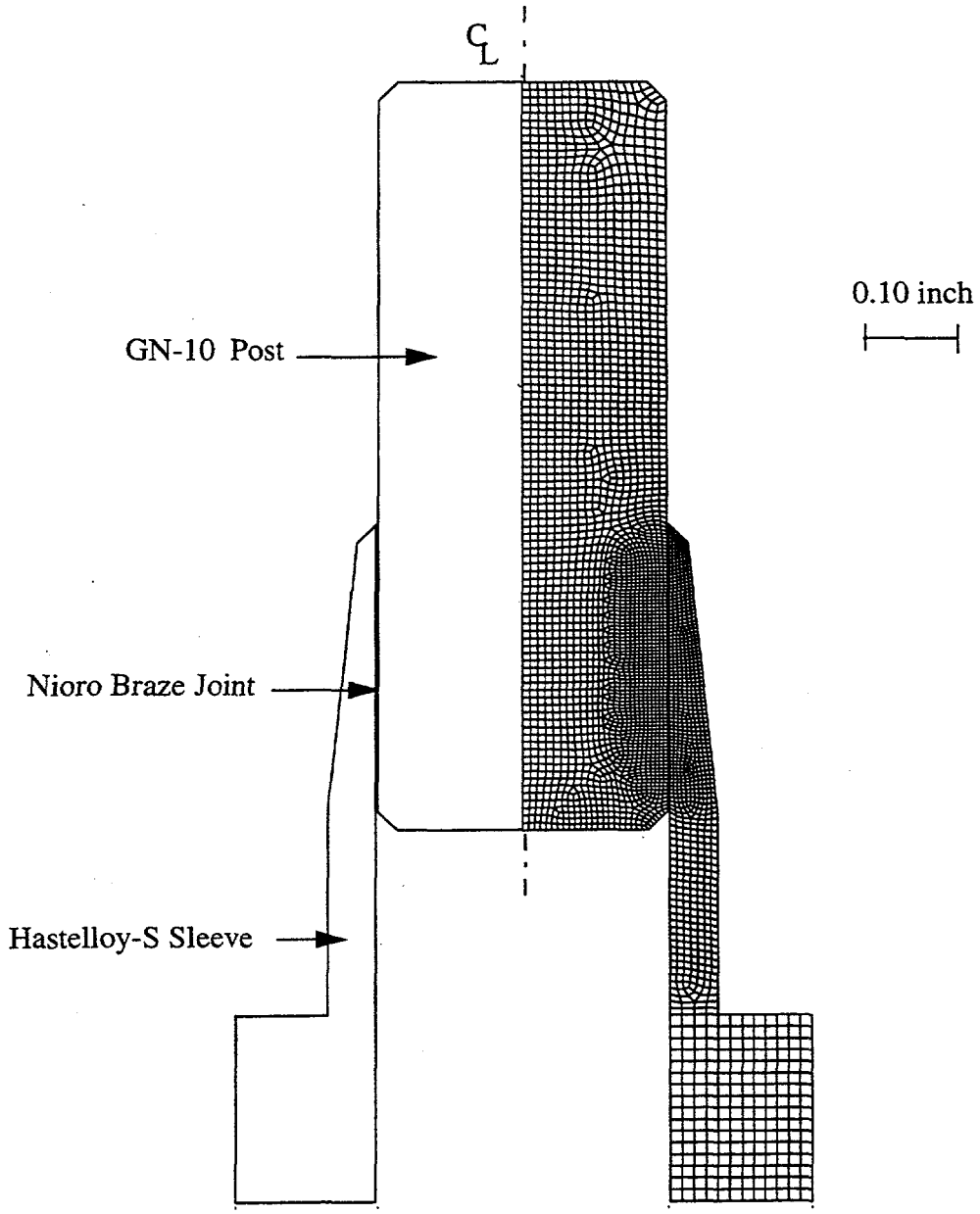

Fig. 17. Axisymmetric finite element model of a sleeve braze joint with a tapered Hastelloy-S sleeve.

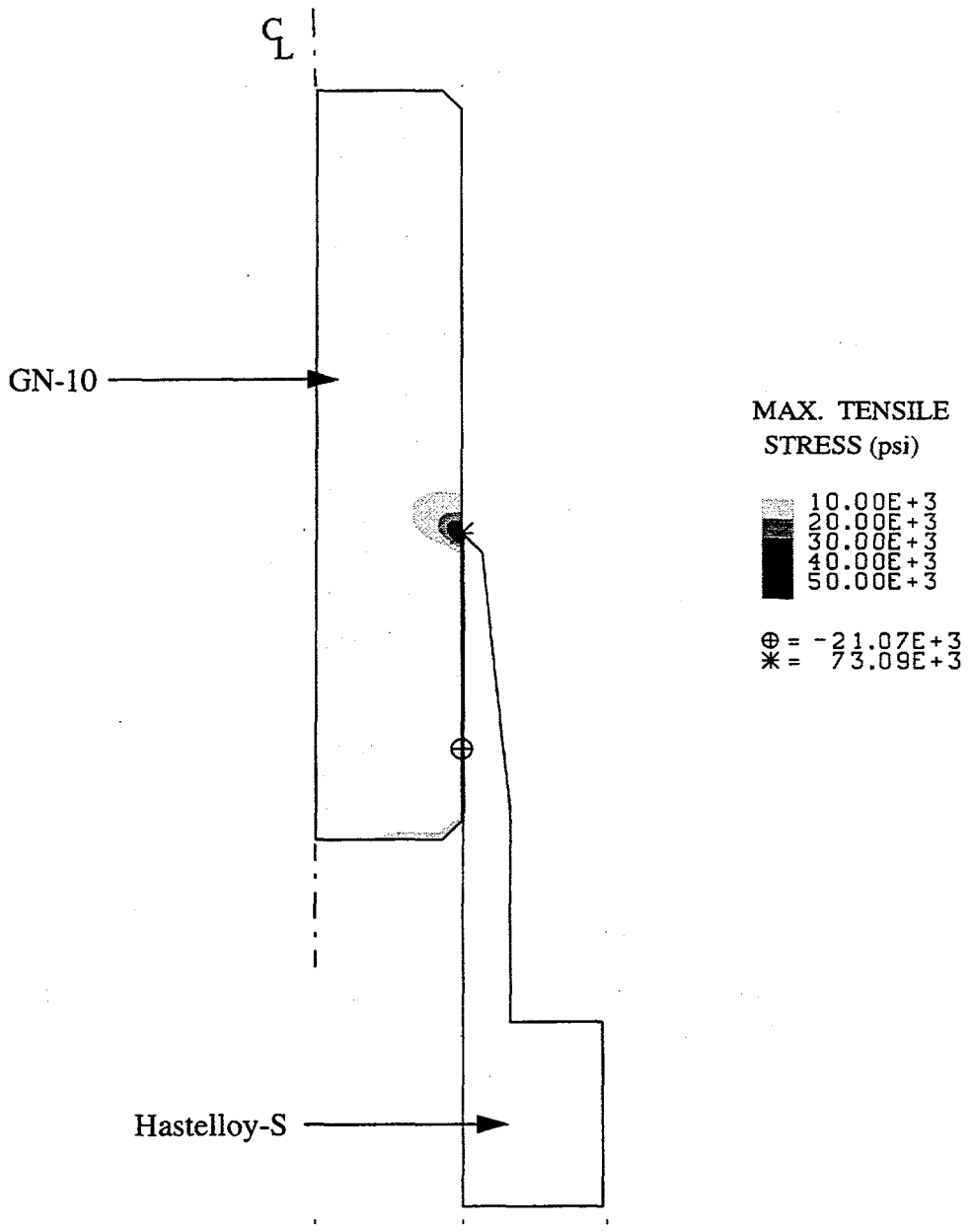

Fig. 18. Maximum tensile stress distribution generated during the brazing of a GN-10 Si_3N_4 post into a tapered Hastelloy-S sleeve.

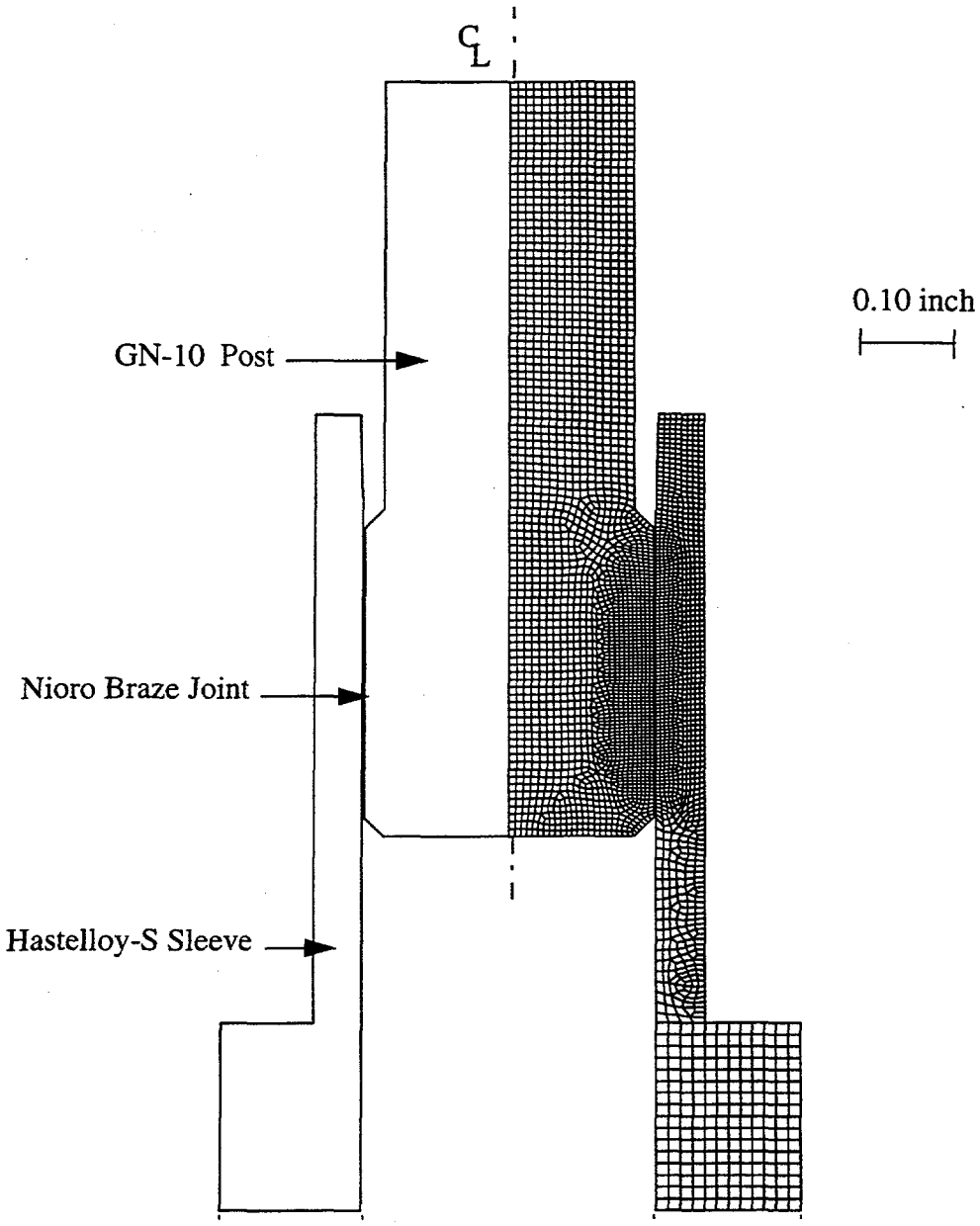

Fig. 19. Axisymmetric finite element model of a sleeve braze joint with a tapered GN-10 Si_3N_4 post and sleeve overlap.

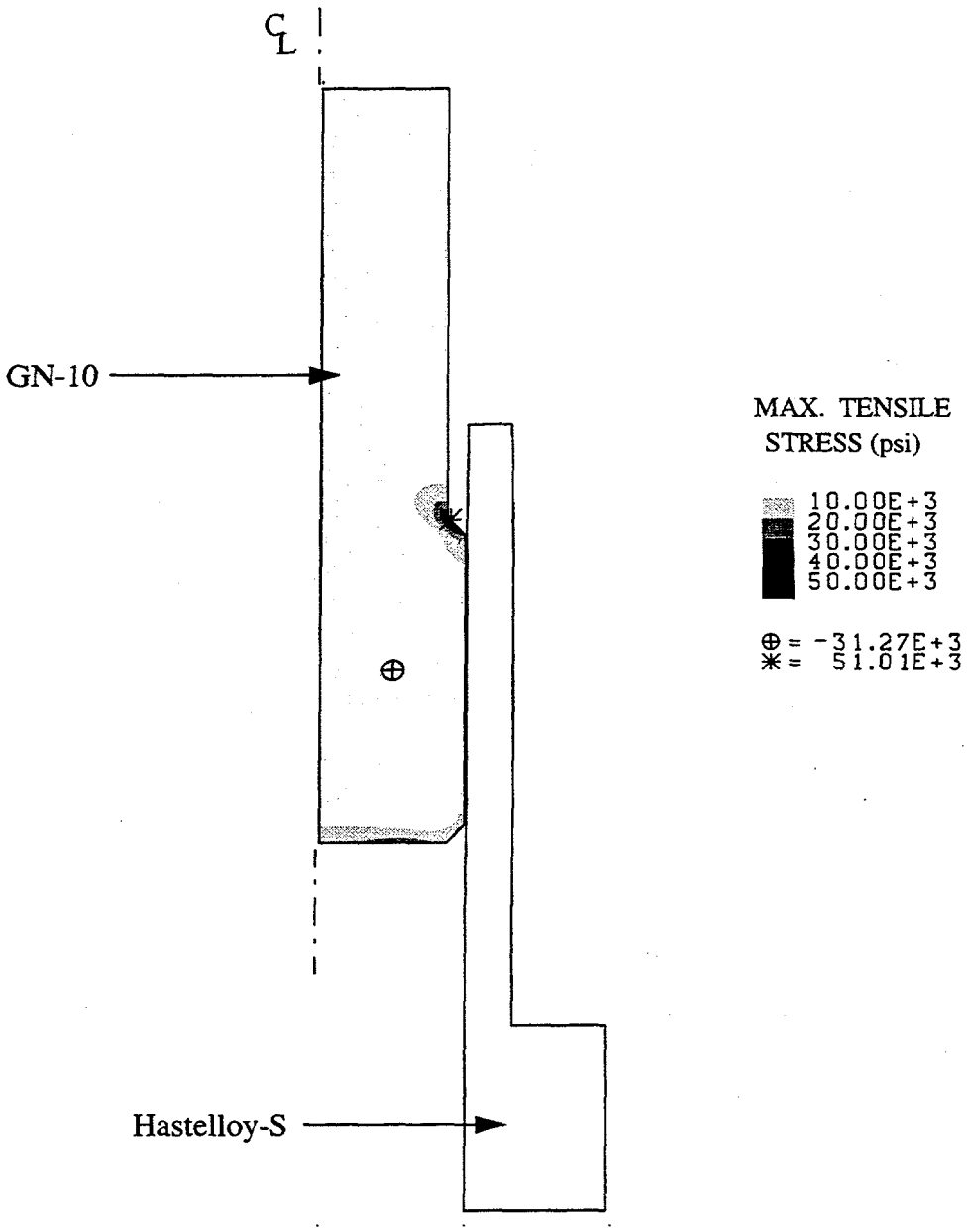

Fig. 20. Maximum tensile stress distribution generated during the brazing of a tapered GN-10 Si_3N_4 post with sleeve overlap.

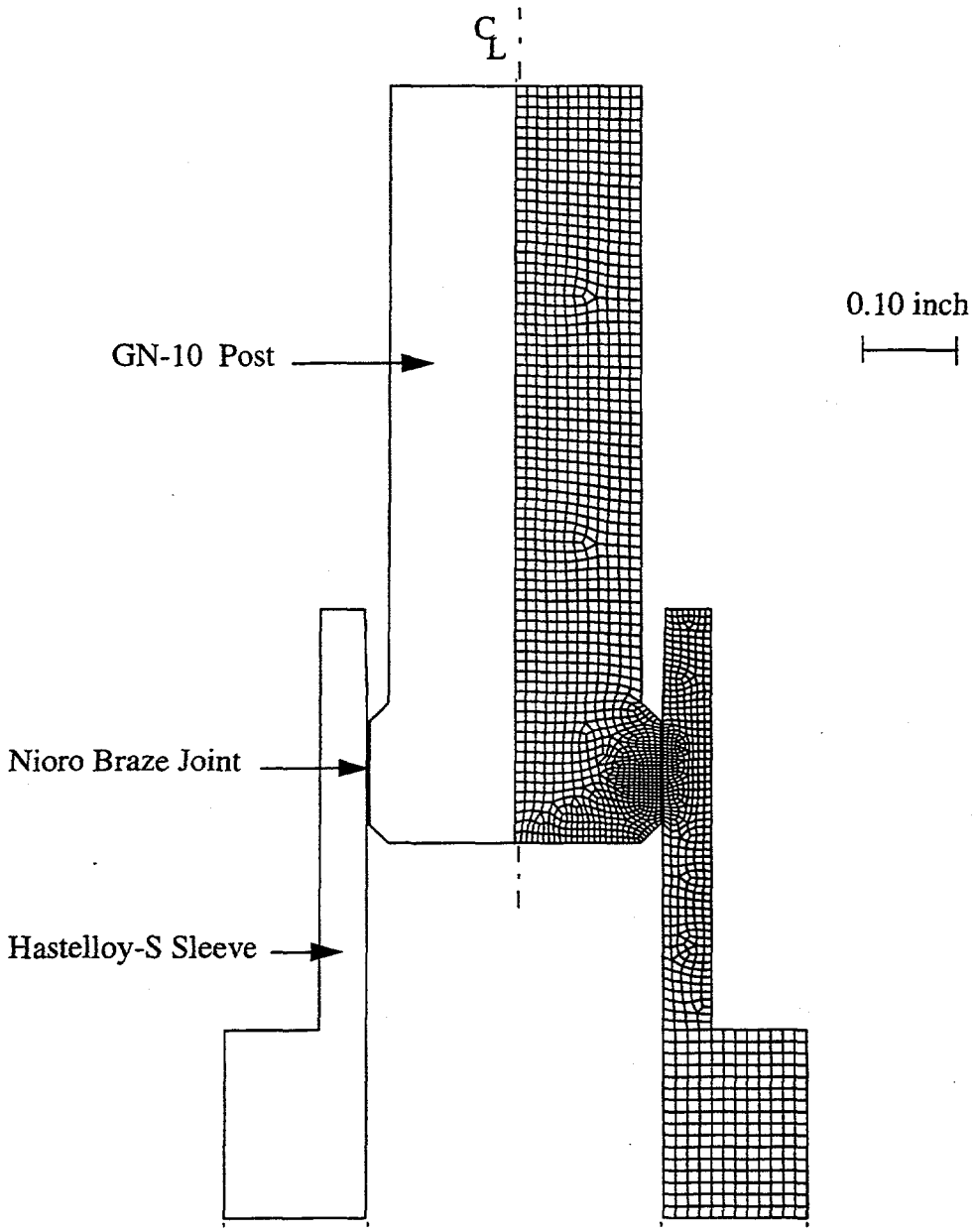

Fig. 21. Axisymmetric finite element model of a sleeve braze joint with a tapered GN-10 Si_3N_4 post, sleeve overlap, and a reduced joint length.

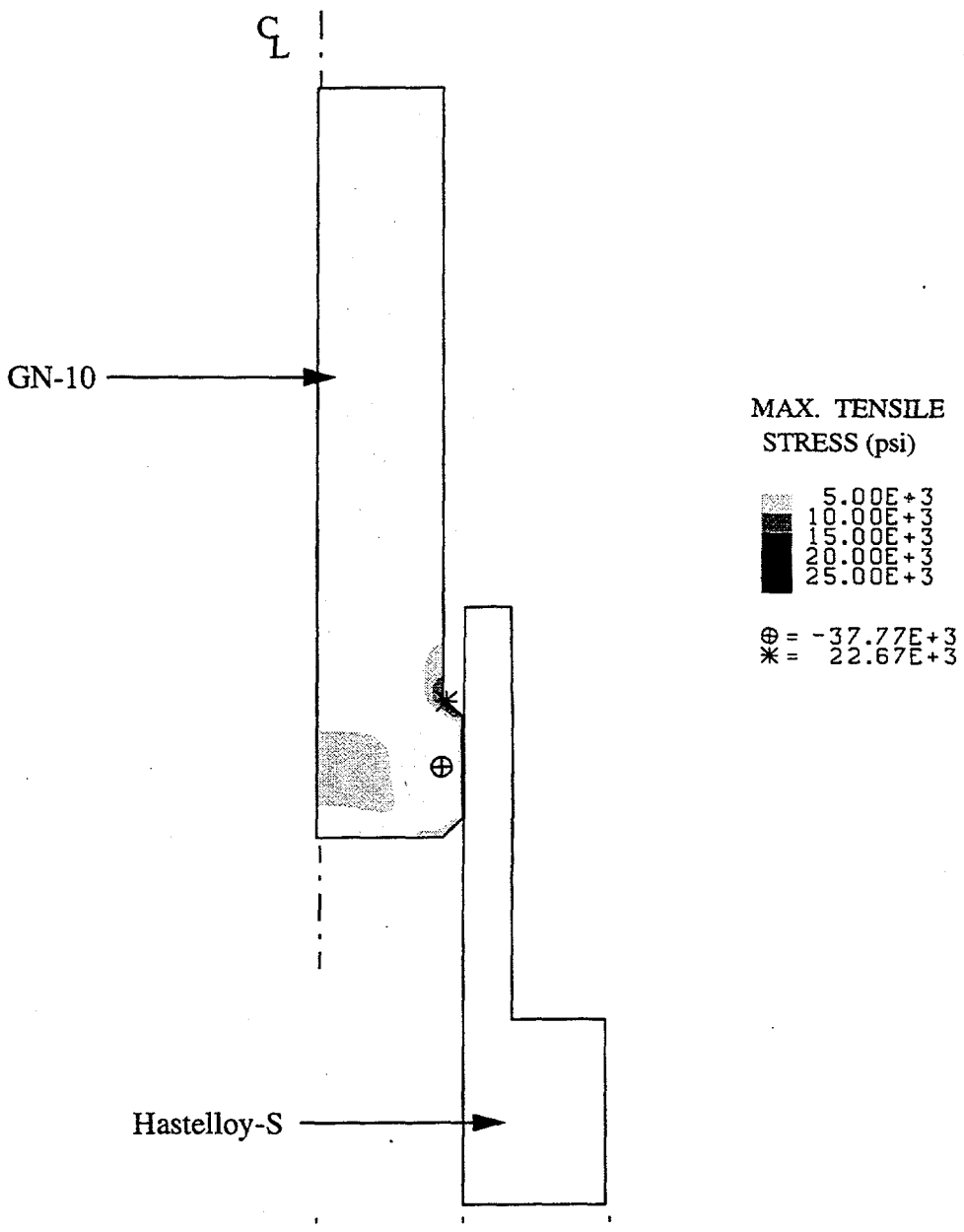

Fig. 22. Maximum tensile stress distribution generated during the brazing of a tapered GN-10 Si_3N_4 post with sleeve overlap and a reduced braze length.

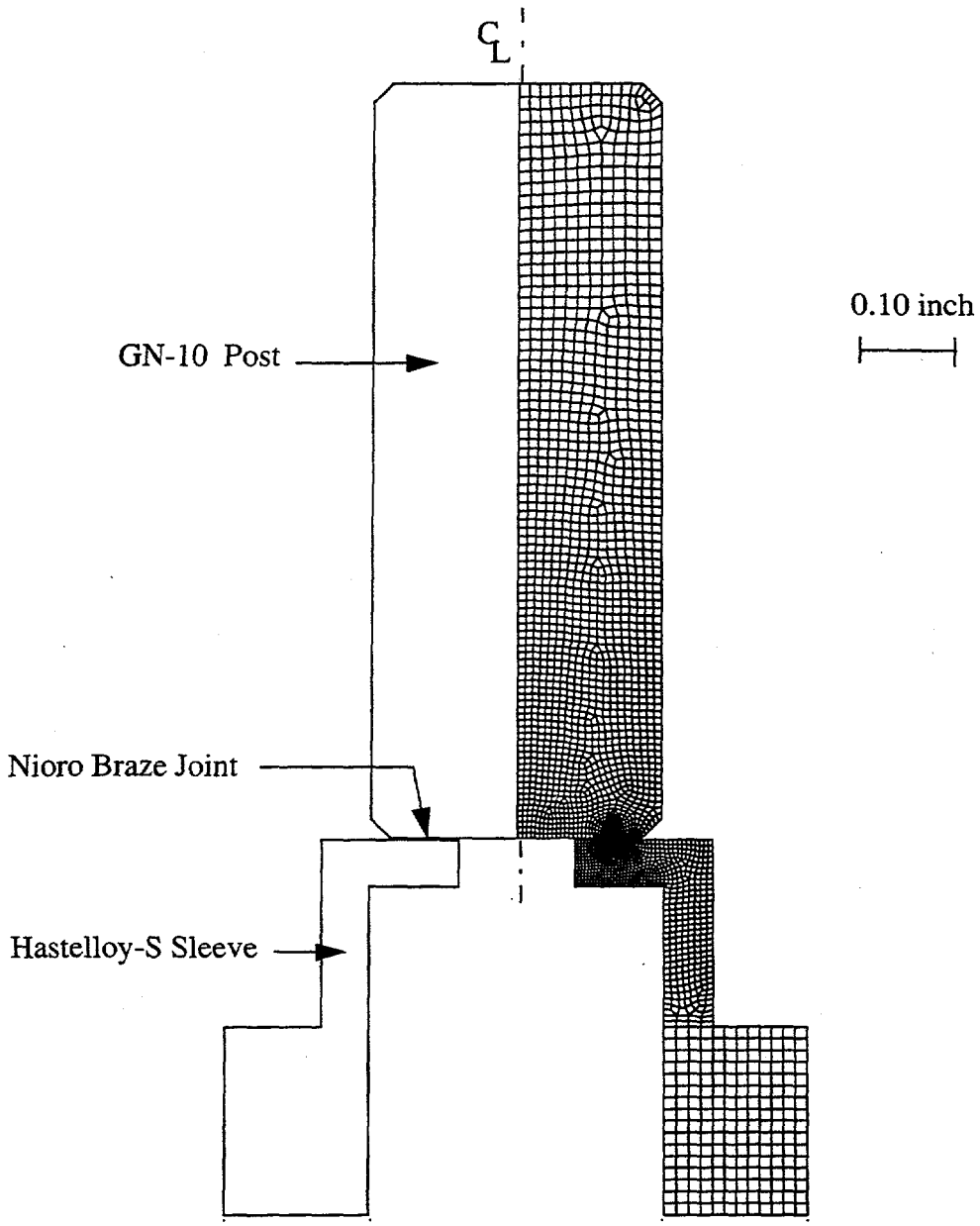

Fig. 23. Axisymmetric finite element model of a sleeve braze joint with a braze joint located on the end of the Si_3N_4 post.

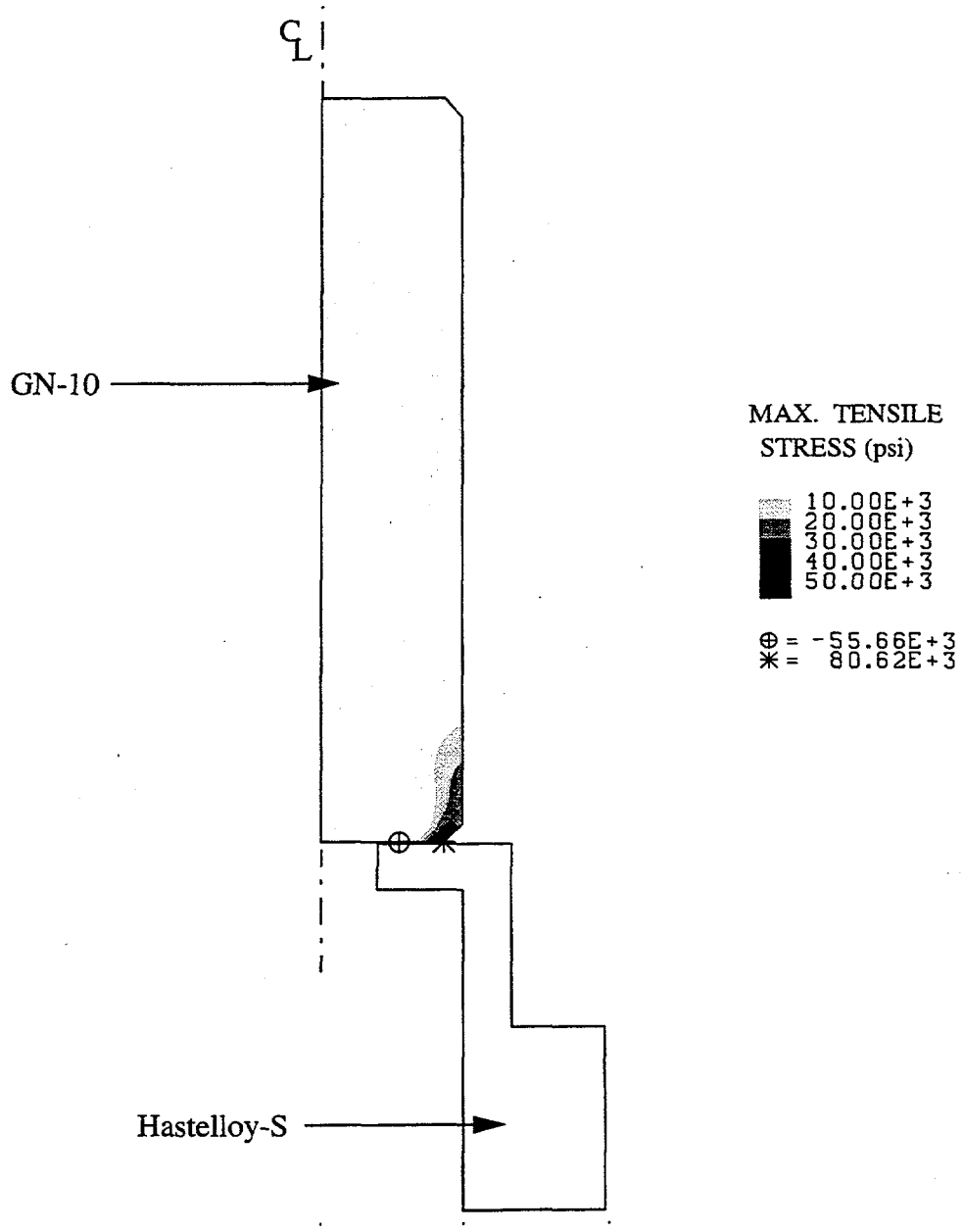

Fig. 24. Maximum tensile stress distribution generated during the brazing of a GN-10 Si_3N_4 post to a Hastelloy-S base support.

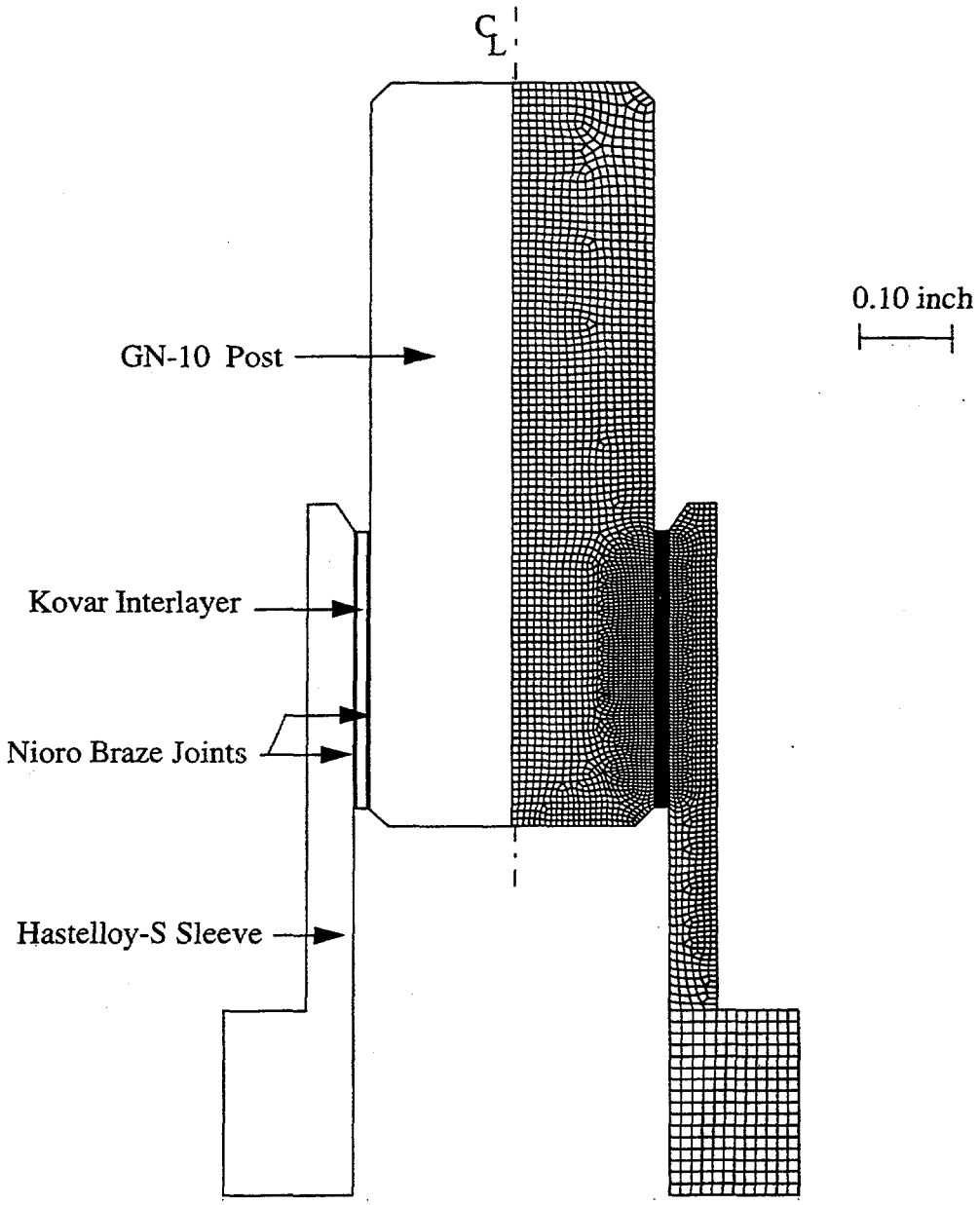

Fig. 25. Axisymmetric finite element model of a sleeve braze joint with a 0.012 inch thick Kovar interlayer.

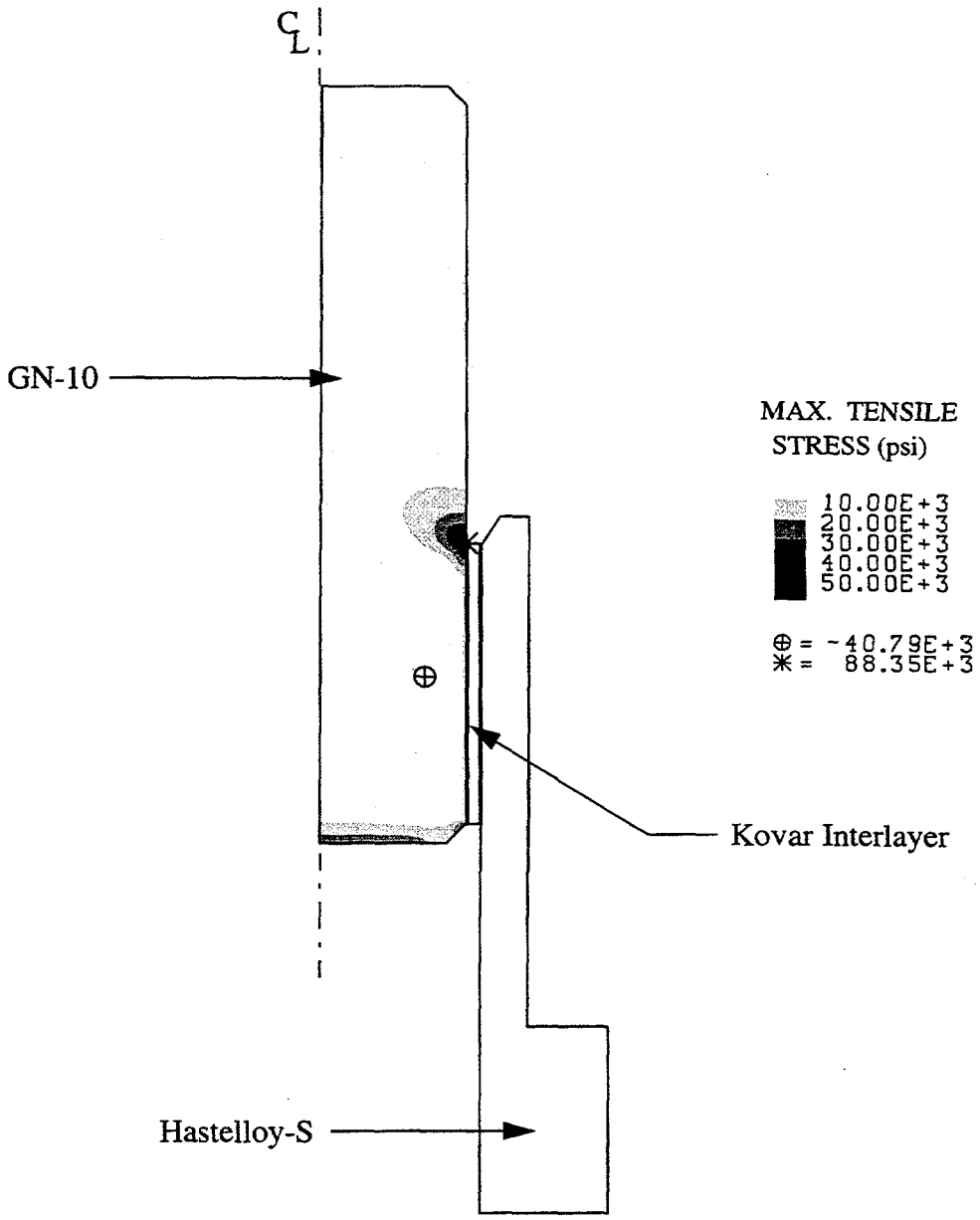

Fig. 26. Maximum tensile stress distribution generated during the brazing of a sleeve joint with a 0.012 inch thick Kovar interlayer.

Dr. J. Pollinger
Tetralux Engineering Services
334 Via Colusa
Redondo Beach, CA 90277

Dr. F. M. Mahoney
Saint Gobain Abrasives
MS420-601
1 New Bond St.
Worcester, MA 01615-0008

Captain B. Quillen
379 Ardennes Circle
Seaside, CA 93955
(Formerly with the Air Force Research Laboratory, Kirtland Air Force Base, NM)

Dr. M. L. Savitz
Honeywell, Inc. Ceramic Components
2525 W. 190th St.
MS 1/5-1 26000
Torrance, CA 90504

Dr. R. G. Rateick, Jr.
Honeywell, Inc.
717 N. Bendix Dr.
South Bend, IN 46637

Dr. J. Yamanis
Honeywell, Inc.
PO Box 1021
Morristown, NJ 07962-1021

Dr. C. Gasdaska
Honeywell, Inc.
PO Box 1021
Morristown, NJ 07962-1021

Dr. T. Oyama
WESGO Inc. - Metals Div.
610 Quarry Road
San Carlos, CA 94070

Dr. M. L. Santella
Oak Ridge National Laboratories
P.O. Box 2008, Bldg. 4508, MS6096
Oak Ridge, TN 37831

Dr. R. Silberglitt
FM Technologies, Inc.
10529-B Braddock Rd.
Fairfax, VA 22032

Dr. Michael Readey
Caterpillar, Inc.
Technical Center – E,
PO Box 1875
Peoria, IL 61656-1875

Dr. J. Jonkouski
United States Dept. of Energy
DOE Field Office
9800 S. Cass Ave.
Argonne, IL 60439-4899

Dr. C. Sorrell
U. S. Department of Energy
Office of Advanced Industrial Concepts, CE-232
1000 Independence Avenue
Washington, DC 20585

Dr. C. H. Henager, Jr.
Pacific Northwest National Labs
Materials/P8-15
902 Battelle Blvd.
P.O. Box 999
Richland WA 99352-0999

Dr. A. P. Thomsia
Lawrence Berkeley Lab
Center for Advanced Materials
MSD Bldg, MS62-203
Berkeley, CA 94720

Dr. I. Reimanis
Colorado School of Mines
Dept. of Met. & Matls. Engrg.
Golden, CO 80401

Dr. R.J. Gottschall (DOE/BES)
U.S. Dept. of Energy
Division of Materials Sciences
19901 Germantown Rd.
Germantown, MD 20874-1290

Copies	MS	
1	1435	K. Hays, 1800
1	1434	J. Phillips, 1802
1	0367	M.F. Smith, 1833
7	0367	F. M. Hosking, 1833
3	0367	J.J. Stephens, 1833
5	1411	P. Vianco, 1833
1	1411	D.B. Dimos, 1843
5	0367	S.J. Glass, 1843
1	0367	S. L. Monroe, 1843
5	1349	R .E. Loehman, 1843
1	1349	W.F. Hammetter, 1846
1	9014	E.L. Hoffman, 2251
1	9402	C.H. Cadden, 8724
1	0847	H.S. Morgan, 9123
1	1421	G. A. Samara, 1120
1	0847	M. Neilsen, 9123
2	0959	C. Walker, 14171
1	0959	R. L. Poole, 14171
2	0899	Technical Library, 9616
1	0612	Review/Approval Desk, 9612 for DOE/OSTI
1	0899	Central Technical Files, 8940-2
1	0161	Patent and Licensing Office, 11500
1	1380	Technology Transfer, 4331